UNIVERSIDADE DA BEIRA INTERIOR

Engenharia

Analysis and Development of Numerical Methodologies for Simulation of Flow Control with Dielectric Barrier Discharge Actuators

Mohammadmahdi Abdollahzadehsangroudi

Tese para obtenção do Grau de Doutor em

Engenharia Mecânica

(3° ciclo de estudos)

Orientador: Prof. Dr. José Carlos Páscoa Marques

Co-orientador: Prof. Dr. Paulo Jorge dos Santos Pimentel de Oliveira

Covilhã, Outubro de 2014

To my mom, Simin, and my dad, Morteza

Acknowledgments

First of all I would like to thank my supervisor, Prof Jose Páscoa for believing in me and for giving me the great opportunity to do this PhD. Thank you Prof Páscoa, as much for the entire thing that you have provided for me to work. I really enjoyed the moments that we had conversations about work and future and everything, specially the moments that you put me back in the correct way of thinking. It was a great pleasure and honor to have your support. It will be a pleasure for me to have opportunities to do research under your supervision.

I also want to thank my co-supervisor, Prof Oliveira, whose cooperation improved the quality of the works that I produced. I need to thank him because of all the moments that I was unexpectedly appearing in front of the door of his office and asking questions.

I want to thank all my colleges (Rui Oliveira, João Morgado, Amilcar Baptista and Carlos Xisto) in the ClusterDEM lab that made me happy and made the working condition full of energy and happiness. Indeed, besides being colleges you were my truly friends that helped me to adapt myself to the new life in Covilhã. Without friends it was looking hard to be concentrated three years on work.

Thank You All

Abstract

The aim of this thesis is to investigate and develop different numerical methodologies for modeling the Dielectric Barrier discharge (DBD) plasma actuators for flow control purposes. Two different modeling approaches were considered; one based on Plasma-fluid model and the other based on a phenomenological model.

A three component Plasma fluid model based on the transport equations of charged particles was implemented in this thesis in OpenFOAM, using several techniques to reduce the numerical issues. The coupled plasma-fluid problem involves wide range of length and time scales which make the numerical simulation difficult. Therefore, to obtain stable and accurate results in a reasonable computational run time, several numerical procedures were implemented including: semi-implicit treatment of coupling of Poisson equation and charge density equation, super-time-stepping and operator splitting algorithm.

We examined our code for a constant positive voltage, testing for the dependency of the behavior of the current density to the selected numerical scheme. In addition, although there is no clear numerical or experimental benchmark case for DBD plasma actuator problem, the developed plasma solver was compared quantitively and qualitively with several numerical works in the literature. Afterward, the developed numerical methodology was used to explore the possibility of influencing the flow, with higher speed, using nano-second (NS) pulsed DBD plasma actuator. Therefore, the interaction of the transonic flow and actuation effects of DBD plasma actuator with nano second pulsed voltage was simulated. The effect of gas heating and body force was calculated by the plasma solver and was supplied into the gas dynamic solver for simulating the flow field. Moreover, the results of the plasma fluid model were used to develop an energy deposition model. It was shown that the energy deposition model is able to capture the main features of the effect of NS DBD plasma actuators correctly, with less computational time. It was also shown that fast energy transfer, from plasma to fluid, leads to the formation of micro-shock waves that modify locally the features of the transonic flow.

Although the numerical efficiency of the plasma fluid model was improved, the computational cost of simulating the effect of DBD plasma actuator on a real scale flow situation was still high. Therefore, a simple model for plasma discharge and its effect on the flow was developed based on scaling of the thrust generated by DBD plasma actuators. The scaled thrust model correctly predicts the nonlinear dependency of the thrust produced and the applied voltage. These scales were then introduced into a simple phenomenological model to estimate and simulate the body force distribution generated by the plasma actuator. Although the model includes some experimental correlations, it does not need any fitting parameter. The model was validated with experimental results and showed better accuracy compared to previous plasma models.

Using a simple phenomenological model that was developed here, a numerical study was conducted to investigate and compare the effect of steady and unsteady actuation for

controlling the flow at relatively high Reynolds number. Firstly it was shown that the size of the time-averaged separation bubble is greatly reduced and the flow structure is sensitive to the frequency of burst modulation of DBD plasma actuators. The results also confirmed that in the case of unsteady actuation, the burst frequency and burst ratio are crucial parameters for influencing the capability of the actuators to control the flow. It was found that burst frequencies near the natural frequencies of the system were able to excite the flow structure in a resonance mode. This observation also confirmed that with proper frequencies of excitation, the flow structure can be well rearranged and the flow losses can be reduced.
In the end, Plasma actuators were used for controlling the flow over the Coanda surface of the ACHEON nozzle. When the plasma actuator was used, it was possible to postpone separation of the flow and increase the deflection angle of the exit jet of the nozzle. To find the optimum position of the actuators, seven DBD actuators in forward forcing mode were placed over the Coanda surface considering the numerically obtained separation points. Results show that when the actuator is placed slightly before the separation point, enhanced thrust vectorizing with the use of DBD actuator is achievable. Preliminary results of the experiments agree with planned/foreseen deflection angle obtained from numerical computation.

Keywords

Dielectric Barrier discharge actuator, Plasma Fluid Model, phenomenological DBD model, Flow control

Resumo

O objetivo deste trabalho visa a investigação e desenvolvimento de diferentes métodos numéricos para modelação de actuadores a plasma de Descarga em Barreira Dieléctrica, (DBD), tendo em vista o controlo do escoamento na camada limite. Esta modelação numérica foi abordada de duas formas diferentes, uma baseada num modelo de "plasma-fluid" e outra fundamentada num modelo fenomenológico.

Neste trabalho é usado um modelo "plasma-fluid" de três componentes que é baseado numa equação de transporte para as partículas electricamente carregadas. Este foi implementado no software OpenFOAM fazendo uso de diversas técnicas para minimização de problemas numéricos que ocorriam na resolução das equações. O cálculo de um problema com acoplamento entre plasma e fluido envolve uma gama diversa de escalas, tanto temporais como dimensionais, trata-se então de uma simulação numérica delicada. Como tal, e por forma a obter resultados estáveis e precisos num tempo de cálculo considerado razoável, foram implementados diversos procedimentos numéricos, tais como o tratamento semi-implícito do acoplamento da equação de Poisson com a equação da densidade de carga, o super-passo-tempo e ainda um algoritmo do tipo divisão de operador.

Foi considerado o caso de uma diferença de potencial positiva, constante, e testada a dependência da densidade de corrente com os diferentes esquemas numéricos. Apesar de não existir atualmente uma base de dados, de tipo numérica ou experimental, com casos de teste para actuadores a plasma tipo DBD, o modelo computacional desenvolvido para calcular o plasma foi validado qualitativamente, bem como quantitativamente, usando os vários trabalhos numéricos disponíveis na literatura. Após esta validação inicial, a metodologia numérica desenvolvida foi utilizada para explorar a possibilidade de influenciar um escoamento de maior velocidade, através de actuadores a plasma tipo DBD com impulsos de tensão da ordem de nano-segundos (NS). Desta forma foi simulada a interacção entre um escoamento transónico e o efeito dos actuadores a plasma tipo DBD sobre o escoamento, usando pulsos de nano-segundos. O efeito térmico do gás, assim como a força resultante, foram calculados usando o modelo numérico para cálculo de plasmas desenvolvido neste trabalho. O resultado obtido é acoplado ao modelo de cálculo para a dinâmica de gases, o que torna possível simular as condições do escoamento resultante. Adicionalmente, os resultados do modelo de "plasma-fluid" foram reaproveitados para desenvolver um modelo de deposição de energia. Este demonstrou ter a capacidade de capturar correctamente as características principais do efeito de actuadores de plasma, de tipo NS-DBD, com um tempo de computação menor. Foi demonstrada que uma rápida transferência de energia, do plasma para o fluido, leva à formação de micro-ondas de choque que alteram localmente as características do escoamento transónico. Apesar da eficiência numérica do modelo de "plasma-fluid" ter sido melhorada, o seu custo computacional para a simulação de actuadores a plasma tipo DBD à escala real continua bastante elevado. Neste sentido, a partir de uma

escala de propulsão gerada pelo actuador plasma DBD, foi desenvolvido um modelo mais simples para a descarga do plasma e para determinar os seus efeitos sobre o escoamento.
O modelo inicial previa correctamente uma dependência não-linear entre a força propulsiva gerada e a diferença de potencial aplicada. Estas escalas foram então introduzidas num modelo fenomenológico mais simples para estimar, e simular, a distribuição de forças geradas pelo actuador a plasma. Apesar de o modelo incluir algumas correlações experimentais, este não requer qualquer parâmetro de afinação. O modelo foi validado com resultados experimentais, demonstrando melhores resultados quando comparado com outros modelos de plasma .
Utilizando um modelo fenomenológico simplificado, que foi desenvolvido no presente trabalho, foi feito um estudo numérico com o objetivo de investigar, e comparar, os efeitos que uma actuação estacionária e não-estacionária exibe sobre o controlo do escoamento a números de Reynolds relativamente elevados. Foi demostrado que a dimensão da bolha de separação é reduzida em muito e que a estrutura do escoamento é sensível à frequência da modulação "burst" do actuador a plasma tipo DBD. Os resultados também confirmaram que, para o caso de actuação não-estacionária, a frequência de "burst" e o "burst ratio", são parâmetros cruciais para influenciar a capacidade de controlo do escoamento por parte dos actuadores a plasma. Determinou-se que as frequências "burst", semelhantes às frequências naturais do sistema, são capazes de excitar as estruturas do escoamento num modo de ressonância. Esta observação confirma igualmente que, com frequências de excitação apropriadas, a estrutura de um escoamento de camada limite consegue ser correctamente modificada, e que as perdas no escoamento são reduzidas. Por fim, os actuadores a plasma foram utilizados para o controlo do escoamento sobre uma superfície Coanda de uma tubeira. Quando nesta foi aplicado um plasma, tornou-se possível retardar a separação do escoamento e aumentar o ângulo de deflexão do jacto gerado pelo propulsor. Por forma a encontrar a posição óptima para os actuadores, sete actuadores de tipo DBD foram distribuídos ao longo da superfície Coanda, tendo em consideração os pontos de separação do escoamento na camada limite obtidos numericamente. Os resultados mostram que quando o actuador DBD é colocado ligeiramente antes do ponto de separação do escoamento, há um aumento da capacidade de controlo e vectorização do jacto gerado. Os resultados preliminares das experiências efectuadas estão de acordo com o ângulo de deflexão do jacto previsto pelo modelo computacional.

Palavras-chave

actuadores a plasma de Descarga em Barreira Dieléctrica, modelo de "plasma-fluid", modelo fenomenológico, controlo do escoamento na camada limite

Table of Contents

List of Figures

List of Tables

Nomenclature

$\vec{a}$	Acceleration of charged particles ($m.s^{-2}$)
$\mathbf{A}$	Advection operator
$\vec{B}$	Magnetic field
C_p	Specific heat capacity at constant pressure ($J\ kg^{-1}\ K^{-1}$)
C_g	Capacitance of the gas side
C_d	Capacitance of the dielectric side
C_v	Specific heat capacity at constant volume ($J\ kg^{-1}\ K^{-1}$)
c	Chord length (m)
C_L	Lift Coefficient
C_D	Drag Coefficient
Co	Courant number
D_k	Charged particle diffusion coefficient (m^2s^{-1})
$\mathbf{D}$	Diffusion operator
e	Electron elementary charge $e = 1.6022 \times 10^{-19}\ C$
$\vec{E}$	Electric field vector ($kg.m.s^{-3}.A^{-1}$)
E	Total specific energy ($J\ kg^{-1}$)
$\vec{F}_{EHD}$	Electric Force density (Nm^{-3})
f	Frequency of applied voltage (Hz)
$f(t)$	Voltage waveform
f_s	Particle distribution function
F_β	Burst frequency (Hz)
F^+	Reduced burst frequency
$G(x)$	Guassian distribution
$\mathbf{H}$	Homogenous operator
I	Unity tensor
$\vec{j}$	Total Electric current flux (Am^{-2})
$\vec{J}$	Conduction current flux(Am^{-2})
k_B	Boltzmann constant ($m^2\ kg\ s^{-2}\ K^{-1}$)
Kn	Knudsen number
L	Actuator characteristic length (m)
l_e	Length of electrode (m)
l_d	Plasma region length (m)
m	Mass of particle (kg)
M	Mach number

n_0	Initial charge particle density (m^{-3})
n_k	Number charge particle density (m^{-3})
$\vec{n}$	Unit normal vector
P	Pressure (N m^{-2})
p_{th}	Electric power density (Wm^{-3})
r	Recombination coefficient (m^3s^{-1})
R	Air specific gas constant (J kg^{-1} K^{-1})
Re	Reynolds number
$\mathbf{R}$	Reaction operator
S	Source term
t	Time (s)
T	Temperature (K)
Δt	Time-step
U_∞	Free stream velocity (m s^{-1})
$\vec{u}$	Velocity of gas flow (m s^{-1})
v_k	Species velocity (m s^{-1})
$\vec{v}_b$	Background flow velocity (m s^{-1})
V_{ap}	Applied Voltage (Volt)
V_0	Voltage ampletitude (Volt)
W	Energy consumption (J)
x	x-coordinate (m)
$\vec{x}$	Coordinate vector (m)
x'	coordinate along the chord of airfoil (m)
y	y-coordinate (m)
y'	coordinate normal to the chord of airfoil (m)
z	Z-coordinate (m)

Greek symbols

λ	Mean free path (m)
$\vec{\Gamma}_k$	Fluxes of charged particles ($m^{-3}s^{-1}$)
ε_d	Dielectric Relative permittivity
ε_0	Permittivity of space (Fm^{-1})
$\bar{\varepsilon}$	Mean kinetic energy of particle
ϕ	Electric Potential (volt)
σ	Surface charge density (Cm^{-2})

δ	Delta function
μ_k	Charged particle mobility ($m^2V^{-1}s^{-1}$)
λ_D	Debye Length (m)
ω	Frequency (Hz)
$\vec{\omega}$	Particles velocity ($m.s^{-1}$)
τ	Average viscous stress tensor
β	Burst Ratio
ρ	Density (kgm^{-3})
ρ_c	Charge density (Cm^{-3})
α	Ionization coefficient, (m^{-1})
η	Attachment coefficient (m^{-1})
η_E	Fractional power deposited in electronic excitation
η_V	Fractional electron power deposited in vibrational excitation
η_{el-R}	Fractional electron power deposited in elastic and rotational excitation
τ_{VT}	Relaxation time for vibrational excitation (s)
κ	Thermal conductivity ($W\ m^{-1}\ K^{-1}$)
ξ	Effective fraction of energy deposition
γ	Secondary electron emission

Subscripts

ap	applied
bd	Break down
d	Dielectric
e	Electrons
ep	Electron-ion
h	Heavy particles
i	Ions
k	Particles
max	Maximum
Loss	Loss
Pro	Production
p	Positive ion
n	Negative ion
np	Ion-ion
0	Reference state
s	Surface
Sep	Separation

Sl	Shear layer
Shed	Shedding
sec	secondary
th	Thermal

1 - Introduction

Obtaining higher efficiency in aerodynamic systems is a crucial need. This could lead to several important advantages including, lower power consumption, lower pollution and safer operation. With advancement of the technology, new techniques need to be considered to replace the conventional methods that were used to achieve these objectives.

1.1 - Why to consider plasma actuators for flow control?

Flow control has been used generally to manipulate a particular flow field to achieve a desired effect. The control strategies are classified in several ways depending on the character of flow instabilities, the presence or lack of walls, the Reynolds number and Mach numbers. Usually, the aim of the control strategy is to reduce drag, enhance lift, augmentate the mixing of mass, momentum or energy, or to suppress the flow induced noise. Flow control techniques are categorized as being active or passive. Passive techniques require no auxiliary power and include geometric shaping to manipulate the pressure gradient, they use fixed mechanical vortex generators for separation control, or the placement of longitudinal grooves or riblets on a surface to reduce drag. Outside of the range of conditions where the flow is controllable by using the passive flow control techniques, for example on any aerodynamic device, the aerodynamic performance might reduce drastically. In other words, these passive flow control methods normally represent a continuous energy loss and they dissipate energy also when the flow does not need to be controlled.

In contrast, active flow control methods require energy expenditure such as jet vectoring using piezoelectric actuator, oscillatory blowing, piezoelectric actuators, synthetic jets. In addition, the most popular flow control methods usually involve the use of mechanical flaps, suction and blowing techniques. A detailed review of actuators suitable for active flow control purposes can be found in [1,2]. The use of active flow control is very important, in the field of aeronautical applications. Being applied to internal or external flows, efficient flow control systems are capable of manipulating the flow to achieve certain desired effects, such as drag reduction, mitigation of noise pollution, and help to increase stall margins on airfoils. In order to achieve these results, flow control techniques are used mainly for separation control and laminar-to-turbulent transition suppression.

Among the several active flow control techniques, flow control techniques that use Electro-hydrodynamic (EHD) devices and electrical discharges (plasma) are considered very promising. Electric discharges generated along the surface of an airfoil have been proposed as micro-actuators able to exert significant forces in the boundary layers of aerodynamic surfaces. In general, plasma can induce a body force on the gas, heating the gas or producing radicals for combustion. Body forces can be exerted on charged species (electrons and ions) by electric

and magnetic fields and coupled to bulk gas by collisions. These forces can then be used to control the flow.

Recently, the introduction of plasma actuators in the field of aerodynamics has demonstrated to be very promising to achieve flow control leading to cost and weight reduction. Plasma-based devices exploit the momentum coupling between the surrounding gas and plasma to manipulate the flow. Unlike other flow control techniques, such as suction and mechanical actuators, plasma actuators require low power consumption, involve no moving mechanical elements, have low parasitic drag and a very fast frequency response that allows real-time control and, moreover, usually they have simple constructive requirements and they are not expensive. For these reasons, the plasma actuator has become a very promising and attractive device in the flow control community. On the other hand, their main drawback is their limited ability to control high speed flows and their sensitivity to the air conditions e.g., humidity.

1.2 - What is a plasma?

Plasma is a (conductive) state of matter (often called as the forth state of matter) consisting of a mixture of positive and negatively charged particles, unstable neutral radicals and ground state atoms and molecules. Owing to self-generated electric fields plasmas are quasi neutral, meaning that the positive and negative charge densities are almost equivalent, except over a small characteristic length scale (the Debye length) where separation of charge is significant.

1.3 - Thermal and non-thermal plasma discharges

Different types of electrical discharges have been used in aerodynamic actuators, such as Dielectric Barrier discharge, DC corona discharge, radio frequency discharge (RF) (Mega Hertz), microwave discharge (MW) ((Giga Hertz)), DC glow discharge and laser created plasmas (Pico Hertz). The selection of the discharge type is determined by the particular flow control conditions. Furthermore, atmospheric pressure plasmas can be classified according to whether they are in thermal equilibrium or non-equilibrium [3]. In a plasma the temperature is determined by the average kinetic energy of its components. However, a plasma can exhibit multiple temperatures, usually one for the heavy particles T_h and one for the electrons T_e unless sufficient collision occurs between them. Because of the large difference in mass between electrons and other particles the temperature of these two species remains different in many conditions. When $T_e \cong T_h$ the plasma is considered in local thermodynamic equilibrium (LTE) and termed as thermal plasma. These discharges are characterized by high temperature of the gas and a Maxwellian velocity distribution function of particles. Arc and inductively coupled plasma discharge, as in Plasma Torches or the fusion plasma devices,

sparks and lightning belong to this group. Microwave plasma sources can be thermal or non-thermal plasma, depending on the operating conditions.

Non-thermal plasmas are typically characterized by a relatively low gas temperature and high kinetic energy of electrons ($T_e >> T_h$). In this case the plasma is called non-equilibrium or non-thermal plasma. Such plasma is formed by applying a very high electric field over a very short time duration (nano-microsecond) which preferentially heats the electrons to very high temperatures (10 electron Volts or more) while preventing thermalization of the gas. Preferentially heating the electrons to very high temperatures allows the discharge to efficiently and rapidly ionize and dissociate the gas mixture without losing too much energy to thermalization or vibrational excitation. The main feature of non-thermal plasmas is that the most part of the electrical energy injected in the system is used for the production of energetic electrons rather than heating the gas, while the neutral species and ions remain relatively cold because of the low energy exchange with light particles. The electrons have enough energy to ionize other molecules and atoms, and to generate excited species and other electrons. Dielectric Barrier discharges (DBD) is often classified in the non-thermal plasma category. In other words, this discharge is characterized by low gas temperatures and rapid chemistry.

1.4 - Dielectric barrier discharges

Among the electrical discharge actuators, surface Dielectric Barrier discharges (sDBD) and surface DC corona discharges (sDCD) are mostly used for low speed flows at atmospheric pressure and they can be generated on the top of the surfaces. The sDCD plasma actuators involve the placement of two electrodes, which are both exposed to the air, on the surface of a dielectric separated by a fixed distance. The application of a high DC voltage potential across the electrodes ignites weakly ionized plasma that is capable of inducing flows up to 5 m/s. One major disadvantage of the corona discharge actuators is the glow-to-arc transition that occurs at large potential differences. This transition introduces a large surge of current towards the anode, effectively creating a short circuit.

sDBD produce highly non-equilibrium plasmas that provide high density active species including radicals, energetic electrons and ions but still has a moderate gas temperature. The major difference between the sDBD and the surface corona discharge is the presence of a dielectric barrier separating the anode and cathode, in the former configuration. The dielectric layer is the key component of the DBD actuator. At high pressures, a non-equilibrium plasma will typically transit to a thermal spark plasma unless there is some mechanism to prevent the transition. The dielectric layer limits the amount of charge transported by a single micro discharge and distributes the micro discharges over the entire electrode. The use of a dielectric layer inhibits the flow of conduction current to the plasma and prevents the discharge from transitioning to a spark keeping the resultant plasma in non-

equilibrium. Such plasma discharges are effective at producing reactive radical species while minimizing energy expended to heat the gas. Therefore, surface DBDs are generally preferred to surface DC corona discharges since sDBD operates on a self-limiting process through the reduced electric field potential by the surface charge accumulation, thus preventing the corona-to-spark transition.

The DBD plasma actuators produce a significant thrust by asymmetric span-wise electrode configurations through momentum transfer. The momentum transfer between the plasma and gas is due to collisional momentum transfer between charged ions and neutral atoms. Such actuation of the flow is active and nearly instantaneous. The advantages of the DBD plasma actuators are the absence of moving parts, their compactness and application in almost any location. Most importantly they do not affect the shape of the aerodynamic element on which they were applied for controlling the flow. Compared to conventional actuators for active flow control, the life of DBD actuators will be much longer than mechanical devices such as synthetic jet actuators.

The basic configuration of a DBD plasma actuator is shown in Fig. (1.1). However, there are several configurations that are possible based on the different arrangements and geometry of the electrodes. In the basic linear surface DBD plasma actuator, two electrodes are typically separated by a dielectric barrier usually glass, Kapton or teflon as depicted in Fig. (1.1). When a high AC voltage signal of sufficient amplitude (5-40kVpp) and frequency (1-20 kHz), is applied between the electrodes, the intense electric field partially ionizes the surrounding air producing non-thermal plasma on the dielectric surface. The collisions between the neutral particles and accelerated ions generate a net body force on the surrounding fluid leading to the formation of the so called “ionic wind”. The body force can be used to impart the desired flow control on a given fluid system. For the sDBD configuration the momentum coupling of the plasma and fluid induces an initial vortex that propagates downstream. This can be observed on the PIV measurements of Post [4]. The dielectric barrier introduces a region of large electric breakdown strength, allowing for the application of larger potential differences and thus larger electric field intensities in the plasma region.

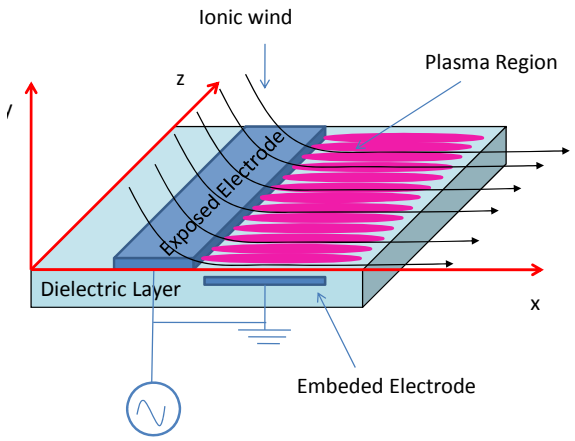

Fig. 1.1: Schematic of sDBD actuator.

As was mentioned before, the presence of the dielectric barrier increases the stability of the plasma, preventing a glow-to-arc transition at typical potentials for which this would occur on the surface corona discharge. The dielectric layer blocks all (or most) of the current flow to the buried electrode and alters the electric potential across the discharge and effectively creates a capacitance in the discharge circuit.

Another main feature of the DBD is its operation over a wide range of pressures [5]; from as low as 0.1 bars to high atmospheric pressures. At low pressures DBDs operate in a Townsend breakdown regime generating a diffuse glow discharge. At atmospheric pressure, the realization of a diffuse discharge is restricted to limited conditions of geometry, electrical parameters and gas composition, and DBDs operate usually in a streamer discharge in which several narrow discharge filaments are typically formed. The streamer regime constitutes a strongly interacting system of discharges exhibiting cooperative behavior. This leads, under specific conditions, to the formation of coherent spatial configurations that have been observed in different types of experimental setups. However, micro-discharges seem, to some extent, to occur at random within the discharge gap for most applications of DBDs.

1.4.1 - Three dimensional DBD plasma actuators

Many varieties of this basic design have been tested (Fig. (1.2)). The serpentine DBD actuators [6–10] were developed to induce flow mixing. Such three-dimensional novel actuators produce much better flow mixing downstream of the actuator than standard two-dimensional (linear) actuator. Three-dimensional plasma effects extract momentum from an upstream flow injecting it into the bulk fluid through localized pinching and spreading effects (local swirl).

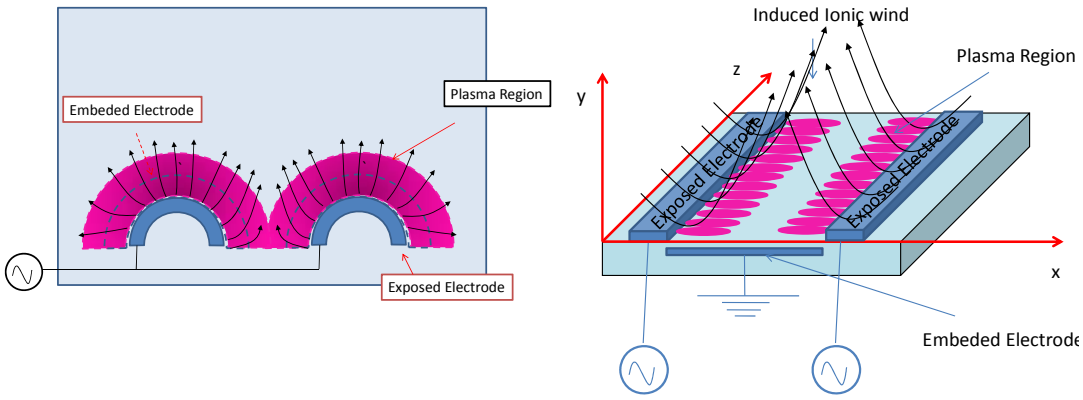

Fig. 1.2: Three dimensional plasma actuators a) Curved electrode (horse shoe) plasma actuator b) plasma actuator synthetic jet.

1.4.2 - Nanosecond-DBD plasma actuators

To improve the performance of DBD plasma actuators and their discharge behavior, different voltage shapes have been employed. However, in the aerodynamic field, two major types of DBD plasma actuators are currently under consideration; The Alternating Current AC-DBD and the Nanosecond DBD (NS-DBD) plasma actuators. They differ in terms of the shape of the voltage signal that drives the discharge and, thus, the mechanism of operation.

As was mentioned before, plasma actuations are capable of influencing the momentum boundary layer significantly in low speed regime. Therefore, non-equilibrium DBD plasma actuators find limited application for high speed flows. This is due to the inherent losses associated with the momentum exchange between the charged and neutral particles, and due to exorbitant power budget. As an alternative, high-voltage nanosecond pulsed plasma actuators are becoming a quite attractive option for high speed applications [6]. The main mechanism of impact for nanosecond pulsed plasma actuators is the energy transfer. When a DBD is excited by a nanosecond pulsed voltage, the temperature near the surface is increased (400K for 50ns pulse durations). Such fast heating (less than microsecond) of the gas layer leads to periodic flow disturbances that could control boundary layer separation and reduce acoustic noise at a Mach number close to one.

1.5 - Applications of DBD plasma actuators

Being one of the most popular plasma discharge and electrode configurations, especially for atmospheric pressure plasma application, DBD has widely been used in various fields and industrial applications. DBD plasma actuators have been used primarly in the chemical industry, mostly for ozone production. They have been used also in the lithography related applications such as Surface cleaning, modification, thin film deposition and surface etching [11].

Very promising results for the application of plasma actuators have been observed in a wide range of applications, in particular targeted at the aeronautic community and for flow control purposes. Moreau [12] and Corke et al. [13] showed detailed reviews of aerodynamic applications of plasma DBD actuators that are effective in controlling the flow. Comprehensive reviews on plasma actuators for aerodynamic flow controls have been published recently [14,15]. Corke et al [13,16] provide an overview of the physics and modeling of SDBD (single dielectric barrier discharge) plasma actuators. They highlight some of the capabilities of plasma actuators through examples from experiments and simulations. Caruana [17] has given a survey of methods of air flow control for aircraft performance improvement. He has presented a short overview of non-plasma devices and studied ways for flow control. Touchard [18] also made a detailed review of the designs and associated setups for different aerodynamic plasma actuators developed in these last twenty years, he further discussed the limits and the prospects of plasma actuators considered for airflow control.

1.5.1 - Flow separation control

Separation control has also been successfully achieved for a wide range of geometries, including airfoils, wings and circular bodies. The mechanism responsible for separation control by DBD plasma is most often associated with the wall jet generation described earlier, however the effects of DBD in boundary layer tripping or in energizing or amplification of instabilities are still in debate and depend on the flow system under consideration. For separation control, explicitly, the state of the boundary layer (laminar or turbulent) just upstream of the actuator will also play a role. Unlike traditional unsteady jets, created with voice coils or piezo-ceramic disks, the exact location at which the plasma actuator accomplishes control is not immediately obvious, but actuators placed at or slightly upstream of the separation location give favorable results.

The pioneering work of Roth et al. [19,20] demonstrated the possibility of using plasma actuators based on surface DBDs for aerodynamic applications. Surface discharges can generate airflow with velocities less than 10 m/s, while active airflow control with SDBDs has been demonstrated for low subsonic velocities up to 30 m/s. Greenblatt et al. [21] studied the mechanism of flow separation control experimentally, and computationally, using pulse-modulated DBD plasma actuation on a stalled flat plate airfoil, at a Reynolds number of 3000. They carried out a parametric study where the pulse-modulation frequency, duty cycle, and peak plasma body-force were varied. A direct effect of the forcing frequency on lift was documented. The mechanism of lift enhancement was based on severing the leading-edge vortical layer, whose downstream component then merged with a naturally growing downstream vortex. Jayaraman et al. [22] numerically investigated the potential of using DBD to control flow at low Reynolds numbers for applications such as micro air vehicle (MAV). Both co-flow and counter-flow actuation strategies were considered for the purpose of the flow control. The co-flow approach offers momentum enhancement via favorable pressure gradient in the near wall region while the counter flow approach can trigger earlier separation, and transition, by introducing adverse pressure gradients. Jolibois et al. [23] studied the influence of the actuator locations on the airfoil surface using both steady and unsteady DBD plasma actuators. These experiments show that the plasma actuator is more effective when it acts close to the natural separation location, and that the power consumption can be highly reduced in using a non-stationary actuation. Mabe et al. [24] tested airfoils of various sizes with varying free stream velocity, angle of attack, and deflection angle. Two different sets of experiments based on the actuator location were conducted. It was determined that the input momentum was very weak and not sufficient to prevent separation at Reynolds numbers greater than 100,000. Results showed that the plasma actuators only provided sufficient momentum to be effective at very low Reynolds numbers, such as those appropriate to micro-air-vehicles.

As was mentioned before, the AC discharge is the most well-known one, and it results in momentum increase due to ionic wind created by the discharge. But this ionic wind is quite

slow (velocities up to several meters per second) and thus the range of flow speeds at which this type of actuators is effective is limited. To expand the range of the applications of the DBD actuators to higher speed ranges nanosecond plasma discharges are considered. The mechanism of flow control by nanosecond plasma discharge is different. It is supposed that the vorticity is created by the shock wave, which is produced from the layer of the hot gas. This hot gas is generated during the fast thermalization process, in which up to 60% of the discharge energy is converted to heat in less than 1 μs.

Little et al. [25] demonstrated the efficiency of NS-DBD pulses on an airfoil leading edge separation up to Reynolds number (Re) = $1x10^6$ (62 m/s). Similarly, Correale et al [26], also performed an experimental study of flow separation control with a nanosecond pulse plasma actuator. Different geometries of the actuator were tested at flow speeds up to 80 m/s to control the flow over three different airfoil models. In stall conditions a significant lift increase of up to 20% is accompanied by drag reduction (up to 3 times). The dependence of this effect on the position of the actuator, on the wing, was studied showing that the most effective position of the actuator is on the leading edge, in case of leading edge separation. Experiments using Schlieren imaging showed that the shock wave propagation and formation of large-scale vortex structure in the separation zone are the mechanism of separation elimination, in the case of the nano second pulsed actuators. Rethmel et al. [27] extended the exploration on the use of dielectric barrier discharge plasma actuators driven by repetitive nanosecond pulses to higher Mach numbers (M) (0.26, 93 m/s) and Re ($1.15x10^6$) using an 8 inch chord NACA 0015 airfoil commonly studied for active flow control. A comparison of NS-DBD and AC-DBD plasma actuations was conducted at various Re to demonstrate the difference in control authority between the two methods.

1.5.2 - Turbo-Machinery application

As DBD plasma actuators are thin, surface mounted, and do not require internal volumes or passages, they are particularly attractive for gas turbine and turbo-machinery applications. Plasma actuators also have been tested for applications regarding turbo-machinery mostly for the purpose of reducing the tip losses in low pressure turbine or increasing the axial compressor pressure ratio. Van Ness et al. [28] proposed using the active flow control capability of a plasma actuator to reduce blade tip losses in a low pressure turbine. A 29.5% reduction in maximum pressure loss, at an axial chord Reynolds number of 10^5, was achieved during actuation. Wall et al. [29] performed experiments using a pulsed DC dielectric barrier discharge plasma actuator to reattach separated flow of a highly loaded turbine blade in the suction surface. Using phase locked particle image velocimetry (PIV) he showed that at a pulse rate of 100 pulses per second the 70% velocity contour in the boundary layer was moved closer to the wall by 39%. Vo [30] modeled a circumferential plasma actuator on a compressor case, near the compressor rotor, to induce axial flow acceleration within the tip clearance gap region, with the intention of suppressing tip clearance flow responsible for spike

formation and short length-scale rotating stall inception. The simulations indicated that actuation effectiveness decreases with increasing compressor speed and that stronger actuation strength than that of conventional plasma actuators may be needed. Wu et al. [31] used plasma actuators in a Teflon compressor case in order to measure the efficiency increase of a subsonic axial compressor during actuation. They determined the pressure rise coefficient and flow coefficient for the compressor test rig with and without plasma actuation to represent compressor performance. The experiment showed that, with plasma actuation, the mass flow coefficients near stall decreased by as much as 5.2% at a constant rotor speed. Williamson [32] studied the flow in an axial compressor using plasma actuators via wake measurements in response to various plasma actuator and compressor operating conditions. Both leading edge and 1/4 chord plasma actuator configurations were examined in the counter and co-flow directions. The compressor rotor momentum measurements showed that leading edge actuation can have an unpredictable effect and may cause an increase in drag. Huang et al. [33] used a linear cascade of turbine blades to examine the effects of using plasma actuators for controlling separation. They characterized the flow using surface pressure, Laser-Doppler Velocimetry, and hot wire measurements. It was determined that unsteady actuation was more effective than the steady actuation at reattaching the separated flow, while using less power.

1.5.3 - Control of laminar to turbulence flow transition

There have been extensive researches on the study on the effect of DBD plasma actuators for turbulent boundary layer control. Most numerical and experimental studies regarding altering the characteristics of turbulent flows with plasma actuators were focused on inducing span-wise flow oscillations for controlling turbulent flows [34–36], including also control of transition from laminar to turbulence boundary layers [37,38] .

Span-wise flow oscillations is one of the most effective techniques applied for turbulent flow control. In this context, Wilkinson [35] had used oscillating weakly ionized surface plasma for turbulent drag reduction. Surface plasma was used as a source of span-wise oscillation of the flow. However, in the experiment of Wilkinson, the induced oscillations were small and the effect was negligible due to the small frequency (100 Hz) of the surface plasma. The applied DBD was in a three electrode configuration with one top electrode and two bottom electrodes. Jukes et al. [36] also tried to use plasma actuators for creating span-wise oscillations on the flow. They have used also a three electrode stream-wise placed plasma actuator configuration, with one common grounded electrode and the other two at the surface. If just one set of electrodes was activated, plasma was formed to one side of the exposed electrode. By switching between the activated set of electrodes, an optimum frequency for the span-wise oscillation of the flow in the near wall region was achieved. The results show around 45% drag reduction downstream of the plasma actuators. In comparison to span-wise flow oscillations span-wise traveling waves are more favorable, as they don’t

need to increase in forcing amplitude to achieve higher drag reduction. Span-wise travelling waves collect the low speed fluid and spread it over the wall surface as the waves are propagated in the span-wise direction. Wally and Choi [39] used DBD plasma actuators to create a four phase span-wise traveling wave instead of a span-wise traveling oscillation to control the turbulent boundary layer. This configuration allows both a generation of bi and uni-directional forces. A review of the control techniques of turbulent boundary layers with span-wise oscillations and travelling waves generated by plasma actuators is presented in [40].

Schatzman and Thomas [41] experimentally studied the effect of span-wise and stream-wise oriented single DBD plasma actuators to control a turbulent boundary layer separation. The stream-wise rotated DBD actuator (plasma stream-wise vortex generator, PSVG) configuration uses a single covered electrode. The multiple exposed electrodes, with spacing, are aligned parallel to the incoming flow. Instead of a wall jet, the PSVG arrangement is designed to generate pairs of counter-rotating vortices that intended to enhance the cross-stream mixing within the boundary layer. The difference between the configuration used for stream-wise oriented actuators and the ones used in [39] is that there is no switching of the activated electrode to create span-wise oscillations or span-wise traveling waves. They have also showed that effective control authority was achieved by creating counter-rotating vortices within the boundary layer that promote mixing of high and low momentum fluid.

Plasma actuators were used to attenuate the transient growth of the disturbances produced by an array of roughness elements by Hanson et al. [42]. Four stream-wise oriented actuators were used to generate impinging wall jets, causing span-wise periodic stream-wise vorticity at a suitable span-wise wave number to damp the disturbance created by the roughness elements. The results of Hanson et al [42] showed that plasma actuators were able to generate a primary disturbance mode and additional weaker modes similar to that of the roughness array and thus, minimize the effect of disturbance caused by the roughness elements. Moreover, Hanson et al [43] extended the use of plasma actuators for closed-loop control of bypass transition based on feedback from wall-shear stress measurements. A controller was designed to minimize the residual disturbance energy in the output measurements at the target instability span-wise wave number. By considering a range of static roughness element heights, measurements of the disturbed flow state were correlated with simultaneous shear stress measurements to form empirical models of the flow state, which were then used for model-based control decisions, by providing them from shear stress inputs to the controller. The range voltages, applied in the tests of the plasma actuators provided disturbance amplitudes similar to those caused by the roughness elements, but with opposite phase.

Widmann et al. [44] presented two different operational modes for the DBD actuators namely: the boundary-layer stabilization mode, in which the actuator is operated continuously (quasi-steady); and the hybrid mode, in which the actuator amplitude is modulated about a steady value to reduce the amplitude of the artificially excited TS

(Tollmein Schlichting) waves to obtain transition delay. The physics of the interaction of the DBD actuators and the TS wave in these two modes is different. For achieving boundary-layer stabilization a quasi-steady body force are applied. By inducing momentum into the boundary layer, its stability characteristics are modified such that the existing perturbations are dampened indirectly by the more stable boundary-layer velocity profile. In contrast, when an unsteady body force is produced, the body force acts directly on the velocity fluctuations of the wave. In the hybrid mode, Because of the force offset, the actuator can counteract positive as well as negative velocity deviations of the waves whereas the active wave cancelation (AWC) only enables forcing in one direction. Results confirmed the impact of the quasi-steady body force on the wave amplification and in the boundary-layer stability, and cancelation of the periodic disturbances when the plasma actuator is operated in hybrid mode. Similarly, Kruz et al. [45] conducted an experimental and 2D numerical study to control the boundary layer transition on an Onera-D airfoil by using DBD plasma actuators. Both steady and unsteady modes of actuation were considered. On one hand, the effect of steady actuation was used to modify the mean velocity profile in order to reach boundary layer stabilization, and on the other hand, unsteady actuation was used to achieve active wave cancelation in a direct frequency mode by counteracting the growing instabilities within the boundary layer (TS waves). The results of the stability computations, as well as experiments, showed that DBD plasma actuators used in a steady mode have a stabilizing effect on the boundary layer. The modification of the mean velocity profiles was such that the amplification of the disturbances was reduced and transition was delayed. In an unsteady mode two DBD actuators were used. The first one was activated for the excitation of the TS waves and the other one was used to counteract with these waves at a higher beating frequency. Also, for efficient counteraction of the TS waves and of the transient plasma force, an active control system with a closed-loop was used to detect the waves and optimize the actuation, by adjusting the phase relation between the TS waves and the actuator excitation signal. The results showed that the destructive interference of the transient body force reduced the amplitude of TS waves locally.

Grundmann et al [38] also studied the effect of plasma actuators on boundary layer flow, both experimentally and numerically. A modified numerical model, based on a linear body force, was calibrated with the results of experiments in quiescent air for considering the effect of plasma actuators. The improvement of the previous model replaces the linear decrease of electric field with asymptotic exponentional decay. The results showed that the calibrated numerical model in combination with RANS (Reynolds Averaged Navier Stokes) model can correctly simulate the effect of plasma actuators with addition of momentum to boundary layer when free stream velocity exist. Following the work of Grundmann et al. [38], Duchmann [46] attempted to delay the boundary layer transition over a flat plate with adverse pressure gradient using plasma actuators. In this case, flow transition was initiated naturally by Tollmien–Schlichting waves. The effect of DBD on the flow control was presented through both statical analysis and integral quantities. The flow control goal was achieved

through attenuating the disturbances inside the flow and altering the flow stability. The results show that the DBD plasma actuator successfully controls the flow near the transition region, it increases the hydrodynamic stability of the boundary-layer flow and reduces the disturbances in stream-wise velocities. However, in the fully turbulent region, the results didn't exhibit any effect of control on the flow. Moreover, Duchmann [46] mentioned that excessively high voltages and associated fluid accelerations have the additional disadvantage that an overshoot in the velocity profile can occur, which leads to a destabilization of the flow, rendering the actuation useless for transition delay.

1.5.4 - Plasma assisted combustion

Recently, studies of plasma assisted combustion (PAC) have shown many possibilities for improving combustion efficiency [3,6,47,48]. It was reported that the improvement in efficiency was achieved: by enhancing the flame propagation speed; enhancing the breakdown of fuel and the creation of reactive radicals; the enhancement of chemical reactions due to heating and active particle generation; mixing oxidizer with fuel in the flow; flow structure modification for combustion stabilization; fast local ohmic heating of the medium; non-equilibrium excitation and dissociation of oxygen and fuel molecules; shocks/instabilities generation; momentum transfer in electric and magnetic fields.

1.6 - Background physics of fundamental processes of plasma

There are several fundamental processes that play the major role in plasma physics. In the following, some of them are explained shortly.

1.6.1 - Electron avalanche

The fundamental mechanism that drives the creation of plasma from a neutral gas by an electric field is the electron avalanche. In any volume of gas, before any voltage is applied, the gas is electrically neutral and only a small quantity of charge carriers (electrons with background densities on the order of $10^4 - 10^9 m^{-3}$) are present that are caused by cosmic rays, natural radioactivity and the detachment of negative ions. Thus, if the electric field is high enough these will accelerate and collide with molecules of the gas, thereby releasing more electrons, which in turn will do the same, creating what is known as an electron avalanche. In other words, the process in which, in the presence of a strong applied electric field, the initial "seed" electrons gain sufficient energy such that as they collide with the neutral gas, creating new electron-ion pairs (impact ionization) is called the electron avalanche.

1.6.2 - Electrical breakdown of gases

Electric breakdown is referred to the process that transforms a non-conducting material to a conducting one when a sufficient strong electric field is applied. Although the breakdown is a rather complex process that strongly depends on the system conditions it always begins with an electron avalanche. As the avalanche forms, the highly mobile electrons drift in the direction opposite to the electric field and diffuse radially outward giving the avalanche a teardrop shape. The large ions formed due to electron impact are relatively stationary compared to the mobile electrons, and tend to trail the electrons as they drift and diffuse. This results in a region of negative charge in the head of the avalanche and a positively charged region left in the trail of the electrons. The breakdown of the gas can be considered as being due to a sequence of electron avalanches which initially start at the electrode and drift towards the anode. In a more simple explanation, at a certain value of applied potential, the electrons gain enough energy to create an electron avalanche. One seed electron accelerates through the field to a high enough energy to knock an additional electron off neutral particles or other positive/negative ions. These additional electrons accelerate and cause even more ionization. This process is known as breakdown and the potential difference required to initiate is called the breakdown voltage.

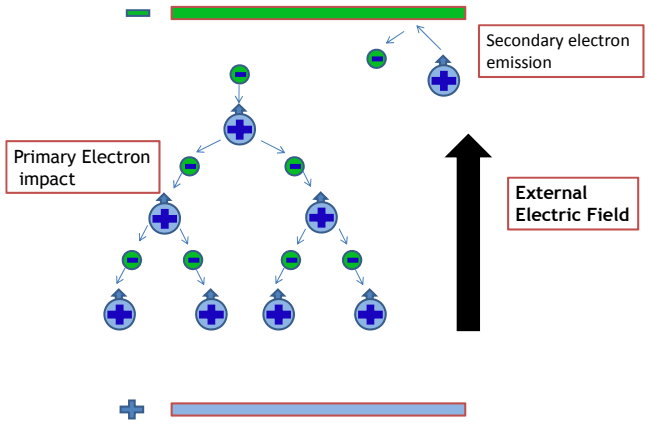

Fig. 1.3: Schematic of the Electron Avalanche process.

1.6.3 - Townsend breakdown mechanism

The discharge process at low pressure is called Townsend. In a simple system of electrodes, shown in Fig. (1.3), the seed electrons generated from an external source are accelerated by the electric field in the gap and reach the anode unless they are lost in the way by ion recombination or interaction with walls. If the external electric field becomes bigger, the smaller fraction of the electrons will be lost before they reach the anode. As a result, the electric current in the circuit, which is proportional to the number of charged species which reach the electrodes, initially increases with increasing voltage. As long as the net charge is

not sufficient to distort the field appreciably, the centre of the avalanche moves with the electron drift velocity appropriate to the uniform applied field. If, during the life of the avalanche secondary electrons are released then new avalanches will be created, and the total current will be amplified. Secondary electrons are released either by positive ions or UV photons hitting the cathode, or by photo-ionization of the gas behind an avalanche. In this way the current grows exponentially by what is known as the 'Townsend breakdown mechanism' [49]. Central to this model of breakdown is the concept that each avalanche must provide a secondary electron prior to its absorption into the anode, in order to constitute a self-sustained discharge. The Townsend theory is generally valid for low to moderate values of Pd (Pd < 200 Torr cm) [50]. At lower pressures, the plasma is typically sustained by multiple electron avalanches which are ejected from the cathode, by ion or UV bombardment, and drift in the electric field.

1.6.4 - Streamer breakdown mechanism

At higher pressures (e.g. atmospheric), the process of gas breakdown occurs at a much faster rate than what is predicted by Townsend theory, due to the considerable space-charge generated during the first avalanche's transit through the gap. This different kind of breakdown is explained by the so called streamer theory. Streamer theory uses the concept of the electron avalanche to explain the breakdown process but it considers a single large electron avalanche rather than a series of avalanches as the mechanism of breakdown. When the electron avalanche grows to a size such that it is capable of partially shielding itself from the applied field, the propagation and growth of the avalanche changes remarkably. A single large avalanche forms an active zone (the streamer head), which propagates into the gap, producing other secondary electron avalanches due to a great enough induced electric field, which are drawn towards the primary avalanche. Essentially, a streamer is an ionization wave. In front of the wave (the streamer head) the separation of positive and negative charged particles shields the interior and causes a sharp enhancement of the electric field over a limited region just outside the streamer head. As the primary avalanche propagates into the gap it leaves behind a long, thin trail of quasi neutral plasma from which comes the term streamer. The subsequent plasma discharge is referred to as a streamer and consists of two features: an active head region where ionization and secondary avalanche production take place and an inert quasi neutral plasma tail left behind by the active region as it propagates.

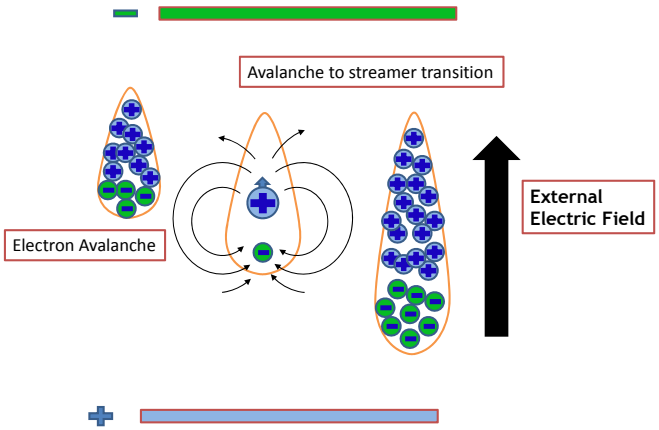

Fig. 1.4: Transition of electron avalanche to streamer.

The criterion for an avalanche to form a streamer is that the induced electric field of the electron avalanche should be of the same order as the applied electric field. In Fig. (1.4), if the gap distance, the gas pressure (density) or applied voltages are large then the amplification factor of electrons in the electron avalanche can become large. The charge produced by the electron avalanche can then become significantly enough that the charge in the electron avalanche head distorts the externally applied field. Unlike the electron avalanche, which propagates due to the drift of electrons in the field, the streamer propagation mechanism is wave like in nature, and is driven by the exchange of energy from kinetic energy of the ionization of charged particles and the subsequent displacement of the electrostatic field due to the new space charge (potential energy).

1.6.5 - Ionization processes

The fundamental process in plasma is the ionization because it is responsible for its generation and sustainment. There are different kinds of such processes (Fig. (1.5)). Direct ionization by electron impact is the basic plasma reaction, and includes the ionizations of non-excited atoms, molecules and radicals. It involves the interaction of an energetic electron hitting the other neutral species when its energy is high enough to create an ion-electron pair.

Preliminary exited neutral species can undergo further ionization in a stepwise ionization by electron impact. This kind of process is important in thermal, or highly energetic discharge, when the degree of ionization (ratio of electron and ion density) is high. Ionization by collision, with heavy particles can generate electrons during ion-molecular or ion-atomic collisions involving also vibrationally or electronically excited species. Chemical reactions are involved too. Photoionization processes generate electrons in the collision process between a heavy particle and a photon. Photoionization is important in thermal plasma and in the propagation process of a streamer channel.

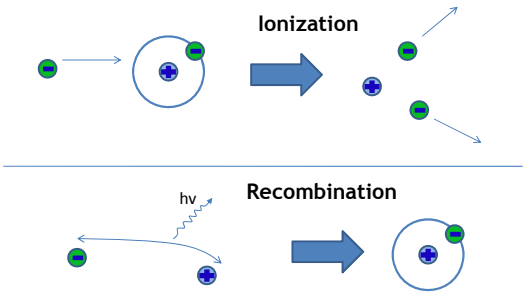

Fig. 1.5: Ionization and recombination processes.

1.6.6 - Electron and charged particles losses

Many processes cause the loss of a free electron and of charged particles. The balance between these processes and the ionization processes determines the degree of ionization and plasma density. Electron-ion recombination processes involve the neutralization of a positive ion with an electron. It is a highly exothermic reaction which needs a channel for accumulation of the energy released during the process. This can lead to molecular dissociation, creation of excited species, photon emission, etc.

Another process that causes the losses of the charged particles is the attachment process. The electron attachment processes are extremely important and are often responsible for the balance of charged particles especially in presence of an electronegative gas (such as O_2). An attachment process typically takes place in electronegative gases when a molecular fragment (dissociation products) has a positive electron affinity.

Ion-ion recombination processes come to play a role in the actual losses of charged particles when the electron attachment processes are involved in the balance of electrons and ions (electronegative gases). This process is the mutual neutralization of positive and negative ions in binary or three-body collisions. These processes can proceed by many different mechanisms and have very high rate coefficients.

1.6.7 - Secondary electron emission

This is a process of generation of new electrons by electrons or ions bombardment. The electron enters the ground state of the atom, and a second electron absorbs excess energy of neutralization [51]. The secondary electrons that are emitted from the cathode is an important process in sustaining a discharge. When ions produced by the electron avalanches drift, and eventually collide with the cathode, they can produce free electrons from the surface in a process called secondary electron emission.

1.7 - State-of-the-art related to the modeling of DBD plasma actuators

The optimization of DBD plasma actuator performance has to rely on a comprehensive numerical modeling. Moreover, a current major gap in the plasma flow control technology is the lack of self-consistent theoretical models, and also of robust computational tools that can provide an adequate simulation of momentum sources induced by the surface plasma discharges. There have been diverse numerical studies on DBD plasma actuators. Computational modeling of discharge plasmas can be classified into three types, namely: fluid models; kinetic/particle models; hybrid approaches; and simple phenomenological or empirical models. Kinetic models involve the solution of the Boltzmann equation for the species velocity or an energy distribution function in both space and time, or particle simulations, often using Monte Carlo methods, which are generally computationally more expensive than the fluid models. The models coming from a phenomenological approach and the circuit based models are the most popular. They have shown some success in mimicking the overall electrical characteristics of the discharge but are still limited, because they are inherently static and/or only allow a predetermined charge imposition. On the contrary, the first principle models are more suitable for capturing detailed fluid dynamics and are also computationally expensive. The choice of the model is also dependent on the regime of interest to model.

Here, in this thesis, we are interested in just two families of plasma actuator models. The first consists of chemistry based models (fluid models) [54–4,52] that attempt to spatially resolve the plasma phenomena directly and consist of a few moments of the Boltzmann equation. The second are algebraic models that are based on the solution of a Poisson's equation. These algebraic models generally require assumptions regarding either the charge density or electric field produced by the actuator. A detailed review of different approaches for modeling plasma actuators can be found in [55–57].

1.7.1 - Plasma-fluid models

The chemistry based family typically consists of drift diffusion type models. These models track the chemical species present in the plasma, such as electrons and ions, using a set of transport equations. The essential plasma physics such as ionization, recombination and streamer propagation are all modeled. In general, these models are capable of accurately resolving and predicting the plasma phenomena. However, the solution of these equations requires a very small spatial resolution, on the order of μm, to resolve the plasma phenomena. This scale is very challenging for realistic engineering geometries. This also imposes a significant restriction on the numerical time step, and prohibits the computation of high voltages at kHz frequencies. Because of this, the chemistry based family is not typically feasible to be used in the design and optimization of plasma actuators.

Primary attempts at DBD modeling were performed in Refs [58–60]. However, the physical models were inadequate and did not allow explaining some well-established experimental results regarding the DBD phenomena, even qualitatively. The challenge in modeling DBD plasma actuators comes from the physics of the problem. Generation, decay, drift, and diffusion of the electrons, and both positive and negative ions, must be correctly described by a consistent, comprehensive, physically-based model, and resolved by an accurate numerical scheme. Since it is the electric space charge that is responsible for the net force acting on the gas, the Poisson equation for the electric potential must be fully coupled with the other equations. Various processes occurring on the dielectric and metallic surfaces, such as electron attachment to the dielectric surface and secondary electron emission from metallic and dielectric surfaces must be included. An additional complexity for the modeling is the relatively high air density at which the DBD actuators operate. Another key issue of DBD operation, and modeling, is that the type of discharge changes as the voltage amplitude increases.

One of the first modeling attempts for DBD plasma actuators using plasma fluid models was accomplished by Roy [60] and Singh and Roy [61]. The modeling was performed in helium-like gas at 300 Torr for DBD, driven by the radio-frequency (RF) sinusoidal voltage. Continuity equations of electron and ion density were solved coupled with Poisson's equation to obtain spatial and temporal profiles of electron density, ion density, and voltage. However, the processes of surface charge accumulation, recombination and secondary emission, which are essential for the plasma discharges, were not taken into account. The simulations provided a qualitatively demonstration that the force in the positive half-cycle is due to the downstream positive ion motion.

Later, Roy and Gaitonde, [62], coupled their developed plasma model with hydrodynamic model for the description of the induced gas flow. Then, the complete problem of a dielectric barrier discharge at high pressure with axially displaced electrodes was simulated in a self-consistent manner. Model predictions for charge densities, the electric field, and gas velocity distributions were shown to mimic trends reported in the experimental literature. In [63], Singh and Roy, used an arrangement of multiple electrodes powered with pulsed DC voltage for controlling the flow on a conical fore body cross section of an aircraft. They had considered the effects of Joule heating of plasma, dielectric heating, and electro-dynamic force. It was found that electro-dynamic force contributes prominently to flow control, although Joule heating results in a high temperature of the dielectric surface.

Duan et al. [64] studied both experimentally and numerically the glow discharge of DBD actuators in sub-atmospheric conditions. Their results pointed to the existence of a critical frequency below which the DBD is uniform for almost all the applied voltages. Moreover, the simulations results reveal that the distribution of the space electron density, at the beginning of each voltage pulse plays an important role in achieving the uniformity, such as uniform space charge results in a uniform DBD. The non-uniform (patterned) DBD always evolves from the initial uniform state to the eventual non-uniform one. During this process, the space

electrons form a patterned distribution ahead of the surface charges and lead to non-uniform discharge channels. Wang and Roy [6] investigated numerically a nanosecond pulsed dielectric barrier discharge (DBD) actuator for combustion stabilization. The plasma actuator used for plasma assisted combustion had a serpentine shape. The results showed that the nanosecond pulsed actuators are able to stabilize the flame near the walls. This may also enhance combustion efficiency for a lean-burn condition. The objective was to increase the fuel efficiency, and thus reducing the emissions.

Boeuf and Pitchford [58] computed the force per unit volume acting on the flow, due to the effect of plasma actuator, based on a two-dimensional fluid model of the surface discharge and by considering positive ions and electrons with the N_2 (inert gas) as the background gas. They have assumed that the gas flow velocity is small with respect to the charged particle drift velocities, and that the gas flow does not significantly affect the plasma (one-way coupling). They have also considered the simplified case where a single, constant voltage pulse of enough magnitude such that the discharge appears in a glow regime is applied to the exposed electrode. They have shown that this force is localized in the cathode sheath region of the discharge, expanding along the dielectric surface, while its intensity is much larger than the analogous force in a direct-current corona discharge. Boeuf et al. [65], extended their previous work to time varying voltage of ramp or sinusoidal voltage waveforms. They have shown that in these cases the discharge consists of large amplitude short current pulses during which filamentary plasma spreads along the surface, separated in time by long duration, and low current discharge phases of a Townsend or corona type. The contribution of the low current phases to the total force exerted by the discharge on the gas is dominant because their duration is much longer than that of the current pulses, and because the force takes place in a much larger volume.

Jayaraman et al. [66] presented a two-dimensional modeling framework to study the evolution and interaction of such non-equilibrium plasma discharges in helium gas, under atmospheric pressure, using a plasma–fluid model. The plasma and fluid species were treated as a two-fluid system considering ionization and recombination as well as being coupled through force and pressure interactions. To overcome the stiffness of governing equations of the plasma, a finite-volume operator-split algorithm capable of conserving space charge was employed. Following their previous work, Jayaraman et al [54] characterized the fundamental process of discharge in the two half-cycles of the actuator operation. Moreover, the power-law dependence on the voltage for the resulting force were observed and confirmed. Furthermore, they have observed that the complex interplay between lower electrode size, applied voltage amplitude and waveform, frequency of applied voltage and dielectric constant determines the actuator performance. Jayaraman and Shyy [56,67], also reviewed the first-principle-based hydrodynamic-plasma model.

Nishida and Abe [68] simulated the time evolution of the plasma DBD actuator with a triangular applied voltage waveform using a simple fluid model similar to [65]. Their results showed that the periodic formation of the streamer discharge is shown by large discharge

current spikes when the positive-going voltage is applied. However, during the negative-going voltage the results showed that periodic breakdown of the gas and step-by-step plasma expansion didn't lead to streamer formation and the plasma expands more smoothly than that in the positive phase, because of its higher breakdown frequency. The validity of the results was confirmed qualitatively as compared with a experiment that comprised an optical observation of the discharge plasma on the DBD plasma actuator with a high speed camera. Wang and Roy [69] studied dielectric barrier discharge plasma actuators for microscale applications. Traditional macroscale DBD actuators suffer from relatively small actuation effect, as characterized by small induced force density and resulting flow velocity. As a remedy they have considered microscale plasma actuators. First, a two-dimensional volume discharge with nitrogen as a working gas was investigated using a first-principles approach, by solving a coupled system of hydrodynamic plasma equations and a Poisson equation for ion density, electron density, and electric field distribution. Second, they simulated a first generation plasma micropump and solved multiscale plasma-gas interaction inside a two-dimensional cross section of the microscale pump geometry. The result showed that a reasonable mass flow rate can be pumped using a set of small active electrodes.

In [52] Singh and Roy expanded their previous modeling efforts for an asymmetric dielectric barrier discharge model by considering real gas air chemistry using a self-consistent multibody system of plasma, dielectric, and neutral gas. The electrodynamic force development mechanism was studied over a flat plate due to charge and neutral species production from adjacent air in a radio frequency driven barrier discharge. Likhanskii et al [70], developed a detailed physical model for asymmetric DBD in air at low sinusoidal voltages. Their model considers both positive and negative ions, and also electrons with relevant plasma kinetics such as recombination, ionization, attachment and secondary electron emission from metallic and dielectric surfaces. Results showed the leading role of charging the dielectric surface by electrons in the cathode phase. They have also explained the mechanisms of plasma formation with sinusoidal voltage and described the force production on the gas in both half-cycles of the sinusoidal voltage. The significant role of negative ions which cause the downstream directed force was elucidated. Moreover, in [53], Likhanskii et al carried out the modeling of a DBD with high voltage repetitive, negative and positive, nanosecond pulses combined with positive dc bias. A second-order accurate MacCormack scheme, with flux corrected transport, was used to model the plasma kinetics. They have shown that the effect of backward-directed breakdown, in the case of negative pulses, results in a decrease of the integral momentum transferred to the gas. The use of positive repetitive pulses with dc bias was demonstrated to be promising for DBD performance improvement. The effects of the voltage waveform are visible on the force magnitude and on the spatial profile of the force, along with the crucial role of background electron density in numerical modeling of the ionization waves. Later, they simulated a realistic experimental condition by computing force and heating rate from the plasma model, and coupling these rates to a viscous flow solver [71].

Afterwards, they have used their model to simulate DBD plasma actuators in air to propose a novel application configuration. In this configuration the sinusoidal driving voltage was substituted by the repetitive nanosecond pulses superimposed on the bias voltage. The advantages of the proposed concept, over the conventional one, were experimentally and numerically validated by simulating a DBD actuator driven by repetitive nanosecond voltage pulses and AC/DC bias with realistic experimental conditions [71]. A detailed description of the modeling accomplishments achieved by Likhanskii et al can be found in [72]. This work presented the first complete, comprehensive, physically- based model, which tracks all essential physics of DBD plasma actuators and uses modern numerical capabilities for efficient simulations.

Similar to the model presented by Likhanskii et al. , Lagmich et al. [73] studied numerically the development of the electro hydrodynamic (EHD) force associated with surface dielectric barrier discharge in air using a 2D fluid model. A ramp voltage with positive and negative slope was applied that was consistent with typical experiments for sinusoidal voltage waveform. The results explained the differences in discharge development during the positive and negative parts of the sinusoidal voltage by considering contributions of negative ions. Boeuf et al. [74] conducted a parametric study, following their previous works, to study the contribution of negative and positive ions on force generation of the DBD plasma actuator with sinusoidal voltage waveforms. Their results confirmed the role of positive ions during the positive part of the cycle and the negative ions effect during the negative part of cycle on force production. Their results also predict that the contribution of negative ions tends to be dominant at low voltage frequencies and high voltage amplitudes. The momentum transfer takes place mainly during the low current phases between high current pulses and the streamers developing along the surface do not contribute significantly to the total EHD force. Nishida et al. [75] used a simple fluid model, similar to [73,76], in which the electron, one type of positive ion and negative ion were taken into account. Both the saw tooth and sinusoidal applied voltage waveform were considered. Results indicated that the discharge mode changes depending on applied voltage slope; when the applied voltage is positive-going, with high applied voltage slope, the corona-type discharge mode turns into the streamer-type discharge mode.

Recently Unfer et al. [77] developed an asynchronous scheme with local time stepping for solving a 2D discharge model. This technique reduces the CPU time required for explicit resolution of Poisson/transport equations while permitting the use of high order spatial schemes. This brings along an advantage in comparison to only first order and quite diffusive semi-implicit schemes and explicit second order Poisson/transport coupling, with prohibitive computational cost. Unfer and Boeuf [78] analyzed two modes of the actuation depending on the driving voltage waveform, using the asynchronous mesh adaptation and time integration developed in their previous work. They used a simplified air plasma model fully coupled with gas dynamics and a high-voltage sine waveform, in the kilohertz frequency range, to transfer momentum from ions to gas molecules, and high-voltage nanosecond pulses to transfer energy

to the neutral gas on a short time scale, thus generating shockwaves. Wang and Roy [79] used a three-species physical model for DBD actuators under atmospheric pressure. The plasma model was loosely coupled with the compressible Navier-Stokes equations through momentum and energy source terms. Two cases of Rf powered, and nanosecond pulsed, barrier discharge actuators were simulated. The influence of DBD actuator was considered through a time averaged electro-hydrodynamic force and power deposition to the neutral gas. The power deposition accounts for ion Joule heating and a percentage of electrons Joule heating.

All of the previous studies assume a span-wise uniformity of the plasma structure. However, the plasma structure in the span-wise direction is non-uniform, even if this non-uniformity in the plasma is expected to be small. To check the validity of the span-wise uniformity of the plasma, Nishida et al. [80] conducted three-dimensional discharge plasma simulations of a DBD plasma actuator by assuming step-like positive and negative applied voltages to simulate micro-discharges in a DBD plasma actuator, and analyzed span-wise non-uniformity in a body force field. In the positive voltage discharge, the minute disturbances at the boundary (that was from the numerical noise) lead to many filamentary structures because of the unstable nature of the streamer discharge. In contrast, the plasma structure of the negative voltage discharge is completely span-wise uniform because the glow-type discharge is more stable. However, both discharge structures are totally different from the experimental observations; the simulation model with the smooth exposed electrode cannot simulate the characteristics of the discharge structure as observed in the experiments. To correctly reconstruct the three-dimensional micro-discharges some minute bumps, as artificial disturbances, were attached on the electrode edge. These disturbances break the span-wise uniformity and successfully reconstruct glow-type micro-discharges and streamer-type filamentary discharges in the negative and positive applied voltage cases. It was also shown that the tentative body force field has strong span-wise non-uniformity corresponding to the plasma structure. However, the span-wise-averaged body force has the same spatial-distribution, and time-evolution characteristics, as obtained by the two-dimensional simulation. Recently, Shang and Huang [81,82] presented a physical based modeling procedure for better understanding the fundamentals of the essential physics of DBD actuators. The drift-diffusion approximation was adopted as a transport property approximation to the non-equilibrium air plasma. The electron impact ionization process at a low-temperature environment was considered by the Townsend mechanism together with electron attachment, detachment, bulk, and ion–ion recombination. Moreover, the effects and quantifications of Joule heating, periodic electrostatic force, as well as the Lorentz acceleration for flow control were considered.

1.7.2 - Empirical and phenomenological models

The most important physics of the flow can be captured using empirical models with much less computational cost. A significant difference between these low-order algebraic models and the drift-diffusion type models is that the former generally involve assumptions on the

behavior of either the electric field or plasma charge density. A simple, yet widely used empirical model was developed by Shyy et al. [83]. Shyy et al. considered an algebraic model by approximating the electric field and by assuming a spatially constant charge density. In this case, the electric field is assumed to decay linearly across the dielectric surface from a specified maximum value. However, this model over-predicts the actuator effect. Furthermore, it also does not reflect differences on the applied voltage waveform.

Singh and Roy [84] used observations of the body forces obtained from a first principles simulation in order to come up with an approximation for the body force components. This approach obtains the body force by solving a curve fitting problem, but it contains no physics on itself. Also, like the model by Shyy et al. [83], it does not give any insight into the temporal characteristic evolution of the body force. Suzen et al. [85] have modified the electrostatic model developed by Enloe et al. [86] to compute a body force field. Suzen et al. [85] divided the electrostatic equations into contributions due to the external electric field and those due to the charged particles. Furthermore, in order to incorporate the time dependence into the model, a weighted Gaussian distribution, with a sine wave input, was used as a time dependent boundary condition for the charge density. The Gaussian distribution was chosen in order to emulate the observations made in the experiments. A scaling parameter was used as a calibration parameter, in order to force the induced velocity profiles to match the experimental results.

Orlov [87] used a model based on lumped circuit elements in order to create a time dependent boundary condition for the governing electrostatic equations. The circuit elements consist of resistors and capacitors. The values of these circuit elements were based on physical constants and on the geometry of the actuator. The electrostatic formulation is based on the assumption that the plasma formation and fluid flow response can be decoupled, due to the disparities in the characteristic velocities associated with each process. This is a reasonable assumption since the characteristic velocities of the fluid transport under consideration were between 10 m/s and 100 m/s and, for electron temperatures between 1000 K and 10000 K, the electron velocities, which is the characteristic velocity of the plasma, is of the order of 10^5-10^6 m/s. While this lumped circuit element model was well validated using PIV results, the calculation of the body force vectors shows some inconsistencies with experimental results. Specifically, the force vectors have almost no normal component to the wall, as it was to be expected by considering the electric field lines.

Lemire and Vo [88] used the two potential based models developed by Suzen et al. [85], but instead of a Gaussian distribution for the charge density boundary condition, the plasma current obtained from the lumped element model, developed by Orlov, was used to calculate a boundary condition for the charge density. Using this "hybrid model," they were able to solve for time dependent body forces, and they applied the model to the simulation of rotor-stator turbo-machinery interactions. However, after time averaging the body force vectors, they found a region where the force vectors are oriented in the negative x-direction. This

does not agree with experimental observations about the induced flow direction, but since these reversed vectors are smaller in magnitude than the vectors near the downstream edge of the exposed electrode, which are oriented in the positive x-direction, the net force is in the correct direction.

Further, Mertz [89] refined the model presented by Orlov by casting the governing equations in terms of a generalized coordinate system, so that it can be applied to curved surfaces. By resorting to this approach the grid dependence of the model was eliminated, and the methodology of applying this model as a boundary condition to the electrostatic equations, in order to calculate the body forces generated by the actuator, was studied. This new formulation of the lumped circuit element model was then validated against various experimental observations, including the force vector orientation needed to produce the observed induced flow. Also, the scaling of the force with the input voltage, and the directivity patterns of force and pressure were validated from measurements.

The above mentioned models had demonstrated that they are able to capture the most important physics of the actuator, in particular without the computational cost associated with first-principle models. Although are useful but, they do not actually analyze the dynamic and kinetic processes in plasmas. Moreover, a common feature amongst each of the above models is the need for an initial empirical Calibration.

1.8 - Objectives

The main objective of the thesis is to numerically analyze DBD plasma actuators. Design and optimization of plasma actuators is strongly dependent on the development of a numerical model able to predict accurately their induced flow. To this aim, a suitable numerical model for simulating the DBDs will be considered and applied to situations resembling a typical flow configuration in propulsion geometries after studying different numerical methodologies for modeling DBD plasma actuators. Therefore, several objectives are presented by this research:

- A classical plasma fluid model will be implemented in OpenFOAM and its accuracy and performance accordingly will be verified. OpenFOAM will provide the flexibility to solve the different physical equations.
- An Analysis of the Plasma-Fluid modeling approaches should be performed and their modeling performance should be verified. These models suffer from severe restrictions due to the time scale and length scale of the plasma. Thus, it will be tried to employ different numerical procedures to improve the numerical performance.
- A number of phenomenological models have been proposed throughout the literature, and all of them need empirical calibrations. A simple analytical model should be developed to simulate the macroscopic effect of DBD plasma actuators.

- The possibility of expanding the range of applicability of plasma actuators for higher speed ranges will be studied by using actuators in unsteady operational mode and nanosecond plasma actuators.
- DBD plasma actuators will be applied to simple propulsion geometries to investigate the potential of these kinds of actuators for controlling flow and improving their performance.

1.9 - Outline of Thesis

The present thesis is built up and based on the published, or under review papers, in peer-reviewed journals. Thus, this thesis is divided into seven chapters:

Chapter I: introduction; in this chapter an overview of the application of plasma actuators for flow control purposes will be presented. Moreover, a short background on the most important fundamental processes of plasma physics is presented. Also, a state-of-the-art on the modeling of DBD actuators is discussed.

Chapter II: Implementation of the Plasma fluid model in OpenFOAM; in this chapter an Implementation of self-consistent model, which is suitable for the simulation of micro discharges, is described to model DBD plasma actuators in OpenFOAM. Different numerical treatments were employed and discussed. Several validation case studies were presented.

Chapter III: Interaction of DBD plasma actuators and transonic flows; in this chapter the nano-second plasma actuator is considered and the mechanism in which it alters the flow characteristic is explained. Moreover the plasma fluid model, described in chapter II, is expanded to model the effect of nanosecond pulsed actuators.

Chapter IV: Modified split-potential model; the development of a new phenomenological model, which needs less experimental calibration, is presented in this chapter. Different case studies are also presented to demonstrate the validity of the presented model. Also, the performance of this model is compared with previous models existing in the literature. Moreover, the influence of the altitude variation is included in the model and is discussed in this chapter.

Chapter V: Unsteady actuation with DBD plasma actuators; the possibility of obtaining improved flow control performance by using unsteady (duty cycled) mode of actuation is discussed in this chapter. The mechanism of flow control in steady and unsteady mode is compared and explained in this chapter.

Chapter VI: Effect of DBD plasma actuator on thrust vectorizing; in this chapter, plasma actuators are used to control the flow in the ACHEON nozzle geometry. The numerical model is based on the model presented in chapter IV. For the verification, the numerical results were compared with preliminary experimental results.

Chapter VII: Conclusions and outlook of the future work.

.

2 - Implementation of the Classical Plasma-Fluid Model

Abstract

This study focuses on the development of numerical methodologies for DBD plasma actuators. To simulate the coupled plasma-fluid flow physics of these discharges, the plasma-fluid is utilized in conjunction with incompressible and compressible flow solvers. The flow solver is responsible for determining the bulk flow kinetics of dominant neutral background species including mole fractions, gas temperature, pressure and velocity. The plasma solver determines the kinetics and energetics of the plasma species and accounts for finite rate chemistry. In the present chapter, the implementation of plasma-fluid model into the OpenFOAM library is discussed. In order to achieve maximum reliability and best performance, we have utilized state-of-the-art numerical and theoretical approaches to the description of the DBD plasma actuator. We have tried to test and compare different numerical treatments for obtaining stable and accurate results. The practical implementation of the model in OpenFOAM is provided together with theory involved behind. Numerical experiments are carried out in order to cross-validate the solvers and in order to investigate the drawbacks/benefits of the solution approaches. The test problems include single DBD actuator with positive and negative constant, ramp and sinusoidal voltage waveforms similar to the ones that could be found in literature[1].

Keywords: OpenFOAM, DBD plasma actuator, Plasma-Fluid Model, Supertime-stepping, Electric discharge

2.1 - Introduction

Among the several active flow control techniques, flow control techniques that use Dielectric Barrier Discharges are considered very promising because of their fast reactivity, low parasitic drag and low energy consumption and moreover since usually they have simple constructive requirements and they are not expensive, they have no moving elements. DBD plasma actuators have shown a great potential for flow control purposes, especially regarding aeronautic applications. In general, DBD plasma actuator can induce a body force on gas or heat the gas. Body forces can be exerted on charged species (electrons and ions) by electric

[1] This chapter is based on the following paper: "M. Abdollahzadeh, J.C. Páscoa, P.J. Oliveira (2014), Implementation of the Classical Plasma-Fluid Model for Simulation of the Dielectric Barrier Discharge Actuators in OpenFoam, Journal of Computational Physics, (Submitted)."

field and are coupled to bulk gas by collisions. These forces can then be used to control the flow.

In this paper the coupled plasma-fluid flow physics simulations (the plasma solver) was conducted after implementation of the suitable physical model. Formation of the Plasma discharges involves multiple-scale processes such as convection, diffusion, and reaction/ionization mechanisms which make the transport equations of the plasma dynamics stiff. To handle the stiffness, a sequential finite-volume operator-split algorithm is employed. Then, a body force or localized heating treatment is devised to link the plasma dynamics and fluid dynamics.

Open source computational fluid dynamics (CFD) codes provide suitable environments for implementation, testing and rapid dissemination of algorithms. As a test platform, we choose the unstructured, finite volume method (FVM) based open source C++ library OpenFOAM. The plasma fluid model then was implemented in the OpenFOAM CFD toolbox [90] along with suitable numerical remedies for obtaining stable and accurate results. OpenFOAM has attracted a lot of attention recently because it is an open source code designed for continuum mechanics applications specially CFD applications. It is a C++ toolbox based on object oriented programming [90]. This makes OpenFOAM sustainable in terms of reuse and development by many users all around the world, in contrast to the single block programming codes which are very hard to develop or even understand. OpenFOAM is as released under the Gnu Public License (GPL), has gained a vast popularity during the recent years. The readily existing solvers and tutorials provide a quick start to use the code. The existing solvers can also be freely modified in order to create new solvers regarding existing and new solution approaches. OpenFOAM gives a flexible framework which combines all the required tools for solving any CFD problem. This framework consists of enormous groups of libraries for different mathematical, numerical and physical models. Linking the mathematical and numerical tools with the physical models in a main C++ function produces different solvers and utilities. OpenFOAM, undoubtedly, opens new horizons for CFD community for efficient models devolving, allowing the industrial sectors to be updated with all new models without any delay for waiting the new models to be implemented in the commercial CFD codes.

The rest of this chapter is arranged in the following format; the details of the plasma-fluid model are summarized in section 2.2, 2.3 and 2.4. Section 2.5 describes the numerical procedure. In section 2.6, the main procedure of the implementation of the entire model in OpenFOAM is explained. Section 2.7 presents the results. Finally, conclusions are drawn in section 2.8.

2.2 - Governing equations and boundary conditions

Plasma fluid models (hydrodynamic models) are based on the Boltzmann equation and its moments [91–93]. Derivation of hydrodynamic or fluid models is always based on a number of simplifying assumptions.

2.2.1 - The Boltzmann equation and its moments

Transport problems (including accelerating forces and collisions) can be treated by solving the Boltzmann equation:

$$\frac{\partial f_k}{\partial t} + \vec{\omega} \bullet \nabla f_k + \vec{a} \bullet \frac{\partial f_k}{\partial \vec{\omega}} = \left(\frac{\partial f_k}{\partial t} \right)_{collision} \tag{2.1}$$

where $f_k(x, y, z, \vec{\omega}, t)$ is the time-dependent particle distribution function, the time evolution of the particle density, in the 6-dimensional configuration-velocity (phase) space. The subscript "k" could designate electrons, positive ions, negative ions or neutral and $\vec{\omega}$ and $\vec{a}$ are respectively velocity and acceleration of charged particles. Assuming that particles have the mass m_k and the charge q_k, acceleration of charged particles $\vec{a}$ would be expressed by acceleration due to electric $\vec{E}$ and magnetic $\vec{B}$ fields, which is then given by $\vec{a} = (q_k / m_k)\left(\vec{E} + \vec{\omega} \times \vec{B}\right)$. First term on left-hand side represents the change in the distribution function over time. The second term describes how the distribution changes in space, or configuration coordinates, as the particles move through the system with a certain velocity and direction. The third shows how the species distribution is changing due to external forces acting to accelerate the charged particles. Gradient, ∇f_k represents the change to the k distribution function with respect to configuration coordinates (x, y, z) whereas $\partial f_k / \partial \vec{\omega}$, represents the change to the distribution function with respect to the velocity coordinates, $\vec{\omega}$. The collision operator $(\partial f_k / \partial t)_{collision}$ in the right-hand side considers the generation or destruction of particles (by impact ionization, recombination or chemical reactions) as well as collision processes.

A combination of the Boltzmann equation for each particle species with the Poisson's equation leads to the solution of the number of particles and the velocity of the particles in a volume element. This solution gives a detailed rigorous description of microscopic view of any given plasma system at any given time. However, Due to the complexity of the resulting system, finding a solution is impossible or is only possible for simple test examples. The numerical effort for more general cases is too high to get solutions in an acceptable time.

It is very difficult to solve the Boltzmann equation for the number of discharge problems due to the strict restrictions. The distribution function contains a large amount of information and generally, the complete information is not necessary for all physical problems. When the system under investigation does not require microscopic detail, it is possible to provide a more practical alternative by considering the moments of the Boltzmann equation. If Eq. (2.1) is multiplied with a set of test functions and integrated over the velocity space (moment of Boltzmann Equation), the six degrees of the freedom and complexity of the Boltzmann equation will be reduced. This operation leads to conservation equations known as the

moments of the Boltzmann equation. The first three moments of Boltzmann equation provide the equation of mass, momentum and energy balance for each species.

In this aspect, from integration of $f_k(x,y,z,\vec{\omega},t)$ over the velocity space, $n_k = n_k(x,y,z,t)$ the particle density per volume can be obtained;

$$n_k(\vec{x},t) = \int_{-\infty}^{+\infty}\iiint f_k(x,y,z,\vec{\omega},t)d\omega_x d\omega_y d\omega_z \tag{2.2}$$

Also, the average drift velocity of the particles $\vec{v}$ can be calculated by multiplying f_k with $\vec{\omega}$ and integrating over the whole velocity space

$$\vec{v}_k(\vec{x},t) = \frac{1}{n(\vec{x},t)}\int_{-\infty}^{+\infty}\iiint \vec{\omega} f_k(x,y,z,\vec{\omega},t)d\omega_x d\omega_y d\omega_z \tag{2.3}$$

The integration of Eq. (2.1) over the velocity space (zeroth velocity moment) will lead to the conservation of mass (continuity equation):

$$\frac{\partial n_k}{\partial t} + \nabla\left(n_k \vec{v}_k\right) = S_k \tag{2.4}$$

In the derivation of the above equation, divergence theorem was used and distribution was set to zero as the surface used in the integral approaches infinity. Here S represents all the processes that lead to a generation or loss of particle.

Neglecting the effect of magnetic field, a conservation equation for momentum can be derived in a similar way. Multiplying Eq. (2.1) with a weight function which is equal to product of the particle mass m and the velocity vector, and integration over the whole velocity space (first moment), the particle momentum equation will be obtained as;

$$n_k m_k\left(\frac{\partial \vec{v}_k}{\partial t} + \vec{v}_k \bullet \nabla\left(\vec{v}_k\right) + \right) + \nabla p_k - n_k q_k \vec{E} - n_k m_k \vec{v} S_k = \int_{-\infty}^{+\infty}\iint m_k \vec{\omega}\left(\frac{\partial f_k}{\partial t}\right)_{collision} d\omega_x d\omega_y d\omega_z \tag{2.5}$$

In the derivation of the above equation, the conservation of mass was used and it was assumed that the distribution function is isotropic. Moreover, a scalar partial pressure p is defined as $p_k = n_k k_B T_k$; where, a local particle temperature $T_k(\vec{x},t)$ can be defined so that the mean random kinetic energy of all particles at the same location can be expressed by as

$$\frac{3}{2}k_B T_k(\vec{x},t) = \frac{1}{n_k(\vec{x},t)}\int_{-\infty}^{+\infty}\iint \frac{m_k}{2}\int |\vec{\omega}|^2 f_k(x,y,z,\vec{\omega},t)d\omega_x d\omega_y d\omega_z \tag{2.6}$$

The mean kinetic energy of the particles is a scalar quantity given by

$$\bar{\varepsilon}_k = \frac{1}{n_k(\vec{x},t)}\int_{-\infty}^{+\infty}\iint \frac{m_k}{2}\int |\vec{\omega}|^2 f_k(x,y,z,\vec{\omega},t)d\omega_x d\omega_y d\omega_z \tag{2.7}$$

To obtain the conservation of energy, the second moment is calculated by multipling Eq. (2.1) by $|\vec{\omega}|^2$ and integrating over the whole velocity space. Again assuming isotropic distribution function,

$$\frac{\partial(n_k \bar{\varepsilon}_k)}{\partial t} + \nabla\left(\frac{5}{2} n_k k_B T_k \vec{v}_k + n_k \vec{v}_k \left(\frac{m_k}{2} \vec{v}_k{}^2\right)\right) = q_k n_k \bar{E} \vec{v}_k + P_{th} \tag{2.8}$$

The advantage of this procedure is that in the most general case, there remain only the three spatial degrees of freedom. The plasma fluid model theoretically can consist of an arbitrary number of equations for each species in the plasma. However, the number of needed equations is limited to the second momentum equation by closing the series with an appropriate assumption of the energy distribution function (for example, isotropic energy distribution). This fact that assumptions about the distribution function have to be made is the most serious drawback.

2.2.2 - Plasma-fluid model

Under atmospheric pressure, the discharge can be simulated using a time-dependent plasma-fluid model instead of a kinetic model. As was mentioned before, the fluid model for modeling the DBD consists of the first few moments of the Boltzmann equation for the various species with a near-Maxwellian distribution function. This fluid model description using the continuity equations for the various particle densities is satisfactory at atmospheric pressures, where the momentum and energy equilibrium times are generally small compared with any macroscopic scale variations of the system [57]. The core of the model consists of solving Navier-Stokes equation, Maxwell equation for electromagnetic and multiple species continuity equations including non-equilibrium chemical reactions to obtain the spatio-temporal distributions of each particle species and electric field.

For simplicity, the plasma is considered as a multi-component fluid considering global categories of charged particles comprising four primary species, namely, neutrals, positive and negative ions and electrons. Multiple charged ions will be neglected. This include the assumption that positive ions or negative ions are in close equilibrium with other positive or negative ions which results in one type of effective positive ion and one type of effective negative ion [94]. The model does not describe the kinetics of excited species and their influence on the plasma evolution. The model only considers that at any instance during the discharge, the ionized species concentration is the net balance between ionization, detachment, attachment and recombination processes. Moreover, the model accounts for the charging of the dielectric surface due to the incident charged particles.

In modeling gaseous discharges using a fluid model, several important assumptions have to be made. Here, it is assumed that the DBD plasma is a weakly ionized plasma. The imbalance of net space charge due to the charged species densities will generate self-consistent electric forces. In the absence of external magnetic field and by assuming that the current densities

are small (weakly ionized plasma), self-consistent magnetic fields can be safely neglected and the Maxwell equations can be reduced to solving a single Poisson equation for the electric potential [82].

There are two characteristic temperatures, heavy species temperature and a separate electron temperature. Each temperature could be obtained separately by solving energy conservation equations. However, as ions tend to thermalize effectively with neutrals by frequent charge exchange collisions, it might be assumed that the ion temperature is in the order of the neutral gas temperature (It is assumed that all heavy species (ions and neutrals) are in thermal equilibrium with each other). In other words; since the ion mass is very nearly the same as the mass of the background gas, the ions are assumed to be in thermal equilibrium with the background, and no energy equation is solved for the ions. For the electrons, due to their lower mass, the exchange of kinetic energy with the other particles is poor, and their temperature can be significantly higher than the other species. Thus, for the simplification, a high constant electron temperature is assumed.

The species flux $\vec{\Gamma}_k = n_k \vec{v}_k$ in Eq. (2.5) can be obtained by solving separate momentum equations for each species. However, at atmospheric pressure, a reasonable and computationally efficient approximation could be made using the so called drift-diffusion approximation [95]. In this approximation, the fluxes of charged particles are calculated by neglecting the inertial and unsteady terms of the momentum equation and balancing the thermodynamic pressure gradient with the drift force and collision terms. This assumption for reduction of the momentum equation for the species is valid at high pressures (e.g. atmospheric conditions) [54]. Such an approximation requires the pressure tensor to be isotropic and is strictly valid only for a Maxwellian distribution. Moreover, this approximation is valid when the mean free path is significantly smaller than the characteristic length scale of the problem. This is typically the case at atmospheric pressures and length scales of the order of millimeters or greater [6]. In other words; As long as the thermal velocity is comparable to the drift velocity and we are in the continuum regime (Knudsen number Kn is low, $\lambda / L = Kn << 1$, as the mean free path λ at atmospheric conditions is O($10^{-7} m$) and the actuator characteristic length L is O($10^{-3} m$)), the inertial components in the momentum equation can be neglected. What is realized is a balance between the collision/ionization effects and the drift-diffusion components instead of the full momentum equation. Thus the fluxes of charged particles could be expressed as:

$$\vec{\Gamma}_k = n_k \vec{v}_k = \pm \mu_k n_k \vec{E} - D_k \nabla n_k + n_k \vec{v}_b \tag{2.9}$$

In Eq. (2.9), the drift-diffusion flux consists of a mobility flux term (for charged species), a diffusive flux term, and the species flux due to the flow velocity field.

The simplest set of equations, within the fluid model framework, containing the basic physics necessary for gaseous discharges, are the continuity equations for electrons, positive ions and negative ions (to account for the development of the space-charge) coupled with Poisson's

equation (to account for the modification of the electric field due to space-charge) which are summarized in Table (2.1).

Table 2.1: Summary of the governing equations.

Equations	
Continuity equations:	
Electron; $\frac{\partial n_e}{\partial t} + \nabla.\vec{\Gamma}_e = S_e$ $S_e = \alpha\left\|\vec{\Gamma}_e\right\| - r_{ep} n_e n_p - \eta\left\|\vec{\Gamma}_e\right\|$	(2.10)
Positive ions; $\frac{\partial n_p}{\partial t} + \nabla.\vec{\Gamma}_p = S_p$ $S_p = \alpha\left\|\vec{\Gamma}_e\right\| - r_{ep} n_e n_p - r_{np} n_n n_p$	(2.11)
Negative ions $\frac{\partial n_n}{\partial t} + \nabla.\vec{\Gamma}_n = S_n$ $S_n = \eta\left\|\vec{\Gamma}_e\right\| - r_{np} n_n n_p$	(2.12)
Momentum equations	
$\vec{\Gamma}_e = n_e \vec{v}_e = -\mu_e n_e \vec{E} - D_e \nabla n_e + n_e \vec{v}_b$	(2.13)
$\vec{\Gamma}_p = n_p \vec{v}_p = \mu_p n_p \vec{E} - D_p \nabla n_p + n_p \vec{v}_b$	(2.14)
$\vec{\Gamma}_n = n_n \vec{v}_n = \mu_n n_n \vec{E} - D_n \nabla n_n + n_n \vec{v}_b$	(2.15)
Poisson equation:	
$\nabla.(\varepsilon \nabla \phi) = -e(n_p - n_e - n_n) - \delta_s \sigma$	(2.16)

2.2.3 - Transport properties

The production terms and loss terms inside the continuity equations of the charged particles include different reactions. If we assume that the working fluid is air and is just composed of N_2 and O_2, following reaction could be considered.

-Ionization

$$e + N_2(O_2) \rightarrow 2e + N^+{}_2(O^+{}_2) \tag{2.17}$$

-dissociative electron-ion recombination,

$$e + O^+{}_2 \rightarrow O + O \tag{2.18}$$

$$e + O^+{}_4 \rightarrow O_2 + O_2 \tag{2.19}$$

-Ion-ion recombination

$$A^+ + B^- + M \rightarrow A + B + M \tag{2.20}$$

-dissociative electron attachment

$$e + O_2 \rightarrow O^- + O \tag{2.21}$$

In the above reaction the ionization coefficient α could be defined which measures the number of ionization by electron per unite distance. In other words, it is a measure of energy gain by charge particles between the collisions. The dissociative electron-ion recombination is the fastest mechanism of the bulk recombination of the weakly ionized gas. The rate is given as $-r_{ep} n_e n_p$. At low pressure environment the ion-ion recombination process takes place through binary collisions and the reaction is similar to charge transfer and at moderate pressures the reaction proceeds through triple collisions. The rate of ion-ion recombination is also given as $r_{np} n_n n_p$. The electron attachment is the formation and depletion of negative charged ions in the partially ionized air. The electron attachment is the main mechanism of removing electron from negatively charged ions. This lost of electron number density can be given by $-\nu_a n_e$, where ν_a is the attachment frequency. However, for the case of stability of the numerical simulation the rate of attachment is defined in similar way to ionization rate as $\eta \left\| \vec{\Gamma}_e \right\|$.

An accurate gas discharge plasma modeling requires an extensive knowledge of the transport parameters of the gas in question. The fluid model uses transport parameters found from the kinetic model or from experimental results. The parameters have been obtained through the solution of the stationary Boltzmann equation. However, we should mention that there are deviations between different correlations reported in the literature, which may affect the results somewhat. The gas properties such as transport coefficients (momentum transfer rate such as μ, and D) , the collisional ionization coefficient α and energy loss rates could be obtained simply by considering the local-field approximation(LFA) or local-mean-energy approximation (LMEA) [96]. This implies that dependence of theses coefficients on the mean energy are supposed to be the same as at equilibrium. By "equilibrium conditions" we mean a situation where the rate of electron energy gain is locally balanced by the energy loss rate [56] . The local equilibrium assumption implies that the transport coefficients depend on space and time only through the local value of the electric field $\vec{E}(x,t)$ (functions of the reduced electric field (E/N) where E is the field amplitude and N the gas number density [6]). In this way, the transport coefficients are assumed to be the same as those which could be measured or calculated under a uniform and constant electric field equal to $\vec{E}$ (hydrodynamic regime). Essentially this means that the electron distribution function is in local equilibrium with the neutral plasma. This assumption is valid as long as the relaxation time for achieving a steady state electron energy distribution function is short compared with the characteristic time of discharge development. Another alternative is to assume the

transport coefficients and the rate coefficients of electron impact reactions to be functions of the electron mean energy [56].

Table 2.2: Summary of property models employed for discharge simulation.

Transport/reaction properties	Value	
$\frac{\alpha}{p}(m^{-1}Torr^{-1})$	$0.21\left[\begin{cases}4.71\times10^{-11}\lvert E/p\rvert^{3}, & \lvert E/p\rvert<1.4\times10^{4}Vm^{-1}Torr^{-1}\\ 3.32(\lvert E/p\rvert-12500)^{0.5} & \lvert E/p\rvert>1.4\times10^{4}Vm^{-1}Torr^{-1}\end{cases}\right]$ $+0.79\left[\begin{cases}1.17\times10^{-10}\lvert E/p\rvert^{3}, & \lvert E/p\rvert<1.1\times10^{4}Vm^{-1}Torr^{-1}\\ 0.0319\lvert E/p\rvert-211 & 1.1\times10^{4}<\lvert E/p\rvert<2.1\times10^{4}Vm\\ 6.32(\lvert E/p\rvert-16300)^{0.5} & \lvert E/p\rvert>2.1\times10^{4}Vm^{-1}Torr^{-1}\end{cases}\right]$	(2.22)
$\mu_e p\left(m^2TorrV^{-1}s^{-1}\right)$	$0.21\left[24.32\exp(\frac{-E/p}{1057})+19.38\exp(\frac{-E/p}{23430})+14.45\right]+$ $0.79\left[173.1\exp(\frac{-E/p}{195.1})+36.19\exp(\frac{-E/p}{12763})+31.73\right],$	(2.23)
$\mu_p p\left(m^2TorrV^{-1}s^{-1}\right)$	$0.79\left[0.05492\exp(\frac{-E/p}{6858})+0.07509\exp(\frac{-E/p}{38175})+0.0308\right]$ $+0.21\left[0.06841\exp(\frac{-E/p}{59678})+0.09194\exp(\frac{-E/p}{12763})+0.0320\right],$	(2.24)
$\mu_n p\left(m^2TorrV^{-1}s^{-1}\right)$	$0.181225,$	(2.25)
$\frac{\eta}{p}(m^{-1}Torr^{-1})$	$0.21\left[1.307+\frac{33200}{\lvert E/p\rvert}\exp(\frac{(\ln(\lvert E/p\rvert)-9.04)^2}{2.53})\right]$	(2.26)
D_k	$k_B T_k \mu_k$	(2.27)
r_{np}	$1.7\times10^{-13}m^3s^{-1}$	(2.28)
r_{ep}	$2\times10^{-13}m^3s^{-1}$	(2.29)

In both cases, to obtain the properties of electron transport such as mobility; diffusivity, mean energy etc, varying as a function of E/N (E is electric field and N is the gas number density) or electron mean energy, the solution of steady state Boltzmann equation is considered under constant field condition to obtain the electron energy distribution function in the gas under investigation. For most of the electron-induced processes the reaction rates are calculated on the basis of energy-dependent cross-sections, and with a separate program, called BOLSIG+ [97]. This program is applied for a wide range of different, fixed reduced electric fields and gives the dependence of the rates of ionization, dissociation, and excitation of the particles in discharges on the reduced electric field E/N or electron mean energy by solving the Boltzmann kinetic equation in a homogeneous field with uniform and

steady conditions. Here, rate constants of the different electron-induced processes corresponding to the above reactions, and the transport coefficients including mobility of the electrons (The corresponding diffusion coefficients are then calculated using Einstein's relation) were obtained from BOLSIG+ Solver or were extracted from [94], and are presented in Table (2.2).

2.3 - Boundary and initial conditions

2.3.1 - Initial Condition

The initial condition used to start the simulation requires specifying the starting number densities for the various species. The value of n_0 is used as a reference value (and also as a measure of pre-ionization of the neutral gas) to define the initial values. Thus, the initial positive ion and electron number densities are assumed to be uniform and equal to n_0 in the plasma domain, while the negative ion charge density is assumed to be equal to zero.

2.3.2 - Electric potential boundary conditions

The boundary value of the electric potential is defined at the two electrodes (Anode and Cathode) using a Dirichlet type boundary as follows;

$$\phi = V_0 f(t) \qquad at\ anode, \tag{2.30}$$

$$\phi = 0 \qquad at\ cathode, \tag{2.31}$$

$f(t)$ is a function representing the time-dependent voltage waveform. Moreover, the homogeneous Neumann boundary condition is applied for the electrostatic potential at the open boundaries (far-field) which simply read as;

$$\frac{\partial \phi}{\partial n} = 0 \qquad at\ \ farfield, \tag{2.32}$$

In addition, the boundary condition of the electric field and electric potential at the dielectric barrier and plasma interface is calculated considering the accumulated surface charges from the Gauss' theorem [82] ;

$$\vec{n} \times (\vec{E} - \vec{E}_d) = 0 \tag{2.33}$$

$$\varepsilon_0 \vec{E}.\vec{n} - \varepsilon_d \varepsilon_0 \vec{E}_d.\vec{n} = \sigma \tag{2.34}$$

In the above equations, ε_0 is the permittivity of the space, ε_d is the relative permittivity of the dielectric layer, $\vec{E}$ and $\vec{E}_d$ are respectively electric field in the gas and the dielectric and σ is calculated by integrating the net charge density over the surface and has the dimension of C/m^2. This charge accumulation on the surface is considered as the result from instantaneous recombination of the charged particles after satisfying the imposed boundary

conditions for the charged species and includes both accumulations of positive and negative charges ($\sigma = \sigma_+ + \sigma_-$) , and is computed using the flux of charged species to the surface [81] as:

$$\sigma = \int_0^t -e\left(\vec{\Gamma}_p - \vec{\Gamma}_e - \vec{\Gamma}_n\right)\vec{n}dt = \int_0^t -\vec{j}.\vec{n}dt \tag{2.35}$$

where $\vec{j}$ is the current due to fluxes of charged particles. We should mention that, in view of the relatively short duration of micro-discharge versus the microsecond time scale of the AC cycle; the instantaneous surface recombination is an acceptable approximation. Eq. (2.33) is stating that that the tangential electrical field strength is continuous across the media interface. For a Cartesian grid, this means that the rate of change for electric potential in *z* must be identical across the interface along the *x* coordinate and the rate of change of electrical potential in *x* must be equal along the *z* coordinate across the media interface. This requirement is automatically satisfied by the two- dimensional formulation.

The second condition expressed by Eq. (2.34), is the balance of the discontinuity of the normal component of the electric displacement across the plasma/dielectric interface by the net surface charge density on the interface by emission, desorption, and accumulation. This condition is independent of all the chemical-physics process on the interface. This equation could be rewritten by considering the electric potential as;

$$\varepsilon_0 \left.\frac{\partial \varphi}{\partial n}\right|_{air} - \varepsilon_0 \varepsilon_d \left.\frac{\partial \varphi}{\partial n}\right|_{d} = \sigma \tag{2.36}$$

In other words, the current continuity is enforced. This equates the drift current and the displacement current in the fluid domain to the displacement current inside the dielectric material [66].

2.3.3 - Charge number density boundary conditions

At the domain boundary away from the dielectric/electrode surface, incoming/outgoing flux of particles is negligible. Thus a zero normal gradient boundary condition is assigned (i.e. the slopes of the solution variables are equal to zero) which assumes that impact far away from the fluid-actuator interface is insignificant. This boundary condition is expressed as;

$$\begin{aligned} \vec{\Gamma}_k.\vec{n} &= 0, \\ \frac{\partial n_k}{\partial n} &= 0, \end{aligned} \tag{2.37}$$

Boundary conditions of the charged particle number density is defined on the electrode and dielectric layer surface through balance between the fluxes of the charge particles absorbed by surface and fluxes of the particles that are reflected from the surface. When the surfaces are in anodic behavior (e.g. exposed electrode as anode and $\sigma > 0$), the incident positive ion

fluxes at the surface is collected considering the thermal equilibrium of the positive ions at the surface. While the electron fluxes are reflected from the surface. In this case, The electron and negative ion flux is also based on the electron thermal velocity ($v_{th} = \sqrt{8k_B T/(\pi m)}$) whose magnitude is given by $\Gamma_{th} = \frac{nv_{th}}{4}$ and is directed towards the wall and it implies that the hydrodynamic flux equals the flux from the dielectric surface.;

$$\vec{\Gamma}_p = -\frac{1}{4} n_p v_{th,p} \tag{2.38}$$

$$\vec{\Gamma}_{nn} = -\mu_n n_n \vec{E} - \frac{1}{4} n_n v_{th,n} \tag{2.39}$$

$$\vec{\Gamma}_e = -\mu_e n_e \vec{E} - \frac{1}{4} n_e v_{th,e} \tag{2.40}$$

In the same way, when the exposed electrode is as cathode and the dielectric barrier is in cathodic behavior ($\sigma < 0$), positive ion fluxes are reflected from the surface and thus the positive ion flux will be equal to its drift part. For the electrons and negative, we assume that all the electron and negative ion fluxes are collected on the surface and thus;

$$\vec{\Gamma}_p = \mu_p n_p \vec{E} - \frac{1}{4} n_p v_{th,p} \tag{2.40}$$

$$\vec{\Gamma}_n = -\frac{1}{4} n_n v_{th,n} \tag{2.41}$$

$$\vec{\Gamma}_e = -\frac{1}{4} n_e v_{th,e} \tag{2.42}$$

The above boundary conditions could be compacted as follows;

$$\vec{\Gamma}_p . \vec{n} = \min(\mu_p n_p \vec{E} . \vec{n}, 0.0) - \frac{1}{4} n_p v_{th,p} \tag{2.43}$$

$$\vec{\Gamma}_n . \vec{n} = \min(-\mu_n n_n \vec{E} . \vec{n}, 0.0) - \frac{1}{4} n_n v_{th,n} \tag{2.44}$$

$$\vec{\Gamma}_e . \vec{n} = \min(-\mu_e n_e \vec{E} . \vec{n}, 0.0) - \frac{1}{4} n_e v_{th,e} \tag{2.45}$$

The above equations, in fact are preventing the zero charged particle fluxes to the wall as the driving force are directed towards the wall. In Eqs. (2.43) and (2.44), the second term is the thermal flux of ions to the wall and the first term is a drift flux contribution due to the sheath potential. This term quantifies a nonzero drift flux for positively charged ions in a positive sheath (i.e., decreasing potential toward the wall) and zero flux in the same sheath for negatively charged ions. The opposite is true for negative sheaths.

When positive ions hit the cathode (either electrode surface or dielectric surface), it releases γ_{sec} secondary electron(s). The secondary emission coefficient γ_{sec} is generally between 0 and 1. Its value depends on the particle, its energy, the surface material and temperature. In this case, the expression of the electron flux due to secondary emission is:

$$\vec{\Gamma}_{\sec} = \gamma_{\sec}\vec{\Gamma}_p \tag{2.46}$$

Thus, the total electron flux at the wall (Eq . (2.45)) becomes,

$$\vec{\Gamma}_e.\vec{n} = \min(-\mu_e n_e \vec{E}.\vec{n}, 0.0) - \frac{1}{4} n_e v_{th,e} - \gamma_{\sec}\vec{\Gamma}_p.\vec{n} \tag{2.47}$$

This boundary condition is essential because the mechanism and speed of the streamer breakdown process depend on the availability of these secondary electrons. As mentioned in [98], this implementation of the secondary emission is not consistent with the experimental value of $\gamma_{\sec}$ at the cathode. In experiments, $\gamma_{\sec}$ is calculated as the ratio between the flux of secondary electrons and the particle flux to the electrodes. As a solution, thermal velocity of zero at the cathode is imposed. However, due to the variation of the plasma potential responding to the applied voltage, it is fairly delicate to detect which wall represents the instantaneous cathode. An alternative solution is suggested in [99,100] .

Here for simplicity, we assume that the thermal velocity is zero on the all the surfaces. As mentioned before, variation of the potential causes the drift flux of electrons to change along surface leading to a jump of the electron concentration at a point where E =0. In some cases, this interrupts computations, because the needed accuracy cannot be achieved in the jump vicinity. thus to determine the instantaneous cathode and insure a smooth and stable variation of the charge boundary condition on the surface, the exact solution of the mentioned boundary conditions is considered as follows;

$$n_p = e^{\frac{\max(\vec{u}_p.\vec{n}, 0.0)\Delta}{-D_p}}(n_p^{Int}) \tag{2.48}$$

$$n_n = e^{\frac{\max(\vec{u}_n.\vec{n}, 0.0)\Delta}{-D_n}}(n_n^{Int}) \tag{2.49}$$

$$n_e = \frac{\gamma n_p \mu_p}{\mu_e} \times (1 - e^{\frac{\max(\vec{u}_e.\vec{n}, 0.0)\Delta}{-D_e}}) + e^{\frac{\max(\vec{u}_e.\vec{n}, 0.0)\Delta}{-D_e}}(n_e^{Int}) \tag{2.50}$$

The above equations are general boundary conditions, which are valid for any surface.

2.4 - Interaction of the discharge and the Flow

The problem can be separated into two parts. One of them is modeling of plasma phenomena (ionization, recombination, evolution of electric field, etc.) that occur on sub nanosecond-to-microsecond time scale on the background of “frozen” flow field. The second problem consists of coupling of the plasma part with the flow by means of plasma-induced force and heating rate. In the first approach, the coupling between the plasma solver and the flow solver is in one way, that is, in this case a gas heating and source term is imposed to the plasma solver and the plasma is only influencing the flow field through the electro-hydrodynamic force or gas heating. The electro-hydrodynamic (EHD) force associated with the

momentum transfer from charged particles to neutral molecules in the volume above the dielectric layer is considered as follows [73].

$$\mathrm{f} = \sum_{k=i,e,n} n_k m_k \nu_k \mathrm{u_k} \tag{2.51}$$

where, n_k is the charged particle density, m_k is particle masse, ν_k is the momentum exchange frequencies for particle-particle collision and $\mathrm{u_k}$ is the charged particle mean velocity. In the above equation, the mean velocity of the neutral particles with respect to the charged particle mean velocities is neglected. Using the definition of the charged particles mobility ($\mu_\mathrm{k} = \frac{e}{\nu_k m_k}$) and considering the dominancy of the drift terms in charged particles current density in the case of discharge ($\mathbf{j_k} \approx e n_k \mu_k \mathbf{E}$), the above equation can be written as;

$$\mathbf{f} = \sum_{k=i,e,n} \frac{\mathbf{j_k}}{\mu_\mathbf{k}} \approx e\left(n_p - n_e - n_n\right)\mathbf{E} \tag{2.52}$$

Above equation thus provides the total force per unit volume acting on the neutral molecules and is equal to the Coulomb force acting on the charged particles. In other words, the momentum gained by the charged particles in the electric field is exactly and locally balanced by collisions, and entirely transmitted to neutral molecules.

When the plasma equations are solved in tandem with an external flow model, the gas heating source terms, p_{th} are collected and communicated to the flow model which is then responsible for determining the bulk temperature. The gas heating source terms are calculated by the plasma solver and include the ion Joule heating term due to the work done on the ions by the electric field, inelastic collisional heating term due to the quenching of electronically excited species such as nitrogen, oxygen metastables, and the elastic collisional heating term due to elastic electron impacts with the background gas. These gas heating source terms get importance for atmospheric DBD plasma actuator driven by a nanosecond voltage.

Here, for the case of simplicity, the one-way coupling of the plasma solver and the flow solver is adopted. We should mention that this is quite a valid assumption for large range of applications, due to the large difference of the fluid characteristic time scales and time scales of operating plasma dynamics.

However, in the case that plasma solver and the flow solver are communicating in two-way coupling, the flow influences the plasma as a momentum source for the species. This momentum source enters in the drift-diffusion equations. This effect is particularly important for the neutral species, as there are no electric forces to modify their speed. Moreover, if the fluid dynamic time scales become comparable, then the two-way coupling will need to be handled and the fluid solution advancement should be performed using the DBD time scale.

2.5 - Numerical procedures

The coupled plasma–fluid problem is inherently nonlinear and exhibits wide ranges of time and length scales. Numerical solution of the charged particles governing equation coupled with Poisson equation is subjected to serious limitations of selection of numerical time-step. Sufficiently small time-steps provide stable and accurate solution, however the computational run time will be massively high for the purpose of simulation. Thus, the approach selected for treating the time discritization and advancing the time-step should be capable of both providing needed accuracy and stability while providing a reasonable computational cost. In this view, different approaches could be found in the literatures that have been tested to reach this purpose. Moreover, existing different time scales in the plasma formation, originating from fast ionization and slow recombination process along with drift and diffusion of the species, typically lead to stiff problem that in this case is the vastly differing time scales. Moreover, high accuracy may be required for all time scales. To resolve this issue, special treatment need to be considered for solving the governing equation of the plasma dynamic, some possible remedies could be:

- Implicit methods are favored for stiff problems. And they are often used but these can be expensive and difficult to derive. Marching the solution in time will typically need to be implicit because of the diffusion terms, which otherwise would cause a severe time step restriction. The reaction terms may also contribute to the necessity of using an implicit method if some fast reactions reach equilibrium on a much faster time scale than the processes being modeled (i.e., if the reaction terms are “stiff”).

- Physically, the presence of diffusion in the system should damp high frequency oscillations. When the full model is solved numerically however, the time-step required to prevent high frequency oscillations from overwhelming the results is very small when the diffusion term is discretised. The diffusion in the continuity equations of the charged particle could be treated as source term. This can lead to numerical stability issues, though; it could reduce the numerical diffusion and increase the accuracy.

-Operator splitting [54,101,102] (or the fractional step method) treats the separate processes independently, i.e. solve the homogenous (convective part) and inhomogeneous (source terms) part of the equations separately. Although splitting allows each component to be modeled efficiently, none should be allowed to vary significantly before interacting with others. In this case, the simulation could take advantage of the best scheme that can be chosen in each case (useful when some terms are insignificant). Moreover, accuracy and stability issues can be dealt with at each stage (aiding robustness) and also it is relatively simple to deal with processes acting on widely differing time scales, due to flexibility in the choice of time-stepping. This is typically relatively simple, cheap to run and fairly stable. But

it also ignores the fact that the processes are coupled and do interact, so it may misinterpret the results. Formally, the scheme is only first order accurate.

- Sub-cycling or dual time-stepping is used as a simpler alternative, particularly when the source terms are complicated and highly nonlinear. This uses many steps of an explicit method to reach the same time level as the global time-step.

- Adaptive time-stepping might be desirable allowing larger time steps when it is possible.

Although the mentioned remedies could benefits the solution, but all of them require that quantities don't change dramatically within a global time-step. Moreover, small time-steps are required to resolve the effects of rapid transients phenomena's. Also, larger time-steps may be necessary to allow the simulation to be run within a reasonable time. In other words, numerical stability governs the length of time-step which can be used to get any results at all. In general, the time-step is constrained by accuracy which must also be balanced against efficiency and stability. In the following sections, some of the numerical treatments, used in this paper for the solution of the governing equations of plasma-fluid model are presented.

2.5.1 - Time discretization

In the present study, we have employed an operator-split sequential solution algorithm. In using time-split algorithms for processes operating in a wide range of time scales, the choice of time-step size is typically determined by the smallest time scale, but need not necessarily be chosen as such. To speed up the solution procedure, an adaptive intermediate time scale is chosen to advance the overall system in time. Also, a predictor–corrector approach is used to ensure sufficient coupling between the solution variables.

2.5.2 - Time-scales of the plasma dynamic

The plasma/flow interaction is fundamentally a multi-scale problem [102] with a large range of time scales from shorter than the pico-second (e.g. dielectric relaxation time) to time scale of the airflow [56]. In the case of RF discharge operating at frequency of f , the time scale of operating frequency is;

$$\tau_{\omega} = \frac{1}{f} \tag{2.53}$$

Moreover, the reaction terms in the continuity equation of the charged particles have different time scales. The characteristic times of ionization, attachment and recombination processes are in the order of;

$$\tau_{ionization} \approx \frac{1}{\alpha|\mu E|} \tag{2.54}$$

$$\tau_{attachment} \approx \frac{1}{\eta|\mu E|} \tag{2.55}$$

$$\tau_{recombination} = \frac{1}{r\max(n_p, n_e, n_n)} \tag{2.56}$$

Also, the convective and diffusive fluxes have different time scales based on the corresponding velocities as;

$$\tau_{drift} = \frac{\min(\Delta x, \Delta y)}{|\mu E|} \tag{2.57}$$

$$\tau_{diff} = \frac{\min(\Delta x^2, \Delta y^2)}{2D} \tag{2.58}$$

In addition, electrostatic relaxation of the electric field consistent to the distribution of charge density in the bulk, on a certain time scale need to be considered when charged particles appear and an electric field comes into play. This relaxation time defines a maximum reaction time on which the field varies when a charge density perturbation is applied:

$$\tau_R = \frac{\varepsilon_0}{e(\mu_p n_p + \mu_e n_e + \mu_n n_n)} \tag{2.59}$$

This temporal scale could be much smaller of both drift diffusion motion time and chemical reactions one. So an implicit treatment, regarding the electric field evolution, is required. This time step restriction is usually one of the most severe and is equivalent to the Courant type stability criterion for the current continuity equation. The origin of the restriction is primarily caused by the non implicit treatment of the electric field in the species transport equations. When the equations are solved explicitly, the time-step needs to satisfy the Courant–Friedrich–Levy (CFL) condition that means time-step needs to be less than the time scale of the problem. The CFL condition can be expressed in function of the transport coefficient, the electric field and the density of charged particles.

$$\Delta t = Co \frac{\min(\Delta x, \Delta y)}{\mu E + \frac{2D}{\min(\Delta x, \Delta y)} + \frac{e}{\varepsilon_0}(\mu_p n_p + \mu_e n_e + \mu_n n_n)\min(\Delta x, \Delta y)} \tag{2.60}$$

The CFL condition presented above has three contributors, the drift velocity μE, the "diffusion velocity" $2D/\min(\Delta x, \Delta y)$, and some contribution of the Maxwell time $\frac{e}{\varepsilon_0}(\mu_p n_p + \mu_e n_e + \mu_n n_n)\min(\Delta x, \Delta y)$. This expression is numerically quite different for the electrons and the ions (electrons transport coefficients are usually more than a 100 times larger than the corresponding ions coefficients).

2.5.3 - The fractional step method and sub-cycling

The continuity equation of the electron and positive ions (Eqs. (2.10)-(2.16)) could be handled by fractional step method. Similar procedure was adopted in [66] for modeling DBD plasma actuators. To this purpose, the main problem needs to be split in two sub-problems. One issue regarding the solution of the continuity of the charged particle is arising due to the presence of very fast chemical rates, and in particular by large decay rates, which make the source terms coupled with drift diffusion terms quite unstable. Therefore, we will treat the terms separately by rewriting the governing equation as follows;

$$\frac{\partial n_k}{\partial t} = \mathbf{H}(n_k) + \mathbf{R}(n_k)\,, \tag{2.61}$$

And splitting them into;

$$\frac{\partial n_k}{\partial t} = \mathbf{H}(n_k)\,, \tag{2.62A}$$

$$\frac{\partial n_k}{\partial t} = \mathbf{R}(n_k)\,, \tag{2.62B}$$

Two different approaches could be considered for dealing with the above equations. First; Eq. (2.62A) could be solved with time-step Δt .Then the results will be used to solve Eq. (2.62B) with time-step Δt .

This approach is often known as Godunov splitting and essentially needs two sub-cycle. However, it is possible to use more cycles using an even number of overall steps while keeping the order in which the solution of Eq. (2.62A) and Eq. (2.62B) are carried out. An alternative approach which requires three sub-cycle is the Strang splitting [103]. In this case,

- Eq. (2.62A) will be solved with time-step of $\Delta t/2$,
- Eq. (2.62B) will be solved with time-step of Δt ,
- Eq. (2.62A) will be solved again with time-step of $\Delta t/2$.

The small modification in Strang splitting allows the overall scheme to be second order accurate. Here also it is possible to use more sub-cycles. In this case, one $\Delta t/2$ step (Eq. (2.62A)) followed by a series of Δt steps (Eq. (2.62B)) until finishing with one $\Delta t/2$ step is necessary. The Strang splitting is a symmetric version of the above procedure of the first form. Another variant of Strang splitting method could be expanded by splitting up the solution procedure into independent steps corresponding to the advection, diffusion, and reaction processes and handling them independently at each step [104]. Similar methodology that uses both explicit and implicit formulation of the advection and diffusion part could be find in [105] .

2.5.4 - Adaptive time-stepping

As mentioned before, for accuracy and stability of the modeling, the time step is defined by the CFL condition, i.e. particles cannot move more than a grid size during the time step. The modified or adaptive time step concept is based on the recognition of the onset of the breakdown. In this way, the time step is defined by electron velocities, considering a threshold, based on maximum electron number density for onset of breakdown [72] .

2.5.5 - Super-time-stepping

As was mentioned before, explicit methods for their solution are easy to implement but have very restrictive time-step constraints. Implicit solution methods can be unconditionally stable but have the disadvantage of being computationally costly or difficult to implement. Recently, super-time-stepping methods [106] for treating unsteady terms occupy an intermediate position. In such methods each super step takes *s* explicit Runge–Kutta like time-steps to advance the parabolic terms by a time-step that is larger than a single explicit time step. Mayer [107] et al. derived the first and second order super-time-stepping scheme based on the Runge–Kutta–Legendre (RKL) methods. The general recursion formula of first order (RKL2) and second order RKL (RKL4) are respectively as follows;

$$
\begin{aligned}
&n^0 = n^t, \\
&n^1 = n^0 \tilde{\mu}_1 \Delta t \mathbf{P}(n^0), \\
&n^j = \bar{\zeta}_j n^{j-1} + \bar{\varsigma}_j n^{j-2} + \tilde{\mu}_j \Delta t \mathbf{P}(n^{j-1}), \quad 2 \le j \le s \\
&n^{t+\Delta t} = n^j \\
&\textit{where} \\
&\tilde{\mu}_j = \frac{2j-1}{j}\frac{2}{s^2+s}, \qquad \bar{\zeta}_j = \frac{2j-1}{j}, \qquad \bar{\varsigma}_j = \frac{1-j}{j}
\end{aligned}
\tag{2.63}
$$

and

$$
\begin{aligned}
&n^0 = n^t, \\
&n^1 = n^0 \tilde{\mu}_1 \Delta t \mathbf{P}(n^0), \\
&n^j = \bar{\zeta}_j n^{j-1} + \bar{\varsigma}_j n^{j-2} + (1-\bar{\zeta}_j - \bar{\varsigma}_j) n^0 + \tilde{\mu}_j \Delta t \mathbf{P}(n^{j-1}) + \tilde{\gamma}_j \Delta t \mathbf{P}(n^{j-1}), \quad 2 \le j \le s \\
&n^{t+\Delta t} = n^j \\
&\textit{where} \\
&\tilde{\mu}_j = \frac{(2j-1)(j+2)(j-1)^2}{j(j-2)(j+1)^2}\frac{4}{s^2+s-2}, \qquad \bar{\zeta}_j = \frac{(2j-1)(j+2)(j-1)^2}{j(j-2)(j+1)^2}, \qquad \bar{\varsigma}_j = \frac{(j-1)^3(j^3-4)}{j^3(j+1)(j-3)} \\
&\tilde{\mu}_1 = \frac{4}{3(s^2+s-2)}, \qquad \tilde{\gamma}_j = \frac{(2j-1)(j+2)(j-1)(j^2+j-2)}{2j^2(j-2)(j+1)^2}
\end{aligned}
\tag{2.64}
$$

However, to be used for advection-diffusion problems, the equations need to be solved in operator split-manner. The number of the stages, of RKL2 could be chosen to be the lowest odd values that satisfy the stability criteria mentioned in [107] . Then, continuity equations of the number density of the charged particles will be divided in two sub-problems, considering the homogenous and non-homogenous operators

$$\frac{\partial n_k}{\partial t} = \mathbf{H}(n_k) + \mathbf{R}(n_k) \,, \tag{2.65}$$

Then, an entire, time step, representing the action of all operators contains the following stages.

- Solve $\left(n_k^{t+\Delta t}\right)^* = \mathbf{H}(\Delta t/2) n_k^t$ over time Δt with data n_k^t to obtain $\left(n_k^{t+\Delta t}\right)^*$
- Solve $\left(n_k^{t+\Delta t}\right)^{**} = \mathbf{R}(\Delta t)\left(n_k^t\right)^*$ over time Δt with data $\left(n_k^{t+\Delta t}\right)^*$ to obtain $\left(n_k^{t+\Delta t}\right)^{**}$
- Solve $n_k^{t+\Delta t} = \mathbf{H}(\Delta t/2)\left(n_k^t\right)^{**}$ over time Δt with data $\left(n_k^{t+\Delta t}\right)^{**}$ to obtain $n_k^{t+\Delta t}$

2.5.6 - Semi-Implicit solution of Poisson-transport equations

When time integration of the Poisson-transport system is treated explicitly, Poisson's equation and charged particle transport equations are solved successively and that the electric field calculated at time t^k is supposed to be constant during the integration of the charged particle transport equation between times t^k and t^{k+1}. However, The strong coupling between the charge density equations and the electric potential results in a severe time step restriction of the explicit methods (the time step must be smaller than the dielectric relaxation time "dielectric relaxation time-step constraint). In order to overcome this constraint, the Poisson equation is solved in a semi-implicit manner for the electric potential [108]. Semi-implicit treatment of the Poisson equation has been proven to be able to provide stable results and allow larger time-steps (similar approach was used by [54,101]). To derive the semi-implicit version of the Poisson equation, species number densities in the source term of the Poisson equation need to be linearized implicitly. This could be accomplished by substitution of charges number density for the source term using the species transport equations, and expanding the right hand side using first order Taylor serious expansion;

$$\nabla.(\varepsilon\nabla\phi^{t+1}) = \rho_c^{t+1} = \rho_c^t + \rho_c^{\Delta t} = -e(n_p{}^t + \Delta t\frac{\partial n_p}{\partial t} - n_e{}^t - \Delta t\frac{\partial n_e}{\partial t} - n_n{}^t - \Delta t\frac{\partial n_n}{\partial t}) \tag{2.66}$$

By substitution of charges number density for the source term using the species transport equations, and treating the terms containing terms with drift velocities (thus electric field), Poisson equation could be rewritten as

$$\nabla.(\left[\varepsilon + \Delta t\left(\mu_p n_p + \mu_e n_e + \mu_n n_n\right)\right]\nabla\phi) = \tag{2.67}$$
$$-e(n_p{}^t + \Delta t\nabla.(\nabla n_p{}^t) - \nabla.(n_p\vec{u}) - n_e{}^t - \Delta t\nabla.(\nabla n_e{}^t) + \nabla.(n_e\vec{u}) - n_n{}^t - \Delta t\nabla.(\nabla n_n{}^t) + \nabla.(n_n\vec{u}))$$

The charge continuity equations are also solved based on a semi-implicit method. In this way, the flux terms are evaluated using the value of charge densities in new time step, while the source terms (ionization, recombination, and attachment) are estimated using the value of the charge densities from previous time step. Semi-implicit Poisson/transport could be attractive in terms of computation time when using large time step compared to the stability constraint (CFL or Maxwell relaxation time). However this scheme is only first order in space and said to be quite diffusive. On the other hand fully explicit second order Poisson/transport coupling is feasible but at prohibitive computational cost.

2.6 - Implementation of the model

The coupled systems of species equations (Eqs. (2.10)-(2.15)) as well as Poisson's equation (Eq. (2.16)) are solved using OpenFOAM by enforcing the above mentioned boundary conditions and using the above mentioned numerical procedures for two dimensional simulations. As mentioned in [58], the 2D Cartesian geometry can provide realistic results if the plasma is not filamentary in the direction perpendicular to the simulation plane or if the width of the filaments in this direction is large with respect to the thickness of the filament above the dielectric surface.

The implementation of the plasma-fluid model needs some extra treatment regarding the multi-region coupled solution of the Poisson equation and inter-coupling between the transport equations and the electric field. Some of these treatments are mentioned below.

2.6.1 - Multi-region coupling of the electric potential

The presence of the Dielectric layer brings the need of the solution of the electric potential equation on gas phase (e.g. air) and the solid phase (e.g. dielectric layer). In Fig. (2.1), a schematic of the multi-region problem is shown. Therefore to be able to obtain the solution of the Poisson equation in multiple regions, a multi-region solver is developed based on the partitioning approach. The main principal idea is to solve governing equations of the similar physics that are coupled through a common boundary.

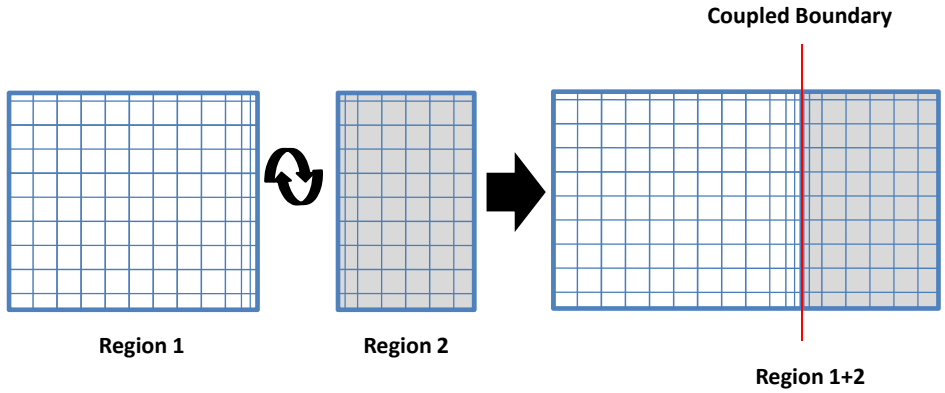

Fig. 2.1: A multi-region coupled domain for electric potential.

In the portioned approach, governing equations (Poisson equation) are solved in each zone with the appropriate boundary conditions using a segregated solver. In other words the iterative solution will be obtained region by region. In addition, the interface boundary condition are treated in a segregated manner where one of the interface equations is applied as a boundary condition to one sub domain and the other boundary condition to the second sub domain. These boundary conditions are implemented using a Mixed BCs for PDE on different parts of the boundary of the domain of the equations. In this way, the resulting conditions are responsible for coupling between different regions and have to be used for each region according to the updated values in the neighboring region. The schematic of the partitioned approach for the plasma-fluid problem is demonstrated in Fig. (2.2).

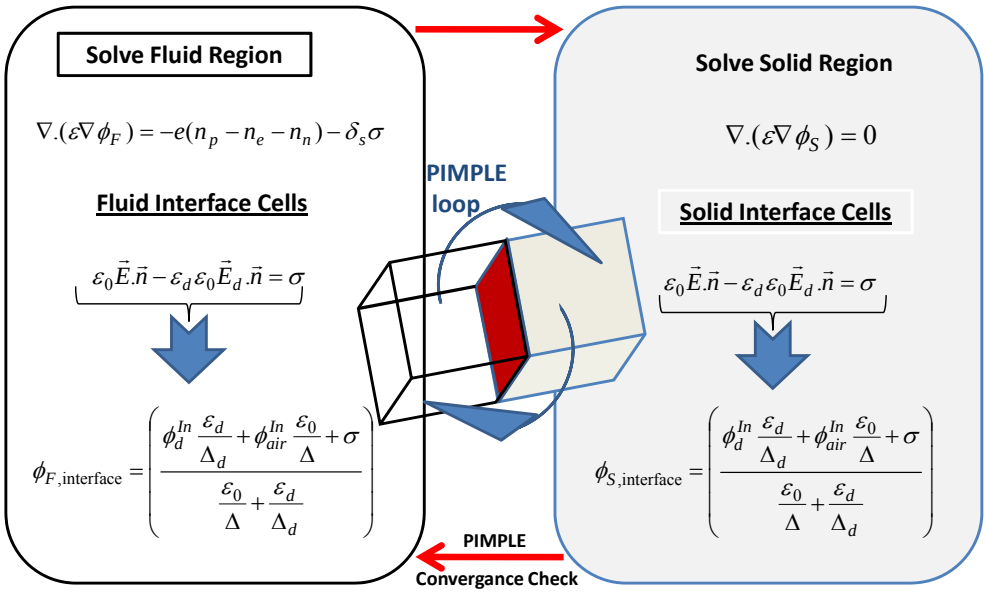

Fig. 2.2: Schematic of the partitioned approach for the plasma-fluid problem.

In this approach the convergence is assured by using a PIMPLE loop for solution of the governing equations. In other words, for each time step, given a maximum number of iterations, the governing equations will be solved alternatively for every cell of the coupled regions and when the convergence is reached, the solution will be proceeded to the next time step.

2.6.2 - Coupling of Poisson and charged particles transport (segregated solution of the Poisson-Transport)

In the plasma-model, there exist two separate problems regarding the coupling of the variables. First is the coupling of the number density of the particles and electric potential, and the second is related to the multi-region solution of the Poisson equation. The first approach that we had adopted is the iterative solution of discredized equation in each time step with sufficient internal iteration to guarantee enhanced coupling between the dependent variables and also convergence of the Poisson solver at the interface of solid zone (Dielectric material) and fluid zone (Air). The main algorithm of the plasma solver, includes a predictor and a corrector loop. The Schematic of the algorithm is shown in Fig. (2.3).

Predictor loop: at the beginning of each time step, the values of charge number densities and transport coefficients are known, and they will be used to solve the Poisson equation. When the electric field is updated, all the transport properties and source terms of the charge continuity equations will be updated according the new value of the electric field.

Corrector loop: continuity equation of the charge density will be solved with updated values of the electric field and source terms. Then, the source term and artificial permittivity arising due to the semi-implicit treatment of the Poisson equation will be recalculated. Moreover, the surface charge density will be corrected also at this step.

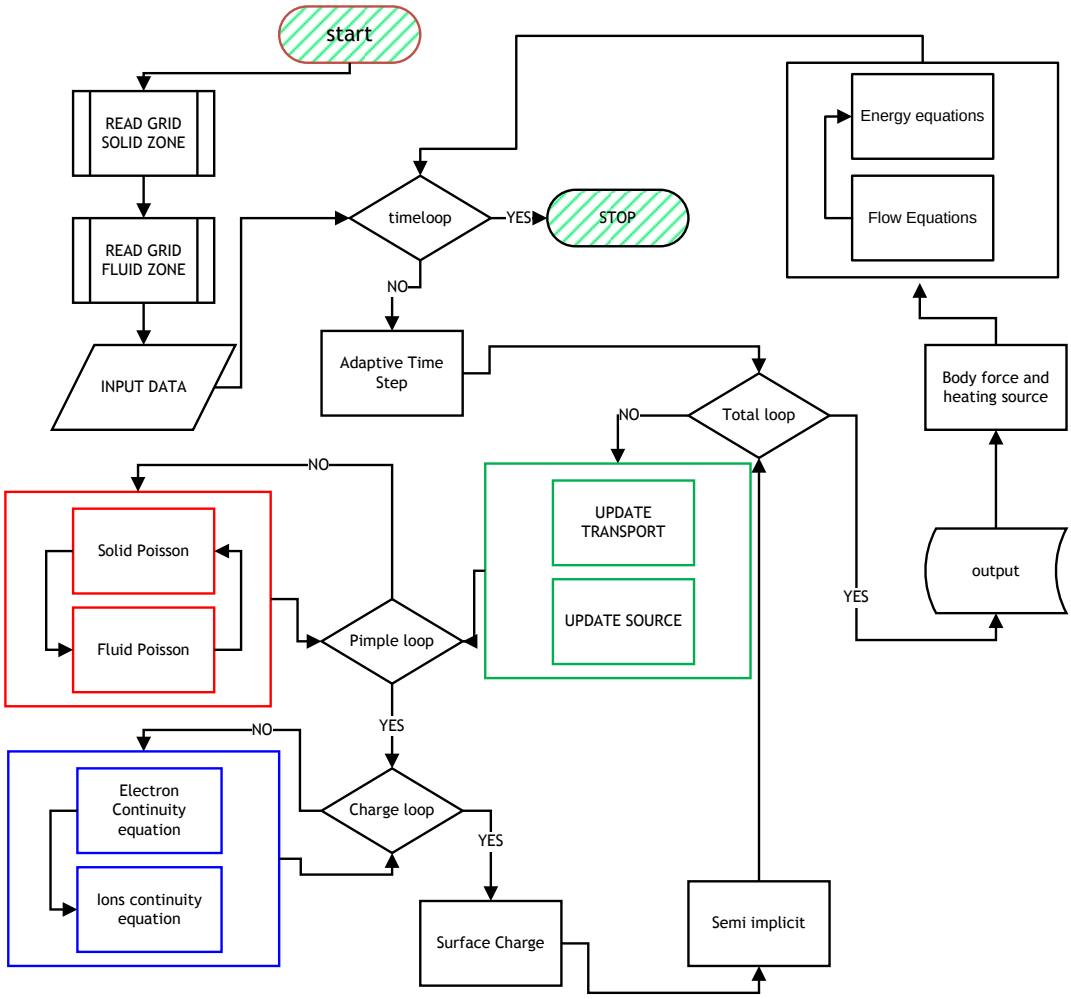

Fig. 2.3: Flowchart.

2.6.3 - Grid requirements

The plasma processes are very sensitive to the local electric field, which in the DBD case varies at the characteristic scale on the order of 10 microns for the high applied voltages. The necessity of the correct resolution of the plasma dynamics leads to a grid size of the order of several microns. However, the increase of the operating voltage leads to the further decrease of the grid size. Thus, the computational grid need to be selected based on the outcome of testing several grid sizes to ensure enough resolution of the steep electric field and electron-ion density gradients relevant to the ionization wave front, and to ensure the plasma sheath near the wall-gas interface can be adequately resolved while balancing the consideration of the computational costs.

2.7 - Results and discussion

Since there is no benchmark case for comparison, we had chosen the recent numerical work of Unfer et al [109] and Boeuf et al [58] (shown respectively by Explicit asynchronized LTS and Semi-implicit (SG method)) for the purpose of comparison of the influence of the each numerical remedies that we had used for alleviating the stiffness of the numerical solution of the plasma-Fluid model. Firstly, a simple case of constant positive voltage is considered. Although this case is simple, it can provide the possibility of correctly analyzing different numerical issues. This case comprises a 2D geometry with exposed electrode as anode (with constant positive voltage). Secondly we will present some validation case, on basically the same geometry but different voltage waveform.

One of the important aspects of the numerical simulation of the plasma dynamics is to determine the proper choice of the global time-step Δt which would require balancing computing efficiency with stability. In Fig. (2.4), effect of the time-step on the accuracy of the current density behavior is shown for a coarse grid with the cell length of 2 μm. This current is the displacement current on the bottom electrode. In Fig (2.4a), upwind scheme is used for discritization of the convective term in continuity equation and the Euler scheme is used for treating the unsteady terms. The results are clearly showing that when the time step is larger, results are more diffusive and the peak value of the current happens later at a smaller maximum magnitude. In addition, the results are showing unstable results when the time step is reduced to smaller than 10^{-11} s. In Fig (2.4b), a second order differed corrected Gamma scheme is used for the convective terms. Comparing the Fig. (2.4a) and Fig. (2.4b), we can see that Upwind scheme, as was expected, shows more diffusive behavior in comparison with the second order differed corrected Gamma scheme. But at the same time this kind of error obviously makes the scheme highly stable even for large time steps, but produces wrong solutions.

In Fig. (2.5a), the grid independency test results are presented for simulations with Euler time and first order upwind spatial discretization. When the grid density is low, effect of the numerical diffusion appears to me more intense, and in contrast when the grid is refined, the resolution of the results is better. Moreover, as shown in Fig. (2.5b), all the time discretization schemes including the Euler, backward and splitted super-time stepping have shown similar accuracy on the refined grid with enough small time steps.

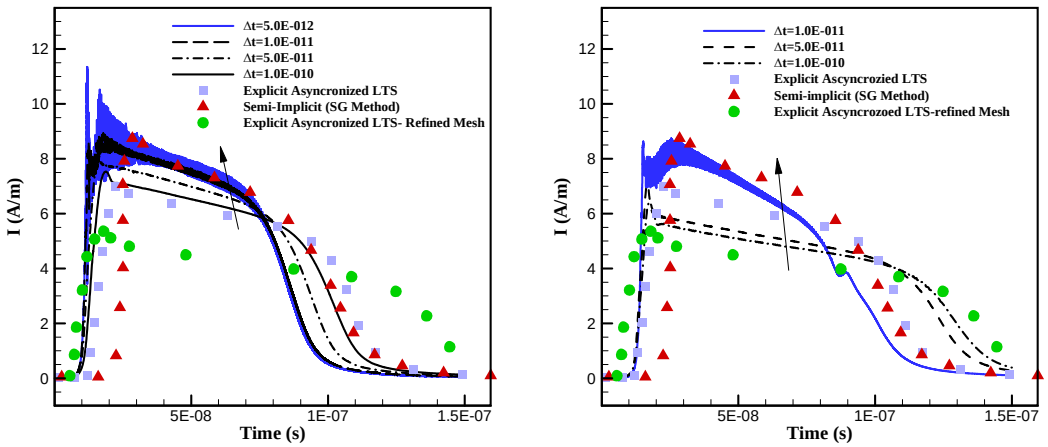

a) b)

Fig. 2.4 : Influence of time-step of implicit Euler scheme on the current density a) first order Upwind Scheme b) Second order differed correction Gamma.

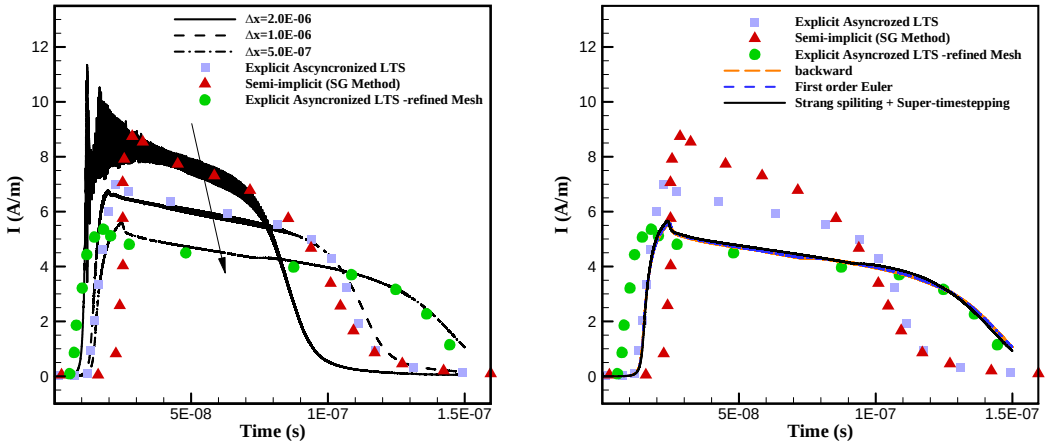

a) b)

Fig. 2.5 : a) Grid dependency of the results for the implicit Euler scheme with first order Upwind b) Comparison of different time discretization for $\Delta t = 5\times10^{-12}s, \Delta x = 0.5\mu m$ **.**

In Fig. (2.6), the effect of the number of the super-time stepping stages with RKL is demonstrated on a medium refined grid with $\Delta x = 1\mu m$ and $\Delta t = 5\times10^{-12}s$. For lower number of super-time stepping stages, the results are more diffusive. This was expected, as increase of n should allow larger time-step to be used for the simulation. However, increasing the number of the super-time stepping, in this case more than 21, didn't change the resolution of the obtained results. We should mention that, while splitted super time stepping is an important technique for improving accuracy and stability, its ability to increase the global time-step is limited.

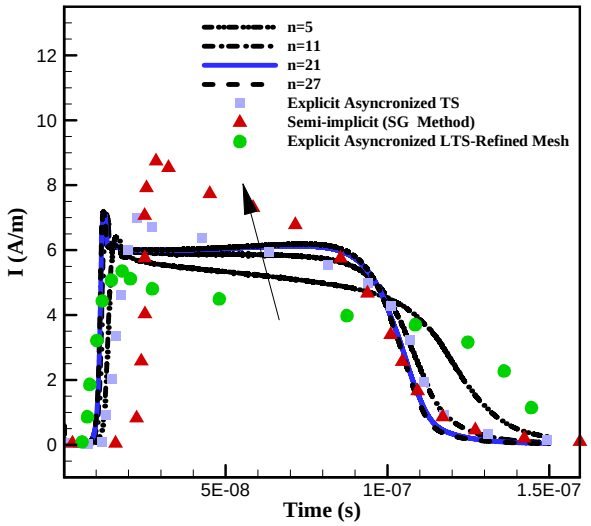

Fig. 2.6: Influence of the super time stepping levels on the resolution of the current density behavior for positive constant voltage.

As now the influences of the main numerical treatments are shown for the positive constant voltage case, we can readily select the numerical approach for our simulations. In the following we will present validation studies for different voltage waveform. In Fig. (2.7), the current density behavior in the case of a constant negative voltage and positive nano-second voltage is shown and the results are compared with numerical results of Boeuf et al [58] and Unfer and Boeuf [110]. The results of the present study are correctly capturing the current evolution versus time.

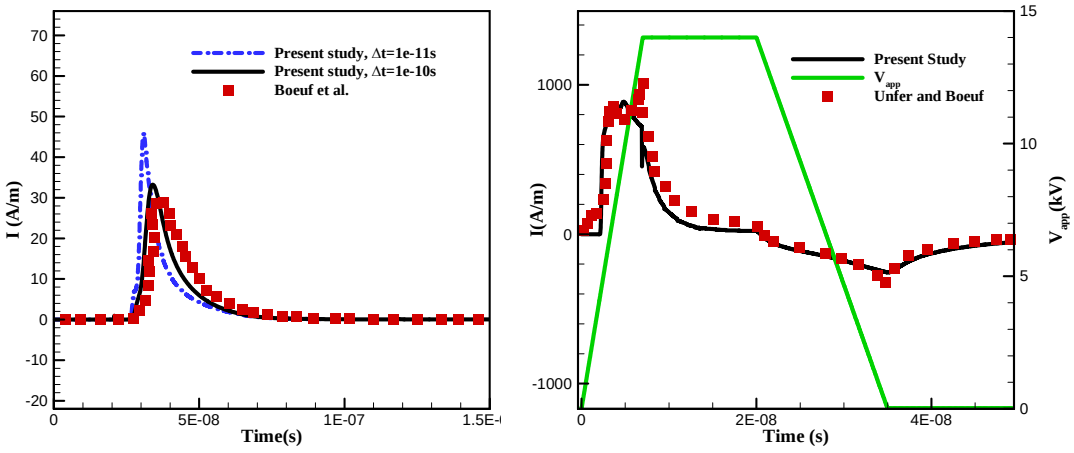

a) b)

Fig. 2.7: Comparison of the current obtained from the present study for: a) constant negative applied voltage with the work of Beouf et al [58] **b) nano-second pulsed voltage with the work of Unfer and Boeuf** [110].

In Fig. (2.8), current behavior in the case of a positive and negative voltage ramp is shown. The results are showing the similar features described in previous papers [65,111,112] and are qualitatively valid. It is clear from the results that there is a difference between the discharge characteristic in these cases. In the case of positive ramp, the electrode above the dielectric layer plays the role of an anode. Once the size and density of the positive ion cloud reach critical values, a high current breakdown occurs, characterized by the development of high amplitude pulses in current profile. The discharge during the positive part of the cycle is composed of successive phases of ion cloud formation and high current breakdown. When a negative voltage ramp is applied, the current profile is also composed of current pulses, but with a frequency much larger than in the positive ramp case and of much lower intensity.

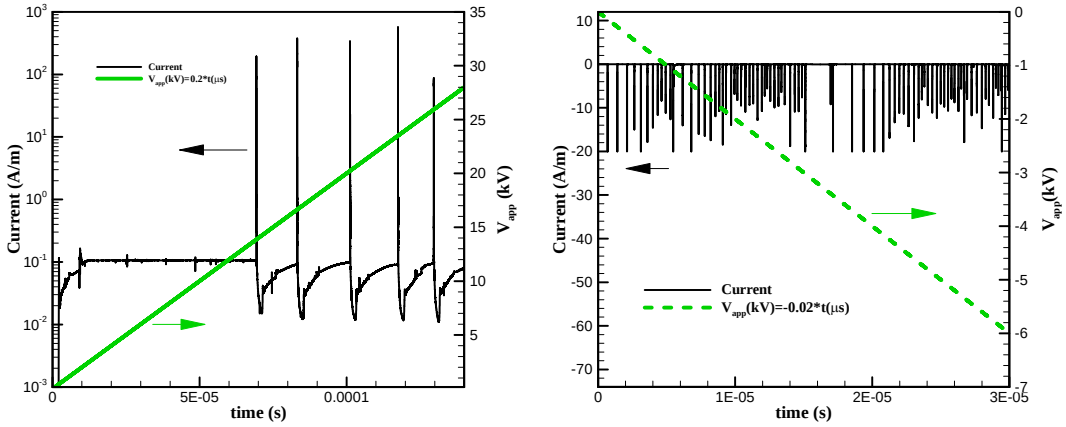

a) b)

Fig. 2.8: current characteristic of the dielectric barrier discharge with a) positive ramp voltage b) negative ramp voltage.

And in the last case, an AC sinusoidal voltage with frequency of 8kHz and 8kV is applied to the exposed electrode and the results are shown in Fig. (2.9). The results are again in qualitive agreements with results presented in [65,76]. The difference observed between the positive ramp voltage and negative ramp voltage (Fig. (2.8)) can be observed also in Fig. (2.9) for positively going and negatively going part of the AC sinusoidal voltage. This difference implies that the EHD force is important not only during the positive part of the sinusoidal voltage cycle but also during the negative part of the cycle.

The component of the force parallel to the plate is shown in Fig. (2.10) for the duration of the voltage similar to Fig.(2.9). During the positive part of the cycle, the EHD force is due to the formation of a positive ion cloud that is periodically interrupted by high current breakdown. The EHD force during the negative part of the cycle is due to the development of a negative ion cloud that continuously grows during the successive high frequency current pulses that form in this regime [73].

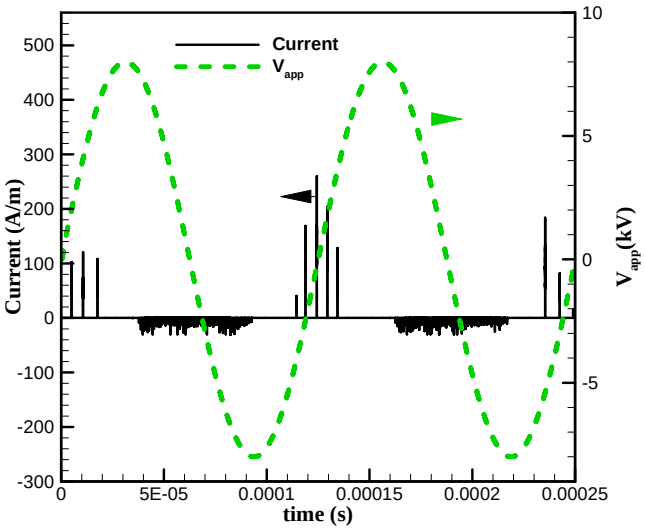

Fig. 2.9: Voltage and current of a DBD actuator with AC-sinusoidal applied voltage.

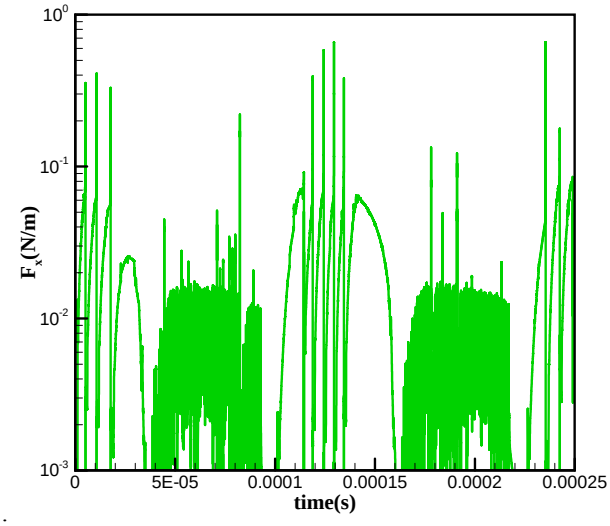

Fig. 2.10: Component of the EHD force parallel to the surface for actuation with AC sinusoidal voltage.

2.8 - Conclusions

Different assumptions and considerations regarding the Plasma Fluid model are discussed. In addition, various numerical issues regarding the stability and accuracy of the model are discussed and explained. To solve these issues, several numerical remedies that have been used in the literature are employed. At the end, a three particle fluid model of the discharge in air that provides the space and time evolution of the charged particle densities, electric field and surface charges was implemented in OpenFOAM. Different voltage waveforms, including positive and negative constant and ramp voltage and a case of AC sinusoidal voltage, have been considered for testing the accuracy of the implementation. In the

following chapter, the Plasma-fluid model will be used for modeling nano-second pulsed voltage waveform DBD actuator.

3 - Two-Dimensional Numerical Modeling of Interaction of Micro-Shock Wave Generated by Nanosecond Plasma Actuators and Transonic Flow

Abstract

The influence of nanosecond pulse-driven, surface-mounted dielectric barrier discharge (DBD) actuators on a transonic flow is studied numerically. An airfoil representing turbo-machinery blades in transonic flow is considered as a test case. A two dimensional fluid model of DBD is used to describe the plasma dynamics. The model couples fluid discharge equations with compressible Navier-Stockes equations. Simulations were conducted with an airfoil of NACA 3506 profile in a transonic condition of M=0.75. When a nanosecond pulse voltage is used, with a rise and a decay time of the order of nanoseconds, a significant amount of energy is transferred in a short time from the plasma to the fluid, which leads out to the formation of micro shock waves and therefore to the modification of flow features. Moreover, a plasma energy deposition model is developed and presented by using the results of the plasma discharge model[2].

Keywords: Nanosecond DBD actuators; plasma Energy deposition model; flow control; transonic flow;

3.1 - Introduction

For future huge airships, which are being designed to fly at very high altitude (as in the case of MAAT project [113]), efficiency increase is a crucial subject. For such airships, any increase in propulsion system efficiency will lead to a decrease in energy consumption through a decrease in size, length and mechanical complexity of propulsion system, thus also lowering the initial investment. At the blades of a propulsion system, separation causes significant total pressure loss causing a reduction in overall efficiency.

The abilities of traditional flow control techniques are limited due to a strict localization and slow response of such systems. Surface dielectric barrier discharges (SDBDs) can modify the boundary layer of a flow and have been studied as possible actuators for flow control. Their

[2] This chapter is based on the following published paper "M. Abdollahzadeh, J.C. Páscoa, P.J. Oliveira (2014), Two-dimensional numerical modeling of interaction of micro-shock wave generated by nanosecond plasma actuators and transonic flow, Journal of Computational and Applied Mathematics, Volume 270, pages 401-416, ISSN 0377-0427, doi:10.1016/j.cam.2013.12.030."

advantages include fast response, real-time control, low weight and no moving mechanical parts. In many applications, airflow control by DBD actuators is based on the generation of the ionic wind at the wall which adds momentum to the boundary layer. At low flow velocities, those actuators have proven to be effective for a wide range of applications [68,114]. At high flow velocities, however, the effect of the induced wall jet is almost negligible. In our previous study [115], the interaction between an AC-driven DBD actuator mounted on a NASA rotor 67 blade profile in transonic flow was investigated and almost no noticeable effect of the actuator on the performance of the rotor was observed. Recently [116,117], it was shown that a DBD actuator driven by nanosecond (NS) pulse has a more significant impact on the transonic flow. It was found that in these types of DBD actuators, there is an overheating in the discharge region, which generates a compression wave emerging from the surface into the flow. In this case, the effective control of the flow implies an appreciable change in its properties by local energy deposition. Fig. (3.1) shows the two main approaches by which DBD plasma actuators may influence the flow.

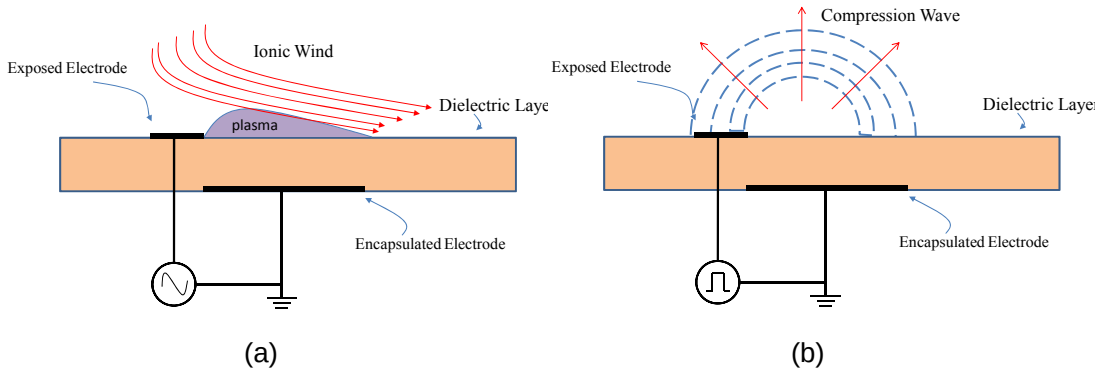

Fig. 3.1: DBD Plasma Actuators a) AC sinusoidal power source b) NS power source.

The purpose of the present study is to describe a numerical model for a surface dielectric barrier discharge in air, which uses a nanosecond voltage pulse generator. A two-dimensional fluid model of the DBD is used to describe the plasma dynamics at first. The model couples the fluid discharge equations with the compressible Navier–Stokes equations, which include momentum and thermal transfer from the plasma to the neutral gas. The 2D fluid model of the discharge in air provides the space and time evolution of the charged particle densities, electric field and surface charges. The model is solved numerically by means of a finite volume technique. A validation of the model is presented in order to assess the capabilities of the computational code here developed using open source code of OpenFoam. Secondly, a new plasma energy deposition model is presented based on the analysis of the results of discharge model.

The remaining of this chapter is organized in four sections. Section two presents the governing equations and the numerical procedure related to the modeling of the plasma discharge and the energy deposition model. In section three, the details of the configuration here considered for the test cases in the numerical experiments are provided. In section four,

comparison and analysis of the obtained numerical results are done. At the end, in section five, some important conclusions are made.

3.2 - Mathematical model and numerical procedure

3.2.1 - Plasma discharge mathematical model

In this model we are not interested in the details of air chemistry and, for the purpose of simplification, we just consider three types of charged particles electrons, one type of generic positive ions, and one type of generic negative ions. By considering the fluid description of electron and ion transport in air by means of classical drift-diffusion and local field approximation, the continuity equations for the electrons and the ions are written as,

$$\frac{\partial n_e}{\partial t} + \nabla.\vec{\Gamma}_e = (\alpha - \eta)\left\|\vec{\Gamma}_e\right\| - r_{ep} n_e n_p \ , \tag{3.1}$$

$$\frac{\partial n_p}{\partial t} + \nabla.\vec{\Gamma}_p = \alpha\left\|\vec{\Gamma}_e\right\| - r_{ep} n_e n_p - r_{np} n_n n_p \ , \tag{3.2}$$

$$\frac{\partial n_n}{\partial t} + \nabla.\vec{\Gamma}_n = \eta\left\|\vec{\Gamma}_e\right\| - r_{np} n_n n_p \ , \tag{3.3}$$

$$\vec{\Gamma}_k = -\mu_k n_k \vec{E} - D_k \nabla n_k + n_k \vec{u} \ , \tag{3.4}$$

where n_e, n_p, n_n are the charged particle densities and $\vec{\Gamma}_k .\ k = e, p, n$ their fluxes, α, η, r_{np} and r_{ep} are, respectively, the ionization coefficient, the attachment coefficient, ion-ion and electron-ion recombination coefficients. Moreover $\vec{E}$ is the electric field vector, μ_k and D_k are the charged particle mobility and diffusion coefficients, respectively, and $\vec{u}$ is the velocity of the gas flow. The recombination coefficients are considered to be constant and equal to $10^{-13} m^3 s^{-1}$ [118]. The charged particles mobility and ionization coefficient's of the air are obtained from Hoskinson [118] and are written as,

$$\mu_e\left(m^2 Torr V^{-1} s^{-1}\right) p = 0.21\left[24.32\exp(\frac{-E/p}{1057}) + 19.38\exp(\frac{-E/p}{23430}) + 14.45\right] + 0.79\left[173.1\exp(\frac{-E/p}{195.1}) + 36.19\exp(\frac{-E/p}{12763}) + 31.73\right], \tag{3.5}$$

$$\mu_p\left(m^2 Torr V^{-1} s^{-1}\right) p = 0.79\left[0.05492\exp(\frac{-E/p}{6858}) + 0.07509\exp(\frac{-E/p}{38175}) + 0.0308\right] + 0.21\left[0.06841\exp(\frac{-E/p}{59678}) + 0.09194\exp(\frac{-E/p}{12763}) + 0.0320\right], \tag{3.6}$$

$$\frac{\alpha}{p} = 0.21\left[\begin{cases} 4.71\times10^{-11}\left|E/p\right|^{3}, & \left|E/p\right| < 1.4\times10^{4}\,Vm^{-1}Torr^{-1} \\ 3.32\left(\left|E/p\right|-12500\right)^{0.5} & \left|E/p\right| > 1.4\times10^{4}\,Vm^{-1}Torr^{-1} \end{cases}\right] \tag{3.7}$$
$$+0.79\left[\begin{cases} 1.17\times10^{-10}\left|E/p\right|^{3}, & \left|E/p\right| < 1.1\times10^{4}\,Vm^{-1}Torr^{-1} \\ 0.0319\left|E/p\right|-211 & 1.1\times10^{4} < \left|E/p\right| < 2.1\times10^{4}\,Vm^{-1}Torr^{-1} \\ 6.32\left(\left|E/p\right|-16300\right)^{0.5} & \left|E/p\right| > 2.1\times10^{4}\,Vm^{-1}Torr^{-1} \end{cases}\right],$$

The charged particle diffusion coefficients in Eqs. (3.1)-(3.3) are expressed by the Einstein relation and the charged particles temperature in the diffusion terms are taken as constant , 1eV for the electrons and 350 K for the ions.

Eqs. (3.1)-(3.4) are coupled to an Poisson's equation for the electric field:

$$\nabla.(\varepsilon\nabla\phi) = -e(n_p - n_e - n_n) - \delta_s\sigma \ , \tag{3.8}$$

where ε is the permittivity. The permittivity of air is considered to be equal to that of vacuum ($\varepsilon_0 = 8.854\times10^{-12}\,Fm^{-1}$) and σ is the surface charge density in $kgs^{-3}A^{-1}$. this is evaluated at the dielectric surface, as indicated by the delta function δ_s, after time integrating the charged particle fluxes at the surface.

$$\sigma = \int_0^t -e\left(\vec{\Gamma}_p - \vec{\Gamma}_e - \vec{\Gamma}_n\right)\vec{n}dt = \int_0^t -\vec{j}.\vec{n}dt \ , \tag{3.9}$$

where $\vec{n}$ is the unit normal vector pointing into the computational domain. For the electric field at the outer boundaries, the following condition is held,

$$\vec{E}.\vec{n} = 0 \ , \tag{3.10}$$

and at the electrode, the value of electric potential is prescribed. The electric field inside the dielectric $\vec{E}_d$ was related to the electric field $\vec{E}$ at the surface through the relation

$$\varepsilon_0\vec{E}.\vec{n} - \varepsilon_d\varepsilon_0\vec{E}_d.\vec{n} = \sigma \ , \tag{3.11}$$

where σ is the surface charge density and $\vec{n}$ is the unit normal vector pointing into the computational domain. By implementing this condition, the effect of the surface charge density in the continuity equation is taken into account. In addition zero normal gradients are considered for the boundary conditions of the charged particles at outer boundaries.

The boundary conditions for charged particles number density at the walls are set out by preventing zero charged particle fluxes towards the wall, since the driving forces are directed out from it, and by enforcing ion-induced secondary emission at cathode or cathode-like walls.

$$\vec{\Gamma}_p \cdot \vec{n} = -\frac{1}{4}\sqrt{8\frac{k_B T_p}{\pi m_p}} + n_p\left[\min(\mu_p \vec{E}.\vec{n}, 0)\right] , \tag{3.12}$$

$$\vec{\Gamma}_e \cdot \vec{n} = -\frac{1}{4}\sqrt{8\frac{k_B T_e}{\pi m_e}} + n_e\left[\min(-\mu_e \vec{E}.\vec{n}, 0)\right] , \tag{3.13}$$

$$\vec{\Gamma}_n \cdot \vec{n} = -\frac{1}{4}\sqrt{8\frac{k_B T_n}{\pi m_n}} + n_n\left[\min(-\mu_n \vec{E}.\vec{n}, 0)\right] , \tag{3.14}$$

For certain cases, these boundary conditions lead to numerical instability. For anode or anode-like surfaces, the boundary condition that would satisfy the real situation for negative ions and electrons is one of zero gradient on the electron number density. The derived boundary condition on ions at anode is a Robin condition for the number density of ions. (However, since the diffusion is always negligible with respect to its drift part in the sheath, it's possible to employ a more robust and simpler condition [119] , namely $n_p = 0$).

On the other hand, for the cathode or cathode-like surfaces, the zero gradient boundary condition could satisfy the condition for the positive ion number density. Here, the boundary condition on electrons is a Robin condition (for simplification, it is possible to neglect the diffusion part). Electrons may be emitted from material surfaces via secondary electron emission. Therefore, the total electron flux near a surface is given by,

$$\vec{\Gamma}_e \cdot \vec{n} = -\gamma \vec{\Gamma}_p \cdot \vec{n} \ , \tag{3.15}$$

where γ is the secondary electron emission coefficient at the surface, which is 0.05 for the dielectric surface, and zero for electrode surface . The minus sign indicates that secondary electron fluxes, away from a surface, are proportional to the ion fluxes into that surface.

3.2.2 - Gas dynamics equations

For modeling the gas dynamics, a mass-averaged fluid dynamics formulation was employed to represent the motion of the gas as a whole. In this view, the compressible Navier-Stokes formulation is written as,

$$\frac{\partial \rho}{\partial t} + \nabla \cdot (\rho \vec{u}) = 0 \ , \tag{3.16}$$

$$\frac{\partial \rho \vec{u}}{\partial t} + \nabla \cdot (\rho \vec{u}\vec{u} + pI - \tau) = \vec{F}_{EHD} \ , \tag{3.17}$$

$$\frac{\partial \rho E}{\partial t} + \nabla \cdot ((\rho E + p)\vec{u}) = \nabla \cdot (\kappa \nabla T) + \nabla \cdot (\tau . \vec{u}) + \vec{F}_{EHD} . \vec{u} + p_{th} \ , \tag{3.18}$$

In the above equations, p is the static pressure, I is the unity tensor , τ is the viscous stress tensor, E is total specific energy and κ is the thermal conductivity of air. The interaction terms are $\vec{F}_{EHD}$, force due to discharge and p_{th} , the dissipated power due to the conduction

current, $\vec{J} = j - e(n_p - n_e - n_n)\cdot\vec{u}$. In the above equations the viscous stress tensor is as follows,

$$\tau = \mu\left[(\nabla u) + (\nabla u)^T - \frac{2}{3}\nabla\cdot\vec{u}I\right] , \tag{3.19}$$

where μ is the dynamic viscosity of air and is calculated from Sutherland formula.

The above system of equation is closed with the equation of state for a perfect gas, $p = \rho RT$. Coupling parameters due to plasma effects inside the gas dynamic equations are represented through the EHD force $\vec{F}_{EHD}$ and the heating power density p_{th} . The EHD force term is written as [110] ,

$$\vec{F}_{EHD} = e(n_e - n_p - n_n)\vec{E} - k_B T_p \nabla n_p - k_B T_e \nabla n_e - k_B T_n \nabla n_n , \tag{3.20}$$

In the work of Che et al [120], the heating power density p_{th} was considered to consist of ion-neutral collisions, the energy deposited by electron elastic collisions, rotational excitation and vibration excitation, and was written as,

$$p_{th} = (\xi_i \vec{J}_p - \xi_i \vec{J}_n - \xi_e \vec{J}_e)\cdot\vec{E} , \tag{3.21}$$

where ξ_e was the effective fraction of energy deposited by electron, considered to be constant and equal to 0.75 [6,120]. Similarly, the term ξ_i is an efficiency factor specified to indicate the amount of Joule heating energy that is converted into thermal energy. This term is typically set to 1 when at higher (atmospheric) pressures or when energy loss to the wall by direct ion impact can be neglected [121].

Here we consider a more accurate formulation for the p_{th} of electrons following Unfer and Boeuf [78]. In this view, the gas heating term is composed by two parts, one contribution of the ion-neutral molecule collisions $p_{th,ions}$ and the other thermal energy transfer from electrons to neutral particles $p_{th,e}$. Assuming that all the energy obtained by ions from electric field is totally transferred into gas heating ($\xi_i = 1$) , $p_{th,ions}$ is expressed as

$$p_{th,ions} = (\vec{J}_p - \vec{J}_n).\vec{E} , \tag{3.22}$$

High electron temperatures and thus highly energetic electrons can provide high excitation rates of different electronically excited state of atoms and molecules by electron impact.

The total energy absorbed by electrons from electric field is equal to $p_{elec} = \sigma_e E^2$, where σ_e is the electron conductivity. In presence of molecules in the plasma an extremely important process is the vibrational excitation of molecules by electron impact. Indeed, in a molecular gas, most of the electron energy can be transferred to the vibrational excitation [50]. For this reason, the vibrational excitation, relaxation, and reaction of vibrationally excited molecules

strongly influence the chemical kinetics of the plasma. Several relaxation processes are important. Vibrational-translational (VT) processes convert vibrational energy in kinetic energy of the whole particle and it is the loss mechanism of vibrational energies. Also the rotational levels of molecules can be excited by rotational excitation of molecules by electron impact processes. Thus, the total energy absorbed by electrons is transferred to neutral molecules and gas heating through electronic excitation, vibrational excitation and elastic and rotational collisions [122,123]. Moreover, it is assumed that the energy absorbed by electrons in elastic and rotational excitation, and 30% of the energy in electronic excitation are released instantaneously into gas heating. But, the vibrational excitation of electrons into gas heating is released at a different time scale, with a time constant of τ_{VT}. Thus the contribution of electrons in gas heating can be expressed as;

$$p_{th,e} = p_{el-R} + p_{VT} + p_E \,, \tag{3.23}$$

with

$$\begin{aligned} p_{el-R} &= \eta_{el-R}\, p_{elec} \\ p_E &= \xi_e \eta_E\, p_{elec} \end{aligned} \tag{3.24}$$

where η_E is the fractional power deposited in electronic excitation and $\xi_e = 30\%$. In Eq. (3.23), considering a relaxation of time of τ_{VT} for vibrational excitation, p_{VT} is obtained by solving a phenomenological equation of the type;

$$\frac{\partial p_{VT}}{\partial t} + \frac{1}{\tau_{VT}} p_{VT} = \frac{1}{\tau_{VT}} \eta_V\, p_{elec} \,, \tag{3.25}$$

where η_V is the fractional electron power deposited in vibrational excitation of air molecules.

The three fractional power deposited by electron ($\eta_E, \eta_V, \eta_{el-R}$) is obtained by fitting curves to data calculated as a function of E/n using BOLSIG+ software [124] as (Fig. (3.2)):

$$\begin{aligned} \eta_E = {} & 1.348001\times10^{-1} \exp(-3.5410\left|\frac{E}{N}\right|) - 9.8365\times10^{-1} \exp(-2.02042\times10^{-1}\left|\frac{E}{N}\right|) \\ & + 4.14522\times10^{-1} \exp(-2.63147\times10^{-3}\left|\frac{E}{N}\right|) + 4.507497\times10^{-1} \end{aligned} \,, \tag{3.26}$$

$$\begin{aligned} \eta_V = {} & -1.6041\times10^{-1} \exp(-6.10797\times10^{+3}\left|\frac{E}{N}\right|) - 1.46957\times10^{-1} \exp(-9.4288\left|\frac{E}{N}\right|) \\ & + 1.02191 \exp(-2.5157\times10^{-1}\left|\frac{E}{N}\right|) + 3.91435\times10^{-2} \end{aligned} \,, \tag{3.27}$$

$$\eta_{el-R} = 2.07278\times10^{-2}\exp(-2.6180\left|\frac{E}{N}\right|) + 4.04597\times10^{-2}\exp(-1.7446\times10^{2}\left|\frac{E}{N}\right|) + 1.68412\times10^{-1}\exp(-7.13103\times10^{+3}\left|\frac{E}{N}\right|) + 2.98161\times10^{-3} \quad (3.28)$$

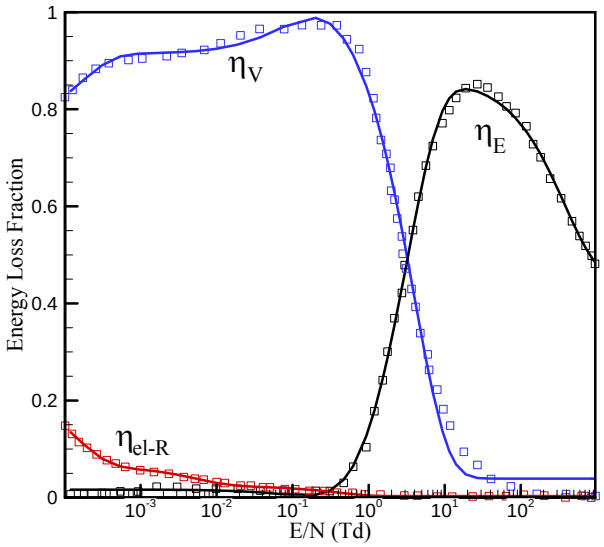

Fig. 3.2: Comparison fractional power deposited by electrons from the current correlations (Eqs. (3.26)-(3.28)) and the data obtained by BOLSIG+ software.

3.2.3 - Surface and volume heating model

Another idea to simplify the numerical complexity and reduce the computational time is to formulate the effect of plasma as volume and surface sources of energy deposition, with a specified frequency inside the flow domain. To this aim, an approach similar to the phenomenological model described in [125-128] is chosen. To reproduce the overall wave structure, wave speed and strength, and power input to the NS-DBD actuators, a surface and volume heating profile is considered in a way to obtain similar results as in the full discharge modeling. The speed and strength of the initial wave are related to the maximum temperature in the heated region, which is obtained by introducing a volume heating component and the shape of the wave correlates with the temperature distribution along the surface. Fig. (3.3) demonstrates the development of the compression wave due to volume and surface heating. Using a simple analysis, the volume heating can be estimated from,

$$Q_{th} = \rho C_v \frac{\Delta T}{t_{E,relax}} \quad , \quad (3.29)$$

Considering the discharge volume of 25e-8 m^3 and temperature ratio increase of 1.4 for the ambient temperature of 300 K, and a relaxation time of $1\mu s$, we can calculate the power

needed per span wise electrode length to actuate the flow as $2.6\times10^4\ W/m$, which is equivalent to 0.026 J/m by integrating the above equation over volume.

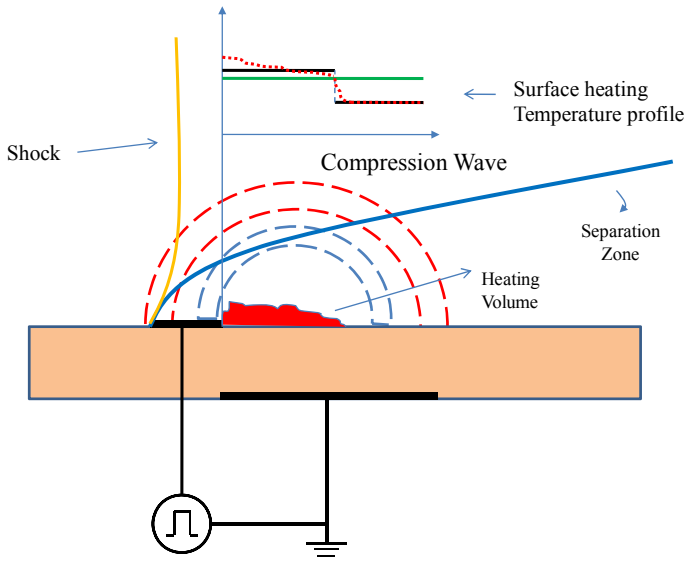

Fig. 3.3: Schematic of the plasma surface and the volume energy deposition model.

Moreover, the process of formation of the plasma micro-shock wave above the surface is separated into two parts. In the first part, the pulse of energy input to the plasma is started at t=0 and switched off at $t_{E,relax}$ (which we consider to be equal to $1\mu s$). During this period the pressure and temperature rise above the surface and the wave front moves just a short distance away from the surface. In the second part, when the pulse of energy input is switched off, an expansion wave is generated and propagates into the domain.

3.2.4 - Numerical procedure

The strong coupling between the charge density equations and the electric potential results in a severe time step restriction (the maximum allowable time step is the dielectric relaxation time). In order to overcome this constraint, the Poisson equation is solved in a semi-implicit manner for the electric potential [78],

$$\nabla.(\varepsilon\nabla\phi) = -e(n_p{}^t + \Delta t\frac{\partial n_p}{\partial t} - n_e{}^t - \Delta t\frac{\partial n_e}{\partial t}) \tag{3.30}$$

In this way the Poisson equation could be rewritten as,

$$\begin{aligned}&\nabla.(\left[\varepsilon+\Delta t\left(\mu_p n_p+\mu_e n_e\right)\right]\nabla\phi)=\\&-e(n_p{}^t+\Delta t\nabla.(\nabla n_p{}^t)-\nabla.\left(n_p\vec{u}\right)-n_e{}^t-\Delta t\nabla.(\nabla n_e{}^t)+-\nabla.\left(n_e\vec{u}\right))\end{aligned} \tag{3.31}$$

Furthermore, a two-stage plasma computation approach [129,130] is implemented. In this approach, during the voltage pulse, the numerical time-step is set to 10^{-3} *ns*, and the full physical model is solved. When the input voltage decays the electric field effects become negligible and the space charge density rapidly goes down. Therefore, in this stage, the electric field and space charge are set to zero and the time-step is increased to the timescale of the dominant physical process (gas dynamics).

The numerical task has been done through Object Oriented Programming in the environment of OpenFoam by developing a new solver (UBIPlasmaFoam). The solution of the gas dynamic equations was accomplished based on a density based explicit algorithm. The numerical fluxes were evaluated using the flux difference splitting Roe scheme [131] and to extend the accuracy in space, a second order MUSCL reconstruction scheme is used. Integration in time is performed by multistage pseudo time integration based on four-stage Runge–Kutta method. Moreover, a two parameter k−ω SST turbulence model with y+ less than one is used for the turbulent transfer description [132].The initial distribution of parameters corresponding to the steady flow around the airfoil without energy addition was obtained with an absolute error of 10^{-6}.The computational grid in the physical region is geometrically adapted towards the wall being refined in the vicinity of the electrode and dielectric surfaces.

3.3 - Test case configurations

3.3.1 - Validation cases

For the validation of the numerical modeling of the plasma discharges, two flat plate DBD actuators are considered (similar to [58]).The electrodes were considered to be infinitely thin and arranged in asymmetric configuration without a gap between the electrode edges. Moreover, in the initial time instant, the gas is considered to be quasi-neutral, the initial charged particle densities (electrons and positive ions) are considered to be uniform and equal to $10^{13} m^{-3}$ in the first case and $10^{10} m^{-3}$ in the second case, in the whole simulation domain. In the first configuration, the length of the exposed electrode and the covered electrode are $100\mu m$ and $400\mu m$, respectively, and a constant voltage of 1200V is applied to the exposed electrode. The dielectric material is Kapton, having electric permittivity of $10\varepsilon_0$ and thickness of $50\mu m$.

The second test case is considered in a way to be similar to the experiment of Straikovski et al [116] and the numerical study of Unfer and Boeuf [110]. The computational domain consists of a 2D rectangular geometry, of dimensions $0.0768m \times 0.0768m$. The length of the exposed electrode is considered to be 5.1mm and the lower electrode is 4.8mm long. The upper electrode is placed at 0.03m from the left wall. A voltage pulse is applied to the upper electrode. The total pulse duration is 35ns and the rise and falling time of the nanosecond pulse are 7ns and 15ns, respectively. The lower electrode is covered by a dielectric layer

$300\mu m$ thick and, permittivity equal to $5\varepsilon_0$.The configuration of these test cases is shown in Fig. (3.4).

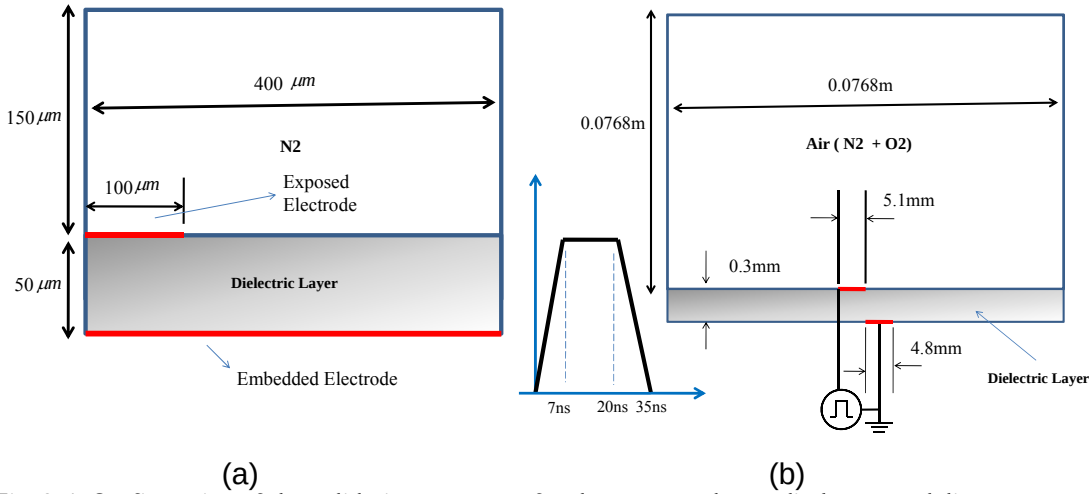

Fig. 3.4: Configuration of the validation test cases for the present plasma discharge modeling.

3.3.2 - Transonic airfoil gas dynamic with plasma dynamic

The transonic range of flying vehicles is the most difficult to simulate in aerodynamics; on the other hand, the feasibility of controlling transonic flows would greatly improve the aerodynamical performance of flying vehicles (and thereby increase the flight range , reduce the carrier cost, etc.) and allow flight control at maneuvering. In this aspect, Peschke et. al [134] had conducted an experimental study on the effect of DBD plasma actuators on transonic flow over a NACA 3506 airfoil. They have concluded that the plasma used did not modify the transonic flow in a significant way. The fact that shock structure does not exhibit significant differences without and with plasma can have several physical causes. The boundary layer is already turbulent in the case without plasma. It is thus not possible in these conditions to generate a transition from a laminar boundary layer to a turbulent one with plasma upstream or below the shock foot. However, the results of [135] show that in some cases, when the aerodynamics situation is sensitive to weak influence, the surface plasma of barrier discharge can effect on the transonic flow. Moreover, Roupassov et. al [136] showed that the discharge effect is negligible till a specified angle of attack and for the angles higher than the stall angle the discharge switches the flow to un-separated flow.

Therefore, for the study of the effect of plasma actuator on gas dynamic, the plasma actuator is mounted on a NACA 3506 profile with a chord length of c=77.57mm, similar to the experiment by Peschke et. al [134] . The electrodes are considered to be infinitely thin. The exposed electrode is located at x/c=0.32 from the leading edge and it is 1mm wide, and the covered electrode is 10mm wide. The electrodes are separated by a 0.1mm thick layer of dielectric material. The permittivity of the dielectric material is $5\varepsilon_0$. A single pulse with a

peak voltage of Vp=5kV and pulse shape similar to that for the second test case, is considered as configuration of the power supply. Two different angles of attack are considered. One corresponds to an angle of attack of four degrees and other to a post stall angle of attack of 20 degrees. The configuration of the electrodes and the computational grid for this case are presented in Fig. (3.5).

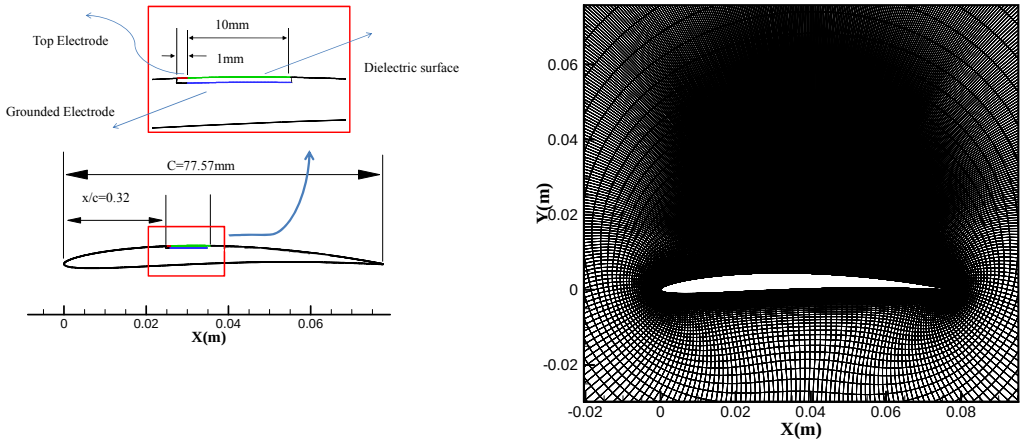

a) b)

Fig. 3.5: a) Electrodes position and b) computational grid around the surface of the NACA 3506 airfoil.

3.4 - Results and discussions

For the first test case the effect of gas heating is not considered and so the only mechanism by which the plasma modifies the flow is through momentum transfer to the fluid. Figs. (3.6)-(3.7) shows a simulation results of the time evolution of the plasma discharge for the case of a constant voltage pulse of 1.2kV. The plasma discharge consists of a quasi neutral plasma column and a non-neutral ion sheath that propagates along the dielectric surface, away from the exposed electrode. It is obvious from these figures that the discharge is of the streamer type. Our results in Fig. (3.6) show similar physical behavior in comparison to the results by Nishida and Abe [68] and Bouef and Pitchford [58].

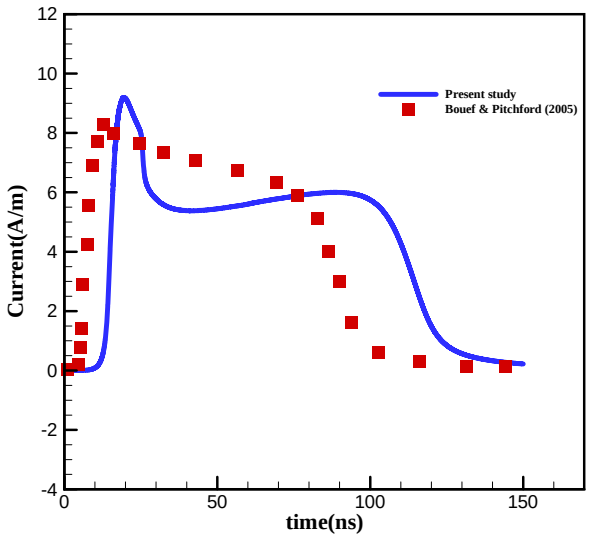

Fig. 3.6: Validation of the first test case with the numerical results of Boeuf and Pitchford (2005) [58].

The distribution of ion charge density is shown in Fig. (3.7). It is apparent that, as the charge density of ions and electrons near the dielectric surface is increased, the electric potential on the surface of the dielectric material raises and thus increasing the extension of the virtual electrode. Fig. (3.7) also shows that the region with higher ion density is located at the point with the largest electric field, and thus a higher rate of ionization exists there.

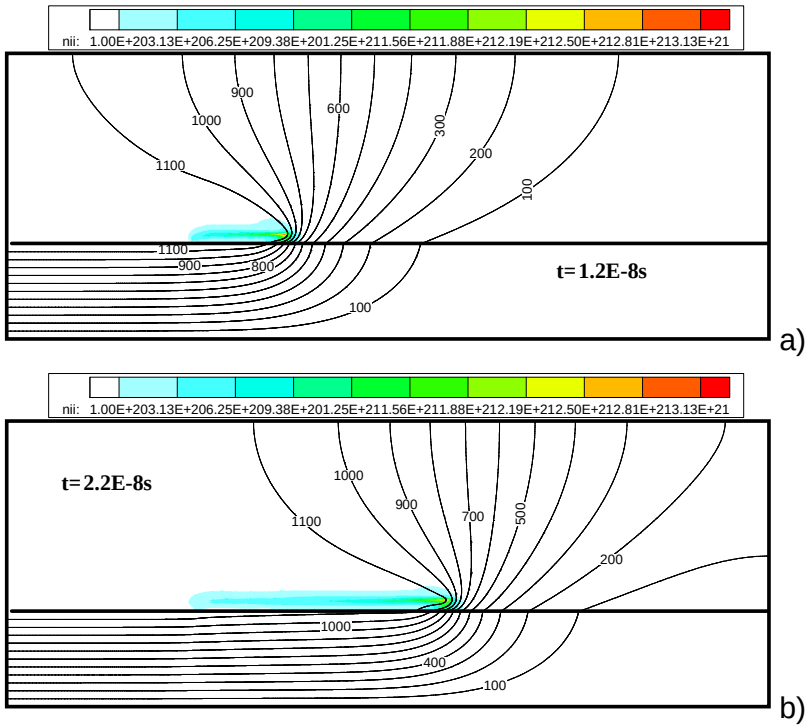

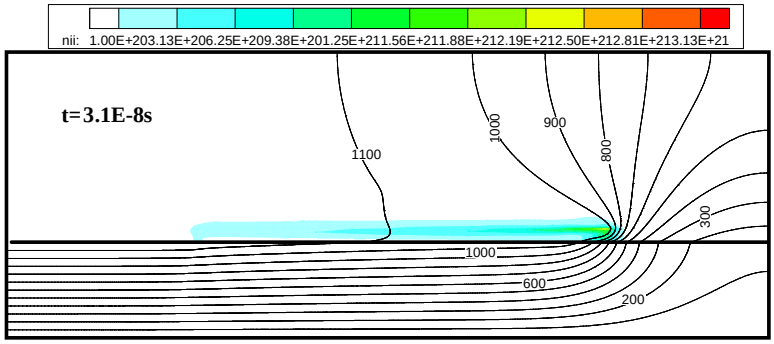

c)

Fig. 3.7: Propagation of the ion sheath along the dielectric surface at: a) *t=12ns*; **b)** *t=22ns;* **c)** *t=31ns* **(values of ion charge density in m^{-3}).**

For the second test case the effect of gas heating was taken into account. Fig. (3.8) shows general good agreement of the predicted current, from the present numerical simulation, in comparison with the numerical work of Unfer and Beouf [110]. Moreover Fig. (3.9) shows the time evolution of the electron and potential density at four different times. Streamer discharge propagation along the surface of the dielectric was observed during the voltage rise when the exposed electrode plays the role of anode.

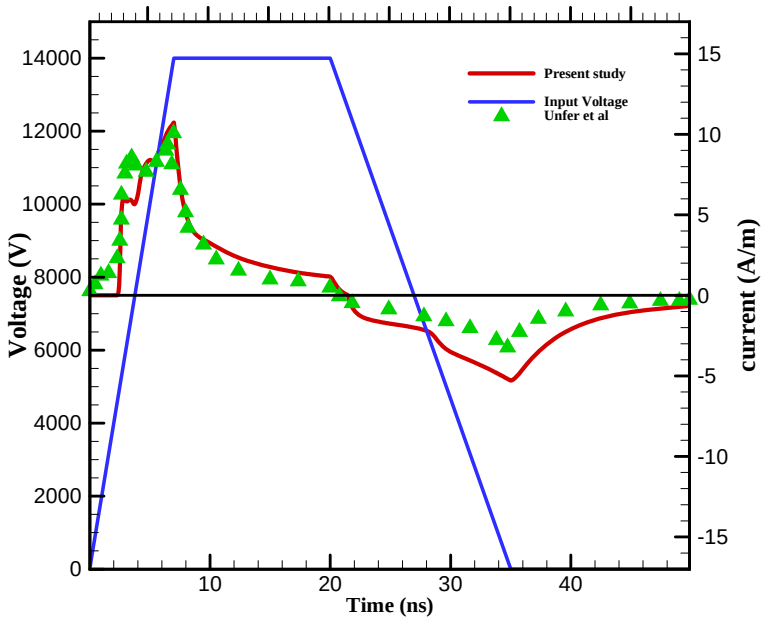

Fig. 3.8: Validation of the second test case for the pulsed input voltage.

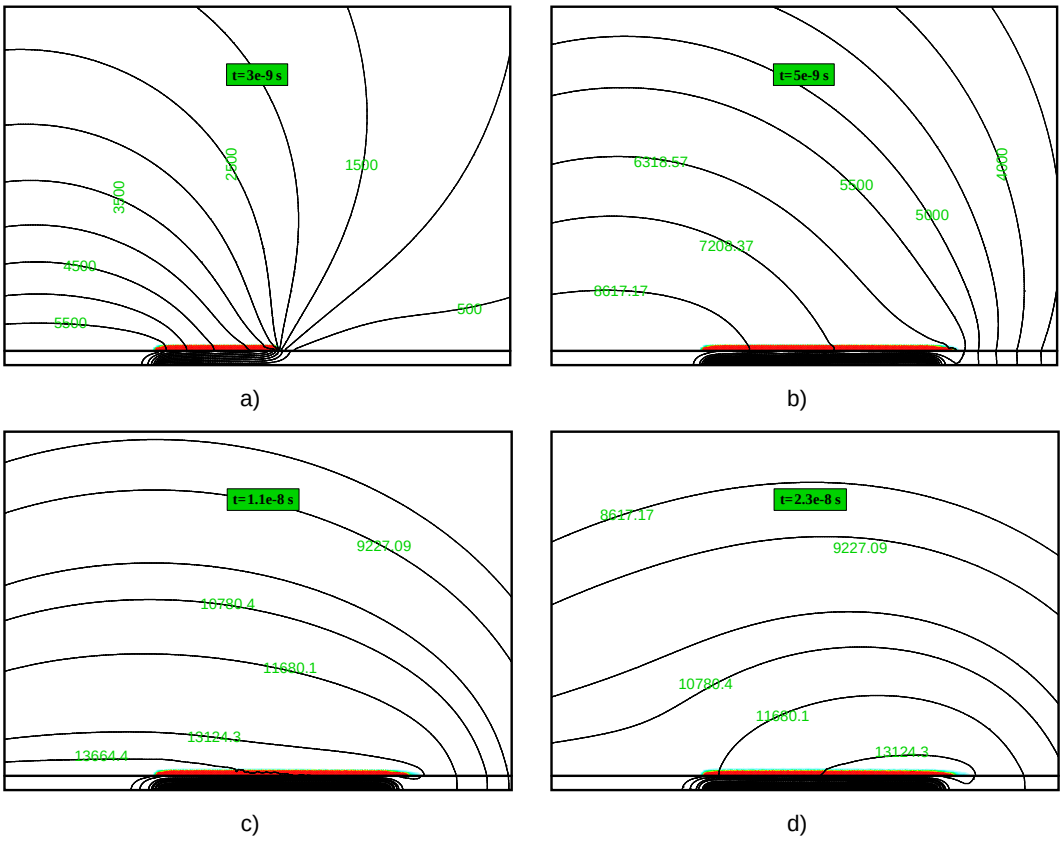

Fig. 3.9: Streamer formation during the voltage pulse at: a) *t=3ns*;**b)** *t=5ns*;**c)** *t=11ns*;**d)** *t=23ns* **(values of electric potential in V).**

Fig. (3.10) illustrates the spatial distribution of the gas pressure induced by the discharge at two different time instants. These results highlight that fast gas heating takes place in the boundary layer, close to the edge of the exposed electrode, thus producing a micro shock wave.

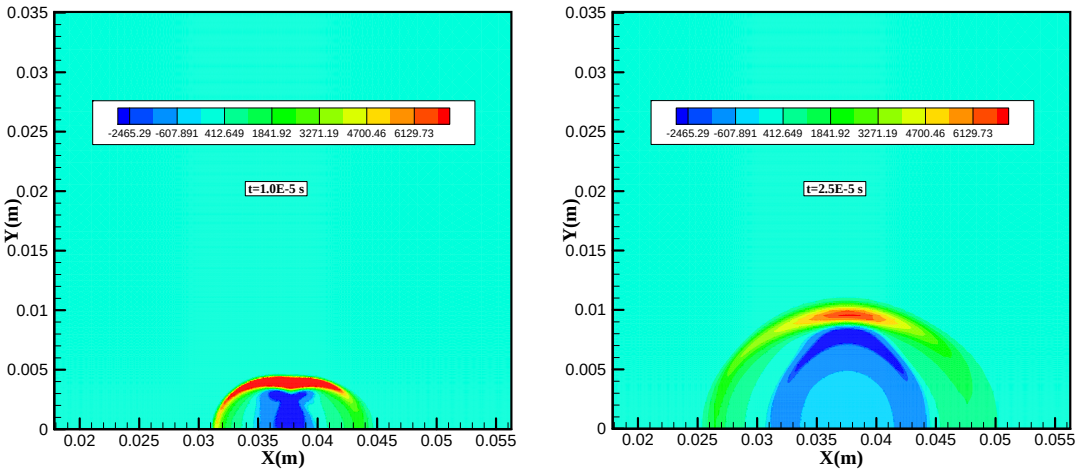

(a) (b)

Fig. 3.10: Micro-shock formation above the dielectric surface (distribution of the induced pressure difference by plasma) at: a) $t = 10\mu s$ **; b)** $t = 25\mu s$ **(** ΔP **contours in (Pa)).**

Fig. (3.11) shows the formation of the micro-shock wave above the dielectric surface mounted on the surface of the NACA 3506 airfoil. The formation of the plasma on the surface of the electrode leads to a very fast gas heating of the fluid near the surface, which in this case results in the formation of a compression wave traveling outward from the surface.

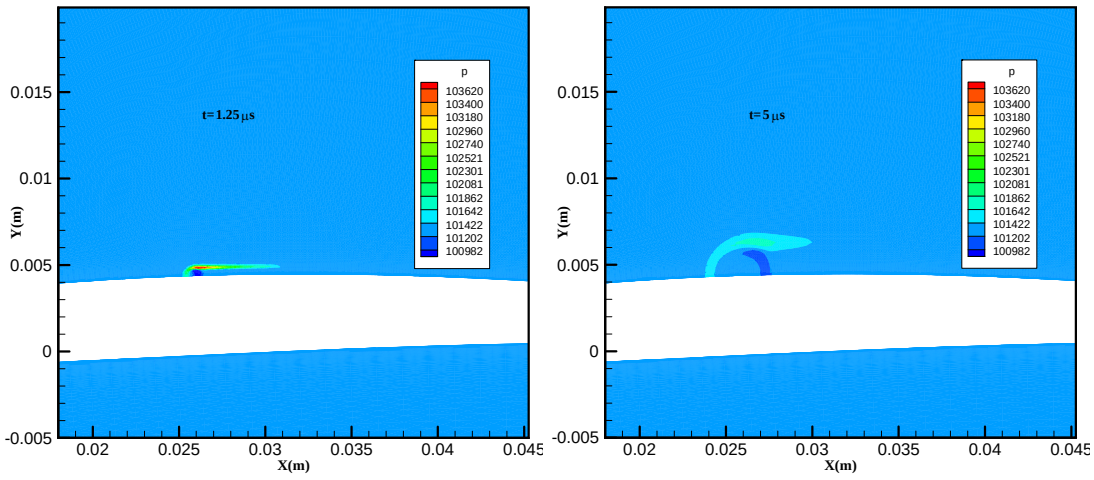

a) b)

Fig. 3.11: Micro-shock wave above the dielectric surface mounted on the surface of NACA 3506 Airfoil in quiescent flow at: a) $t = 1.25\mu s$ **; b)** $t = 5\mu s$ **(pressure contours (Pa)).**

In general, the solution of the coupled plasma dynamics and gas dynamics equations together, is computationally very expensive. To increase the efficiency of the numerical computations, two different approaches may be adopted, as referred to before. The first is the two stage plasma calculation technique, and the second is the plasma energy deposition model. In Fig. (3.12), the computed temperature profile at the surface of dielectric material, for the NACA

3506 airfoil, is shown together with the imposed profile. The surface heating profile is a step profile that has a jump at a critical point x_c. Two important parameters of this profile are the temperature ratio and the critical step point.

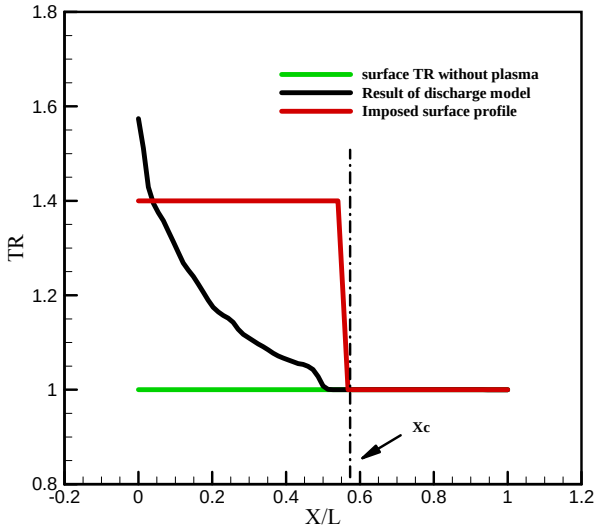

Fig. 3.12: Dielectric surface temperature ratio (imposed model -red line; at initial case-green line; discharge model- black line) for the NACA 3506 airfoil at $\alpha = 4^{\circ}$.

Fig. (3.13) gives the time evolution of the drag coefficient over the surface of the airfoil until $70\mu s$ as predicted by the two approaches just mentioned. It is clear from this figure that the difference of the computed results by the two different modeling approaches is less than 1e-3. The jumps in the plots represent the instants of time at which the plasma pulse is active.

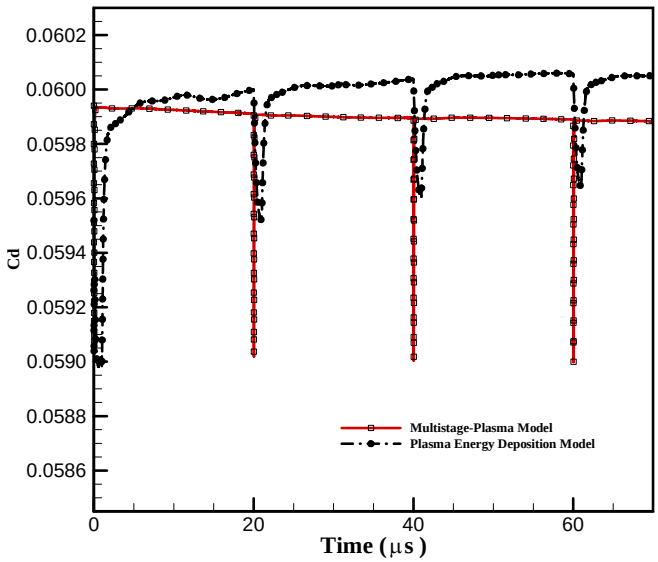

Fig. 3.13: Comparison of the drag coefficient obtained on the surface of the NACA 3506 airfoil at $\alpha = 4^{\circ}$ by different models.

Additionally, Fig. (3.14) shows the time variation of pressure at three different locations near the surface of the airfoil at angle of attack of $\alpha = 20^{\circ}$. The peak values show the waves that reach the probe locations. There is a small difference in the values of the wave strength seen by the pressure sign arriving at the point, for each model. This is completely natural as the energy input and distribution in the plasma energy deposition model is not the same as in the plasma discharge model. However, the difference remains within an acceptable range.

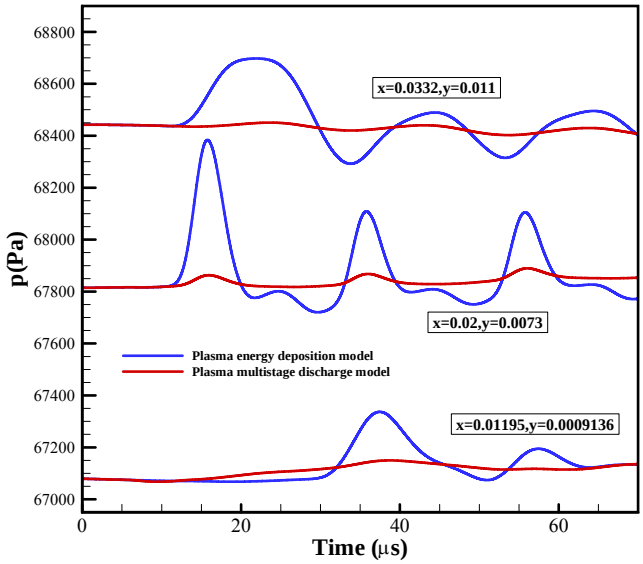

Fig. 3.14: Time variation of pressure at three probe locations.

Fig. (3.15) compares the shape, position and strength of the plasma micro shock wave obtained by the energy deposition model and the multi-stage plasma calculation approach. By comparing the contour plots, we see that the plasma energy deposition model is able of capturing the plasma micro shock wave structure with good accuracy, without the need of solving the plasma dynamics equation, for the whole duration of the calculation. In this case, there is an imposed external transonic flow (M=0.75) in the vicinity of the NACA 3506 airfoil, at an angle of attack of 20 degree. A micro shock wave is formed and propagates into the flow at the speed of sound and, interacting with the flow over the surface. High local density gradients whirl the heated air downstream. The combined effects of heating convection and repetitive pulse discharge lead a modification of the flow features .The plasma micro shock wave in the vicinity of the NACA 3506 with the angle of attack of 20 degree is shown.

$t = 1\mu s$

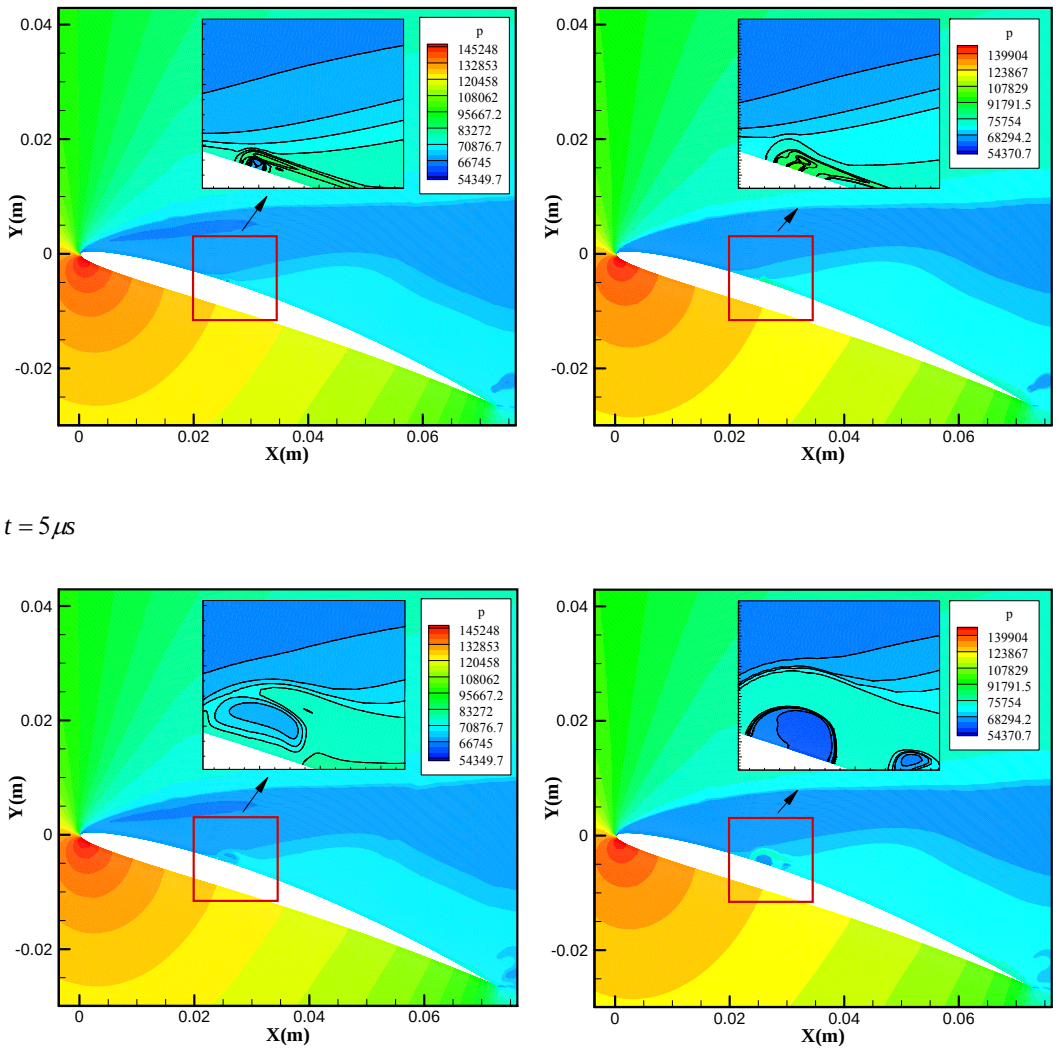

a) b)

Fig. 3.15: Comparison the wave location and shape obtained by: a) plasma multistage solution; b) plasma energy deposition model.

Moreover Fig. (3.16) compares the current obtained results with the experimental results of Pescheke et al. [134]. In this figure, contour plots of pressure and density variation $\Delta\rho = \rho^{t} - \rho^{t_0}$ are presented, for the purpose of comparison with the experimental results of Pescheke et al. The figure shows qualitively the level of agreement of the current plasma calculation.

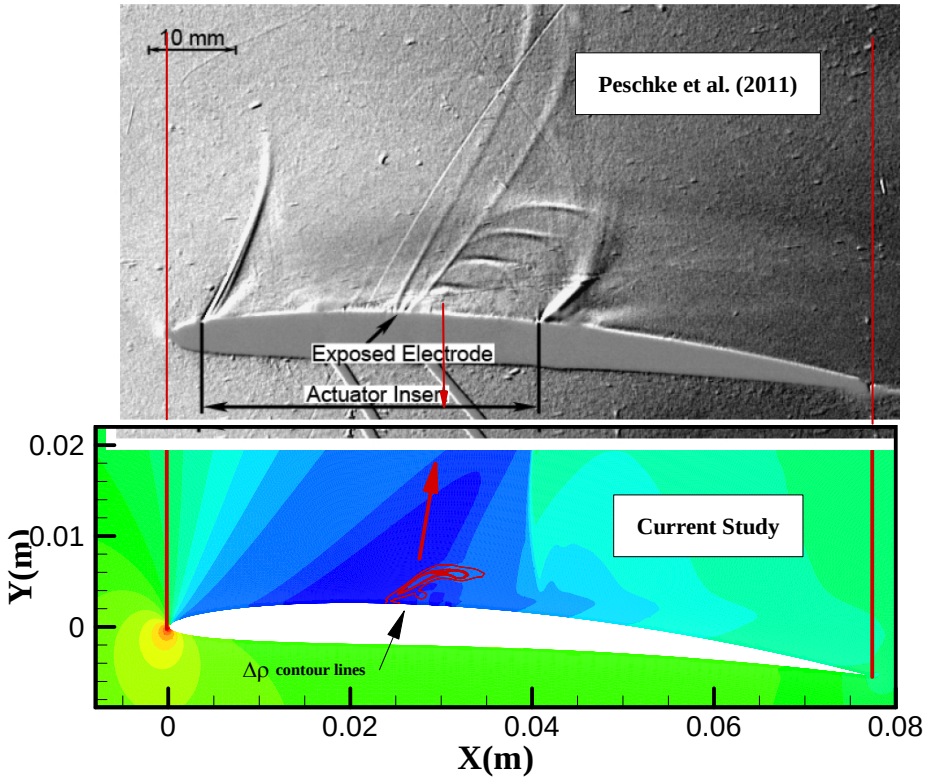

Fig. 3.16: Comparison of the present numerical simulation with the experimental results of Pescheke et al. [134] **at** $t = 10\mu s$ **.**

Table (3.1), gives the CPU time required by each model for the completion of 1ms of simulation time for the case of the NACA 3506 airfoil. Clearly, the plasma energy deposition model is a lot less computationally expensive in comparison to other models. Although this model does not have the complexity of the others but is still able to capture the main features of the effects of NS DBD plasma actuators correctly. Thus it presents itself as a good candidate to be used for modeling large scale problems.

Table 3.1: Comparison of the computational time for various models.

	Plasma discharge model	Plasma multistage model	Plasma energy deposition model
CPU time for 1ms	884 h	132 h	1.74 h

3.5 - Conclusions

A solver for both plasma and gas dynamics, based on the transport equations of charged particles and the Navier-Stokes equations, is developed in the OpenFoam environment for

modeling nanosecond plasma actuators. Based on the results of plasma discharge model, an energy deposition model was also developed for the simulation of the effects of DBD actuators. The accuracy of the solver was tested through comparison with the available results in the literature. It was shown that fast energy transfer, from plasma to fluid, leads to the formation of micro-shock waves responsible for modifying the main flow features. Also, a nano-second plasma actuator for transonic flow over an airfoil was tested numerically. Although this model does not have the complexity of others, it was shown that it is able to capture the main features of the effect of NS DBD plasma actuators correctly, with less computational time. Thus it could be viable for modeling large scale problems when using standard plasma discharge models is not viable.

4 - Modified Split-Potential Model for Modeling the Effect of DBD Plasma Actuators in High Altitude Flow Control

Abstract

Surface DBD plasma actuators are novel means of actively controlling flow. They have shown promising ability in reducing drag, postponing transition from laminar to turbulent flow, suppression of separation, noise reduction and enhancement of mixing in different applications. The CFD simulation of the effect of plasma actuator in such kind of applications could provide more information, and insight, for optimization and design of close looped flow control systems. However, the fluid models for simulating the formation of the plasma and its effect are computationally expensive such that, although they provide more detailed information about the physics related to the formation plasma, they are still not viable to be used in large scale CFD simulations. In this paper, we present the modified version of a simpler model that predicts the thrust generated by the plasma actuator with acceptable accuracy and can be easily incorporated in CFD calculations. This model is also free of empirical fitting parameters, being based on pure flow physics scaling[3].

Keywords: DBD System Capacitance; Semi-empirical; Thrust estimation; Body force; Barrier Discharge; flow control;

4.1 - Introduction

Dielectric Barrier Discharge (DBD) plasma actuators gained increased interest during the past decade for different applications[115,137–139]. It has been proven that they have a promising potential for controlling flow in diverse applications. Many experimental and numerical works have been done for the purpose of better understanding the mechanisms by which these kind of actuators influence the flow and also for the optimization of their design and improvement of their performance [68,140,141]. DBD plasma actuators mostly influence the flow through two different mechanisms, depending on the type of the excitation voltage shape employed. If the DBD plasma actuator is excited through a nano-second voltage pulse, the characteristics of the flow around the DBD actuator is altered through fast energy deposition and creation of micro shock-waves. In contrast, if some kind of radio frequency excited voltage is used, the flow will be accelerated around the actuator plate due to the formation of ionic-wind.

[3] This chapter is based on the following published paper: "M. Abdollahzadeh, J.C. Pascoa, P.J. Oliveira (2014), Modified Split-Potential Model for Modeling the Effect of DBD Plasma Actuators in High Altitude Flow Control, Current Applied Physics, Volume 14:8, Pages 1160-1170, ISSN 1567-1739, doi:0.1016/j.cap.2014.05.016."

The plasma fluid model [65,70,117,142] and the particle in cell model [143] are the most sophisticated and common models for simulating plasma actuators. However, due to large difference between the spatial and temporal scales of the flow and the plasma, the computational time of these techniques is excessively high. Even with multi-processor modeling approaches and some kind of unsteady acceleration techniques[144], such as adaptive local time stepping. The solution of large scale problems in realistic geometries is not viable with those models. A more simplified approach needs to be devised in order to have both acceptable accuracy and fast simulation times.

In this aspect, a semi-numerical modeling of the effect of plasma actuator could provide a rapid tool to ascertain the effect of plasma actuators. Different such numerical models have been proposed, including semi-experimental [145,146], basic phenomenological models[88,89,114,147–151] and PIV measurement-based models [152–155]. Obviously, the accuracy of the simulation results reduces when the simplicity of models is increased. However, high fidelity fluid models are too much computationally expensive to be used for simulation of large scale problems. PIV data based models also need availability of complex experimental results for the tested plasma actuator. Moreover, since the major influence of the DBD actuator occurs at large scales, such as energy deposition and ionic field, the overall effect could be captured by simpler phenomenological models.

Different simplified models can be found in the literature. Shyy et al [83]considered a body force formulation. The electric field region was confined to a triangular shaped region over the actuator plate, whose size was estimated by the length of the actuator and an assumed value for the height of the plasma region. The maximum body force in that model would occur at the edge of the exposed electrode and this body force was directed parallel to the shape of the body force region. The height of the plasma region and a constant charge density were considered to be the fitting parameters of the model. Suzen et al [85] developed a model Assuming a Gauss law, by additionally considering the electric potential to be produced by the accumulated charge density over the dielectric surface to obtain the charge density distribution. The distribution of the charge density was assumed to be Gaussian in accordance to the observed experimental distribution. Scales for the space charge density (maximum charge density), shape factors of the Gaussian distribution, and Debye length were selected to match experimental results. Both these models were not able to accurately capture the applied voltage-thrust dependency which was observed experimentally by [4] to be $U_{\max} \alpha V_{app}^{7/2}$.

An involved unsteady phenomenological model was presented by Orlov et al [150], who considered the DBD actuator system as an electric circuit with several electric components, including capacitances and resistances. In this way, they were able to calculate the so called memory voltage over the surface of the dielectric layer. The model successfully predicted the ratio of the voltage-thrust dependency. However, the value of the body force was too much over estimated in comparison to experimental results. Mertz [89] modified the model presented by Orlov et al to increase the accuracy of the direction of the predicted induced

flow. These models required some parameters, such as plasma resistivity and plasma height which were fitted to match experimental results. Recently, Lemire [156]developed a hybrid model, by estimating the charge density distribution over the embedded electrode as in the model of Suzen et al, and by considering the virtual electrode concept from the circuit model of Orlov et al [150].

Although the above mentioned models have gained success in modeling some experimental cases, as shown by Palmeiro [157], their predictive capability varies significantly depending on particular experimental situations. Moreover, most of them involve fitting parameters that need to be predefined by observing experimental results. These aspects restrict their practicality as a tool for the purpose of designing and testing flow control applications for which experimental results are not available. In the present paper, we wish to propose a modification to the model presented in [85]. This modification will serve to reduce the dependency of the results to fitting parameters, to capture correctly the voltage-thrust dependency, and to increase the range of validity of the model for different experimental situations.

4.2 - Modified split-potential model

In this section we will present the modification to the split-potential model. The model is modified through scaling the components of the body force (section 4.2.1) and introducing these new scales in the split-potential model to simulate body force distribution generated by the plasma.

4.2.1 - Scaling of generated thrust and body force

The thrust produced by the DBD plasma actuator is proportional to the power consumption of the DBD actuator system. For estimating the scale of power consumption the dielectric barrier discharge actuator is regarded as an AC circuit having a capacitor. Two cylindrical capacitors are considered, similarly to the work of Yoon et al [146]. C_g includes the upper electrode and the generated plasma over the dielectric surface, while C_d is the embedded electrode and the dielectric barrier. These capacitances are estimated as:

$$C_g \propto f\left(t_e, t_d, \varepsilon_0, l_p\right) = 2\pi\varepsilon_0 \frac{l_p}{\ln\left(\frac{0.5t_e + \lambda_d}{0.5t_e}\right)}; \tag{4.1}$$

$$C_d \propto f\left(t_e, t_d, \varepsilon_d, l_e\right) = 2\pi\varepsilon_d \frac{l_e}{\ln\left(\frac{0.5t_e + 2t_d}{0.5t_e}\right)} \tag{4.2}$$

The difference in the definition of the capacitance with that of [146] is the inclusion of the length of the embedded electrode l_e ,which is known, and the plasma region length l_p ,

which is unknown. Here, for simplicity the span wise length of the electrodes is assumed to be finite and equal to unity. And the considered cylindrical capacitors for each electrode are aligned in the stream-wise direction. The schematic of the typical DBD actuator and the corresponding AC circuit is presented in Fig (4.1), where the various lengths appearing in Eqs (4.1) and (4.2) are depicted. C_g and C_d capacitors are connected in a serial way to each other. Thus, the equivalent capacitance of the DBD actuator can be readily calculated as:

$$C_{eq} = \frac{C_g C_d}{C_g + C_d} \tag{3}$$

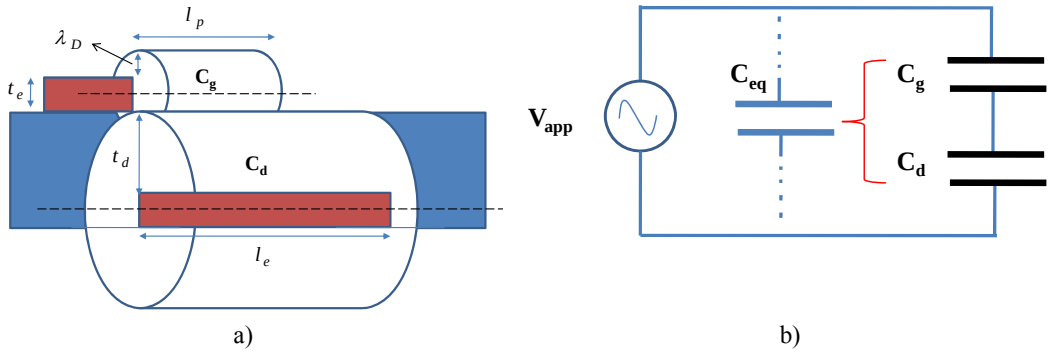

Fig. 4.1: a) Schematic of the considered DBD capacitor system b) Equivalent circuit for the DBD plasma actuator system.

The Debye length ($\lambda_D(m)$) is estimated through the relation presented by Bouchmal [158], as

$$\lambda_D = 0.2\left(0.3\times10^{-3}V_{app}(kV) - 7.42\times10^{-4}\right) \tag{4.4}$$

in which V_{app} is the applied voltage in kilo Volts.

The property that governs if ionization occurs is the electric field (threshold value at which the ionization occurs). To define this threshold value, the critical voltage at which the air is observed to first ionize (the critical voltage) is considered to be equal to the breakdown voltage V_{bd}, of the DBD. Yoon et al [146] correlated the break down voltage taken as the initial operation voltage in the work of Thomas et. al [159], as;

$$V_{bd}(kV) = 4.8289 + \left(8.063145\times10^{2}t_d\right) \tag{4.5}$$

where $t_d(m)$ is the thickness of the dielectric. However it is well known that the break down voltage is dependent on the operating pressure p, the secondary emission coefficient γ and the dielectric thickness. An alternative relation, for calculating the break down voltage is adopted from the work of [160] as,

$$V_{bd}(V) = \pi B\sqrt{\frac{p(Torr)t_d(cm)\ln(1+\gamma^{-1})}{2A}}. \tag{4.6}$$

where $A = 15\ cm^{-1}Torr^{-1}$, $B = 365\ Vcm^{-1}Torr$ for air as working fluid. The effect of the plasma actuator arises through the electrostatic pressure which can be interpreted as the total energy consumption of the plasma actuator. The DBD plasma actuator was considered as a circuit with equivalent capacitance C_{eq}, thus the energy consumption of the plasma actuator over the period τ is related to the energy consumption (W) of the equivalent capacitance, calculated as,

$$W = \int_0^{\tau} VI\ dt = C_{eq} \int_0^{\tau} V \frac{dV}{dt} dt. \tag{4.7}$$

Plasma only discharges when the electric field strength (applied voltage (V_{app})) is larger than the critical value of electric field for the ionization to occur E_{cr} (the break down voltage (V_{bd})), and therefore, the consumed power (P) of the capacitance is estimated by taking the integration only in the effective plasma period (Δt) as,

$$W = \frac{1}{2} C_{eq} \left(V_{app} - V_{bd}\right)^2; \tag{4.8}$$

$$\Delta t = \left(\frac{1}{2\pi f} \left[\frac{\pi}{2} - \sin^{-1}\left(\frac{V_{bd}}{V_{app}} \right) \right] \right) \approx \frac{1}{4f}; \tag{4.9}$$

$$P = \frac{W}{\Delta t} = 2\, f C_{eq} \left(V_{app} - V_{bd}\right)^2. \tag{4.10}$$

where f is the frequency of the applied voltage. In the above equations, it was assumed that C_{eq} is the average equivalent capacitance over the effective plasma period. Moreover, In Eq. (4.9), the effect of voltage shape was ignored for the approximation of Δt. In fact, Eq. (4.10) provides an estimation of the area of the characteristic Lissajous figure of the DBD actuator. As we have already mentioned, the thrust generated by the DBD actuator is proportional to its power consumption, and thus

$$T \cong 2\alpha f C_{eq} \left(V_{app} - V_{bd}\right)^2. \tag{4.11}$$

where α is a fitting coefficient which is considered to be unity. Moreover the dimension of the region in which this thrust is effective is obtained from an experimental correlation presented by [146], as,

$$l_p = 0.005 \left(\frac{T}{0.04} \right)^{0.5}, \qquad h_p = 0.0018 \left(\frac{T}{0.04} \right)^{0.5} \tag{4.12}$$

where l_p, h_p are respectively the length and the height of the plasma region in (m), and thrust T, is in(N/m).

However the dependency of thrust on the extension of the plasma region was observed in the experimental work of Durscher and Roy [161] to have a linear relation, with a minimum length for the plasma region of 2.5mm. Thus, If we consider,

$$C_{g0} = \frac{C_g}{l_p}, \qquad C_{d0} = \frac{C_d}{l_e}, \tag{4.13}$$

and replace the thrust in Eq. (4.12) from Eq. (4.17)), and then the length of the plasma region is calculated directly as,

$$l_p = \max\left[\begin{cases} \dfrac{2^{2/3}40^{4/5}}{40^2}\dfrac{\left(2^{2/3}\rho f C_{d0}^2 C_{g0}^2 l_e^{10}(V_{app}-V_{bd})^2(C_{g0}+C_{d0})^8\right)^{1/5}}{(C_{g0}+C_{d0})^2} \\ 0.0025 \\ l_g \end{cases}\right] \tag{4.14}$$

where l_p, l_g, l_e are in [m]; C_{g0}, C_{d0} [F/m] and V_{app}, V_{bd} in [V]. l_g is the asymmetric gap length between the trailing edge of the exposed electrode and the leading edge of the grounded electrode. Optimum gas spacing could higher thrust for the plasma actuator. Here, we have assumed that the minimum length of the plasma region is equivalent to the gap spacing (if exists).

To approximate this dependency of the thrust on the power consumption, we assume a situation of uniform flow ($m^{\bullet} = \frac{dm}{dt} \approx cte$), and this results in:

$$T = \frac{dm}{dt}v, \quad P = \frac{1}{2}\frac{dm}{dt}v^2, \quad \frac{dm}{dt} = \rho A v, \tag{4.15}$$

$$T = \left[4\rho A P^2\right]^{1/3}. \tag{4.16}$$

where A is the area of the actuator.

Substituting Eqs. (4.11) and (4.10) in Eq. (4.16), we have an estimation of the thrust generated by plasma actuator,

$$T = \alpha\left[4\rho l_p\left(2f\frac{C_{g0}C_{d0}l_e l_p}{C_{g0}l_p + C_{d0}l_e}(V_{app}-V_{bd})^2\right)^2\right]^{1/3}. \tag{4.17}$$

The air density ρ in the above equation is calculated from the ideal gas law.

4.2.2 - Numerical modeling of plasma generated body Force

Since Eq. (4.17) already provides us with a correct scale for the thrust generated by the plasma, we only need the correct distribution and direction of the body force generated by the plasma actuator to close the formulation of the model. The body force generated by the plasma actuator depends on the charge density (ρ_c) and the electric field ($\vec{E}$) as expressed by,

$$\vec{F}_0 = \rho_c \vec{E} \tag{4.18}$$

With this and the Eq. (4.17), we define the scales for the charge density and the electric field as,

$$, \qquad \rho_{c,\max} = 2 f C_{eq} \frac{(V_{app} - V_{bd})}{f_{corr} \lambda_d}, \qquad f_{corr} = \frac{1}{2}\sqrt{2\pi}\frac{\sigma}{l_p}\left[\operatorname{erf}\left(\frac{1}{2}\frac{\mu\sqrt{2}}{\sigma}\right) + \operatorname{erf}\left(\frac{1}{2}\frac{\sqrt{2}(l_p - \mu)}{\sigma}\right)\right] \tag{4.19}$$

$$\vec{E} = E_0 \vec{E}^* \qquad E_0 = \frac{(V_{app} - V_{bd})}{l_p}, \tag{4.20}$$

where $\vec{E}$ is the electrostatic field vector $\vec{E} = -\nabla\Phi$, and the star indicates normalized fields. To arrive at Eq. (4.19), we have assumed that plasma is distributed uniformly in the span wise direction and the effective height of the equivalent capacitor that is storing the same charges is equal to the Debye length and the accumulation of the charge occurs during the time interval Δt. Moreover, this effective height is corrected (with an error function) in a way to compensate for the charge density drop over the dielectric surface (Eq. (4.27)). Solution of the charge density field and the electric potential was based on the model developed in [85],with a modified boundary condition for the electric field on the surface of the dielectric layer. We should mention that, a key advantage of the parameter scaling in Eqs. (4.19) and (4.20) is that the voltage dependency of power and body force can be predicted more accurately and also that the model thus needs less unknown fitting parameters.

By considering Gauss law, we need to solve the following Poisson equation for the electric field,

$$\nabla \bullet \left(\varepsilon \vec{E}\right) = \rho_c. \tag{4.21}$$

According to the split-potential field model, the electric potential is separated in two parts, one being a potential due to the external electric field, and the other being a potential due to the net charge density in the plasma,

$$\Phi = \phi + \varphi. \tag{4.22}$$

Assuming that the Debye length is small, as well as the charge on the wall above the encapsulated electrode, then the distribution of charged particles in the domain is governed by the potential due to the electric charge on the wall, being unaffected by the external electric field. The smaller the Debye length, the narrower the plasma region located near the electrode and dielectric surface become. Therefore, the governing equations for the potentials due to the external electric field and for the net charge density are:

$$\nabla \bullet \left(\varepsilon \nabla \phi\right) = 0, \tag{4.23}$$

$$\nabla \bullet \left(\varepsilon \nabla \varphi\right) = -\rho_c. \tag{4.24}$$

The charge density and Debye length are related by

$$\frac{\rho_c}{\varepsilon_0} \approx -\frac{\varphi}{\lambda_d^2}. \tag{4.25}$$

and after replacing the above equation into Eq. (4.24), we obtain the governing equation for the net charge density,

$$\nabla \bullet \left(\varepsilon_r \nabla \rho_c\right) = \frac{\rho_c}{\lambda_d^2}, \qquad \varepsilon = \varepsilon_0\, \varepsilon_r \tag{4.26}$$

Eq. (4.23) is solved for the electric potential, using the applied voltage on the electrodes as boundary conditions. Applied AC voltage is imposed at the exposed electrode while the embedded electrode is prescribed as ground by setting the electric potential to zero. At the outer boundaries, $\partial\phi / \partial n = 0$ is assumed. Eq. (4.26) is solved for the net charge density on the air side of the domain. A zero normal gradient for the net charge density is imposed on the solid walls except in the region covering the lower electrode. The charge density is set to zero on the outer boundaries. To close the formulation of the model, the distribution of charge density on the surface of the dielectric, over the embedded electrode, is prescribed in the stream wise direction by a half Gaussian distribution function $G(x)$, which follows closely the experimental plasma distribution over the embedded electrode, that is:

$$G(x) = \exp\left(-\frac{(x-\mu)^2}{2\sigma^2}\right), \tag{4.27}$$

In Eq. (4.27), μ is the location parameter indicating the position of the maximum, and σ is a scale parameter determining the rate of decay. The location and scaling parameters depend on the voltage and operating characteristics of the DBD. We should mention that the correct distribution of the charge density on the dielectric surface ($\rho_{c,w} = \rho_{c,\max} G(x) f(t)$) can have a great influence on the accuracy of the simulation results. However, for the purpose of simplification of the computations, the assumption of a simple Gaussian distribution is viable. The location parameter is chosen such that the peak of charge density corresponds to the middle of the plasma region extension over the embedded electrode. In addition, the value of scaling parameter is selected in a way to allow a gradual decay of the charge density distribution to the end of the plasma region length. Moreover the dielectric shielding boundary condition introduced by Ibrahim and Skote [162] for the electric potential is also adopted which reads as,

$$\nabla_n \phi = \nabla_t \bullet \left(\lambda_d \varepsilon_r \nabla_t \phi\right) \tag{4.28}$$

The condition produces a thin layer across the boundary that shields the electric field formed by the two electrodes, thus giving rise to the formation of the so called memory voltage on the dielectric surface.

4.3 - Numerical procedure and flow solver

We note that Eqs. (4.23) and (4.26) do not contain a time derivative term. Only the boundary condition for the applied voltage at the exposed electrode and the boundary condition for the charge density at the dielectric surface are time dependent. Therefore, Eq. (23) can be normalized and solved by imposing a constant boundary condition equal to unity at the upper electrode and similarly Eq. (26) can be normalized for charge density. The normalized parameters for a two dimensional coordinate system are as follows:

$$\rho_c^* = \frac{\rho_c}{\rho_{c,\max} f(t)}, \quad \phi^* = \frac{\phi}{\phi_{\max} f(t)}, \quad \vec{E}^* = \nabla \phi^* = l_p \left(\frac{\partial \phi^*}{\partial x} \vec{i} + \frac{\partial \phi^*}{\partial y} \vec{j} \right), \tag{4.29}$$

where $f(t)$ is a function representing the shape of the applied voltage.

Once the dimensionless distribution is determined, the dimensional values at any given time can be obtained by multiplying this distribution with the corresponding normalization factor. In this manner, there is no need to solve the plasma model in an unsteady manner. The methodology is explained in detail in [114].

The interaction of the plasma actuator is implemented as an explicit source term inside the momentum equation. The flow governing equations were solved by finite volume method using the Commercial CFD solver FLUENT. The plasma model was then coded as an UDF (User Defined Function) and was used alongside for the simulation purpose. A two dimensional Cartesian orthogonal grid was used for the numerical simulation. Note that the grid spacing should not be larger than the Debye length. For enforcing this and reaching grid independency of the obtained results, and also reducing the numerical cost, the numerical grid was refined toward the electrodes and surface of dielectric layer. Moreover, the grid was refined in the regions where higher values of electric field and charge density exist. Thus, the grid spacing was stretched toward the electrode both in the normal direction and in the stream wise direction leading to the minimum cell size of about 2 μm. The total number of cells varies for the different test cases as the size of the computational domain varies.

4.4 - Results and discussion

For the purpose of validation and to ascertain the improvement due to this new modeling approach, three different test cases have been selected. The first validation test case is the experimental work of Thomas et al. [159],in which the experimental correlation of the plasma extension is based on. Table (4.1), presents the details of the DBD plasma actuator used in that work of Thomas et al [159]. The computational grid of this case (Mesh A) consists of around 47×10^4 cells for a rectangular domain of $1.1\,m \times 0.5\,m$.

Table 4.1: Details of the first validation test case (Thomas et al [159]).

	Dielectric Material	ε_{rd}	$l_e(cm)$	$t_e(\mu m)$	$t_d(mm)$	$f(kHz)$
A-	Teflon	2.0	5.08	40.0	3.18,6.35	2.1
B-	Derlin	3.5	5.08	40.0	6.35	2.3
C-	Quartz	4.2	5.08	40.0	6.35	2.3
D-	Kapton	3.9	5.08	40.0	0.15	4.4
E-	Macor	6.0	5.08	40.0	3.18	2.3

Fig. (4.2a) shows the comparison of the scaled calculated thrust and experimental results of Thomas. It is clear that model provides the correct trends regarding the influence of the different effective components of DBD actuator. Also, the model reasonably predicts the nonlinear dependency of the thrust and applied voltage although the rate of increase of the data is somewhat lower that the predictions. It should be mentioned that, considering the simplicity of the model, the difference between the calculated and experimental results is reasonable and in line with experimental results. In Fig. (4.2b), the correlation between the applied voltage and thrust dependency is depicted. As it was shown in [4] the voltage and thrust are related through $T \propto V_{app}^{7/2}$, and here we have calculated this to be $T \propto V_{app}^{6.54/2}$. it is interesting to note that the thrust data of [159] in Fig. (4.2a) show an even smaller rate of variation with voltage.

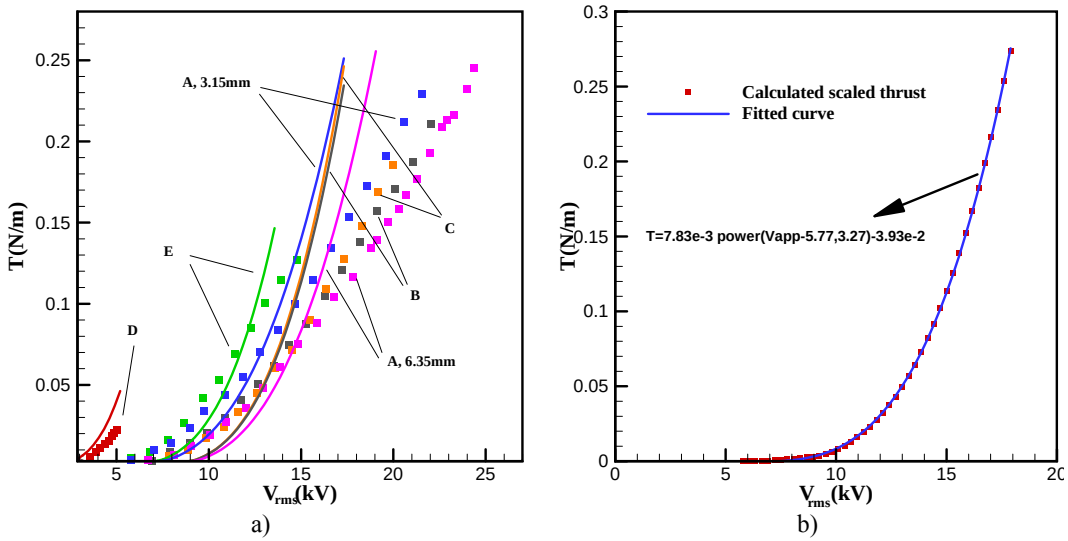

Fig. 4.2: a) Comparison of the computed scaled thrust (solid lines)with the experimental results of [159] **(symbols) b) Correlation between the voltage and the calculated scaled thrust for the 6.35 mm thick Teflon material.**

Moreover, a comparison between the unmodified split-potential model and the present modified model shown in Fig. (4.3) reveals that much improved level of agreement is achieved. The addition of the scaling to the model clearly modifies and improves the results. We should mention that for the unmodified model the values of the $\rho_{c,\max}$ and λ_d were taken from the work of Suzen et al [85] being 0.0008 C/m^3 and 0.001m respectively.

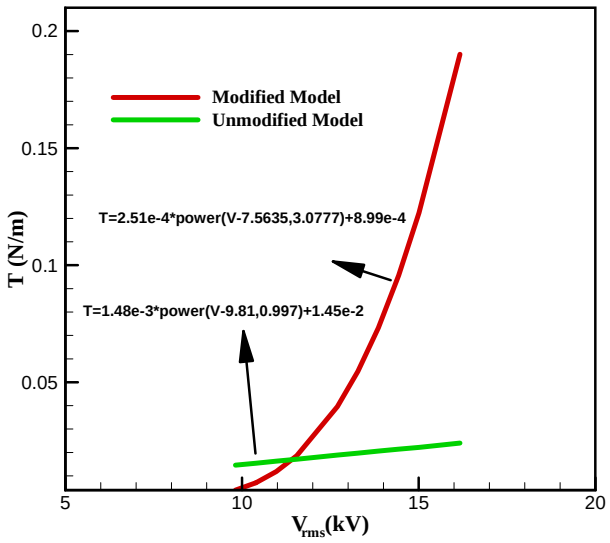

Fig. 4.3: Comparison between the numerically obtained thrust from the present modified model (which is more accurate) and the previous unmodified split-potential model.

For the second test case, we selected experimental work of Durscher and Roy [161] in order to examine the predicting capability of the model in a range of the experimental data outside that used for the fitting of Eq. (4.12) which was, we recall, correlated from the experimental results of Thomas et al [159]. The DBD plasma actuator used in the experiments of [161] includes an exposed electrode with a length of 0.5cm and an embedded electrode with length of 2 cm. Both electrodes were built from $70\,\mu m$ thick copper strips. Also, the dielectric was 3mm thick layer of acrylic with relative permittivity of 3.0. The computational domain for this case (Mesh B) was a rectangular with the dimension of $1.0\,m \times 0.5\,m$ with around 3.1×10^4 grid cells. Fig. (4.4) compares the thrust calculated by the present model and the experimental results of Durscher and Roy [161] for two frequencies over a range of applied voltage. The computed thrust is in reasonable agreement with the experimental results and thus confirming that the considered correlations been proposed are sufficiently general for thrust estimation outside of the range of parameters on which they were based.

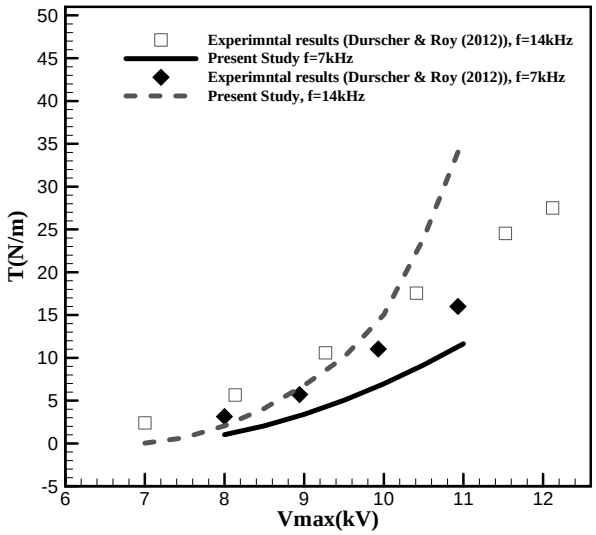

Fig. 4.4: Comparison between the calculated thrust from the present modified model and the experimental results of Durscher and Roy [161].

Fig. (4.5) depicts the normalized electric potential distribution around the electrodes along with the normalized distribution of the charges over the surface of the dielectric material. It should be mentioned that the effect of finite electrode thickness is considered just for the scaling of the body force, as explained in the previous section, while the actual numerical domain for simulations assumes infinitely thin electrodes. In addition Fig. (4.5c) illustrates the induced ionic wind by means of the contour of velocity magnitude and velocity vectors. The direction of most of the induced flow is in stream wise direction because the vertical component of the force generated by the plasma actuator is smaller than the horizontal component. Since the spatial distribution of the generated plasma body force and the ionic wind are obtained numerically, different actuators arrangement and electrode geometries could be modeled and analyzed easily.

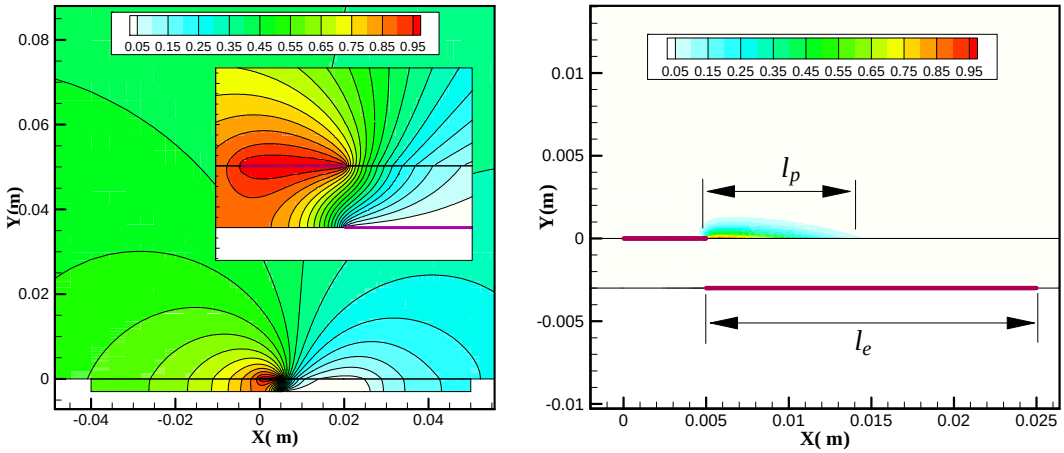

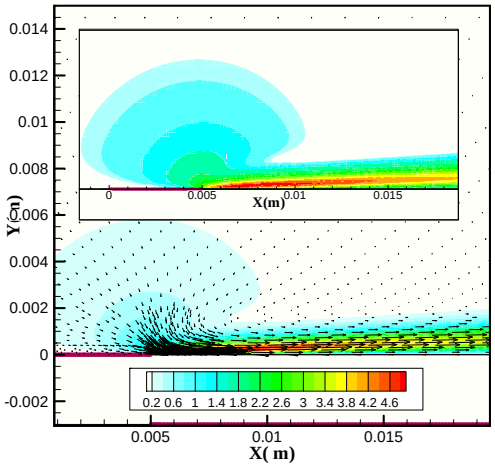

(c)

Fig. 4.5: a) Electric potential field around the DBD actuator for $V_{\max} = 10kV$, $f = 14kHz$. b) Charge density distribution over exposed electrode. c) Induced ionic wind velocity magnitude contour (m/s).

In Fig. (4.6) , calculated profiles of the steam wise velocity component are compared with the PIV data of Durscher and Roy [161] at two stations, x=25 and 35 mm for $V_{\max} = 10kV$, $f = 14kHz$. The trend is well captured but there is a difference between the maximum values of the velocities for both profiles. This is related to the underestimation of the thrust computed by the present model for the applied voltage (as can be seen in Fig. (4.4)). However, for a simplified model the accuracy is acceptable and the predictions are in line with the experiments. Moreover, the figure shows that the position of the maximum velocity is predicted correctly by the present model.

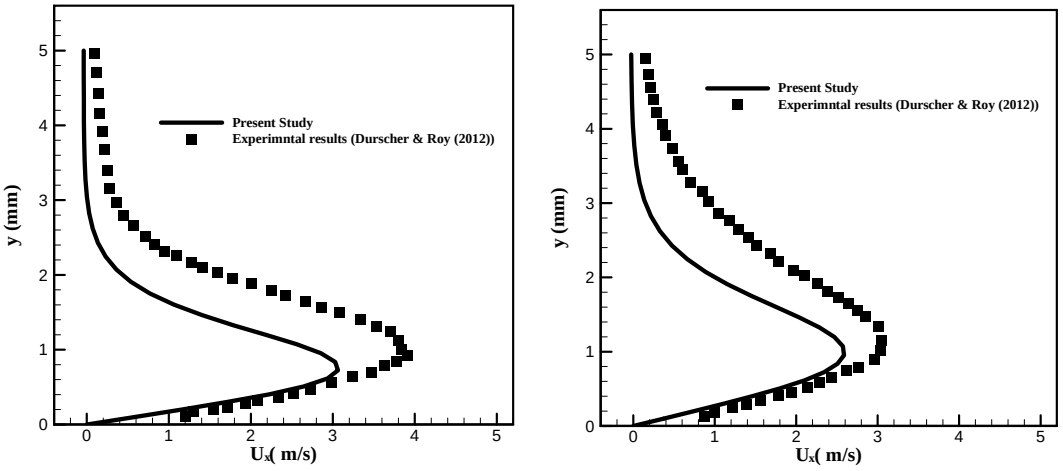

(a) (b)

Fig. 4.6 : Comparison between the calculated profile of the horizontal velocity and the experiments of Durscher and Roy [161]**. at a) x=25 mm b) x=35mm, downstream of the exposed electrode.**

One of the parameters that is known to affect the thrust is the length of the plasma region, which was estimated by Eq. (4.14). The obtained plasma region length from the present model was then compared with experimental results of Durscher and Roy [161], and the results are shown in Fig. (4.7) .As can be seen the experimental results show approximately a linear relation between thrust and plasma region length while the numerical calculation is showing a quadratic tend. The deviation of the estimated scaled thrust (under estimation at low voltages, and over estimation at high voltages) is related to this point, i.e. the correct evaluation of the flow regime.

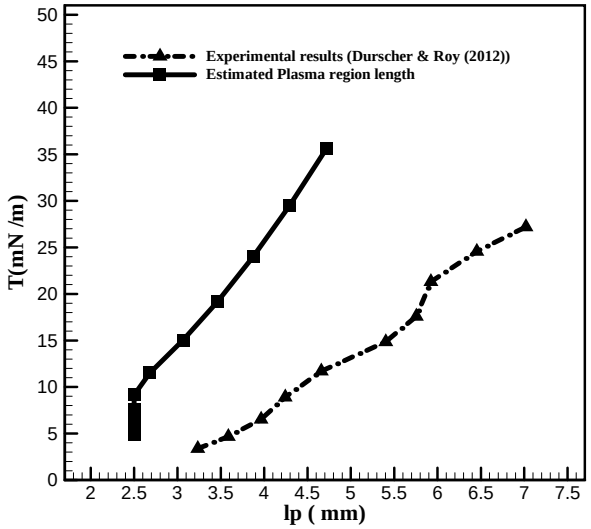

Fig. 4.7 : Comparison of the estimated length of the plasma zone and the experimental results of Durscher and Roy [161].

Finally, the experimental and numerical work of Palmeiro [157] is considered to compare the present model with other models and with experimental results. Three test cases are considered following [157], with different electrode geometry and applied voltage and some of their details are tabulated in Table (4.2). As shown in [157], the existing phenomenological models have diverse accuracy for different cases.

Table 4.2: Details of the test cases of Palmeiro [157].

Test Case	ε_{rd}	$l_e(mm)$	$l_g(mm)$	$t_d(mm)$	$f(kHz)$	$V_{\max}(kV)$
(1)	2.9	6.35	1.0	0.19	3.0	6.0
(2)	2.9	12.7	1.0	0.57	3.0	7.5
(3)	2.9	5.0	0	0.18	2.75	5.0

Table (4.3) compares the maximum velocity obtained from the present model with other phenomenological models and the experiments. It is obvious from this table that although our model is simple, it offers a more uniform predictive capability for the various test cases compared with the other models. The maximum velocity shown in Table (4.3) is obtained at a specified stream-wise measuring location which was equal to 10mm, 10mm, and 5mm from

the leading edge of the exposed electrode, respectively for cases (1), (2) and (3). The present model shows acceptable accuracy for all the three cases. Although the hybrid model of Lemire et al. [156] shows good accuracy for two of the cases ,it is not capable of replicating the experimental results of the other case.

Table 4.3: Maximum induced velocity $U_{\max}(m/s)$

Test Case	Experiments [157]	Simple body force model [83]	Split-potential model [85]	Lumped-circuit model [89]	Hybrid Model [156]	Present Model
(1)	1.9458	0.7266	0.2110	8.9311	1.5339	1.05642
(2)	1.2772	0.8383	0.2495	7.3674	0.2927	1.10435
(3)	1.5181	0.3042	0.2124	3.9770	1.2382	0.959561

In Fig. (4.8) the obtained x-velocity profiles at the measuring locations mentioned above, are compared with experimental and numerical results of Palmeiro [157]. The velocity profiles for each measuring station and modeling methods are normalized by the corresponding maximum velocity. For each case four sets of results are presented, namely A) the experimental results [157] ; B) unmodified split-potential model ; C) the model giving the closest behavior to the experiments ; D) and the results obtained from the present model. After removing the discrepancies introduced by the correct prediction of the velocity peak, we see that our model is the best to predict test cases (2) and (3), and none of the models is able to predict adequately the very narrow boundary –layer behavior of test case (1).

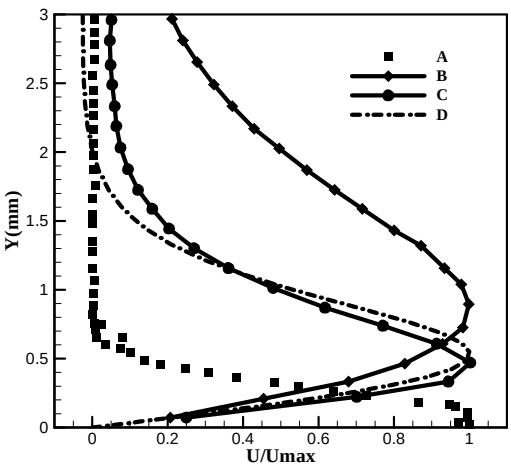

(1)

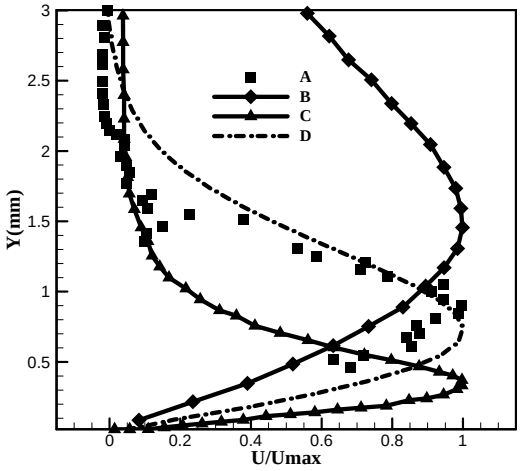

(2)

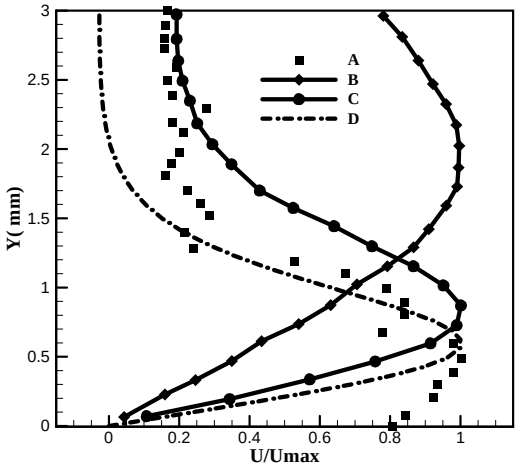

(3)

Fig. 4.8: Comparison of the x-velocity profile at the specified measuring location a) Case (1) b) Case (2) c) Case (3).

4.4.1 - Effect of altitude on the thrust generation of plasma actuators

For a flow control system to be used in real applications, for which the altitude, for example, will vary significantly the characteristics of the thrust generated by the plasma actuators under various ambiental parameters need to be assessed to prove that they have adequate capability of usage. When the altitude of the aeronautical system is changed, several properties, including pressure, temperature and humidity, will change. These factors could alter various parameters of the plasma actuator system. As an example, the dielectric permittivity, secondary emission coefficient of the surface of the dielectric material, space ionization and attachment coefficient are dependent on the local characteristics of the environment. The results of such assessment will serve to help the design of a novel flow control system using DBD plasma actuators, for high altitude airships which consists of both cruiser and feeder airship, with a wide range of change of altitude [113].

Several studies addressed the influence of the variation of altitude, temperature and relative humidity, such as [163] who concluded that the effectiveness of the actuator increases with relative humidity also the [164–169] studied the influence of the operating pressure on the performance of the plasma actuator. Wu et. al[164] considered the reduction of the operating pressure below atmospheric pressure level. They showed that the reduction of operating pressure causes a decrease of the rotational temperature of the electrons, and also an initial decrease in vibrational temperature of the electrons followed by an increase. They also observed that the pressure reduction causes a change of the discharge mode at a transition pressure of 45 torr. Litvinov et al[165] mentioned that the larger thrust resulting from a decrease in pressure could be associated with an increase in the plasma volume, ahead of the electrodes, allowing for a larger total number of ions, moreover, it was shown that the relative area occupied by the plasma on the dielectric surface varies with pressure by

$(p_0(200torr)/p)^{7/5}$. Benard et al [166] also showed that the plasma extension increases when reducing the operating pressure. Their results revealed that the extension of the plasma region was smaller than the length of the embedded electrode, when the pressure is equal to 1 atm (in accordance to the assumption we made in previous section 4.2), however, when the operating pressure is reduced the plasma tended to extend more.

Abe et al [168] investigated the effect of operating pressure on the plasma actuators performance and reported the same result, the power consumption of the DBD increases with a decrease of pressure. In essence, pressure influences the thrust generating capability of the plasma actuator by decreasing the voltage required to create a discharge (Eq. (4.6)). In other words, when the gas density is reduced, current pulses become more intense as the electric field is kept constant and fewer collisions between charged particles and surrounding neutrals occur. Versailles et al [170] looked to the effect of pressure in a range above atmospheric pressure. They concluded that, for a given actuator input, the plasma density and extent tends to decrease with increasing pressure.

For the purpose of examining the ability of the proposed model to capture the effect of altitude on the thrust produced by the plasma actuator, several test cases were considered. Table (4.4) shows the geometrical details of the actuators employed for testing the effect of operating pressure. The first test case is related to pressures below the atmospheric pressure level, and the second is related to pressures above the atmospheric level.

Table 4.4: Case details – Effect of operating pressure.

Test Case	t_e	$l_e(mm)$	$l_g(mm)$	$t_d(mm)$	ε_d	Dielectric Material
P1 [166]	0.1	10	5	4	3	PMMA
P2[170]	0.076	12.7	2	1.6	2	Teflon

Eq. (4.17) provides us thrust exerted by a unit mass of working fluid, per unit length of plasma region. Moreover, using Eq. (4.18), source term for the momentum equations of air with density ρ, the thrust which is generated by the force induced by the plasma actuator on the surface, can be numerically calculated.

An extra correction needs to be done for the Debye length. Valerioti et al [141], considered a pressure dependency of the Debye length as $\lambda_D \propto p^{(-4/3)}$. Debye Length is related to the electron charge density and electron temperature as $\frac{1}{\lambda_d} \cong \left[\frac{e^2 n_e}{\varepsilon_0}\left(\frac{1}{k_b T_i}+\frac{1}{k_b T_e}\right)\right]^{\frac{1}{2}}$. We have fitted the variation of the electron density and electron temperature with operating pressure from the work of Wu et al [164]. We have obtained the Debye length dependency to operating pressure as $\lambda_D \propto p^{(-3/5)}$ by replacing the fitting of the electron density and electron temperature in the formula of the Debye length and then replaced in the mentioned equation , resulting to the dependency of the Debye length to operating pressure.

In Fig. (4.9) the variation of the normalized thrust obtained from (Eq. (4.17)) and normalized body force (from Eq. (4.18), with decreasing pressure is presented for this case. As indicated in this figure both parameters posses a maximum point, whose value is in accordance with the results presented by [164,166,168] . The peaks of the scaled thrust and body force, estimated by Eq. (4.17) and Eq. (4.18) are occurring respectively at 0.59 atm and 0.71 atm, while the experimental results suggest a peak at 0.6 atm. However, the main point is that the simple model presented here could capture the behavior of thrust correctly.

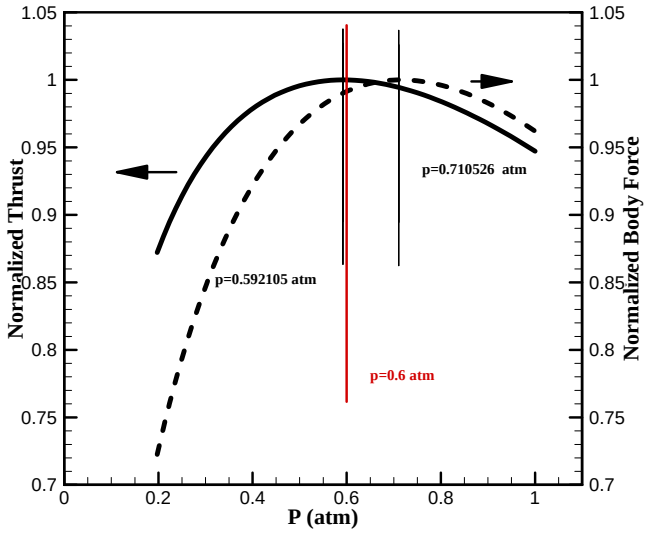

Fig. 4.9 : Variation of normalized thrust and force with decreasing pressure (below atmospheric).

For test case P1, the velocity profiles obtained at different stream-wise sections over the plasma actuator, are presented in Fig. (4.10). The maximum value of the induced velocity is in accordance with the experimental results for this case at atmospheric pressure.

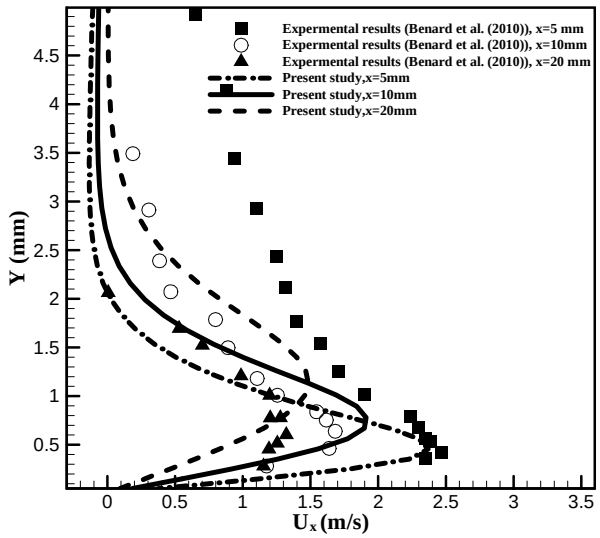

Fig. 4.10 : Velocity profile at different stream-wise sections for atmospheric pressure, p=1 atm.

For the case in which operating pressure is higher than the atmospheric pressure, the thrust obtained from the present study is compared with the experimental results of [170]. For pressures higher than atmospheric pressure, no pressure correction for the Debye length is considered. The results are plotted in Fig. (4.11) and show the correct trend: reduction of the thrust by increasing the pressure. As was explained in [170], increase in operating pressure in constant temperature causes an increase in air density. Therefore the mean free path between the particle and the kinetic energy of them when they collide reduces. Thus the rate of the momentum transfer decreases. Secondly the ignition voltage (break down voltage) is increasing with increase in operating pressure. Thus at higher operating pressure, the voltage needed for the plasma region to form is larger. In this study, the secondary electron emission (γ), was considered constant and equal to 0.01. In fact, γ depends on surface characteristic, ionization energy, and primary electron energy. As shown by Wu et al [164], when the operating pressure is changed the electron energy and temperature will change. Thus, it may be expected that the secondary electron emission γ would also be depend on pressure. To approximate the sensitivity of the results to the level of γ , in Fig. (4.11) the estimated thrust is shown for two values of γ and the lower $\gamma = 0.001$ seems to offer results closer to the experiments in which pressure varies in a range $p = 150 - 250\, kPa$.

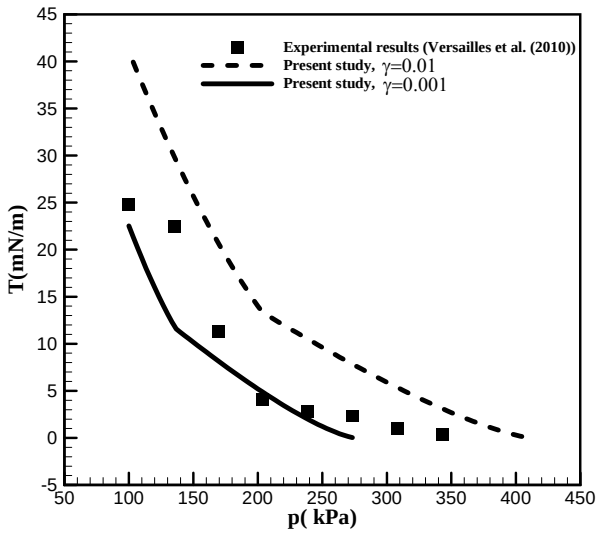

Fig. 4.11 : Comparison of the effect of higher atmospheric pressure on thrust estimated by the present study with the results obtained in[46].

4.5 - Conclusions

A simple model for plasma discharge and its effect on the flow was developed based on scaling the thrust generated by DBD plasma actuators. The scaled thrust model correctly predicts the nonlinear dependency of the thrust produced and the applied voltage. These scales were then introduced into a simple phenomenological model to estimate and simulate the body force distribution generated by the plasma actuator. Although the model includes

some experimental correlations, it does not need any fitting parameter. The model was validated with experimental results and showed better accuracy compared to previous plasma models. Moreover, the generality of the model was confirmed through validation with three different experiments. Finally, the model was tested for predicting the thrust for cases in which the altitude (pressure) is changing.

5 - Comparison of DBD Plasma Actuators Flow Control Authority in Different Modes of Actuation

Abstract

The principal mechanisms by which DBD plasma actuators influence flow characteristics, and are thus able to control the flow, depend strongly on their modes of actuation. Here two different modes based on steady and unsteady actuation are compared and investigated. A simple sinusoidal voltage distribution and a duty cycled sinusoidal voltage were considered for these purposes. Leading edge separation around a stalled NACA 0012 airfoil at $\mathrm{Re} = 3 \times 10^6$ is considered as test case. A simple phenomenological model which uses the correct scale of the plasma body force is considered for the modeling of the plasma actuator effects. The steady actuation results show that flow control can be effectively achieved and moreover this mode can be used for noise control by continuous injection of momentum in the boundary layer. Unsteady actuation with an imposed frequency equal to the calculated natural frequencies of the flow gives rise to a resonance actuation effect[4].

Keywords: Unsteady actuation; optimum frequency; flow control; analytical model; resonance mode;

5.1 - Introduction

The use of effective active control flow techniques can provide higher efficiency for the controlled system. Among different Active Flow Control (AFC) techniques, DBD plasma actuators are novel means of actively controlling flow and have gained increased interest during the past decade for different applications [117,171–174]. This kind of actuators may be operated in different modes depending on the type of the input voltage signal. If a sufficiently high continuous sinusoidal voltage is applied to the electrodes, the plasma actuator will accelerate the fluid. In this mode the main mechanism of flow control is by locally imparting momentum to the nearby flow. The use of a plasma actuator in steady operational mode would cause significant modification of the stability properties in a boundary layer. The amplitudes of the oscillations would tend to decrease. If the voltage source operates in a burst mode, with a specified duty cycle, the momentum injection will be done discontinuously (unsteady mode) with a frequency equal to the frequency of duty cycle. In this mode, the plasma actuator might mitigate or stabilize the natural instabilities of the

[4] This chapter is based on the following paper: "M. Abdollahzadeh, J.C. Páscoa, P.J. Oliveira (2014), Comparison of DBD Plasma Actuators Flow Control Authority of the in Different Modes of Actuation, Journal of Applied Physics: D, (Submitted)."

flow in a more efficient way by generating large coherent vortical structures. In this case, the plasma induced instabilities would counteract the disturbances already present in the flow. The amplitude of the flow instabilities would decrease due to superposition of velocities. In the case of unsteady or pulsed actuation, the power requirement of the actuator is lower than in steady actuation due to the short duty cycles of the input voltage. In fact, the duty cycle percentage correlates linearly with power consumption. In Fig. (5.1), the schematic of the plasma actuator and the different operational modes of a plasma actuator are shown. In the unsteady mode, the forcing of the actuator during the active period accelerates the flow. When the actuator is turned off periodically, a large vortex forms due to wall effect and decouples from the actuation region. This process is then repeated at every cycle [175].

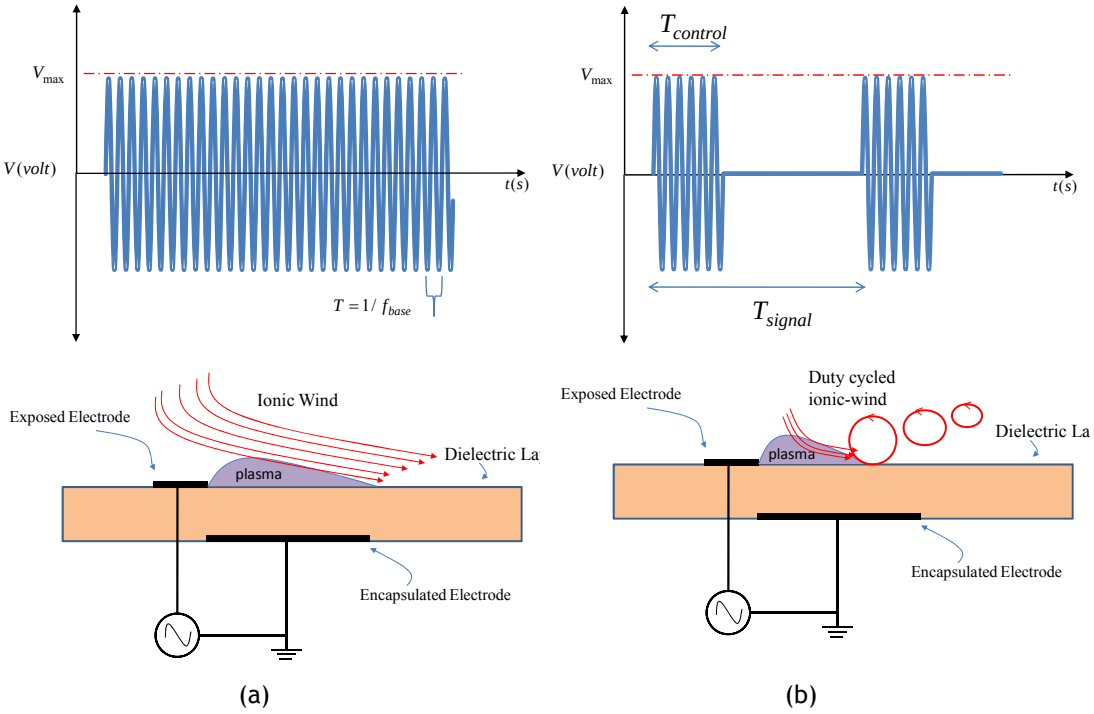

Fig. 5.1: a) plasma actuator in steady operation mode; b) plasma actuator with duty cycle applied voltage.

One of the most common situations in which the importance of flow control is more relevant is the control of flow in stall and post stall condition. Several studies have been reported in the literature showing the capability of plasma actuators for controlling flow in such situations [176]. To increase the efficiency of the plasma actuators, some of the relevant parameters can be optimized to reach higher performances [46,147]. Tsubakino and Tanaka [177] have shown that the location of the plasma actuator has an influence on the flow control capability. In our previous work [114], we have shown that, for optimum flow control, plasma actuator should be placed before the separation point. The shape of the voltage wave has also an influence on the electric discharge and thus on the trust generated by plasma

actuators [178–180]. In the case of unsteady actuation, the burst ratio and the duty cycle are the major factors that may influence the efficiency of the plasma actuator [181].

Asada et al [182] have studied experimentally the effect of burst ratio and burst frequency. They concluded that smaller burst percentage allows increased flow control capability and at higher duty cycle frequency the voltage needed for controlling the flow is smaller and thus higher burst frequencies are more efficient. They have also shown that the reduced frequency of $F^+ = 9.1$ is optimal for flow control. Similar results have been reported by Audir et al [183] .Patel et al [184], reported that the optimum frequency of unsteady actuation at which the voltage needed to reattach the flow is minimum is equal to $F^+ = 1$. To obtain the optimum frequency, the actuator voltage was varied until a sudden rise in the lift coefficient was observed for the specified frequency. Moreover, they mentioned that if the burst frequency is not optimal, the effect of the plasma actuator would be negligible, and showed that the minimum voltage to control the flow varies with the angle of attack and flow velocity. In the experiments conducted by Sidoenko et al [185], the existence of an optimum frequency for both pulsed voltage and burst modes of actuation was observed ($F^+ = 2.6 - 14$). Mitsuo et al [186] showed that flow control authority of the plasma actuator is sensitive to the frequency of the unsteady plasma actuation. However, their measurements showed a value around $F^+ = 0.5$ for the optimum burst modulation frequency. Benard et al [187] studied experimentally the effect of steady and unsteady actuation on the lift and drag coefficients. Their results showed an aerodynamic enhancement when the frequency coincides with natural vortex frequency. Furthermore, Benard and Moreau [188], explored the use of multi-frequency excitation voltage signal to cover a wide range of the frequency of the flow instabilities. These studies suggest that there exists an optimum point for the parameters involved in unsteady or burst mode of actuation. Akansu et al [189], experimentally investigated the effect of four DBD plasma actuators on the manipulation of separation over a NACA0015 airfoil at low Reynolds number. They studied several parameters including the effects of applied voltage amplitude, dielectric thickness and unsteady actuation. Another situation for which periodic force generation by plasma actuators would benefit flow control is the dynamic stall, where unsteady plasma actuation enhances the lift and production of concentrated vortex structure near the leading edge [190].

Although most of these studies report an optimum value of $F^+ = 1$ for the bust frequency, there are still discrepancies between the values suggested by some studies. The objective of the present chapter is to investigate and compare the flow control ability of DBD plasma actuators under different modes of actuation. All of these modes of actuation were tested with only one single DBD actuator to control the leading edge separation of the airfoil, at stall condition. Since plasma actuation in unsteady mode could influence the stability of the boundary layer and turbulization (higher frequency) or the instabilities of the separation layer and shedding structure (lower frequency), we have applied FFT analysis on the velocity components in order to obtain the natural frequencies of the flow. Then, for the unsteady

mode of actuation, different values of the burst frequencies were tested including the natural frequencies of flow instabilities.

5.2 - Plasma effect modeling

Recently, we have presented a simple phenomenological model based on the scaling of the plasma generated thrust which allows us to compute the body force in the momentum equation due to plasma actuation [191]. The model uses the Gauss law to obtain the electric field distribution, in conjunction with an experimentally verified distribution of the particles charge density over the surface of the dielectric material for obtaining the body force. The governing equations of the model (electric potential and charge density) are as follows:

$$\nabla \bullet \left(\varepsilon \nabla \phi\right) = 0, \tag{5.1}$$

$$\nabla \bullet \left(\varepsilon_r \nabla \rho_c\right) = \frac{\rho_c}{\lambda_D^2}, \qquad \varepsilon = \varepsilon_0\, \varepsilon_r \tag{5.2}$$

These equations do not contain a time derivative term. It is only the boundary condition for the applied voltage at the exposed electrode and for the charge density at the dielectric surface which are time dependent. Therefore, Eqs. (5.1) and (5.2) can be normalized as follows for a two dimensional coordinates:

$$\rho_c^* = \frac{\rho_c}{\rho_{c,\max} f(t)}, \quad \phi^* = \frac{\phi}{\phi_{\max} f(t)}, \quad \vec{E}^* = \nabla \phi^* = l_p \left(\frac{\partial \phi^*}{\partial x} \vec{i} + \frac{\partial \phi^*}{\partial y} \vec{j} \right), \tag{5.3}$$

where

$$, \qquad \rho_{c,\max} = 2\, f C_{eq} \frac{(V_{app} - V_{bd})}{f_{corr} \lambda_d}, \qquad f_{corr} = \frac{1}{2}\sqrt{2\pi}\, \frac{\sigma}{l_p} \left[\operatorname{erf}\left(\frac{1}{2} \frac{\mu\sqrt{2}}{\sigma} \right) + \operatorname{erf}\left(\frac{1}{2} \frac{\sqrt{2}\left(l_p - \mu\right)}{\sigma} \right) \right] \tag{5.4}$$

$$\vec{E} = E_0 \vec{E}^* \qquad E_0 = \frac{(V_{app} - V_{bd})}{l_p} \tag{5.5}$$

In the above equations $f(t)$ is a function representing the shape of the applied voltage and $\vec{E}^*$ is the normalized electric potential. Once the dimensionless distribution is determined, the dimensional values at any given time can be obtained by multiplying this distribution with the corresponding normalization factor. In this manner, there is no need to solve the plasma model in an unsteady manner. The body force generated by the plasma actuator depends on the charge density (ρ_c) and the electric field ($\vec{E}$) as expressed by,

$$\vec{F}_0 = \rho_c \vec{E} \tag{5.6}$$

The normalized governing equations and the corresponding boundary conditions for the plasma model are summarized in Fig. (5.2) for the considered DBD actuator geometry.

5.3 - Problem statement and numerical procedure

The test case consists of flow around a NACA 0012 airfoil with chord length of 1m in atmospheric conditions. The Reynolds number based on the chord length and the free stream velocity equals 3×10^6 ($U_\infty = 43.81\, m/s$). A single DBD plasma actuator is placed at the leading edge of the airfoil, mostly for controlling the stall. The exposed electrode length is 15.47 mm and it starts at x/c=0.001481. The embedded electrode is 26.57 mm long and its leading edge is placed at x/c=0.01149 .Both electrodes were assumed to have thickness of $70\,\mu m$. The embedded electrode is covered with thin layer of dielectric material which is 4mm thick and has a dielectric permittivity equal to $\varepsilon = 4\varepsilon_0$. A schematic of the electrodes and dielectric layer configuration is presented in Fig 2. Although the plasma model makes use of the thickness of the electrode for estimating the thrust induced by the plasma actuator, the numerical grids were built assuming that electrodes are infinitely thin layers.

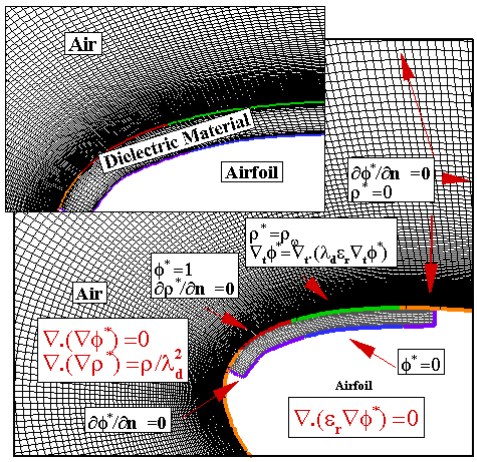

Fig. 5.2: Schematic of the DBD configuration near the leading edge of the airfoil and the corresponding boundary conditions of for the plasma model.

Two dimensional unsteady incompressible Navier-Stokes equations are considered for obtaining the flow field variables (velocity and pressure) and are written in tensor form as:

$$\frac{\partial u_i}{\partial x_i} = 0 \tag{5.7}$$

$$\rho\frac{\partial u_i}{\partial t}+\rho\frac{\partial u_i u_j}{\partial x_j}=-\frac{\partial p}{\partial x_i}+\frac{\partial \tau_{ij}}{\partial x_j}+f_i$$
$$\tau_{ij}=\mu\frac{\partial u_i}{\partial x_j} \tag{5.8}$$

In the above equations, the indices $i=1,2$, represent respectively the x and y direction, p is the pressure, μ is dynamic viscosity, t is the time, τ_{ij} is viscous stress tensor, u_i is the i-component of the velocity vector and f_i is the component of the body force vector arising from the plasma model.

Numerical solution of the governing equations stated above and in the previous section was accomplished by discritizing them with a finite volume approach, using a cell centered collocated arrangement of primitive variables. The numerical implementation was conducted by developing a new solver in OpenFoam [90]. All the convective fluxes were approximated by the GAMMA scheme using face center values for velocity. The pressure-velocity coupling is solved by the PISO algorithm and time is advanced with a second-order backward-differencing scheme. In simulating the procedure of different frequencies of excitation, the time step is kept in the order of $10^{-5}s$, with 50 sub-iterations, so that there are sufficient discrete time steps in each period of excitation. Although the predictability of the URANS and Hybrid LES-RANS models for the case of unsteady actuation needs to be verified [192,193], here we have used those methods together with k-w SST turbulence model [194] and a scale-adaptive simulation technique (SAS) [195]. The uncontrolled flow is a multi-frequency system, which may have different major frequencies including frequency of shear layer, frequency of separation bubble and frequency of the vortex shedding. Since URANS models could filter out fluctuations above some specified frequency level (e.g. the shear layer), when measuring natural frequencies of the flow, SAS model had been used. A C-type computational grid was created and the grid spacing was refined near the airfoil surface to assure the condition y+ < 1 for correctly capturing the boundary layer development. Different grid densities have been tested for assuring that the results obtained are independent of the numerical grid. The boundaries representing the free stream conditions were considered far enough from the airfoil (15c ahead of the airfoil and 20c at the back).

The solution procedure consists of two main steps. The first step is two solve the normalized form of the governing equations for the plasma model in order to obtain the magnitude and distribution of the body force generated by the plasma actuator. In the second step the normalized body force was introduced as an explicit source term in momentum equations which are solved in a sequence fashion with the continuity equation in order to obtain the velocity and pressure fields. The convergence of the numerical procedure is assured by reaching a minimum relative error of 10^{-6} at each time step for all variables. An example of the computational grid and the corresponding boundary conditions is shown in Fig. (5.3).

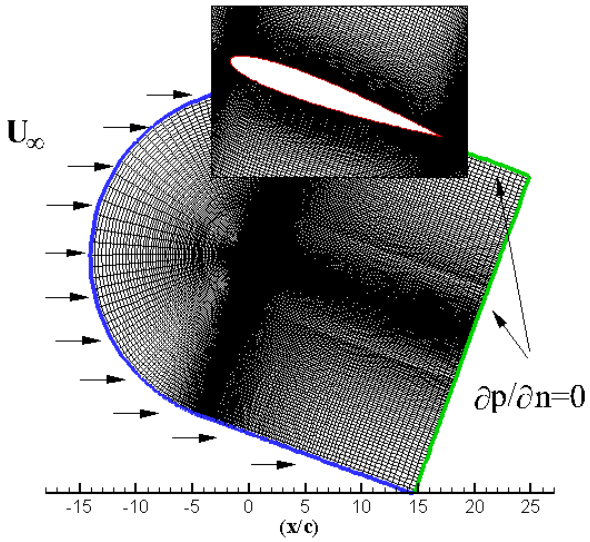

Fig. 5.3: The computational grid and boundary conditions for the flow field.

5.4 - Results and discussion

For the purpose of validation, the results of the present simulations without the effect of the plasma actuator are compared with the experimental study of Ladson [196]. When there is no actuation applied on the surface of the airfoil, the onset of the stall is around 16 degree. Above this angle of incidence, a large separation bubble is formed and the lift coefficient drops sharply. Fig. (5.4a) illustrates the flow structure at an angle of 20° without actuation and Fig. (5.4b) compares the results of the present study for the lift coefficient with the experimental results of Ladson. It is clear that the present numerical modeling approach provides acceptable accuracy in predicting the flow except for a small discrepancy when stall is approached.

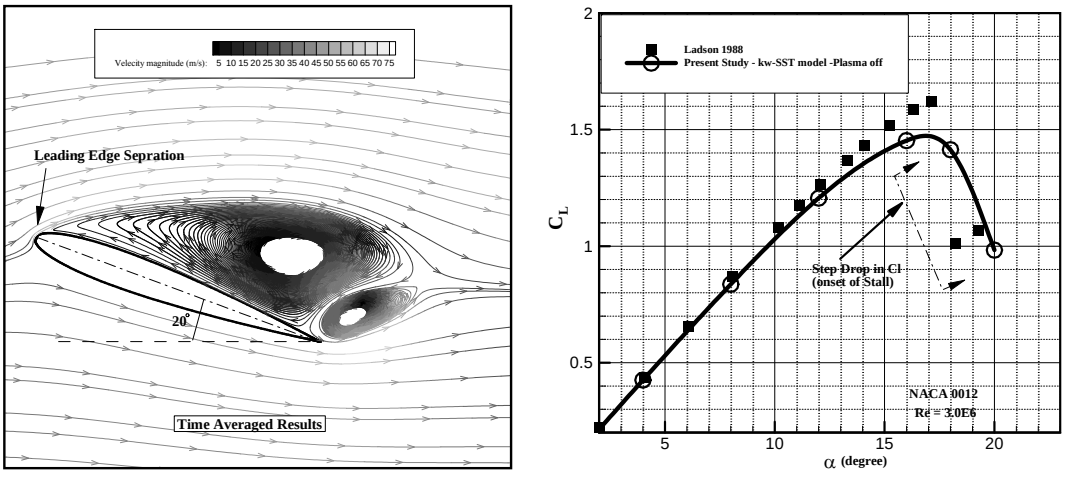

(a) (b)

Fig. 5.4 : a) Stream lines of the velocity field at an angle of attack of $\alpha = 20^\circ$, showing the time-averaged separation bubble b) Comparison of the lift coefficient (C_L) obtained from the present study and experimental results of [196].

For the purpose of controlling the flow, a single DBD actuator with the configuration specified in Table (5.1) was applied. A high-voltage continuous sinusoidal signal of 15KV with frequency of 15 kHz was used for actuation. It should be mentioned that this configuration might not be the optimum for the actuation process.

Table 5.1: Configuration of the single DBD actuator.

V_{ap}	15 kV
f_{ext}	15 kHz
t_d	4 mm
ε_d	4
l_{exposed}	15.47mm
l_{embedded}	26.57mm
t_e	4 mm

When a steady actuation is applied, the fluid beside the actuator is accelerated and the so-called ionic wind is formed. This accelerated flow region will extend along the airfoil surface. The maximum value of velocity obtained by plasma actuation is around 18.5 m/s and the core of the region of accelerated flow is located at x/c=0.02699, which is after the separation point for the angle of attack of 20° (x/c=0.020022). The ionic wind will impart momentum to the flow around the location of actuator and stabilize the nearby flow fluctuations and promote reattachment of the boundary layer. Fig. (5.5) illustrates these features by showing the velocity contour of ionic wind formed due to the steady operation of the DBD actuator.

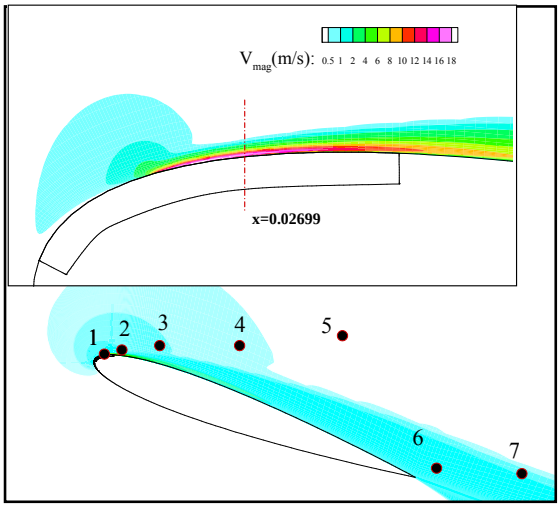

Fig. 5.5: Velocity contours of the plasma ionic wind at an angle of attack of $\alpha = 20^{\circ}$ in quiescent air.

At the specified incidences, when separation occurs over the airfoil surface three different frequency scales are identifiable. Existence of all these frequencies depends on that the separated shear layer will reattach before the trailing edge. These frequencies may be classified according to their origin: the frequency of the shear layer f_{Sl} ; frequency of the separation bubble f_{sep} ; and frequency of global instability f_{shed} which is related to vortex shedding. They can be scaled as $f_{Sl} \approx \frac{\overline{U}}{\theta}$, $f_{sep} \approx \frac{U_\infty}{L_{sep}}$ and $f_{shed} \approx \frac{U_\infty}{L_{wake}}$ where $\overline{U}$ is average velocity in the shear layer, θ momentum thickness at the separation point, L_{sep} is the length of separation bubble, and L_{wake} is characteristic width of the wake. Using the results of the simulations without actuation, the characteristic frequencies of the flow were determined by computing power spectra of time-series of v-velocity in the shear layer, the separated region, and the wake, using FFT analysis. For this purpose, seven different probe locations were considered for monitoring the variation of the velocity components. The locations of these points are tabulated in Table (5.2), with the origin of the x,y coordinates at (0,0) , and are shown by the dots in Fig. (5.5).

Table 5.2: Velocity sensors monitoring locations.

Probe Number	x (m)	y (m)
1	0.0300	0.0187
2	0.0812	0.0308
3	0.1918	0.0435
4	0.4255	0.0435
5	0.7264	0.0723
6	1.0018	-0.3152
7	1.2515	-0.3312

In Fig. (5.6), the variation of the cross-stream velocity (v-component) at different probe locations for the angle of attack of 20° is shown along with the corresponding power spectra (PS). It is noted that the frequency of shear-layer instability cannot in principle be captured in the numerical simulation using URANS. Firstly because the time step may filter out the fluctuations of that level, and secondly because using RANS might distort the correct spectral content of the signal (as an outcome of the RANS averaging procedure). Typically, the URANS approach could provide accurate results in situations where the rate of the time variation of the flow is of much lower frequency than that of the turbulence. To overcome this issue, the SAS model was here applied. As can be seen from Fig. (5.6), the shear layer, separation bubble and the wake are all locked on a major dominant frequency which is equal to 24.4 Hz. However, two other characteristic frequencies are also observable, one around 3.7Hz and the latter around 46 Hz. Since these frequencies are less energetic, they could possibly be some

sub/super harmonics of the main natural frequency. The reduced/normalized frequency can then be calculated using the scales introduced above, and the resultant reduced frequencies are presented in Table (5.3). The value of the reduced shedding frequency of 0.189 is in the range reported in literature [21].

Table 5.3: Dominant normalized frequencies of the flow without actuation.

Measured frequency f(Hz)	**Normalized** $f^{+}_{sep} = \frac{f_{sep} c}{U_{\infty}}$	**Normalized** $f^{+}_{shed} = \frac{f_{shed} c \sin\alpha}{U_{\infty}}$
3.7	0.084	0.02872
24.3	0.554	0.1894
43.5	0.9929	0.3395

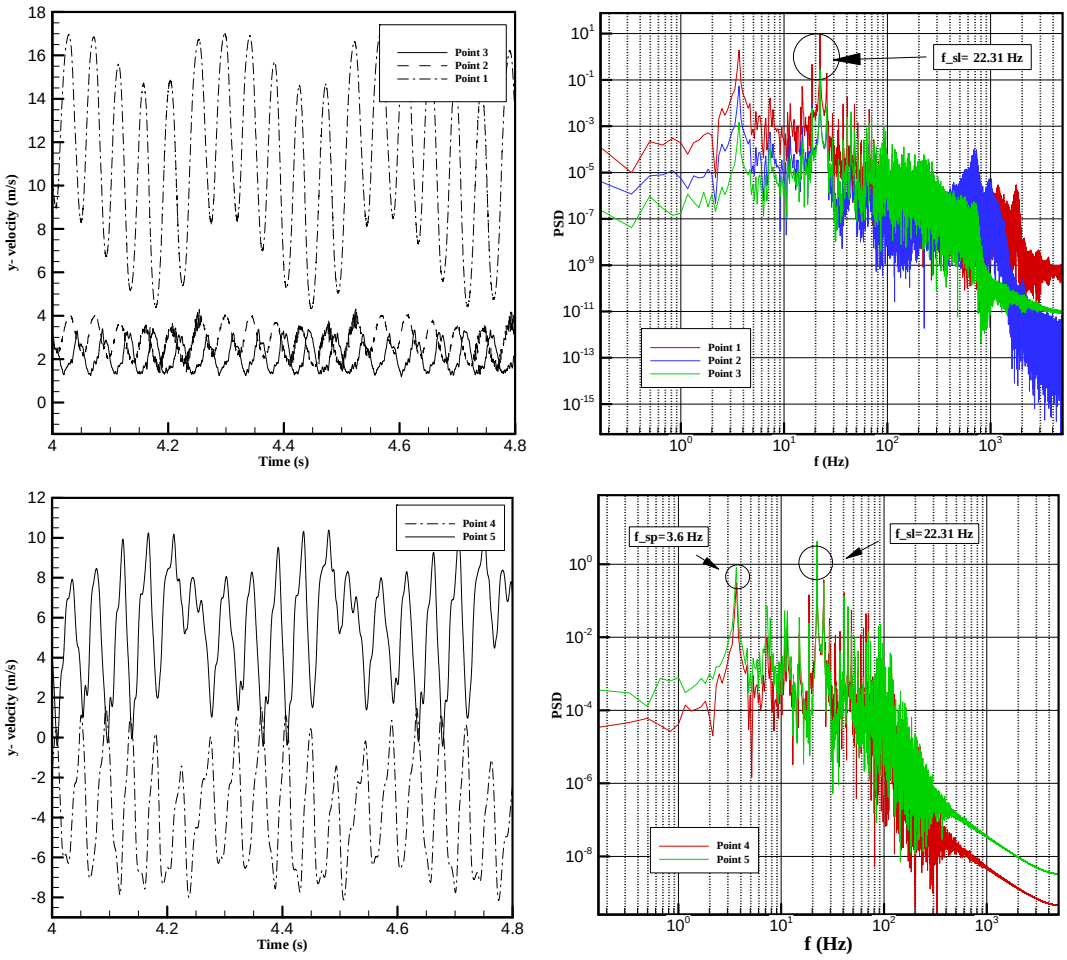

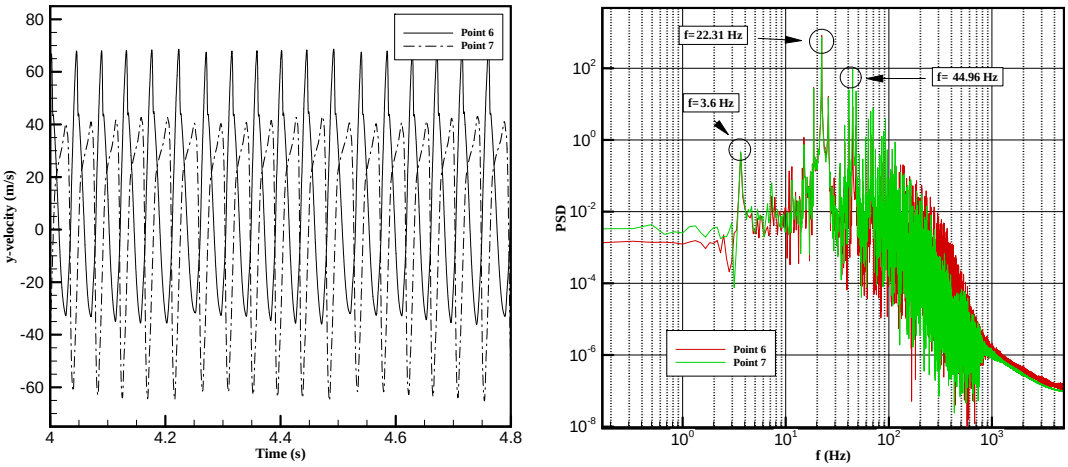

(a) (b)

Fig. 5.6: Cross-stream velocity component signals at different probe locations without actuation: a) time variation; b) power spectra.

Since the plasma actuators were placed slightly upstream of the separation point so as to have an optimum controlling effect, they can be used either in steady mode for stabilization, or in an unsteady manner to lock on the major frequencies of the flow and their harmonics, to initiate a hydrodynamic resonance or optimum controlling effect. In Fig. (5.7a), the time averaged velocity stream lines reveal the significant reduction of the size of the separation bubble in the case of steady actuation, for the angle of attack of 20 degree. Figs (5.7b) and (5.7c) compare the variation with α of lift coefficient and the lift/drag ratio of the airfoil C_L/C_D for the cases with and without actuation. These results show that the steady operation of the DBD actuator successfully improves the lift coefficient of the airfoil. At high angle of attack, the increment of C_L is more pronounced when stall occurs. At the angle of attack 20°, the lift coefficient was increased approximately by 16% with its value raising from 0.99 to 1.16. Moreover, the reattachment of the flow decreases the effective angle of attack of the airfoil and therefore, improves the aerodynamic performance of the airfoil (Fig. (5.7c)).

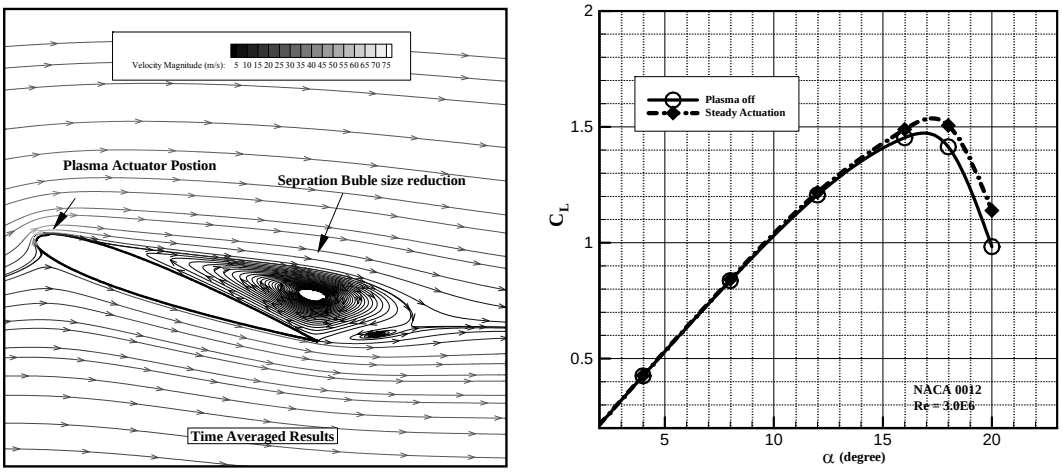

(a) (b)

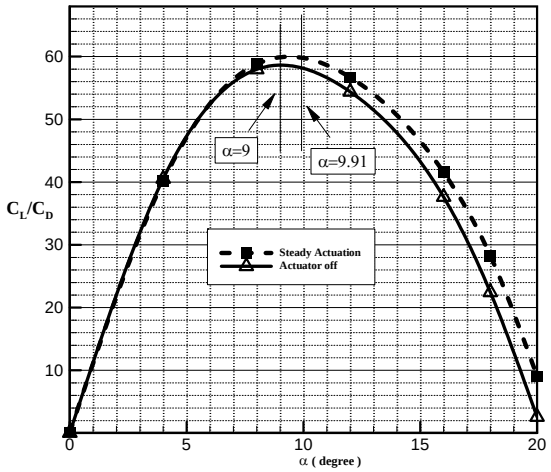

(c)

Fig. 5.7 : Results with the DBD actuator in steady mode: a) Stream lines of the velocity field at angle of attack of $\alpha = 20^{\circ}$ showing the time-averaged separation bubble; b) enhancement of the lift coefficient (C_L) by actuation c) effect of steady plasma actuation change on the pick aerodynamic performance point.

Fig. (5.8) illustrates the changes brought about to the velocity fluctuations and the corresponding power spectra when the steady actuation is applied. As can be seen, when the plasma actuator is working in steady mode, all the major frequencies of the flow vanish and the flow becomes more stabilized. There is also a reduction in the power spectrum peak, and regulation of the fluctuations indicating that possibly noise reduction might be achievable by using the DBD plasma control.

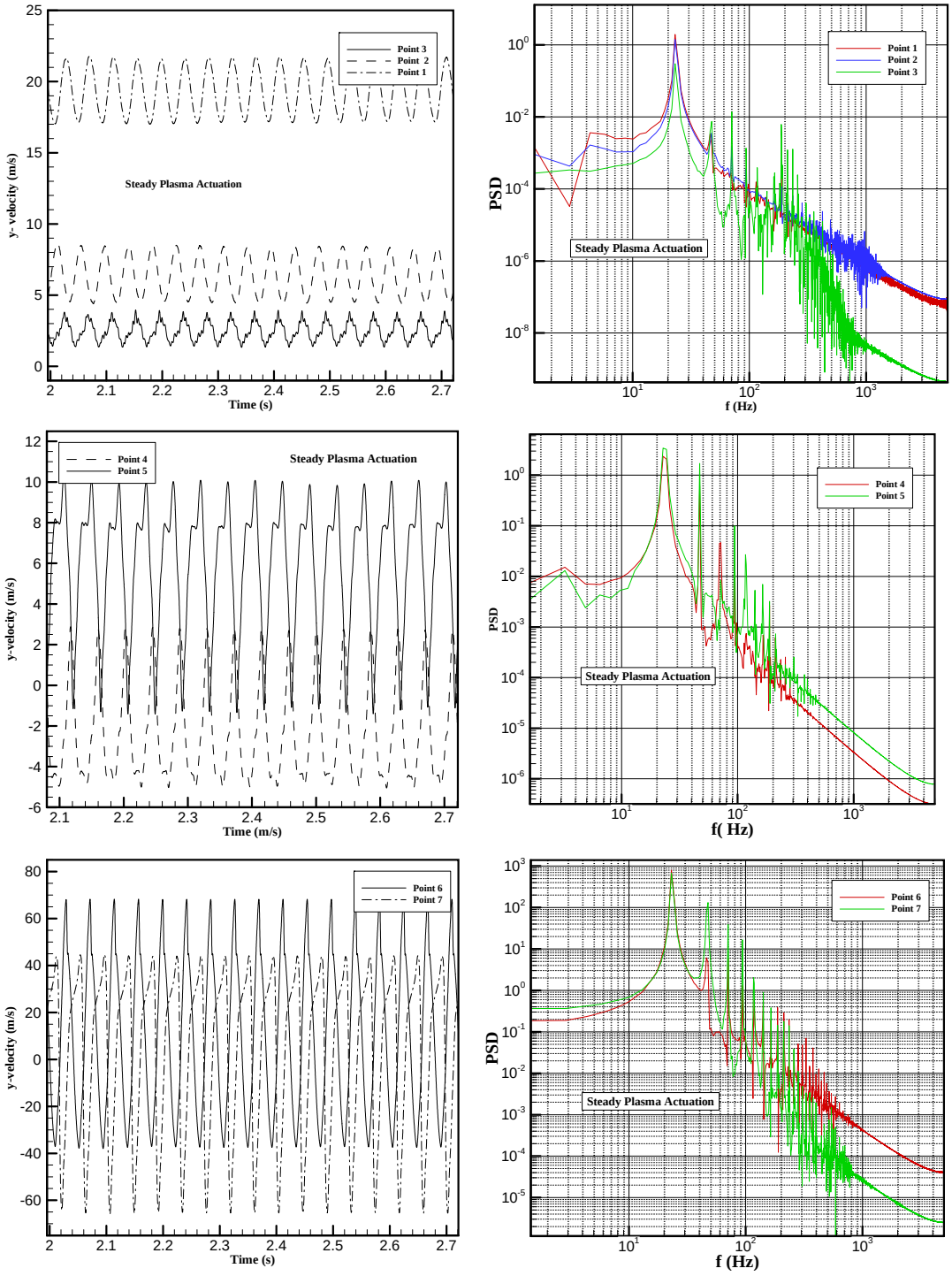

(a) (b)

Fig. 5.8: Cross-stream velocity component signals at different probe locations with steady plasma actuation: a) time variation; b) power spectra.

In the case of unsteady actuation with alternative current (AC), reduced frequencies in the range 0.1 to 23, with two burst modulations of 10% and 50%, were tested for possible observation of resonance behavior. Due to the actuation, ionic wind is formed during the

active part of the cycle. When the actuation stops, the plasma induced vortex separates from the actuation location and interacts with the main flow separation bubble and thus allowing some control of the flow.

In Fig. (5.9), the time averaged streamlines are superimposed on velocity field contours and are shown at these burst frequencies and burst ratios ($\beta = 10\%$ on the left and $\beta = 50\%$ on the right). The shape of the separation bubble varies significantly with the burst frequency and burst ratio. The size of the separation bubble is reduced when $\beta = 50\%$ for all the burst frequencies employed here. The center of circulation region moved further downstream when the frequency is increased from $f = 25Hz$ to $f = 250Hz$. In the case of $\beta = 10\%$, the suppression of the separation bubble was not significant for the lower frequencies, $f = 25Hz$ and $50Hz$. However, the size of secondary vortex near the trailing edge is reduced in these cases in comparison to the base case (Fig. (5.4a), $\beta = 0$). When the burst frequency is increased to 250 Hz, the unsteady actuation was successful in controlling the separation bubble.

$f = 25Hz$

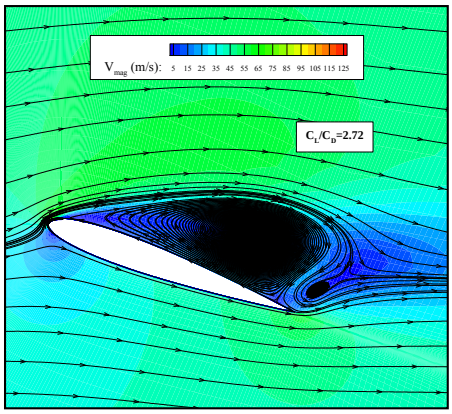

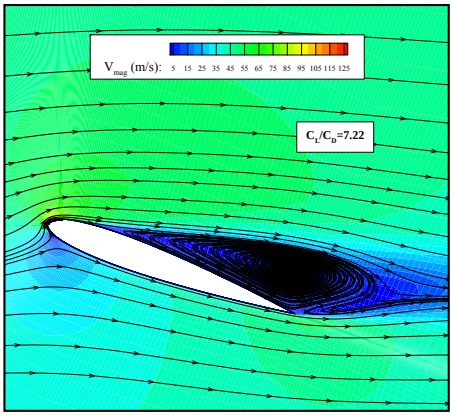

$f = 50Hz$

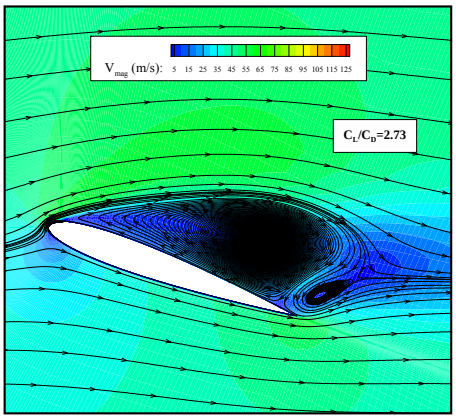

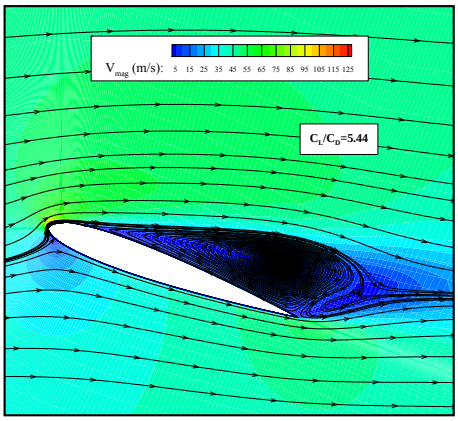

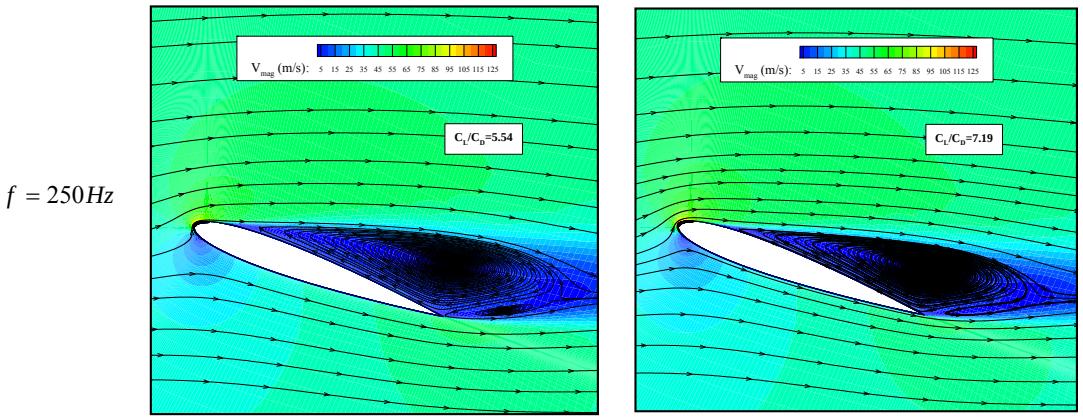

Fig. 5.9: Time-averaged velocity contours and streamlines at angle of attack of 20° for a) $\beta = 10\%$ **and b)** $\beta = 50\%$ **.**

Both the steady and the unsteady actuation processes have improved the pressure recovery in the separation region. In this aspect, the steady actuation was slightly better than the unsteady one. This is quite different from the results for laminar separation control where unsteady actuator operation (mostly at F+ = 1) has always been found to be better than steady actuator operation. Similar results for controlling turbulent separation bubble were reported by He et al [197]. However, this conclusion from the numerical results could be related to the assumption of the two-dimensional flow followed in the present study. Asada and Fuji [192], suggested that important phenomena related to the effect of the burst mode on separation control using the plasma actuator may be three-dimensional vortices generated by plasma actuator which induce the strong longitudinal vortices.

Mean surface pressure coefficients for the base flow and steady and unsteady actuator cases are compared in Fig. (5.10). When the plasma actuator is off, the flow-field around the airfoil separates from the leading edge and the pressure coefficient has a flat distribution over the whole suction side of the airfoil. However, when the steady or unsteady actuation is on, the body force produced by the plasma actuator locally accelerates the ambient air, thus producing a strong low pressure region and thus a sharp decline in the Cp level at the actuator position at the leading edge, which is then followed by a rapid pressure recovery towards the trailing edge. The peak value of the pressure coefficient in the presence of the plasma actuator is reduced. For unsteady cases the largest value of the peak occurred for $F_\beta = 250Hz$ and $25Hz$ for $\beta = 10\%$ and 50% respectively. Moreover for $\beta = 10\%$ at $F_\beta = 250Hz$, the size of large plateau the Cp on the suction surface (characteristic of the separation side) significantly reduces. Therefore, the lift of the airfoil can be improved. However, this figure shows that the steady actuation (normal mode) is more effective than unsteady actuation (burst mode) on the control of separation in this flow condition.

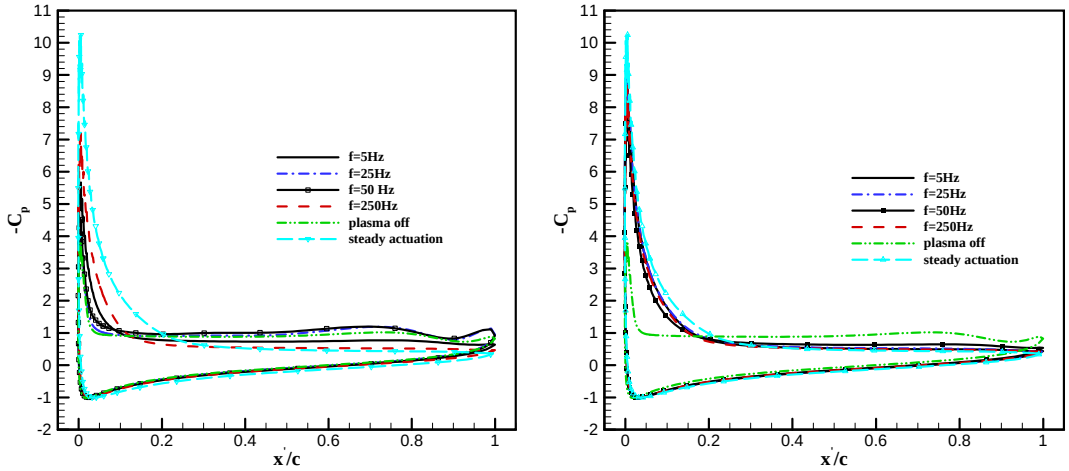

Fig. 5.10: Pressure coefficient distribution around the NACA0012 airfoil at an angle of attack of 20° for steady and unsteady plasma actuation for a) $\beta = 10\%$ **; b)** $\beta = 50\%$ **.**

In Fig. (5.11), the effect of two burst ratios, 10% and 50%, and different burst frequencies on the lift and drag is demonstrated. At burst ratio of 10%, the lift and drag coefficients had respectively experienced a maximum increment of 12.51% and 10.22% at $F_\beta = 25Hz$. Even duty cycles of 10% were able to increase the lift coefficient. However at the same burst ratio, when the burst frequency is increased to 250 Hz, both lift and drag reduce to minimum by 9.66% and 21.5 % respectively. Moreover, it was observed that almost for all the cases the increase in lift was accompanied by decrease in drag and vice versa. When $\beta = 50\%$, the lift and the drag curves just have a extremum at $F_\beta = 50Hz$. The results also confirmed that it was possible to obtain the same lift coefficient by consuming less amount of energy (eg. $F_\beta = 100Hz$).

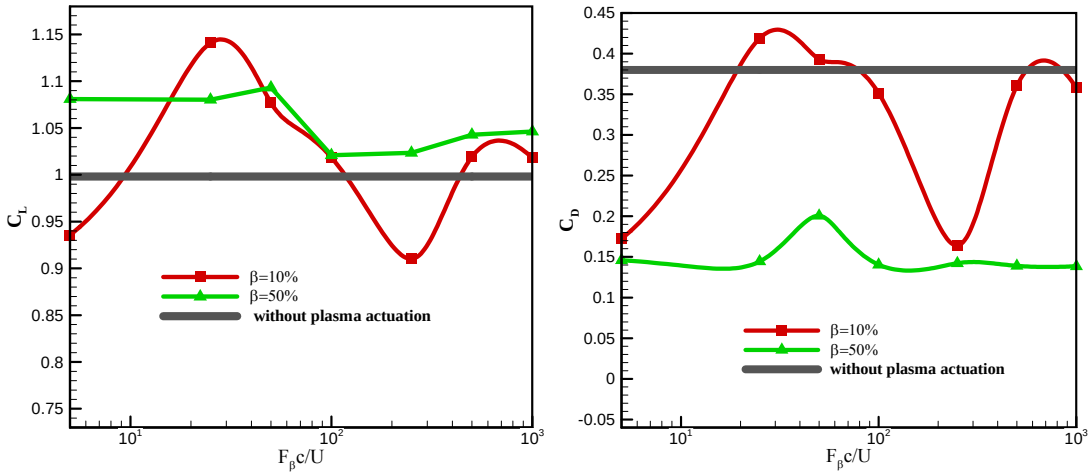

Fig. 5.11: Effect of unsteady actuation frequency and burst percentage on: a) lift coefficient; b) drag coefficient.

The predicted lift and drag coefficients for different burst frequencies and two different burst percentages, together with their variance are also summarized in Table (5.4). These data show that, for all the cases, the separation point for all the cases moves downstream when unsteady actuation is on, in comparison to the case without plasma actuation. When the burst frequency is equal to 50 Hz, the oscillation amplitude of the lift and drag (excitation-induced oscillations) is maximum for both cases with $\beta = 10\%$ and $\beta = 50\%$. This shows that instabilities in the flow were excited, and not damped, by the plasma actuation. When $\beta = 50\%$, the variance of lift and drag coefficients is seen to reduce continuously by an increase in the burst frequency and are much smaller in comparison with the case of $\beta = 10\%$. It should be clear that such an increase in burst ratio causes the plasma actuator to act closer to the steady operation mode, which is more effective in stabilization of the broad band frequencies of the flow (see Fig. (5.7)).

In Table (5.4), the rows belonging to the frequencies for which optimum or resonance behavior is observed are highlighted for emphasis. Considering the results obtained, the optimum or resonance frequency in unsteady mode of actuation could be interpreted in two ways. As shown by Patel et al [184] and Asada et al [182], there exists a frequency for which the actuation voltage controlling the flow in unsteady manner has the smallest (minimum) amplitude (optimum mode). The second viewpoint is that, disregard of the voltage there exists a frequency for which the controlling/disturbing effect of the actuator is more pronounced (resonance mode).

We should note that, although the unsteady actuation employed in the current study was not found to be more efficient that the steady actuation, a careful analysis of our results confirms the recently reported data of [185] in the sense that at a burst frequency of $F^+ = 1$, the major flow structures are exited in a resonant manner (the variance of the oscillations were maximum as well as the lift and drag increments) and for $F^+ \geq 5.75$, best aerodynamic efficiencies were obtained (similar to [182,185]). In addition, our results show that at $F_\beta = 5Hz$ the aerodynamic efficiency was enhanced. This observation might be related to the fact that this low frequency is of the order of the frequency of the shear layer here predicted and sufficient for exciting the roll up vorticities at the leading edge and thus promoting separation control.

Table 5.4: Summary of the influence of the unsteady actuation.

$\beta = 0\%$						
-	C_L	C_D	C_L / C_D	x_{sep}	Var_{cl}	Var_{cd}
	0.9981	0.38	2.626579	0.020022	0.005199	0.000524
$\beta = 10\%$						
F_β	C_L	C_D	C_L / C_D	x_{sep}	Var_{cl}	Var_{cd}
5	0.935366	0.17213	5.434061	0.082837	0.0008141	6.33E-05
25	1.140893	0.41886	2.723805	0.03826	0.005806389	0.0006336
50	1.076958	0.393098	2.739668	0.023833	0.015185	0.001784
100	1.018479	0.351313	2.899062	0.026955	0.004855	0.000209121
250	0.91012	0.164078	5.546874	0.1158	0.0001029	1.37E-06
500	1.019219	0.36028	2.828964	0.081117	6.15E-03	0.0002623
1000	1.017927	0.358106	2.842528	0.0329	0.006054	0.00026
$\beta = 50\%$						
F_β	C_L	C_D	C_L / C_D	x_{sep}	Var_{cl}	Var_{cd}
5	1.08089	0.14598	7.40437	0.171168	0.00103016	0.00012035
25	1.080187	0.1444	7.221219	0.178534	0.00188	6.58E-05
50	1.09316	0.20061	5.44918	0.14785	0.0073944	0.004399
100	1.02082	0.1404	7.270798	0.168786	1.60E-06	1.60E-06
250	1.023525	0.142204	7.197572	0.164954	5.84E-05	1.74E-06
500	1.042744	0.138942	7.504887	0.172284	7.05E-07	4.18E-08
1000	1.04623	0.138444	7.557063	0.173402	8.00E-07	2.40E-08
$\beta = 100\%$						
-	C_L	C_D	C_L / C_D	x_{sep}	Var_{cl}	Var_{cd}
	1.16795	0.118068	9.892181	0.23079	-	-

To further clarify the effect of the burst frequency and burst ratio for the case of unsteady actuation, Fig. (5.12) shows the power spectra for the time variation of the cross-stream velocity (y-component) at different probe locations for an angle of attack of 20°. These cases correspond to the frequencies $F_\beta = 50Hz$ and $250Hz$. PSD of the y-component of the velocity at points 1-3 correspond to unsteady flow in the shear layer. When the burst ratio is 50% the peaks of the flow instabilities are shifted to lower frequencies, however the PSD shows several weak oscillations in a frequency range larger than 52Hz. In the separation zone and the shedding region, the frequency bump is slightly shifted in a way that, in the separation region, the major frequency is locked at a value around 52 Hz (resonance situation). When

the frequency of the actuation is increased to 250 Hz, the magnitude of the power spectra density at those locations is reduced and the peak of the frequency map for the vortex shedding frequency is locked at the imposed excitation frequency, moreover all fluctuations with a frequency range below 250Hz are filtered (optimum case). In this case, the interaction and resonance between shear layer and wake vortex shedding results in optimum control authority.

In contrast, when the burst ratio is 10% and burst frequency is equal to $F_\beta = 50Hz$, the power spectra exhibit strong peaks at the burst frequency and its harmonics in the range 24.66 Hz to 100.76Hz, that showing that the plasma actuator is clearly contributing to the production of turbulence. This may explain the drag increase in unsteady actuation at this frequency, in comparison to the steady actuation. Essentially, the coexistence of fluid motions with different frequencies of movement in the wake, and thus the momentum and energy exchange among these structures, could result in disorganization of the flow motions and extra losses. However, the flow in the shedding region and separation bubble is more organized and regulated, since the low amplitude and high frequencies in the flow disappear in this case. When the burst frequency is increased to 250Hz, the FFT analysis shows that the motions at lower frequency in the flow field are successfully suppressed (similar behavior to the case of $\beta = 50\%$).

a)

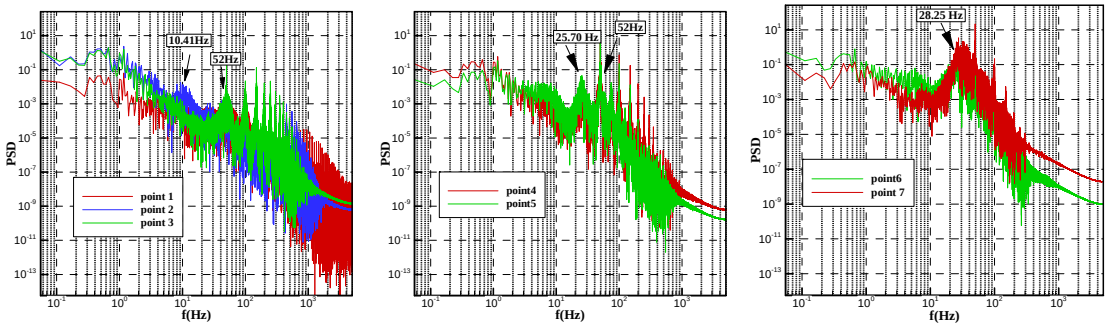

b)

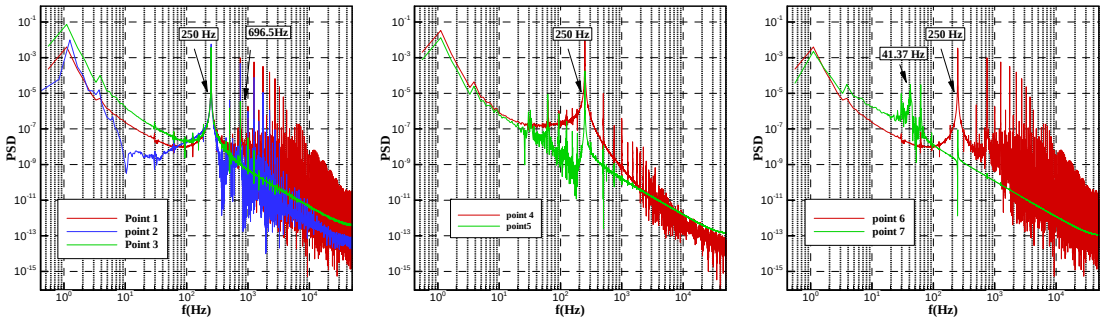

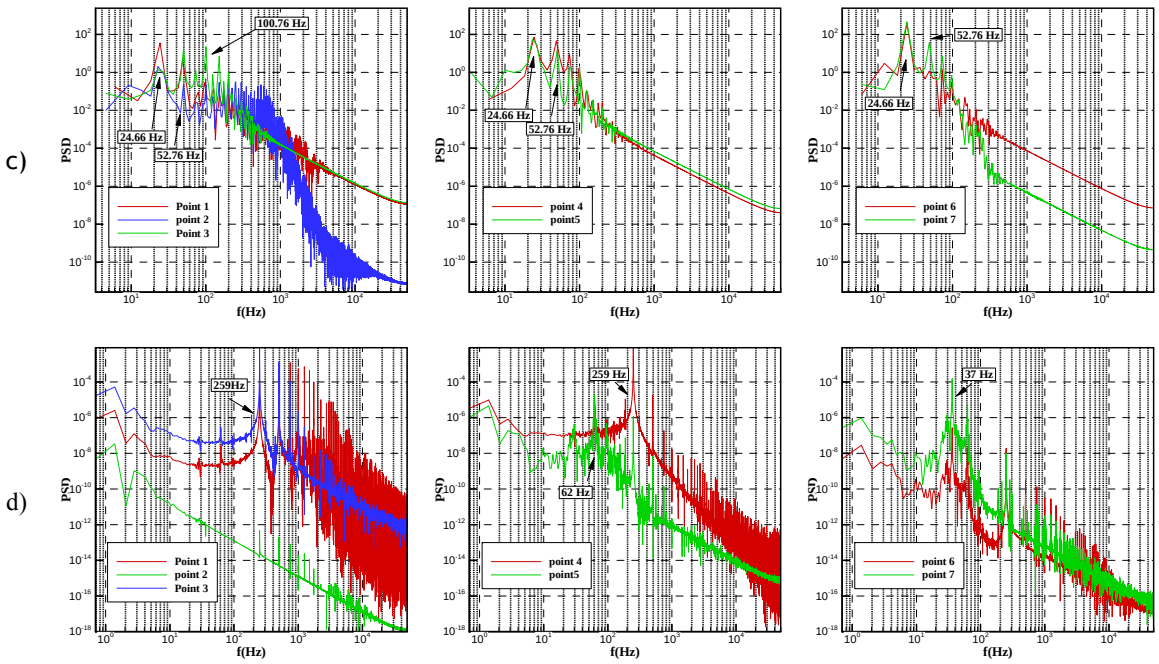

Fig. 5.12: Power spectra of y-velocity component for a) $F_\beta = 50Hz, \beta = 50\%$ **b)** $F_\beta = 250Hz, \beta = 50\%$ **c)** $F_\beta = 50Hz, \beta = 10\%$ **d)** $F_\beta = 250Hz, \beta = 10\%$ **.**

We might hypothesize that the efficiency of the unsteady plasma actuation could be dependent on different parameters, including the electrical and geometrical characteristics of the DBD and also the characteristic of the regime of the flow to be controlled [198] . For example if the frequency of actuation does not match the natural frequencies of the flow, either the actuation is not in the optimum mode or the perturbation injected by the plasma actuator is destabilizing the flow in a negative way. On the other hand when the voltage amplitude is considerable and the steady actuation already controls the flow, the unsteady actuation with large forcing amplitude may induce unwanted oscillations in the flow which will reduce the efficiency of flow control. Also, efficiency of momentum injection and mixing will be reduced when the free stream velocity is large or the boundary layer is too energetic (turbulent boundary layer). Thus when the flow velocity is higher, the flow structure is less receptive to the unsteady disturbances produced by the plasma actuator and the effect of unsteady actuation would tend to decrease [199]. For example, Asgar et al [200,201] have shown that the Reynolds number could be used as a scaling parameter for considering the effectiveness of the DBD plasma actuator. Moreover, the configuration of the DBD could influence the potential of the actuator for flow control. Since steady and unsteady actuation follow different approaches for controlling the flow, the optimum configuration (e.g. DBD position) might work in one case and might fail to control the flow in other cases.

5.5 - Conclusions

A numerical study was conducted to investigate and compare the effect of steady and unsteady actuation for controlling flow at relatively high Reynolds number. A new phenomenological model was used to simulate the effect of the plasma actuator. It can be concluded that the DBD plasma actuator is an effective mean for controlling the stalled airfoil flow. The large separation region on stalled airfoil was not completely removed by the plasma actuator in the present configuration of the DBD, however the size of the time-averaged separation bubble was greatly reduced. The flow structure is sensitive to the frequency of burst modulation.

The results showed that in the case of unsteady actuation, the burst frequency and burst ratio are crucial parameters influencing the flow capability of the actuators. This actuation mode consumes less power and achieves the desirable control effect. Burst frequencies near the natural frequencies of the system were able to excite the flow structure in a resonance mode. In this case, the instabilities and the losses in the flow structure increase (resonance mode) which limits the efficiency of the actuators. However, higher frequencies of around of 250 Hz show better flow control. In this case the flow frequencies become less energetic, implying that the internal process of exchanging momentum and energy among the flow structures becomes more constrained and thus the flow losses are reduced. This observation also confirms that with proper frequencies of excitation, the flow structure can be well rearranged and the flow losses can be reduced.

The computational study presented here clearly confirmed the effect of the burst frequency and duty cycle percentage on controlling and regulating the flow structure. However, the unsteady actuation employed here showed lower efficiency in comparison to the steady actuation mode. The reason could be ascribed to several factors considering the mechanism of the flow control by plasma actuators. To further investigate the flow control mechanism, 3D simulations need to be done using more sophisticated turbulence models (e.g. LES models) to eliminate the averaging procedure of the RANS models and also to better simulate the three dimensional vortex structures.

6 - Numerical Design and Analysis of Multi-DBD Actuator Configuration for Experimental Testing of ACHEON Nozzle Model

Abstract

Two dimensional numerical simulations of plasma actuator flow control of the ACHEON nozzle are conducted to give insight on the design of an experimental setup. Three configurations of the plasma actuators with single and multi DBD actuators are used in steady mode of operation. DBD actuators in standard mode (forward forcing mode), reverse mode (backward forcing mode) and plasma synthetic jets mode were used. Three different main groups of test cases were investigated by varying the reference velocity at the inlet of the nozzle stream from 4, 5 and 6m/s. Moreover, each group includes four velocity ratios VR=1, 1.5, 2, 2.5. The locations of the flow separation points are obtained numerically for all these cases and the plasma actuators are placed slightly upstream of these points leading to a system of seven DBD plasma actuators in the forward forcing mode over the Coanda surface. The induced thrust of the plasma actuators was estimated using a phenomenological model which considers the maximum achieved voltage and frequency from the experiments. Using an excitation voltage with maximum amplitude of 12 kV pp and frequency of 20 kHz, ionic wind was formed with 2.4 m/s velocity. The effects of plasma actuator are presented through change of the thrust and velocity angle and thrust vectoring efficiency. Preliminary results of the experimental set-up correlate well with the numerical design values[5].

Keywords: Plasma actuators, Plasma synthetic jets, flow control, thrust vectoring, Acheron nozzle

6.1 - Introduction

To maximize the agility and safety of flight missions, thrust–vectoring flight control (TVFC) is applied to complement conventional aerodynamic flight control systems. The ACHEON (Aerial Coanda High Efficiency Orienting jet Nozzle) is a novel design of thrust vectoring propulsion system without moving parts. The work is supported by European Union through consortium of six institutions [202].

[5] This chapter is based on the following paper: "M. Abdollahzadeh, F. Rodrigues, J.C. Páscoa, P.J. Oliveira (2014), Numerical Design and Analysis of a Multi-DBD Actuator Configuration for the Experimental Testing of ACHEON Nozzle Model, Aerospace Science and Technology 41 (2015) 259–273"

ACHEON nozzle [171,203] makes use of two main inlet jet streams for vectoring the thrust generated by the nozzle. The idea is similar to fluidic thrust vectoring techniques, thus having similar advantages of being lightweight, simple and built on a fixed geometry, in comparison to mechanical thrust vectoring systems. However, the ACHEON nozzle, in contrast to traditional fluidic thrust vectoring system does not possess a secondary air jet and the nozzle is made up of two main primary air jets. When the velocity ratio between the primary jets is altered from unity, the exit jet of the nozzle tends to deflect toward the Coanda surface at the side of the inlet with higher velocity. However, the thrust vectoring is limited due to separation of the boundary layer over the Coanda surfaces, which are almost entirely composed by a section of cylindrical surfaces. Flow control techniques that could suppress the separation and enhance the flow streaming over the Coanda surface, while maintaining the same functionality of the nozzle would be highly beneficial.

DBD Plasma actuators [12,204] are novel means of flow control. Being fully electrical and less complex they can be easily applied in different application for controlling flow in different situations. They have also been used and studied for controlling flow separation [205], transition to turbulent flow [41], enhancement stabilization and mixing of the flow, noise control [206], turbo-machinery flows [207,208]. Several papers have reported the mechanism through which plasma actuators influence the surrounding flows. However the objectives of flow control in those works are different from those in the present research, in spite of the mechanisms of controlling the flow with plasma actuators acting through the same principles.

As was mentioned before, one of the novel mean of controlling flow, and especially suppressing the flow separation, is to use surface dielectric barrier discharge (sDBD) actuators. As shown in previous studies, this kind of actuators has proven to offer great potential for flow control in different applications. The specific application we intend to demonstrate here is related to nozzles, specifically to how increase the efficiency of thrust vectoring in nozzles. Do et al [209] used multiple DBD actuators to delay flow separation behind a bluff body in atmospheric pressure air. The bluff body was similar to Coanda surfaces of the ACHEON nozzle and was made of a flat plate connected, tangentially, to a half cylinder as a round-cornered trailing edge. The flow speed was altered in a range from 10 m/s to 25 m/s. Ginn et al [210], patented the usage of the DBD plasma actuators for manipulating the flow in jet engine nozzles. They also suggested that the dielectric barrier discharge plasma actuators could be used to direct cooling air flow near the surface of the nozzle, thus avoiding excessive heating of the nozzle, to create thrust vectoring and reduce noise associated with the exhaust flow exiting the nozzle. Benard et al [211–213] showed that the DBD plasma actuators could alter the deflection angle of the asymmetric jet by detaching the turbulent airflow. They have employed both steady and unsteady plasma actuators and concluded that unsteady actuation allows energizing the coherent structures and reduce power consumption while the forced jet properties are conserved. Their electrode arrangement allows production of counter-flow action on the initial region of the free turbulent shear layer.

Plasma actuators are also employed in burst mode with the applied voltage being duty cycled with a specified burst frequency and burst ratio. Kopiev et al [214] conducted an experimental study on the effect of high frequency DBD actuator on nozzle exit jet. They claimed that the plasma actuator effect is related with the acoustic radiation of the discharge, and showed that jet noise suppression and intensification was achievable depending on the jet excitation frequency. Kim et al [215] and Samimy et al [216] used localized arc filament plasma actuators (LAFPAs) which were powered by a pulsed radio frequency (RF) plasma generator for flow control of a high speed circular jet. Theses arc plasmas were shown to be capable of flow excitation by depositing energy at fast rate in the flow. The principles are similar to energy addition and micro-shock wave generation with nano-second pulsed DBD plasma actuators [117]. Keliman et al [217] demonstrated numerically the control ability of LAFPAs to alter the development of supersonic turbulent jets and suppress their noise. Recently, Das et al [218], showed that multiple electrode configuration of plasma actuators is effectively capable of changing the exit jet flow direction. In the continuation of these studies, we will consider here the application of DBD plasma actuators to improve the ACHEON nozzle thrust vectoring efficiency.

As a part of ongoing research in ClusterDEM lab [219], the experimental facilities were prepared for testing the ACHEON nozzle geometry with plasma actuators [220]. The schematic of the experimental setup is shown in Fig. (6.1). However, due to limitation of the achievable voltage, the controlling effect of one single actuator is restricted. The objective of the present work is to design a single or multi DBD actuator configuration capable of controlling the flow in the ACHEON nozzle. The design output should include the position of the electrodes and number of DBD pairs. The procedure considers the available experimental facility such as the maximum excitation voltage and frequency and the experimental inlet velocities.

Fig. 6.1: Experimental test setup for controlling flow of ACHEON nozzle with plasma actuators.

6.2 - Presentation of the acheon nozzle

The dimensions of the ACHEON nozzle model are presented in Fig. (6.2). The Coanda surfaces are sections of cylindrical surface made of 2mm thick polycarbonate sheet. The two main primary jets where created by using two electric ducted turbofans (EDTs) at the inlets with diameter of 70mm.

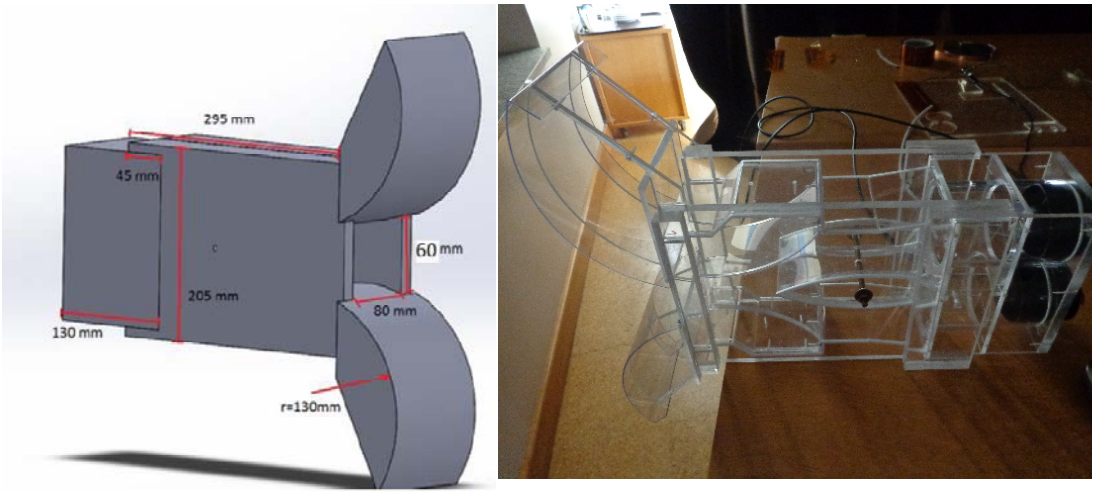

Fig. 6.2: Dimensions of the ACHEON nozzle.

Previous studies have shown that the control authority of the DBD actuators is dependent on their position in particular for the case of suppressing separation; the best functionality will be achieved when the actuator is placed slightly before the separation point [23]. Thus, to correctly define the position of the DBD actuators, the velocities at the inlet of each stream are required for the computation of the flow field and the locations of flow separation on the Coanda surfaces. According to the available experimental facility, three different test cases were selected, see section 6.4.

6.3 - Governing equations and numerical procedure

CFD simulations of the flow field without the DBD actuator were done initially to obtain the necessary data for designing the experimental setup. For simplicity, a 2D computational domain was considered by ignoring three dimensional effects and the numerical grid used for the simulation is presented in Fig. (6.3).

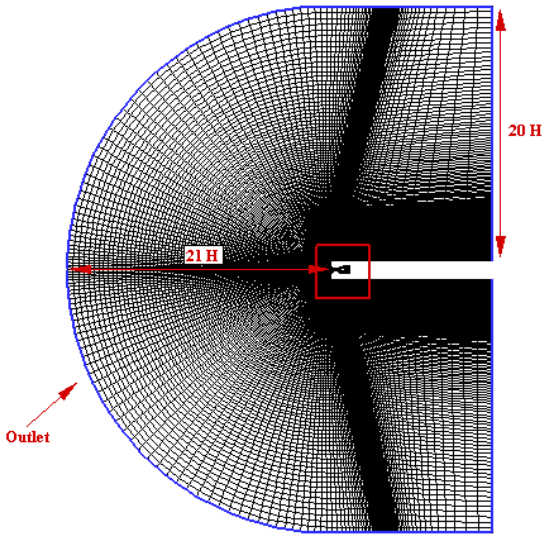

Fig. 6.3: 2D computational mesh (328000 grid cells).

The initial simulations were performed with the Commercial CFD solver FLUENT by discretizing the governing equation with finite volume method (FVM) using a cell centered collocated arrangement of primitive variables. For this purpose, the steady two dimensional (2D) incompressible Reynolds-Averaged Navier-Stokes (RANS) equations were solved with a coupled solver. The second order upwind scheme was used to discretize the convective terms, and the k-omega SST model was employed for modeling turbulence. Moreover, the interaction of the plasma actuator is implemented as an explicit source term in the momentum equation. A simple phenomenological model developed by Abdollahzadeh et al [191] was used for modeling the plasma actuators effect. This model is based on correct scaling of the plasma generated thrust for computing the body force and provides the distribution of the body force vector field. The governing equations of flow and the plasma model (electric potential and charge density) are as follows:

$$\nabla.(\vec{v}) = 0, \tag{6.1}$$

$$\rho\frac{\partial\vec{v}}{\partial t} + \rho\nabla.(\vec{v}\vec{v}) = -\nabla p + \nabla.(\tau) + \vec{F}_0 \tag{6.2}$$

$$\tau = \mu\nabla^2\vec{v}$$

$$\nabla \bullet \left(\varepsilon\nabla\phi^*\right) = 0, \tag{6.3}$$

$$\nabla \bullet \left(\varepsilon_r\nabla{\rho_c}^*\right) = \frac{{\rho_c}^*}{\lambda_D^2}, \qquad \varepsilon = \varepsilon_0\,\varepsilon_r \tag{6.4}$$

where

$$\vec{F}_0 = \rho_c\vec{E} \tag{6.5}$$

$$\rho_c^* = \frac{\rho_c}{\rho_{c,\max} f(t)}, \quad \phi^* = \frac{\phi}{\phi_{\max} f(t)}, \quad \vec{E}^* = \nabla\phi^* = l_p\left(\frac{\partial\phi^*}{\partial x}\vec{i} + \frac{\partial\phi^*}{\partial y}\vec{j}\right), \tag{6.6}$$

$$\rho_{c,\max} = 2\,fC_{eq}\frac{(V_{app} - V_{bd})}{f_{corr}\lambda_d}, \qquad f_{corr} = \frac{1}{2}\sqrt{2\pi}\frac{\sigma}{l_p}\left[\mathbf{erf}\left(\frac{1}{2}\frac{\mu\sqrt{2}}{\sigma}\right) + \mathbf{erf}\left(\frac{1}{2}\frac{\sqrt{2}(l_p - \mu)}{\sigma}\right)\right] \tag{6.7}$$

$$\vec{E} = E_0\vec{E}^* \qquad E_0 = \frac{(V_{app} - V_{bd})}{l_p} \tag{6.8}$$

In the above equations $f(t)$ is a function representing the shape of the applied voltage and $\vec{E}^*$ is the normalized electric potential. Once the dimensionless distribution is determined, the dimensional values at any given time can be obtained by multiplying this distribution with the corresponding normalization factor. In this manner, there is no need to solve the plasma model in an unsteady manner. The corresponding normalized boundary conditions of the plasma model are presented in Fig. (6.4) for the DBD actuator geometry.

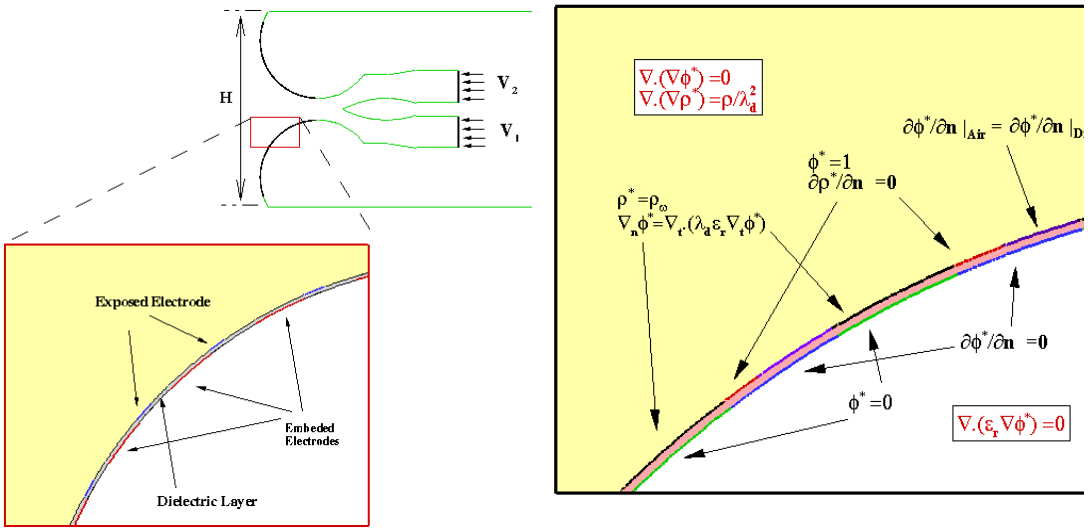

Fig. 6.4: Normalized Boundary condition of the plasma model applied to compute the DBD induced force.

The plasma model was then coded as an UDF (User Defined Function) and was used alongside for the simulation purpose. We note that the grid spacing should not be larger than the Debye length and condition y+<1 where $y^+ = \frac{u^* y}{\nu}$ must be satisfied for correctly resolving the development of the turbulent boundary layer. For enforcing these conditions and reaching grid independency of the results at reasonable numerical cost, the numerical grid was refined toward the electrodes and surface of dielectric layer. Moreover, the grid was refined in the regions where higher values of electric field and charge density exist. Thus, the grid spacing

was stretched toward the electrode both in the normal direction and in the stream wise direction, thus leading to minimum cell size of about 2 μm.

At the inlet of the nozzles, the velocity magnitude and direction are prescribed along side with turbulent intensity and turbulent viscosity ratio. At the walls, the no-slip boundary conditions are used. The boundary representing the outlet is considered to be far enough from the exit of the nozzle (As shown in Fig. (6.3)). Pressure outlet boundary condition was used at this boundary by assigning the value of the static pressure and turbulent intensity (0.1 %) and viscosity ratio. It is true that at the inlet there should be high levels of turbulence. As this is the case, because of high level of turbulence at the inlet, the transition is bypass type, and most of the turbulence models do not capture it accurately. However, the purpose of this investigation is only to analyze the coanda flow separation. Therefore, we had assigned really low turbulent intensity values to avoid bypass transition. Although this is not the probably a true case of experiments, we want to make sure that bypass transition is not observed prior to flow separation. Thus the flow will be laminar before separation and turbulent after separation. Due to the high level of turbulence in the experiments, the separation on Moreover, the k-omega SST model used here is one of the best for near wall and separational flows. Study of the influence of turbulent intensity on flow deflection is the subject of our future work.

6.4 - Description of the experimental set-up

In the experiments, two turbofans HET EDF 6904 were used to produce the two inlet flows to the nozzle. The turbofans contain brushless motors Typhoon EDF 4W and were controlled with electronic speed controllers 80A-Eco-6S ESC and pulse generators PWM Hobbyking LED Servo Tester. The DBD plasma actuators were feed by PVM 500, that is a high voltage frequency power supply, and the voltage waveform was produced by PWM 500 and measured with digital oscilloscope software designated by PicoScope. Together with the PicoScope, was used an accessory designated by Secondary Ignition Pickup allowed us measure the voltage and the frequency of the signal. A laser sheet and a digital camera CCD C10600-10B Orca-R2 was used to visualize the flow field. The laser used was a 1 L2S-SL-660-130-S-A-60 SteamLine Laser System and it can work in a continuous mode or in a pulse mode. It was feed with 5V and 250mA by a power supply ITT Instruments AX 322 Metrix. Solid particles were seeded uniformly using a cyclone particle generator at the turbofans intakes. The cyclone particle generator contains an inlet where compressed air is introduced and an outlet to exit the mix of air and solid particles. Talcum powder was used to mark the flow once the talcum particles can follow the flow without change its properties and present a good reflection of the incident light. Before starting the experiments a compressor with 110 L reservoir was used to compress and store the air at a pressure of about 8 bar and the talcum powder was deposited in the base of the solid particle generator. The digital camera CCD C10600-10B Orca-R2 was positioned perpendicularly to the laser sheet and connected to the computer. The

configurations of the capture and the reception of the images were done using the software HCImage Live. The schematic of the experimental set-up is shown in Fig. (6.1).

To make a PIV analysis and to acquire a pair of images with a very small time interval between them, the PIV mode of the camera was used which allows the capture of two consecutive images taking only 2μsfrom the end of the first exposure until the beginning of the second exposure. This operation mode of the camera requires the control by an external TTL signal and to produce it, asignal generator was used. Then a square signal with 5V of amplitude and about 6kHz was created with the signal generator. At an input trigger signal edge (rising or falling edge), the camera startsthe acquisition of one image pair. As the frequency of the external signal is very high, the camera capturesconsecutive acquisitions of image pairs until reachingthe number of images defined by the user. Before starting the acquisition of image pairs, one calibration image was captured in order to define the relation between the pixels of the image and the metric scale. After the acquisition of the image pairs the software PIVLab was used to make the PIV analysis and obtain the velocities of the flow. The final result of the PIV measurement was obtained by the average values of 10 PIV measurements. These ten PIV measurements were performed for ten consecutive image pairs. The exposure time of each image was 100μsbut the time between each image pair was 60ms. The images of the flow visualization were captured with 60ms of exposure. To measure the deflection angle a reference point was defined for all the images. The reference point was located at 67 pixels from the left side of the image and 519 pixels from the top of the image. Lines were drawn from the top of the flow until the bottom of the flow and the middle point of these lines was calculated. These lines were drawn at a distance of 400, 700 and 1000 pixels from the left side of the image and the angle was measured between the reference point and each of the middle points of the lines. The position of the DBD actuator sets used in the experiments is shown in Fig. (6.5). The width of the covered electrode is 2cm and the width of the exposed electrode is 1cm. In Table2, we give some of the basic information about the DBDs available in the experiments. The dielectric material was made from a 2mm polycarbonate layer and electrodes were made from 0.1μm copper tape. An AC-sinusoidal voltage with 12kVpp and 20kHz was used as an excitation voltage.

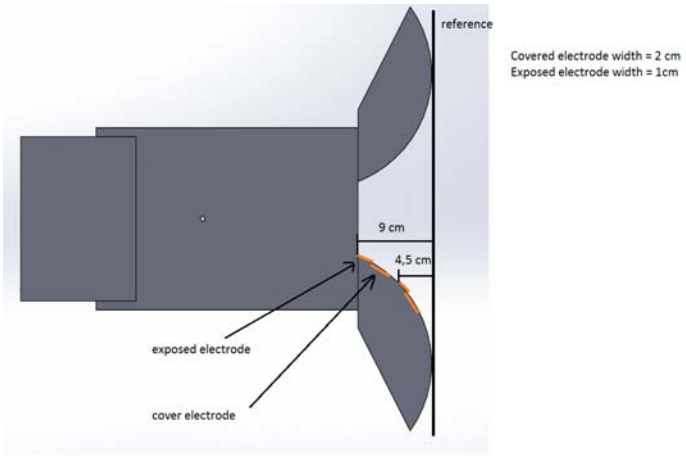

Fig. 6.5: Schematic of the configuration of the DBDs in experiments.

6.5 - Results and discussion

The ACHEON nozzle was tested with simulations based on values for the velocity magnitude at the inlet of the nozzles given in Table (6.1). When the velocity ratio is equal to unity, the jet out of the nozzle and the induced thrust are horizontal. This is considered the base case for comparing the capabilities of the plasma actuators for thrust vectoring. When, the velocity ratio is increased, the jet at the exit starts to deflect towards the coanda surface at the inlet side with higher velocity magnitude. For each case, we are interested on the following results: the location of separation point; maximum velocity at the nozzle ($V_{\max}$), the thrust (T), the angle of thrust generated at the nozzle (α_T); and angle of the exit jet stream of the nozzle (α_V). Table (6.1), gives the data calculated by the numerical simulation. For comparing the vectoring capability, two parameters are considered, the induced thrust angle and the exit jet angle. It is possible to define efficiency parameters based on these angles and the mass flow rate at the inlet of nozzles ($\dot{m}_1$, $\dot{m}_2$) as follows;

$$\eta_T = \frac{\alpha_T}{\left(\frac{\dot{m}_1}{\dot{m}_1 + \dot{m}_2}\right)} \tag{6.9}$$

Essentially, to insure a secure flight mission, a safety angle (maximum desirable design angle) for the thrust vectoring purpose could be defined. Here, arbitrarily, we assume that the thrust safety angle should be equal to 45 degree. This angle depends in a complex way on the flight speed, thrust magnitude and weight and size of the system. Considering this value we can reformulate Eq. (6.9) as follows:

$$\xi_T = \frac{2\alpha_T}{45(V_R + 1)} \tag{6.10}$$

$$\eta_T = 1 - 2\frac{|\alpha_T - 45|}{45}\frac{1}{(V_R + 1)} \tag{6.11}$$

The detailed numerical results obtained by the simulations are presented in Table (6.1). It is clear that when the velocity ratio between nozzle inlets increases the deflection angle of the jet is increased also. However, the thrust angle increment is not at the same rate as the angle of the exit jet. It should be reminded that this improvement in vectoring capability is obtained by spending more power in comparison to the case of V_R=1.0. The position of separation point was also calculated for different cases and presented in Table (6.1). These results show that flow separation over the Coanda surface is postponed when the velocity ratio increased. This enhanced tendency of the flow to follow the surface curvature could be ascribed to enhanced injection of momentum from outside the boundary layer to zones with lower velocity magnitude, because of the difference of pressure drop between the two inlet jet stream sections.

Table 6.1: Input and Output data for the nozzle flows without plasma actuators.

V_R	$V_1(m/s)$	$V_2(m/s)$	$T(N)$	$V_{\max}(m/s)$	α_V (degree)	α_T (degree)	*Ysep*
Test 1							
1	4	4	4.14	12.19	0	0.00	-0.0284
1.5	4	6	7.63	17.23	21.01	26.21	-0.0411
2	4	8	12.80	21.68	30.22	33.52	-0.0520
2.5	4	10	19.80	25.86	38.41	37.51	-0.0640
	Test 2						
1	5	5	6.26	15.23	0	0.00	-0.0289
1.5	5	7. 5	12.02	21.54	22.68	27.97	-0.0434
2	5	10	21.09	27.08	34.43	35.46	-0.0581
2.5	5	12.5	37.92	32.34	52.87	38.75	-0.0884
	Test 3						
1	6	6	8.77	18.27	0	0.01	-0.0290
1.5	6	9	17.79	25.85	25.11	30.21	-0.0466
2	6	12	31.95	32.44	37.86	36.83	-0.0643
2.5	6	15	58.13	39.01	63.98	38.67	-0.1006

In Fig. (6.6), the velocity contours of the ACHEON nozzle are shown for various velocity ratios for the first test case. These figures illustrate how, with increase in velocity ratio, higher deflections of the exit jet angle are achieved. Moreover, by comparing the results for the three main test cases indicated in Table (6.1) (low, medium and high velocity range), it is possible to conclude that when the inlet velocity magnitude is increased, the deflection angle of thrust and velocity become larger, but the thrust angle reaches its maximum possible value (imposed by design and geometrical limitations) sooner.

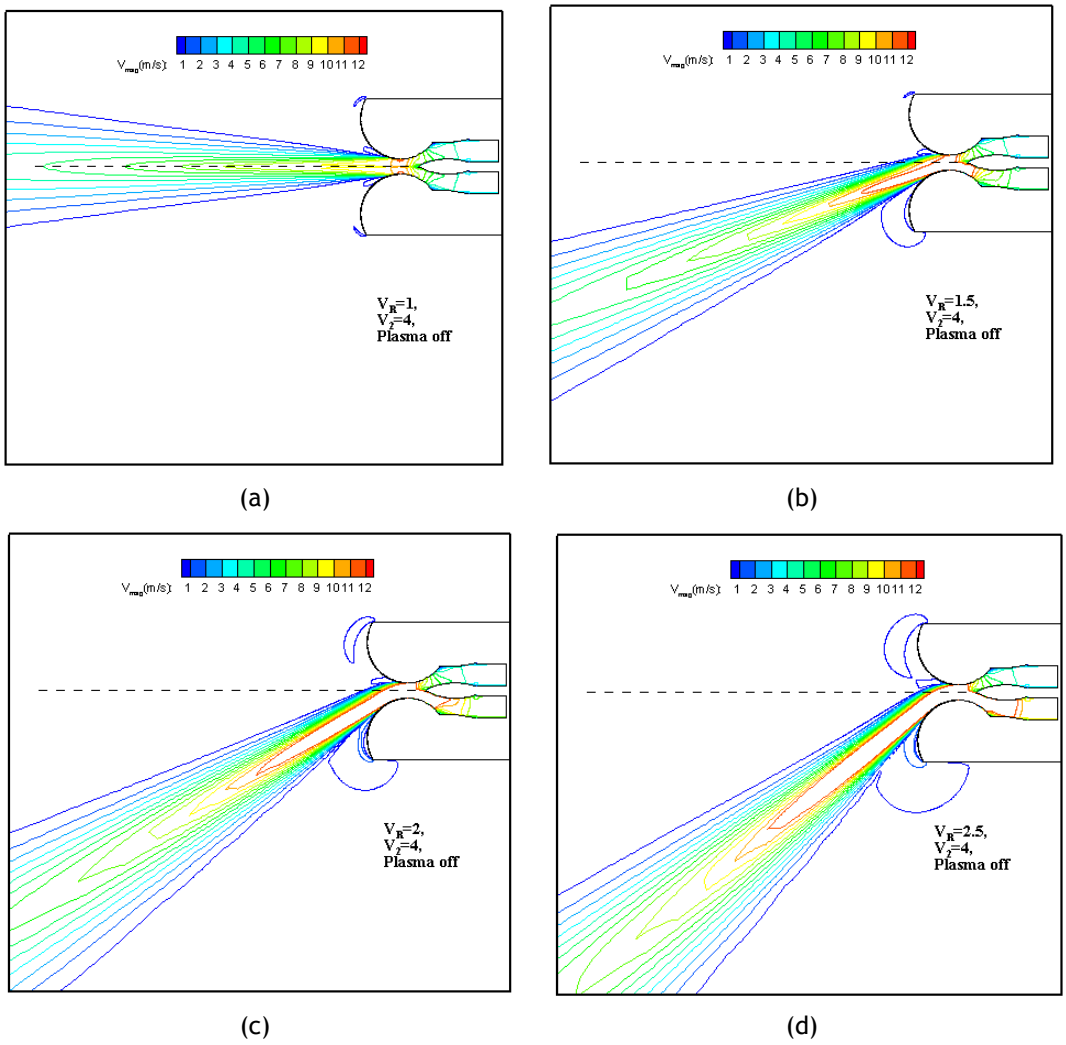

Fig. 6.6: Velocity contour at the exit of the nozzle at a) V_R=1.0 b) V_R=1.5 c) V_R=2.0 d) V_R=2.5. (all cases with V_2=4 m/s).

In Fig. (6.7), the velocity angle at the exit of nozzle, the thrust angle and the performance ratios (Eqs. (6.9) and (6.10)) are plotted for different velocity ratios. The results clearly point out the existence of a limiting thrust angle for the considered dimensions of the ACHEON nozzle. As can be seen, the plot of thrust angle versus velocity ratio meets a plateau at a maxim angle of around 39 degrees. It may also be observed that, when the nozzle exit velocity magnitude is increased (going from Test1 to Test3), the limiting thrust angle occurs at lower velocity ratios. However, the velocity angle is seen to increase almost constantly over the velocity ratios here tested. We see that this does not always imply increase in the thrust vectoring capability.

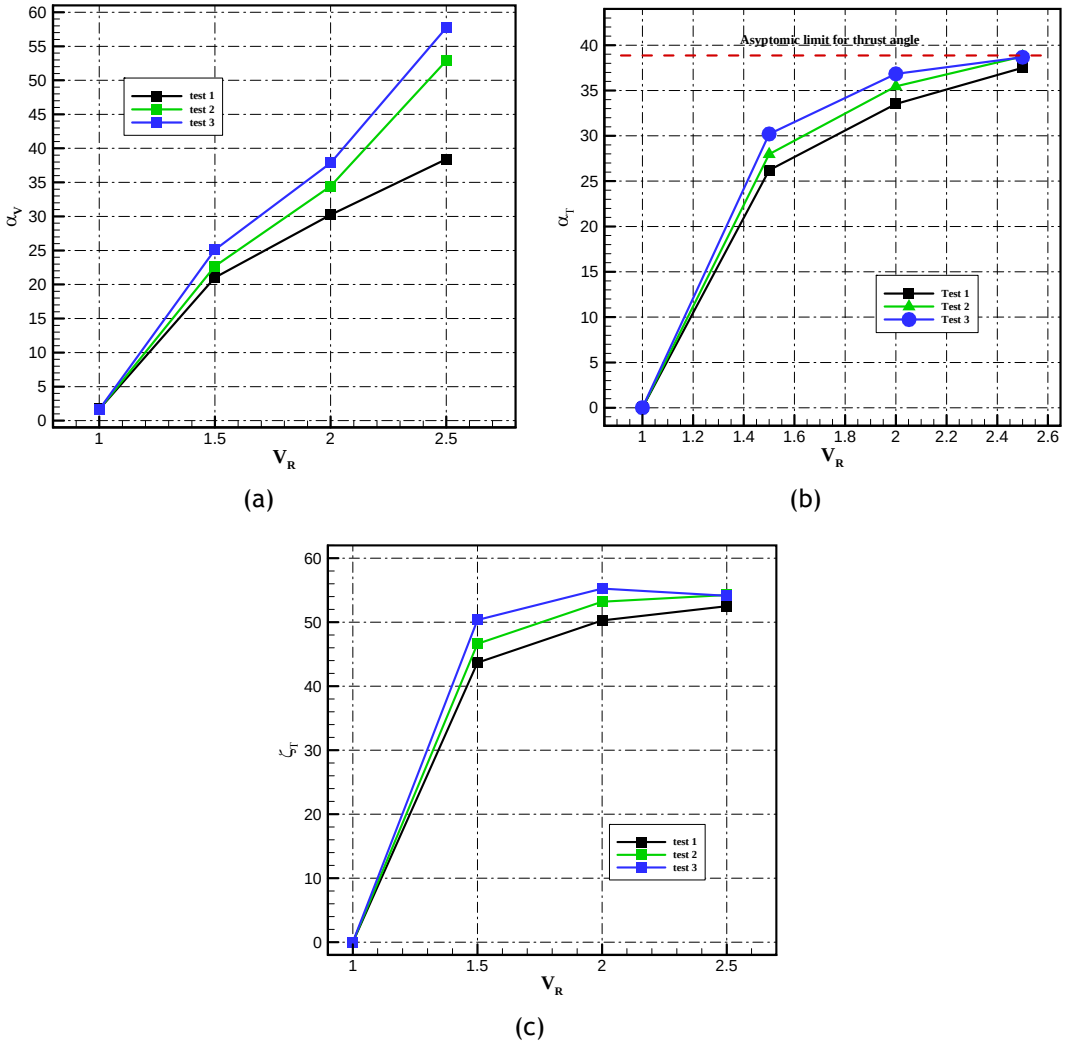

Fig. 6.7: Results of the simulations without plasma actuators for increasing velocity ratios of V_R=1,1.5,2,2.5 a) Angle of the jet deflection b) angle of the thrust vector; c) thrust vectoring performance number .

The experimental facility of our lab provides us with a specified range of operating conditions that need to be considered for the design of the DBD system. Table (6.2), presents the power source characteristic, the thickness of the available electrode, thickness of the dielectric material and permittivity of the dielectric material.

For the problem under consideration here, the previous CFD results showed that when the velocity ratio of the nozzle is increased, the separation point varies. Thus to design a flow control system based on DBDs able to act almost universally over the whole duration of flight mission (velocity ranges and velocity ratios), a multi-DBD actuator system should be adopted taking into consideration the location of the various flow separation points. That is, for global functionality, a DBD actuator is positioned at each major separation point, and distance between the separation points is covered by the length of the each DBD actuator system. Since each actuator can operate separately, there should be enough space between the

electrodes of each for preventing arc and short-circuit formation. Therefore we consider seven sets of actuator with 15mm length embedded electrode and 6mm exposed electrodes.

Table 6.2: Operating conditions.

t_e	$0.1\mu m$
t_d	2 mm
ε_d	3.1 Poly Carbonate
V_{app}	6 kV
f	20 kHz
T	293.15 K

Previous results have shown that the influence of the DBDs on each other is additive and our CFD results [221] have shown that, the Multi-DBD system will causes ionic wind with higher intensity. To confirm this and to better understand how a multi-DBD actuator is more effective than a single DBD actuator, Fig. (6.8) shows simulation results for the ionic wind of a single DBD set and for multiple DBD set (four actuators). The maximum ionic wind induced by the multiple DBD is clearly greater than with the single DBD case and the plasma wall jet is seen to cover a much larger controlling surface area.

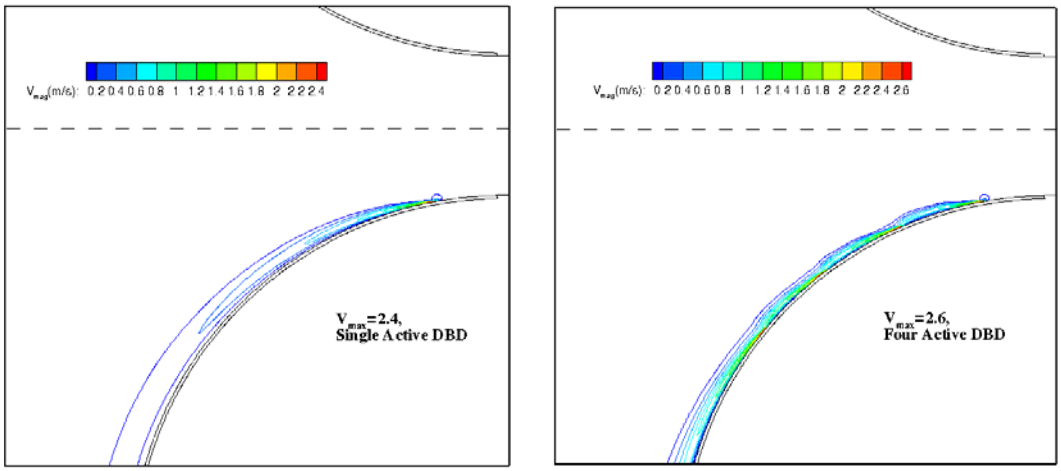

(a) (b)

Fig. 6.8: Induced ionic wind: a) single DBD actuator; b) multiple DBD actuators.

For the purpose of comparing the effect of actuator location and number of active DBDs, a series of numerical tests have been carried out. To limit the number of cases to be studied, we have considered one active DBD (seven test cases indicated from E1, the DBD at the beginning of the Coanda surface to E7, with DBD at the end of the trailing edge of the Coanda surface), two active DBDs in row (six test cases, E12 to E67, with numbers showing the location of the DBDs), and three active DBDs in row (five test cases, E1-3 to E5-7) and also

four cases with four to seven DBDs active (E1-4, E1-5, E1-6, E1-7) and we also only considered the velocities equal to the condition of Test1. Fig. (6.9) shows the comparison between these cases for different value of velocity ratios. The dependency of the actuation efficiency is clearly obvious from this figure. When the actuation zone is slightly located before the separation point, the plasma actuators have effective performance on controlling the flow. Actuator E6 and E7 which are installed at the end part of the Coanda surface, alone don't put effect on the flow characteristics. Thus in the case of single active actuator, depending on the velocity ratio, one of the actuators among E2 to E5 will be turned on. It is possible to increase the tolerance of controlling algorithms by using two sets of side by side active actuators. In this case, at each velocity ratio (except V_R=1), there are two possible selection for the active actuator set. Moreover in this case, we observe that, the velocity deflection angle is improved in all velocity ratios (for V_R=1.5 it wasn't significant). When three side by side DBDs are active, the controlling effect is improved. The number of possible configurations which can be used for flow actuation also increases. In Fig (6.9d), more than four DBD set are active. Difference between E1-6 and E1-7 is almost negligible and when V_R=1 and 1.5 all the cases are showing almost the same efficiency. However, when velocity ratio is increased, especially at V_R=2.5), cases that cover greater part of the Coanda surface has larger performance. However, when the numbers of electrodes are increased the total power consumption will increase.

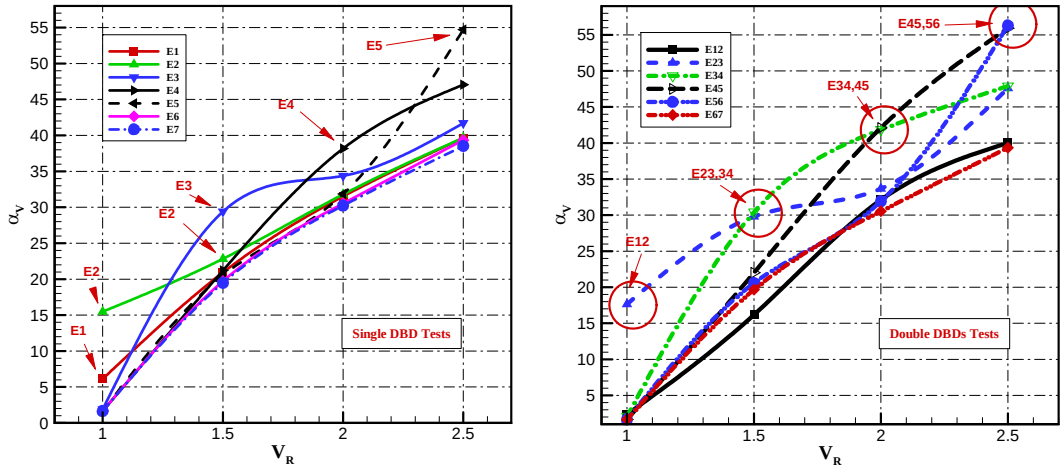

(a) (b)

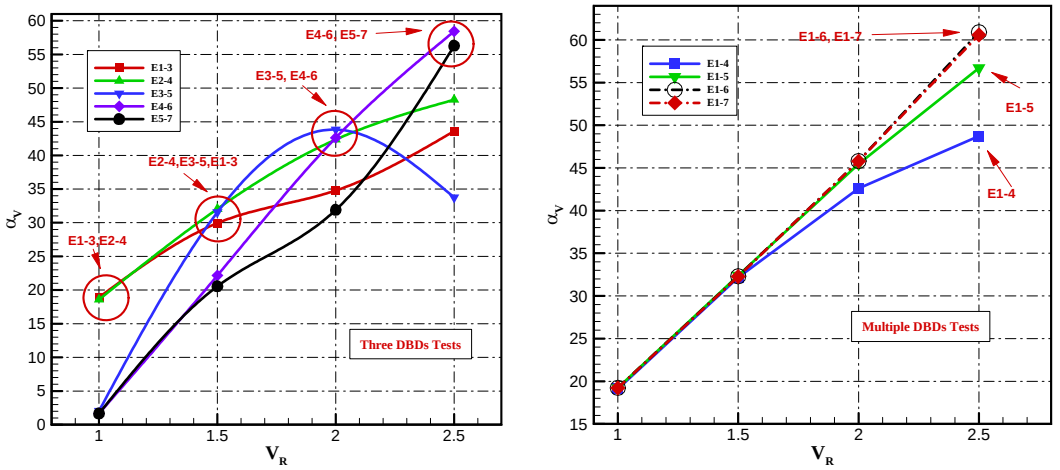

(c) (d)

Fig. 6.9: Effect of DBD plasma actuator on exit jet angle from the nozzle: a) single DBD actuator; b) two DBD actuator; c) three DBD actuators; d) multiple DBD actuators.

It is interesting to mention that, it was possible to alter the velocity angle by minimum 10 degree by altering the active DBD location. In Fig. (6.10), velocity contours corresponding to the selected cases at V_R=2.0 and with single and double DBDs are shown. When single DBD is used, by using an actuator at E5 the velocity angle just changes around 31.85 degree. Changing the position of the DBD to E3 and E4 causes the thrust angle to increase respectively to 34.3 and 38.1 degree. This is quite interesting, since if one covers the control surface with suitable number of actuators, and using a suitable control algorithm, it will be possible to alter the flow angle arbitrarily with less power consumption.

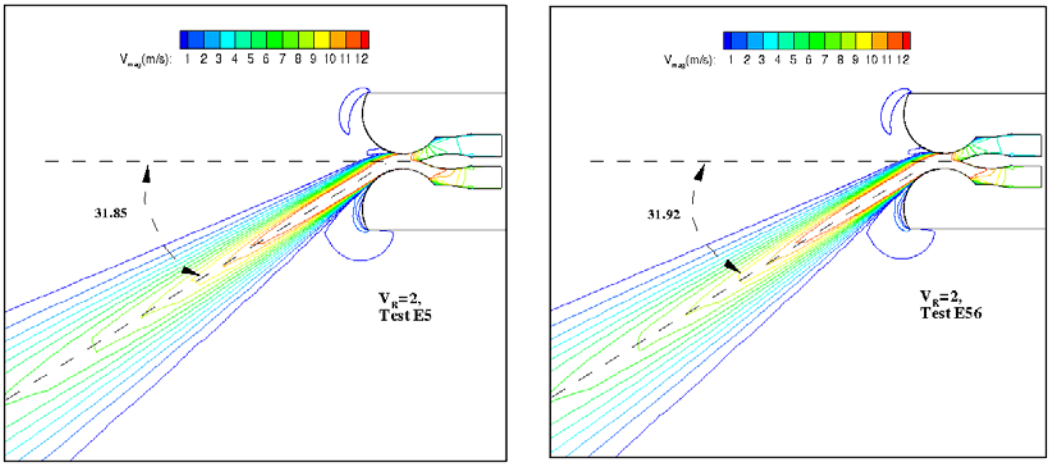

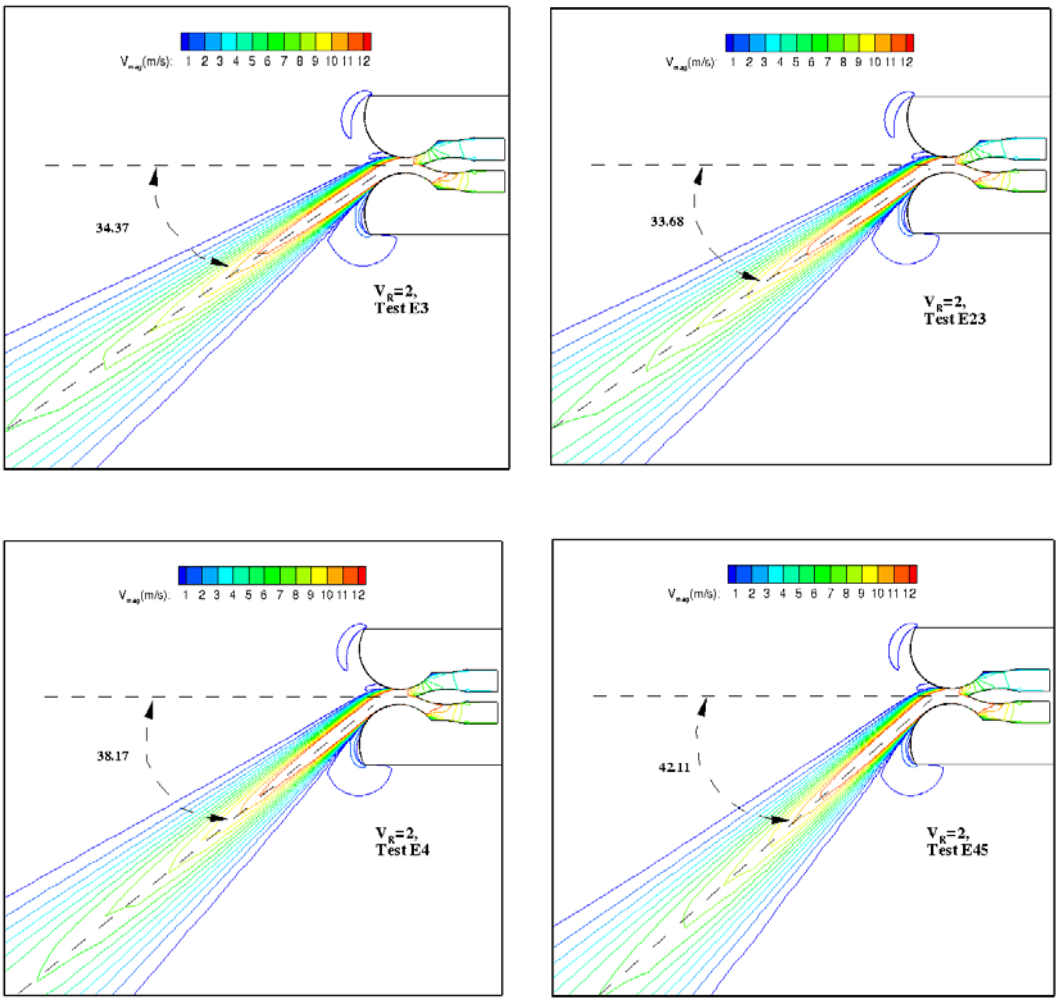

a) b)

Fig. 6.10: Effect of DBD plasma actuator on direction of the exit jet of the ACHEON nozzle a) single DBD b) double DBD.

In Fig. (6.11), the thrust vectoring performance number and efficiency for different configuration of DBD plasma actuators, and nozzle velocity ratios, are shown. η_T and ζ_T are showing the point for optimum thrust vectoring on different velocity ratios . However, both are showing that maximum thrust vectoring is happening at medium velocity ratios. This result could be justified in thes way that, at higher velocity ratios, boundary layer already had attached to the Coanda surface to the maximum extent (look at asymptotic value of thrust), thus further increasing the velocity ratio or using plasma actuators would not add more efficiency to the system but it will use more power.

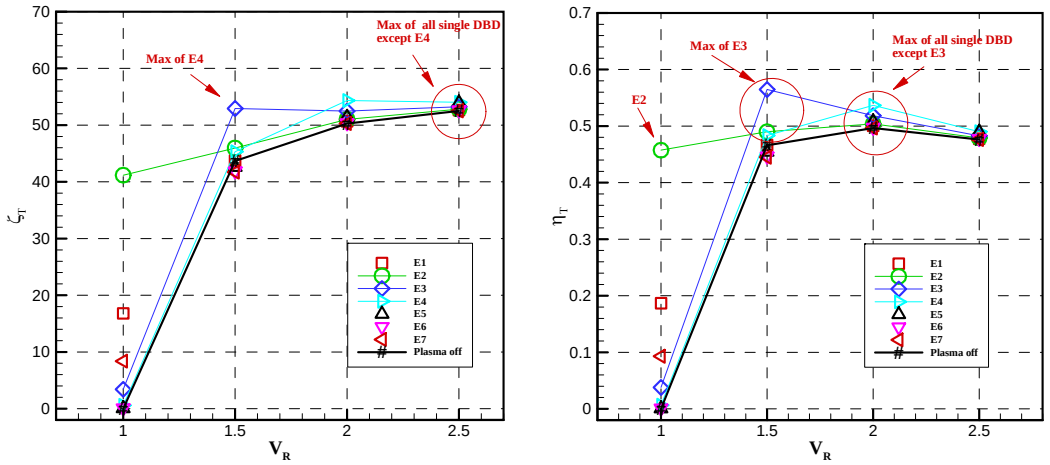

Fig. 6.11: Effect of DBD plasma actuator on a) thrust vectoring efficiency b) thrust vectoring performance number.

In Tables (6.3) and (6.4), the flow and thrust deflection angle are tabulated for all the cases with plasma actuators. As can be seen if the plasma actuator is placed at optimum location, the increment in the velocity vectorizing is large as 16.5 degree for single actuator and 23.39 degree for multiple DBDs. We should mention that this increment will reduce when the velocity magnitude at the inlet of the nozzle is increased. However, by analysis of the data of thrust angle, we will see that the influence of DBD system on thrust vectorizing is just pronounced at low velocity ratios and even in the presence of single or multiple DBD actuators the thrust angle won't increase more than its asymptotic value shown in Fig. 6.6b. Moreover, we should mention that, the increment in thrust angle at those cases that DBD is installed at exit section of the Coanda surface is not related to increase in Coanda effect for suppression of separation over the surface. It is only related to the surface jet created by the plasma actuator (here with 2.4 m/s speed).

Table 6.3: Influence of single and Double DBD plasma actuators on thrust and velocity angle.

	V_R	$(\alpha_T - \alpha_{0T})$	$(\alpha_V - \alpha_{0V})$		$(\alpha_T - \alpha_{0T})$	$(\alpha_V - \alpha_{0V})$
E01	**1**	8.40	6.12	E12	21.16	17.4
	1.5	0.04	-0.08		1.95	8.49
	2	0.26	1.30		0.68	3.28
	2.5	0.10	1.21		0.04	4.59
E02	**1**	20.59	15.48	E23	22.77	17.64
	1.5	1.36	1.82		5.80	8.79
	2	0.49	1.58		1.57	3.46
	2.5	0.22	1.25		0.68	9.19
E03	**1**	1.71	0.24	E34	2.01	0.43
	1.5	5.55	8.39		6.17	9.41
	2	1.45	4.15		3.32	11.63

	2.5	0.51	3.29		1.11	9.49
E04	**1**	0.30	0	E45	0.09	0.00
	1.5	0.98	0.19		0.62	1.00
	2	2.70	7.95		3.36	11.89
	2.5	1.08	8.64		0.96	17.51
E05	**1**	0.02	0	E56	0.15	0.00
	1.5	-0.66	-0.48		-0.63	-0.44
	2	0.74	1.63		0.52	1.70
	2.5	1.02	16.30		0.90	17.89
E06	**1**	0.05	0	E67	0.11	0.00
	1.5	-1.08	-1.29		-1.12	-1.34
	2	0.06	0.31		0.05	0.32
	2.5	0.12	0.93		0.12	0.93
E07	**1**	4.19	0.00			
	1.5	-1.18	-1.54			
	2	-0.01	0.01			
	2.5	0.00	0.11			

Table 6.4: Influence of three DBD plasma actuators on thrust and velocity angle.

	V_R	$(\alpha_T - \alpha_{0T})$	$(\alpha_V - \alpha_{0V})$		$(\alpha_T - \alpha_{0T})$	$(\alpha_V - \alpha_{0V})$
E123	**1**	23.69	18.92	E1-4	23.90	19.10
	1.5	6.01	8.93		6.76	5.95
	2	1.66	4.57		3.47	9.08
	2.5	0.80	5.19		1.12	11.22
E234	**1**	23.17	18.59	E1-5	23.97	19.21
	1.5	6.54	11.04		6.88	6.17
	2	3.42	12.14		3.76	11.95
	2.5	1.13	9.86		0.85	19.20
E345	**1**	1.81	2.04	E1-6	23.92	19.23
	1.5	6.36	10.55		6.84	6.10
	2	3.64	13.61		3.78	12.28
	2.5	0.93	-4.67		0.35	23.39
E456	**1**	0.05	0.00	E1-7	23.87	19.21
	1.5	0.64	1.15		6.83	6.07
	2	3.46	12.39		3.77	12.27
	2.5	0.75	20.01		0.29	23.07
E567	**1**	0.20	0.00			
	1.5	-0.68	-0.46			
	2	0.51	1.68			
	2.5	0.91	17.87			

Besides the standard configuration of the actuator that was shown with single and multiple DBDs, plasma actuators can be used in several different configurations [8,10,162,214,222]. Here, using 2D modeling we only consider two of these configurations. In the first case, a plasma actuator is added in the top Coanda surface in a reverse mode to promote separation of the jet stream earlier. In the second case, a linear plasma synthetic jet actuator [223] (two plasma actuators, one act in forward mode and other acting reverse mode) are placed over the top surface to induce a jet normal to the surface. In Fig. (6.12) the induced ionic winds of the plasma actuator for the mentioned configurations in quiescent air are presented.

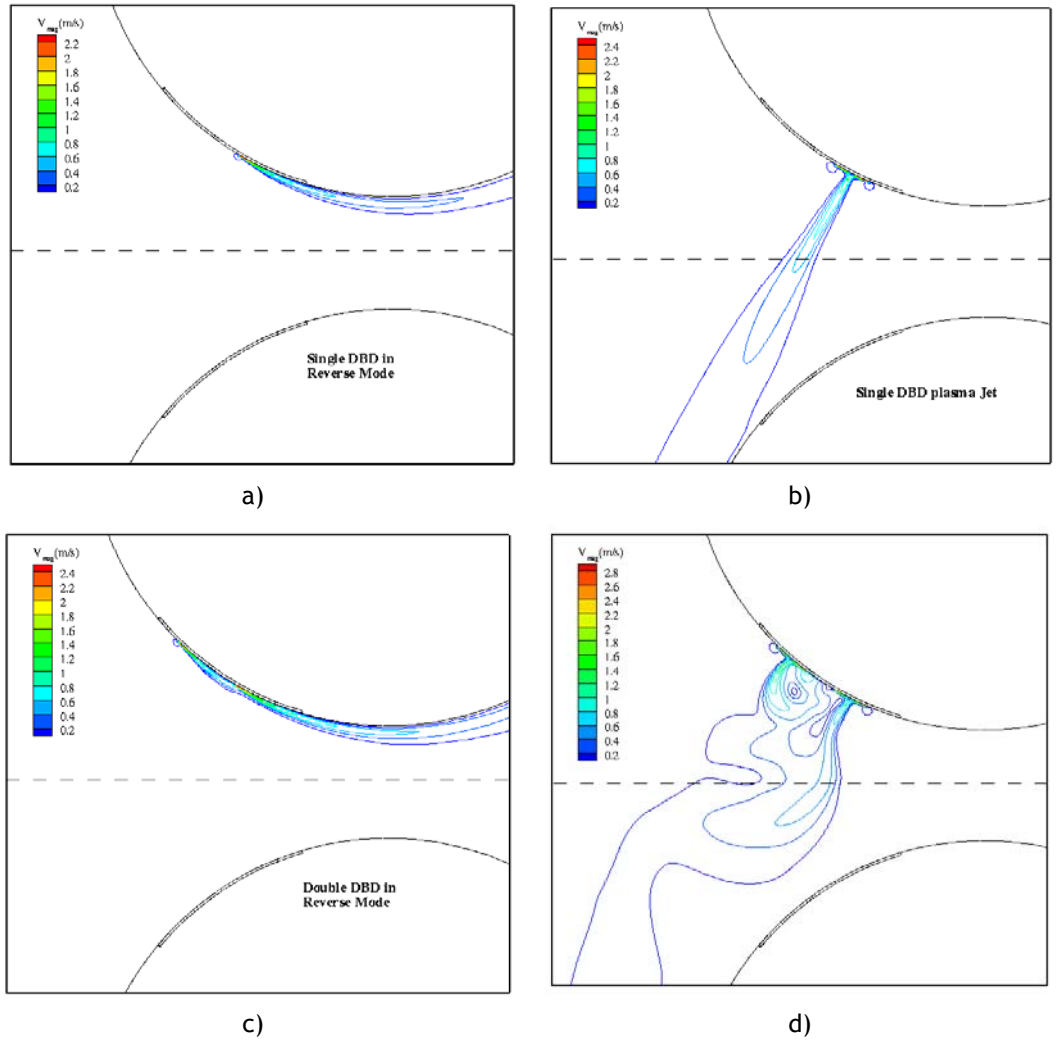

Fig. 6.12: velocity contour of the induced ionic wind of a) single reverse actuator b) single DBD plasma jet c) multiple reverse DBD actuators d) multiple DBD plasma jets, installed on the top coanda surface.

The velocity contours corresponding to the cases with single and multiple (two) DBD actuators in reverse mode and single and double DBD plasma jets are shown in Fig (6.13). These results are for the velocity ratio equal to unity with the inlet velocity of 4m/s. When the actuator is used in reverse mode on the top Coanda surface, the separation is promoted and exit jet of

the nozzle is deflected downward. Using multiple DBD actuators also increases the deflection of the jet. Interestingly, when DBD plasma jets are used, the flow tends to be directed upwards.

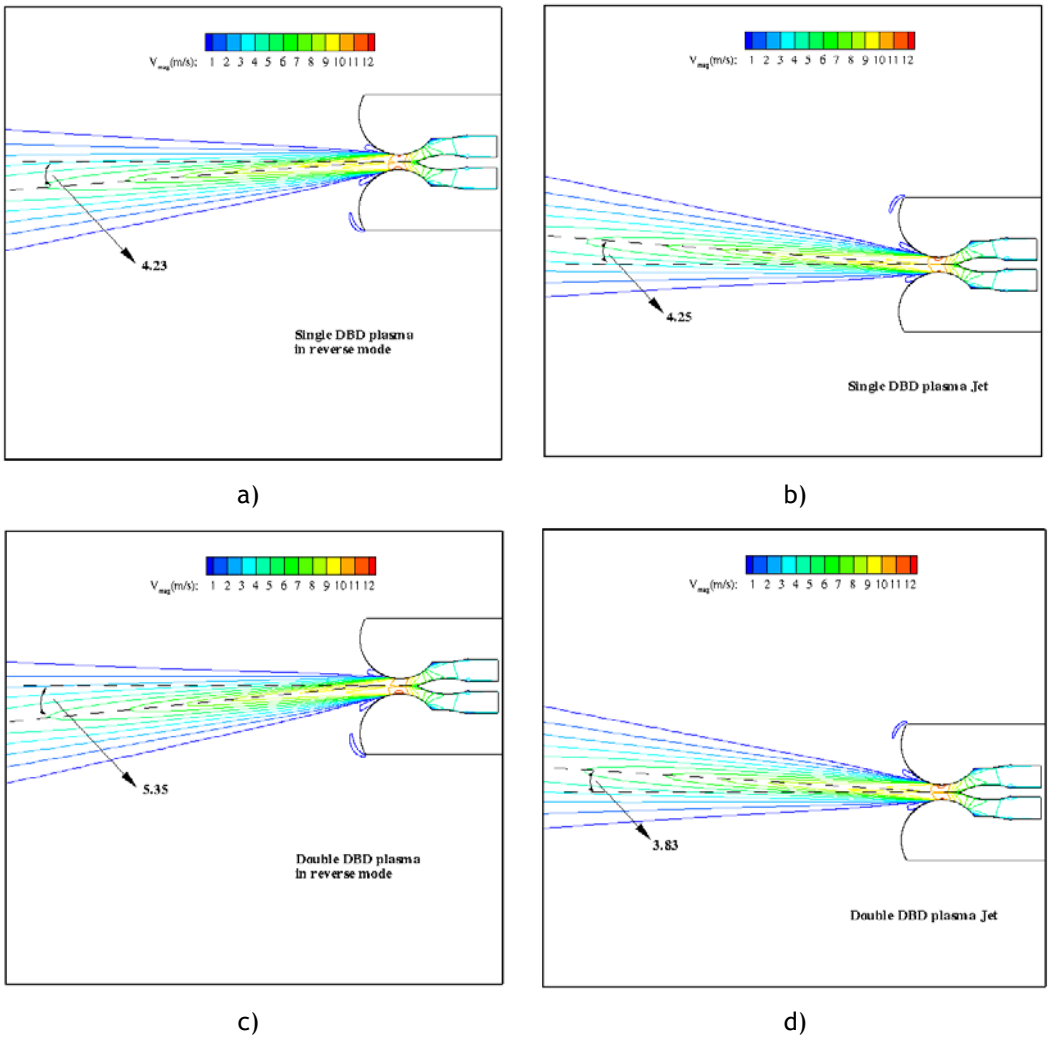

a) b)

c) d)

Fig. 6.13: velocity contour at the exit of the ACHEON nozzle with a) single reverse actuator b) single DBD plasma jet c) multiple reverse DBD actuators d) multiple DBD plasma jets, installed on the top coanda surface.

To verify the accuracy and validity of the numerical simulation, basic PIV measurements of the exit jet of the nozzle were used for measuring the average velocities, as shown in Fig. (6.14) for validating the baseline flow. The PIV measurements were conducted for V_R=1 and V_2≈2m/s. The average velocities in five velocity profiles are tabulated and are compared with numerical simulation in Table (6.5). The small differences between the numerical and experimental results are related to the fact that the numerical results are a 2D approximation of the 3D experiments. Moreover, the imposed boundary conditions in the numerical simulations V_1 and V_2 are pure axial velocities. However swirl velocity induced by the two fans reduces the velocity vector exit angle. In the 3D experiments the flow, after exiting the

nozzle starts to spread towards the lateral areas, thus the velocity level in that regime should be lower than the computed by 2D numerical simulation.

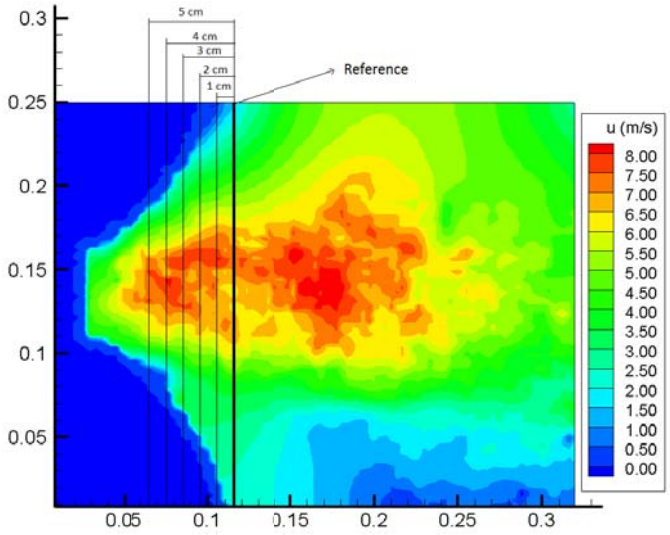

Fig. 6.14 PIV results of exit jet of the nozzle without DBD.

We should note that PIV computes instantaneous velocity fields and a large number of PIV results are needed to achieve an asymptotic averaged solution, for the velocity field obtained experimentally to be comparable with averaged results of CFD computation. We should note that due to difficulty in the experiments and high levels of unsteadiness, obtaining a perfectly averaged solution was difficult.

Table 6.5. Comparison of the Average velocity magnitudes between the experimental and numerical results for the case without DBD at V_R=1 and $V_2 \approx 2m/s$.

Velocity Profile	Average Velocity from experiments (m/s)	Average velocity from numerical computations with V_2=2
Profile 1 (1 cm from the reference)	4.084	3.437
Profile 2 (2 cm from the reference)	4.175	3.869
Profile 3 (3 cm from the reference)	4.201	4.304
Profile 4 (4 cm from the reference)	4.251	4.733
Profile 5 (5 cm from the reference)	4.639	5.160

From the preliminary result of the experimental tests, the jet deflection angle was calculated by analyzing more than 20 images for the cases with the actuators off and on, in order to decrease the error of the measurement. The jet angle is calculated by defining the potential core center of the jet. This center is defined as the mean distance between the upper and

lower shear layers. In Fig. (6.15), for the purpose of conciseness, only three consecutive snapshots of the air jet are plotted for both the uncontrolled case and the controlled case. The uncertainty of a final result obtained by the mean of a series of measurements is given by the standard deviation of the mean ($\sigma_{\bar{x}}$). The standard deviation of the mean can be calculated by:

$$\sigma_{\bar{x}} = \left(\frac{1}{N(N-1)} \sum_{i=1}^{N} (x_i - \bar{x})^2 \right)^{1/2} \tag{6.12}$$

where x_i is the result of ith measurement, $\bar{x}$ is the mean of the measurements and N is the number of measurements. Using the standard deviation of the mean, in the case with actuators off, the average angle is 0.687±0.056◦ and the relative error is 9.18%. In the case with actuators on, the average angle is 4.86 ±0.23◦ and the relative error is 4.93%. This is only an error in the sense of obtaining averaged solution and not specifically an error of the measurement of flow field. The experimental results also confirm that when DBD actuators are active the flow is deflected.

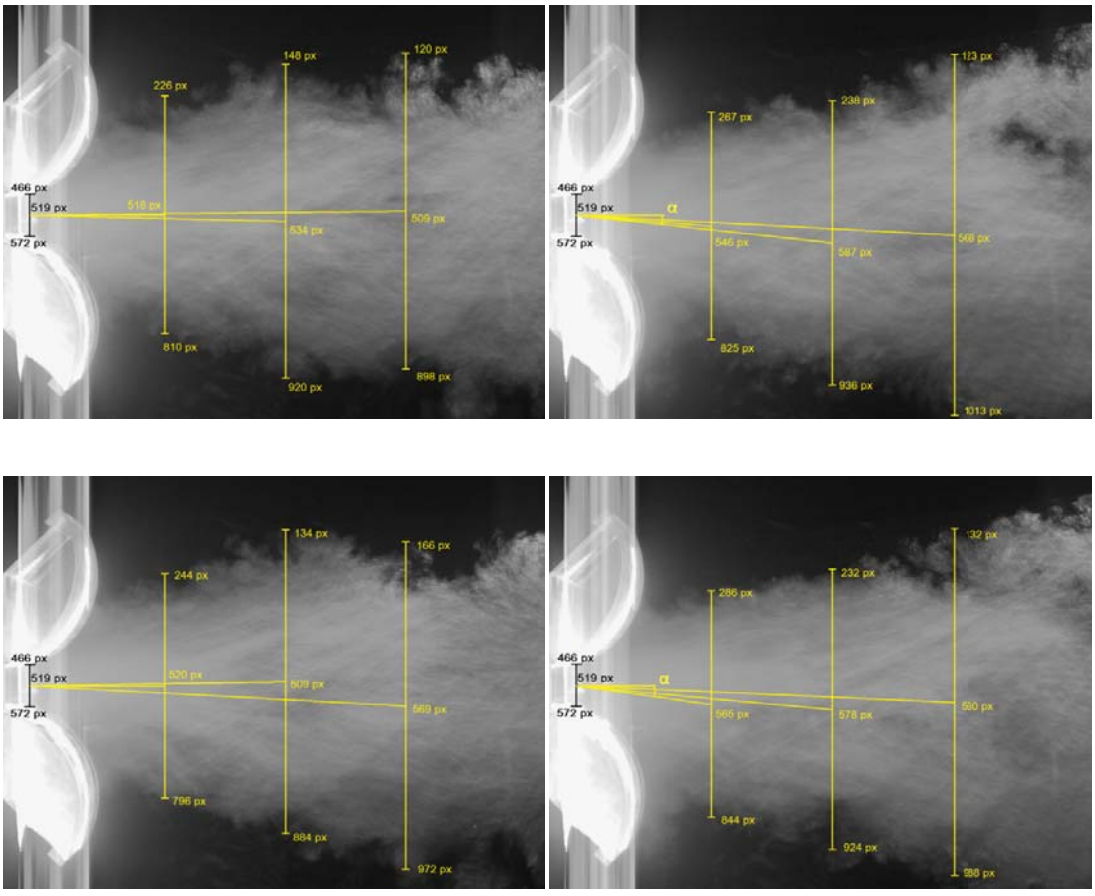

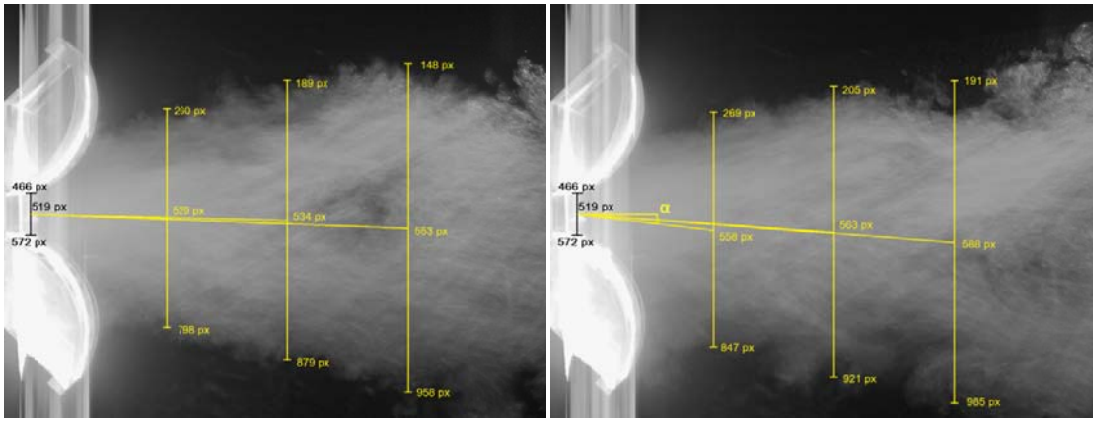

(a) (b)

Fig. 6.15: Exit jet velocity angle at V_R=0.0 a) DBD plasma off b) DBD plasma on.

Experimentally measured velocity angles for both cases, without plasma actuation and with plasma actuation with V_R=1 corresponding to Fig. (6.15) are tabulated in Table (6.6). The results are actually an averaging procedure to obtain the steady average angle since the real flow is unsteady. Experimental results predict a lower value for the angle of deflection. As was mentioned before, these discrepancies between the computed and experimental results are ascribed to 3D effects existing in the experiment, pure axial velocities as imposed boundary conditions in numerical experiments. Thus, it is to expect a high degree of deflection obtained by the numerical computation in comparison with the experimental and it was correctly expected that 2D exit model is "guiding" more directly the flow as compared to the 3D experiments. However, we should mention that although the experimental results are preliminary, the objective of the paper is not a direct numerical-experimental quantitative comparison. Instead the objective is to show through a qualitative comparison that numerical results could be used to confirm the possibility of using DBDs for thrust vectorizing and better designing the experimental tests.

Table 6.6. Comparison of numerical results with experimentally measured exit jet velocity angle.

		Mean Angle	**Average angle of deflection**	**Numerical Result**
Withut Plasma Actuators	First Snapshot	$\alpha_V = -0.17^\circ$	$\alpha_V = 0.90^\circ$	$\alpha_V = 0.0^\circ$
		$\alpha_V = 1.36^\circ$		
		$\alpha_V = -0.61^\circ$		
	second Snapshot	$\alpha_V = 0.17^\circ$		
		$\alpha_V = -0.91^\circ$		
		$\alpha_V = 3.07^\circ$		

	third Snapshot	$\alpha_V = 1.72^\circ$		
		$\alpha_V = 1.36^\circ$		
		$\alpha_V = 2.09^\circ$		
With Plasma Actuators	First Snapshot	$\alpha_V = 4.64^\circ$	$\alpha_V = 4.93^\circ$	$\alpha_V = 6.12^\circ$
		$\alpha_V = 6.13^\circ$		
		$\alpha_V = 3.01^\circ$		
	First Snapshot	$\alpha_V = 7.86^\circ$		
		$\alpha_V = 5.32^\circ$		
		$\alpha_V = 2.52^\circ$		
	First Snapshot	$\alpha_V = 6.68^\circ$		
		$\alpha_V = 3.98^\circ$		
		$\alpha_V = 4.23^\circ$		

6.6 - Conclusions

Plasma actuators were used for controlling the flow over the Coanda surface of the ACHEON nozzle. When the plasma actuator is used, it was possible to postpone separation of the flow and increase the deflection angle of the exit jet of the nozzle. To find the optimum position of the actuators, seven DBD actuators in forward forcing mode were placed over the Coanda surface considering the numerically obtained separation points. Different combinations of the multiple DBD actuators were also used. Results show that when the actuator is placed slightly before the separation point, enhanced thrust vectorizing with the use of DBD actuator is achievable. Moreover, both single and multiple DBD actuators were used in reverse operating mode and also single and multiple DBD plasma jets were used for increasing the thrust vectoring characteristic of the nozzle. Results have shown that utilization of DBD plasma actuators in reverse mode will promote the separation on the surface, thus will force the exit jet of the nozzle to deflect toward the other Coanda surface. Although, reverse DBD plasma actuators and DBD plasma jets were not tested for all the range of velocity ratios, we could expect that using a combination of these actuators and normal operational mode of DBD actuators will provide flexibility for controlling the flow direction. Preliminary results of the experiments were compared with the results of numerical simulation. We should note that it is difficult to fully compare the present 3D experimental results with result of 2D numerical simulation, since firstly, the numerical results are 2D approximations of the 3D experimental configuration and in the 3D experiments the flow, after exiting the nozzle starts to spread towards the lateral areas. Moreover, the imposed boundary conditions in numerical cases are

pure axial velocities that differ from the ones of the experiments. However, the present experimental and numerical results are consistent in the sense of demonstrating the capabilities of the CFD to help to system design by avoiding a large number of experiments. Detailed experimental study of the effect of plasma actuators on thrust vectoring efficiency of ACHEON nozzle will be presented in future work.

7 - Summary and conclusions

Numerical modeling of the DBD plasma actuator is investigated using both fluid models and phenomenological models. The fluid models provide comprehension of the discharge properties. However, they are more complex and are not feasible to be used for modeling large scale cases such as a propulsion component. In contrast, phenomenological models are based on more simplistic assumptions but in reverse their usage requires less computational costs. Thus, the two approaches are complementary and together they could provide tools to the understanding of the discharge physics and mimic the macroscopic effect of the plasma actuator.

As was stated before, one of the main drawbacks of the DBD plasma actuator is their relatively low intensity of induced ionic wind and the ability to control with higher speed range. To explore this issue, DBD plasma actuator were employed considering different modes of actuation. When the excited voltage is nano-second pulse, the effect of the plasma actuator is translated into instantaneous heating of the gas and thus the creation of micro-shock waves. In contrast, using the AC sinusoidal voltage waveform, the effect of the plasma actuator is pronounced mostly as a body force. This body force can also be created by imposing a duty cycle on the applied voltage, leading to lower power consumption and larger influence on the flow field.

Following the objectives and the motivation of the thesis, we have analyzed the implementation of classical plasma-model in OpenFOAM. The problem involves several numerical issues regarding the numerical stability, restriction on the time step and grid size. Therefore, we have studied the most well known procedures for solving the governing equations of the plasma fluid and the ways to increase the performance of the solver. In the end, we have used the novel technique for treatment of the time advanced using a combination of the Strang splitting and super-time-stepping. Afterwards, we had used the developed solver for modeling the interaction of transonic flow and DBD plasma actuators. To this aim, the rate of heat generation by plasma actuator was correctly considered and added to the model. Since the direct application of the model to solve the plasma dynamic and gas dynamic together increased the computational cost, we have devised two different approaches to overcome this problem. In the first approach, we have used the fact that the time of the discharge development and energy transfer to the flow are different which allowed us to proceed the solution in multi-stage manner. In the first stage, the plasma dynamic and the gas dynamic equation were solved together, and the problem was advanced in time with the time-step needed for the plasma solver. In the second stage, only the gas dynamic problem was considered. In the other approach, the plasma dynamic was solved only for one pulse duration, and the heating source term was saved to be used and activated after a estimated relaxation time. Using both approaches allowed us to save computational time.

Later, we have developed a new simple phenomenological model, which is not dependent on calibration of the model for different cases. The model, in principles is based on using a simple circuit model to define the correct scaling of the parameters of the body force produced by split potential model. We have validated the model with different experimental results regarding the value of the induced thrust and induced velocity profile. Interestingly, the accuracy of the model appeared to be better than most of the other existing models. We have further developed our model to be able to consider the influence of the altitude variation on the DBD plasma actuator. This was done simply by including the effect of pressure and temperature in the model. Our results showed that this new model could also correctly model the influence of sub and super atmospheric conditions.

We have used our newly developed phenomenological model to study steady and unsteady mode of actuation, and analyze the possibility of obtaining better actuation results in unsteady mode at a frequency near the natural frequency of the flow. We have considered a stalled flow around an airfoil at a relatively high Reynolds number. The simulation results confirmed the possibility of controlling stall over the airfoil using the plasma actuator with both steady and unsteady mode of actuation. In addition, the simulation results were supported by frequency analysis of the flow at different probe location for providing information about the effect of the plasma actuator on flow instabilities. We have shown that there are frequencies that cause the flow to respond to actuation in a resonance or optimum mode.

In the end, we have employed plasma actuators to control the flow at the exit of a nozzle. The objective of the flow control was to enhance the thrust vectoring capability of the nozzle. Therefore, we have considered several cases including single and multiple actuator sets. These DBDs were placed in two exit Coanda surfaces of the nozzle and were tested for several velocity ratios. The results verified our preliminary experimental tests and showed that by using DBD actuators, we can reach higher values of thrust vectoring efficiency.

Considering our mentioned studies, we explicitly highlight our findings and conclusions as follows;

- Implementation of the Plasma Fluid model in OpenFOAM.
- Increasing the performance of the numerical simulation considering a new approach by using super-time-stepping and multi stage plasma solution.
- Development of new simple phenomenological model which is more accurate and needs less calibration.
- Including the effect of changes of the altitude in the phenomenological model.
- Showing the existence of optimum or resonance frequencies of the actuation to reach higher flow control efficiency.
- Showing the possibility of the use of the developed numerical tools to correctly model real scale geometry such as nozzle.

- Showing the possibility of the application of plasma actuators for controlling flow to enhance thrust vectorizing

In the end we should mention that there are still cases that need further and deeper investigation. The implemented plasma fluid model could be improved by including asynchronized time-stepping to further decrease the computational cost. The present implementation of the plasma fluid was done using a segregated algorithm. However, a fully coupled solution of the governing equation could provide better accuracy and more stability and thus implementation of such algorithm will be worthless. In addition, more components could be added easily to the developed code, including the photonization effects, radiation losses, more complex chemistry and so on. Regarding the phenomenological, in the future the influence of the gas composition should be added to the model. Also adding a more sophisticated circtut model would be essential for further develoment of the versatility of the model and improving the consistency between simulations and experimental measurements.

8 - References

[1] L.N. Cattafesta, M. Sheplak, Actuators for Active Flow Control, Annu. Rev. Fluid Mech. 43 (2011) 247–272. doi:10.1146/annurev-fluid-122109-160634.

[2] L. Wang, Z. Luo, Z. Xia, B. Liu, X. Deng, Review of actuators for high speed active flow control, Sci. China Technol. Sci. 55 (2012) 2225–2240. doi:10.1007/s11431-012-4861-2.

[3] D.P. Breden, Simulations of Atmospheric Pressure Plasma Discharges, PhD Thesis, The University of Texas at Austin, 2013.

[4] M. L. Post, Plasma actuators for sepration control on staintionary and osciliatary airfoils, PhD Thesis, University of Notre Dame, 2004.

[5] A.A. El-deib, Modeling of and Driver Design for a Dielectric Barrier Discharge Lamp, PhD Thesis,University of Toronto, 2010.

[6] C. Wang, S. Roy, Numerical Simulation of a Gas Turbine Combustor Using Nanosecond Pulsed Actuators, in: AIAA 2013-0894, 2013: pp. 1–17.

[7] M. Riherd, S. Roy, Serpentine geometry plasma actuators for flow control, J. Appl. Phys. 114 (2013) 083303. doi:10.1063/1.4818622.

[8] R.J. Durscher, S. Roy, Three-dimensional flow measurements induced from serpentine plasma actuators in quiescent air, J. Phys. D. Appl. Phys. 45 (2012) 035202. doi:10.1088/0022-3727/45/3/035202.

[9] C. Wang, S. Roy, C. Plasma, T. Facility, Physics Based Analysis of Horseshoe Plasma Actuator for Improving Film Cooling Effectiveness, (2010) 1–12.

[10] C. Wang, R. Durscher, S. Roy, Three-dimensional effects of curved plasma actuators in quiescent air, J. Appl. Phys. 109 (2011) 083305. doi:10.1063/1.3580332.

[11] J. Hong, Atmospheric pressure plasma chemical depostion by using dielectric discharge system, MSc Thesis, University of Illinois at Urbana-Champaign, 2013.

[12] E. Moreau, Airflow control by non-thermal plasma actuators, J. Phys. D. Appl. Phys. 40 (2007) 605–636. doi:10.1088/0022-3727/40/3/S01.

[13] T.C. Corke, C.L. Enloe, S.P. Wilkinson, Dielectric Barrier Discharge Plasma Actuators for Flow Control, Annu. Rev. Fluid Mech. 45 (2010) 505–529. doi:10.1146/annurev-fluid-121108-145550.

[14] J.-J. Wang, K.-S. Choi, L.-H. Feng, T.N. Jukes, R.D. Whalley, Recent developments in DBD plasma flow control, Prog. Aerosp. Sci. 62 (2013) 52–78. doi:10.1016/j.paerosci.2013.05.003.

[15] M. Gad-El-Hak, Flow Control: Passive, Active, and Reactive Flow Management, Cambridge University Press, New York, 2000.

[16] T.C. Corke, M.L. Post, D.M. Orlov, SDBD plasma enhanced aerodynamics: concepts, optimization and applications, Prog. Aerosp. Sci. 43 (2007) 193–217. doi:10.1016/j.paerosci.2007.06.001.

[17] D. Caruana, Plasmas for aerodynamic control, Plasma Phys. Control. Fusion. 52 (2010) 124045. doi:10.1088/0741-3335/52/12/124045.

[18] G. Touchard, Plasma actuators for aeronautics applications - State of art review-, Int. J. Plasma Environ. Sci. Technol. 2 (2008) 1–25.

[19] J.R. Roth, Aerodynamic flow acceleration using paraelectric and peristaltic electrohydrodynamic effects of a One Atmosphere Uniform Glow Discharge Plasma, Phys. Plasmas. 10 (2003) 2117. doi:10.1063/1.1564823.

[20] J.R. Roth, D.M. Sherman, S.P. Wilkinson, BOUNDARY LAYER FLOW CONTROL WITH A ONE ATMOSPHERE UNIFORM GLOW DISCHARGE SURFACE PLASMA, in: AIAA, 1998.

[21] D. Greenblatt, T. Schneider, C.Y. Schule, Mechanism of flow separation control using plasma actuation, Phys. Fluids. 24 (2012) 077102. doi:10.1063/1.4733399.

[22] B. Jayaraman, Y. Lian, W. Shyy, Low-Reynolds Number Flow Control Using Dielectric Barrier Discharge Actuators, in: AIAA, 2007.

[23] J. Jolibois, M. Forte, É. Moreau, Application of an AC barrier discharge actuator to control airflow separation above a NACA 0015 airfoil: Optimization of the actuation location along the chord, J. Electrostat. 66 (2008) 496–503. doi:10.1016/j.elstat.2008.03.008.

[24] J.H. Mabe, F.T. Calkins, B. Wesley, R. Woszidlo, L. Taubert, I. Wygnanski, Single Dielectric Barrier Discharge Plasma Actuators for Improved Airfoil Performance, J. Aircr. 46 (2009) 847–855.

[25] J. Little, K. Takashima, M. Nishihara, I. Adamovich, M. Samimy, High Lift Airfoil Leading Edge Separation Control with, in: AIAA, 2010: pp. 1–23.

[26] G. Correale, I.B. Popov, A.E. Rakitin, A.Y. Starikovskii, S.J. Hulshof, L.L.M. Veldhuis, Flow Separation Control on Airfoil With Pulsed Nanosecond Discharge Actuator, in: AIAA, 2011.

[27] C. Rethmel, J. Little, K. Takashima, A. Sinha, I. Adamovich, M. Samimy, et al., Flow Separation Control over an Airfoil with Nanosecond Pulse Driven DBD Plasma Actuators, in: AIAA, 2011: pp. 1–17.

[28] D. VanNess, T. Corke, S. Morris, Turbine tip clearance flow control using plasma actuators, in: AIAA Pap. 2006–0021, 2006.

[29] R.R. J. D. Wall, I. C. Boxx, Effects of pulsed d.c. discharge plasma actuators in a separated low pressure turbine boundary layer, in: AIAA Pap. 2004–0842, 2004.

[30] H. D. Vo, Control of rotating stall in axial compressors using plasma actuators, in: AIAA Pap. 2006–0021, 2007.

[31] Y. WU, Y. LI, J. ZHU, C. SU, H. LIANG, G. LI, Experimental investigation of a subsonic compressor with plasma actuation treated casing, in: AIAA Pap. 2007–3849, 2007.

[32] C.A. Williamson, Compressor blade flow control in an axial compressor with plasma actuators, MSc Thesis, Oklahoma Christian University, 2008.

[33] J. Huang, T.C. Corke, F.O. Thomas, Plasma actuators for separation control of low-pressure turbine blades, AIAA J. 44 (2006) 51–57.

[34] K. Choi, T.N. Jukes, T. Segawa, H. Yoshida, Recent Developments in Turbulent Flow Contro l, in: Proc. 40th JAXA Work. “Investigation Control Boundary-Layer Transition,” 2006: pp. 11–12.

[35] S.P. Wilkinson, Investigation of an Oscillating Surface Plasma for Turbulent Drag Reduction, in: AIAA 2003-1023, 2003.

[36] T. Jukes, K. Choi, G. Johnson, S. Scott, Turbulent Drag Reduction by Surface Plasma through Spanwise Flow Oscillation, in: AIAA 2006-3693, 2006: pp. 2–3.

[37] B.A. Belson, R.E. Hanson, D. Palmeiro, P. Lavoie, C.W. Rowley, Comparison of plasma actuators in simulations and experiments for control of bypass transition, in: AIAA, 2012: pp. 9–12.

[38] S. Grundmann, S. Klumpp, C. Tropea, Experimental and Numerical Investigations of Boundary-Layer Influence Using Plasma-Actuators, in: Act. Flow Control. Notes Numer. Fluid Mech. Multidiscip. Des., Springer, 2007: pp. 56–68.

[39] R. Whalley, K. Choi, Turbulent Boundary Layer Control by DBD Plasma: A Spanwise Travelling Wave, in: AIAA 2010-4840, 2010: pp. 1–19.

[40] K.-S. Choi, T. Jukes, R. Whalley, Turbulent boundary-layer control with plasma actuators, Philos. Trans. R. Scociety A. (2011) 1443–1458. doi:10.1098/rsta.2010.0362.

[41] D.M. Schatzman, F.O. Thomas, Turbulent Boundary-Layer Separation Control with Single Dielectric Barrier Discharge Plasma Actuators, AIAA J. 48 (2010) 1620–1634. doi:10.2514/1.J050009.

[42] R.E. Hanson, P. Lavoie, A.M. Naguib, J.F. Morrison, Control of transient growth induced boundary layer transition using plasma actuators, in: Seven IUTAM Symp. Liminar-Turbulent Transtion, Springer, 2010: pp. 183–188.

[43] R.E. Hanson, P. Lavoie, M. Engineering, E. Lansing, Steady-State Closed-Loop Control of Bypass Boundary Layer Transition Using Plasma Actuators Ronald, in: AIAA 2012-1140, 2012: pp. 1–14.

[44] A. Widmann, A. Kurz, B. Simon, S. Grundmann, C. Tropea, Characterization of the Interaction between Tollmien-Schlichting Waves and a DBD Plasma Actuator using Phase-locked PIV, in: 10TH Int. Symp. Part. IMAGE Velocim. - PIV13, 2013.

[45] A. Kurz, S. Grundmann, A. Seraudie, N. Goldin, R. King, Boundary Layer Transition Control using DBD Plasma Actuators, J. Aerospacelab. (2013) 1–8.

[46] Duchmann, Boundary-Layer Stabilization with Dielectric Barrier Discharge Plasmas for Free-Flight Application, PhD thesis, Technischen Universität Darmstadt, 2013.

[47] A. Starikovskiy, N. Aleksandrov, Plasma-assisted ignition and combustion, Prog. Energy Combust. Sci. 39 (2013) 61–110. doi:10.1016/j.pecs.2012.05.003.

[48] A.S. ANKALA, Numerical simulation of plasma assisted turbulent combustion, MSc Thesis, University of Florida, 2011.

[49] J.M. Meek, J.D. Craggs, Electrical Breakdown of Gases, Wiley, New York, 1978.

[50] R.A. Siliprandi, Atmospheric Pressure Plasmas for Surface Modifications, PhD Thesis, UNIVERSIT` A DEGLI STUDI DI MILANO-BICOCCA, 2007.

[51] C. Wang, Numerical modelling of microscale plasma actuators, PhD Thesis, University of Florida, 2009.

[52] K.P. Singh, S. Roy, Modeling plasma actuators with air chemistry for effective flow control, J. Appl. Phys. 101 (2007) 123308. doi:10.1063/1.2749467.

[53] A. V. Likhanskii, M.N. Shneider, S.O. Macheret, R.B. Miles, Modeling of dielectric barrier discharge plasma actuators driven by repetitive nanosecond pulses, Phys. Plasmas. 14 (2007) 073501. doi:10.1063/1.2744227.

[54] B. Jayaraman, Y.-C. Cho, W. Shyy, Modeling of dielectric barrier discharge plasma actuator, J. Appl. Phys. 103 (2008) 053304. doi:10.1063/1.2841450.

[55] J. van Dijk, G.M.W. Kroesen, a Bogaerts, Plasma modelling and numerical simulation, J. Phys. D. Appl. Phys. 42 (2009) 190301. doi:10.1088/0022-3727/42/19/190301.

[56] B. Jayaraman, W. Shyy, Modeling of dielectric barrier discharge-induced fluid dynamics and heat transfer, Prog. Aerosp. Sci. 44 (2008) 139–191. doi:10.1016/j.paerosci.2007.10.004.

[57] G.E. Georghiou, a P. Papadakis, R. Morrow, a C. Metaxas, Numerical modelling of atmospheric pressure gas discharges leading to plasma production, J. Phys. D. Appl. Phys. 38 (2005) R303–R328. doi:10.1088/0022-3727/38/20/R01.

[58] J.P. Boeuf, L.C. Pitchford, Electrohydrodynamic force and aerodynamic flow acceleration in surface dielectric barrier discharge, J. Appl. Phys. 97 (2005) 103307. doi:10.1063/1.1901841.

[59] S. Roy, D. Gaitonde, Modeling Surface Discharge Effects of Atmospheric RF on Gas Flow Control, 43rd AIAA Aerosp. Sci. Meet. Exhib. (2005) 10–13. doi:10.2514/6.2005-160.

[60] S. Roy, Flow actuation using radio frequency in partially ionized collisional plasmas, Appl. Phys. Lett. 86 (2005) 101502. doi:10.1063/1.1879097.

[61] K.P. Singh, S. Roy, Simulation of an asymmetric single dielectric barrier plasma actuator, J. Appl. Phys. 98 (2005) 083303. doi:10.1063/1.2103415.

[62] S. Roy, D. V. Gaitonde, Force interaction of high pressure glow discharge with fluid flow for active separation control, Phys. Plasmas. 13 (2006) 023503. doi:10.1063/1.2168404.

[63] K.P. Singh, S. Roy, Vortical flow control on a conical fore body cross section using an array of pulsed dc actuators, J. Appl. Phys. 101 (2007) 093301. doi:10.1063/1.2720256.

[64] X. Duan, F. He, J. Ouyang, Uniformity of a dielectric barrier glow discharge: experiments and two-dimensional modeling, Plasma Sources Sci. Technol. 21 (2012) 015008. doi:10.1088/0963-0252/21/1/015008.

[65] J.P. Boeuf, Y. Lagmich, T. Unfer, T. Callegari, L.C. Pitchford, Electrohydrodynamic force in dielectric barrier discharge plasma actuators, J. Phys. D. Appl. Phys. 40 (2007) 652–662. doi:10.1088/0022-3727/40/3/S03.

[66] B. Jayaraman, S. Thakur, W. Shyy, Modeling of Fluid Dynamics and Heat Transfer Induced by Dielectric Barrier Plasma Actuator, J. Heat Transfer. 129 (2007) 517. doi:10.1115/1.2709659.

[67] B. Jayramann, Computational Modeling of glow discharge-induced fluid dynamics, PhD Thesis, University of Florida, 2006.

[68] H. Nishida, T. Abe, Numerical analysis of plasma evolution on dielectric barrier discharge plasma actuator, J. Appl. Phys. 110 (2011) 013302. doi:10.1063/1.3603001.

[69] C.-C. Wang, S. Roy, Microscale plasma actuators for improved thrust density, J. Appl. Phys. 106 (2009) 013310. doi:10.1063/1.3160304.

[70] A. V. Likhanskii, M.N. Shneider, S.O. Macheret, R.B. Miles, Modeling of dielectric barrier discharge plasma actuator in air, J. Appl. Phys. 103 (2008) 053305. doi:10.1063/1.2837890.

[71] A. V Likhanskii, M.N. Shneider, D.F. Opaits, R.B. Miles, Numerical modeling of DBD plasma actuators and the induced air flow, in: AIAA 2007-4533, 2007.

[72] A. Likhanskii, Study of plasma phenomena at high electric fields in applications for active flow control and ultra-short pulse laser drilling, PhD Thesis, The Pennsylvania State University, 2009.

[73] Y. Lagmich, T. Callegari, L.C. Pitchford, J.P. Boeuf, Model description of surface dielectric barrier discharges for flow control, J. Phys. D. Appl. Phys. 41 (2008) 095205. doi:10.1088/0022-3727/41/9/095205.

[74] J.P. Boeuf, Y. Lagmich, L.C. Pitchford, Contribution of positive and negative ions to the electrohydrodynamic force in a dielectric barrier discharge plasma actuator operating in air, J. Appl. Phys. 106 (2009) 023115.

[75] H. Nishida, T. Nonomura, T. Abe, Characterization of Electrohydrodynamic Force on Dielectric-Barrier-Discharge Plasma Actuator Using Fluid Simulation, World Acad. Sci. Eng. Technol. 71 (2012) 321–325.

[76] J.P. Boeuf, Y. Lagmich, L.C. Pitchford, Contribution of positive and negative ions to the electrohydrodynamic force in a dielectric barrier discharge plasma actuator operating in air, J. Appl. Phys. 106 (2009) 023115. doi:10.1063/1.3183960.

[77] T. Unfer, J. Boeuf, F. Thivet, Modeling of Dielectric Barrier Discharge and coupling with Computational Fluid Dynamics, in: AIAA 2008-1375, 2008.

[78] T. Unfer, J.-P. Boeuf, Modeling and comparison of sinusoidal and nanosecond pulsed surface dielectric barrier discharges for flow control, Plasma Phys. Control. Fusion. 52 (2010) 124019. doi:10.1088/0741-3335/52/12/124019.

[79] C.-C. Wang, S. Roy, Energy and force prediction for a nanosecond pulsed dielectric barrier discharge actuator, J. Appl. Phys. 111 (2012) 103302. doi:10.1063/1.4722202.

[80] H. Nishida, T. Nonomura, T. Abe, Three-dimensional simulations of discharge plasma evolution on a dielectric barrier discharge plasma actuator, J. Appl. Phys. 115 (2014) 133301. doi:10.1063/1.4870384.

[81] J.S. Shang, P.G. Huang, Modeling of ac dielectric barrier discharge, J. Appl. Phys. 107 (2010) 113302. doi:10.1063/1.3415526.

[82] J.S. Shang, P.G. Huang, Surface plasma actuators modeling for flow control, Prog. Aerosp. Sci. 67 (2014) 29–50. doi:10.1016/j.paerosci.2014.01.001.

[83] W. Shyy, B. Jayaraman, A. Andersson, Modeling of glow discharge-induced fluid dynamics, J. Appl. Phys. 92 (2002) 6434. doi:10.1063/1.1515103.

[84] K.P. Singh, S. Roy, Force approximation for a plasma actuator operating in atmospheric air, J. Appl. Phys. 103 (2008) 013305. doi:10.1063/1.2827484.

[85] Y. Suzen, G. Huang, J. Jacob, D. Ashpis, Numerical Simulations of Plasma Based Flow Control Applications, 35th AIAA Fluid Dyn. Conf. Exhib. (2005) 1–11. doi:10.2514/6.2005-4633.

[86] C.L. Enloe, T.E. McLaughlin, R.D. VanDyken, K.D. Kachner, E.J. Jumper, T.C. Corke, ,Mechanisms and Responses of a Single Di- electric Barrier Plasma Actuator: Plasma Morphology, AIAA J. 42 (2004).

[87] D.M. Orlov, Modelling and simulation of single dielectric barrier discharge plasma actuators, PhD Thesis, University of Notre Dame, 2006.

[88] S. Lemire, H.D. Vo, Reduction of Fan and Compressor Wake Defect Using Plasma Actuation for Tonal Noise Reduction, J. Turbomach. 133 (2011) 011017. doi:10.1115/1.4000540.

[89] B.E. Mertz, Refinemet, Validation, and Implemention of Lumped Circut Element Model for Single Dielectric Barrier Discharge Plasma Actuators, PhD thesis, University of Notre Dame, 2010.

[90] H.G. Weller, G. Tabor, H. Jasak, C. Fureby, A tensorial approach to computational continuum mechanics using object-oriented techniques, Comput. Phys. 12 (1998) 620. doi:10.1063/1.168744.

[91] P. Scheubert, Modelling and Diagnostics of Low Pressure Plasma Discharges, PhD Thesis, Technischen Universitat Munchen, 2001.

[92] K.G. Marchand, Computational Model of One-Dimensional Dielectric Barrier Discharges, MSc Thesis, Air force institude of technology, 2005.

[93] C.S. Charles, Computaional modeling of the dielectric barrier discharge (DBD) device for aeronautical applications, MSc Thesis, Air Force Institute of Technology, 2006.

[94] D. Marshall, A. Federov, V. Soloviev, Mathematical Fluid Dynamics of Plasma Control over High Speed Wings, 2009.

[95] A. Fiala, L.. Pitchford, J.P. Boeuf, Two-dimensional, hybrid model, Phys. Rev. E. 49 (1994) 5607–5624.

[96] T. Martens, A. Bogaerts, W. Brok, J. van Dijk, Computer simulations of a dielectric barrier discharge used for analytical spectrometry, Anal. Bioanal. Chem. 388 (2007) 1583–94. doi:10.1007/s00216-007-1269-0.

[97] W. Morgan, J.P. Boeuf, L.C. Pitchford, BOLSIG Boltzmann Solver Monument, USA— Toulouse Fr. (1996).

[98] N. Balcon, Atmospheric pressure Radio Frequency discharges , diagnostic and numerical modeling, PhD Thesis,Australian National University, 2007.

[99] G.J.M. Hagelaar, Modeling of microdischarges for display technology, PhD Thesis, Technische Universiteit Eindhoven, 2000.

[100] G.J.M. Hagelaar, F.J. De Hoog, G.M.W. Kroesen, Boundary conditions in fluid models of gas discharges, Phys. Rev. E. 62 (2000) 1452–1454.

[101] R. Arpa, D. D'Ambrosio, High-Order Accurate Implicit Scheme for Drift-Diffusion Equations and Application to Dielectric Barrier Discharges, 40th AIAA Plasmadynamics Lasers Conf. (2009) 1–17. doi:10.2514/6.2009-3909.

[102] B. Jayaraman, W. Shyy, S. Thakur, Modeling of dielectric barrier discharge and resulting fluid dynamics, 44th AIAA Aerosp. Sci. Meet. Exhib. (2006) 1–20. doi:10.2514/6.2006-686.

[103] G. Strang, On the Construction and Comparison of Difference Schemes, SIAM J. Numer. Anal. 5 (2013) 506–517.

[104] R. Tyson, L.G.S. Randall, Fractional step methods applied to a chemotaxis model, Math. Biol. 475 (2000) 455–475.

[105] D.L. Ropp, J.N. Shadid, C.C. Ober, Studies of the accuracy of time integration methods for reaction–diffusion equations, J. Comput. Phys. 194 (2004) 544–574. doi:10.1016/j.jcp.2003.08.033.

[106] C.D. Meyer, D.S. Balsara, T.D. Aslam, A stabilized Runge–Kutta–Legendre method for explicit super-time-stepping of parabolic and mixed equations, J. Comput. Phys. 257 (2014) 594–626. doi:10.1016/j.jcp.2013.08.021.

[107] C.D. Meyer, D.S. Balsara, T.D. Aslam, A second-order accurate Super TimeStepping formulation for anisotropic thermal conduction, Mon. Not. R. Astron. Soc. 422 (2012) 2102–2115. doi:10.1111/j.1365-2966.2012.20744.x.

[108] G.J.M. Hagelaar, G.M.W. Kroesen, Speeding Up Fluid Models for Gas Discharges by Implicit Treatment of the Electron Energy Source Term, 12 (2000) 1–12. doi:10.1006/jcph.2000.6445.

[109] T. Unfer, Méthode asynchrone pour la modélisation d'actuateurs plasma destinés au contrôle d'écoulement, PhD Thesis, UNIVERSITÉ DE TOULOUSE, 2008.

[110] T. Unfer, J.P. Boeuf, Modelling of a nanosecond surface discharge actuator, J. Phys. D. Appl. Phys. 42 (2009) 194017. doi:10.1088/0022-3727/42/19/194017.

[111] H. Nishida, T. Abe, Numerical analysis of plasma evolution on dielectric barrier discharge plasma actuator, J. Appl. Phys. 110 (2011) 013302. doi:10.1063/1.3603001.

[112] Y. Lagmich, T. Callegari, L.C. Pitchford, J.P. Boeuf, H. Search, C. Journals, et al., Model description of surface dielectric barrier discharges for flow control, J. Phys. D. Appl. Phys. 41 (2008) 095205. doi:10.1088/0022-3727/41/9/095205.

[113] A. Dumas, M. Madonia, I. Giuliani, M. Trancossi, MAAT Cruiser/Feeder Project: Criticalities and Solution Guidelines., SAE Tech. Pap. 01 (2011) 2784.

[114] M. Abdollahzadeh, J.C. Páscoa, P.J. Oliveira, Numerical Modeling of Boundary Layer Control Using Dielectric Barrier Discharge, in: Conferência Nac. Em Mecânica Dos Fluidos, Termodinâmica E Energ. MEFTE, 2012: p. Paper No 61, pp. 1¬10.

[115] M. Abdollahzadeh, J.C. Páscoa, P.J. Oliveira, Numerical investigation on efficiency increase in high altitude propulsion systems using Plasma actuators, in: ECCOMAS 2012 - Eur. Congr. Comput. Methods Appl. Sci. Eng., 2012: pp. 6563–6581.

[116] A.Y. Starikovskii, A.A. Nikipelov, M.M. Nudnova, D. V Roupassov, SDBD plasma actuator with nanosecond pulse-periodic discharge, Plasma Sources Sci. Technol. 18 (2009) 034015. doi:10.1088/0963-0252/18/3/034015.

[117] M. Abdollahzadeh, J.C. Páscoa, P.J. Oliveira, Two-dimensional numerical modeling of interaction of micro-shock wave generated by nanosecond plasma actuators and transonic flow, J. Comput. Appl. Math. 270 (2013) 401–416. doi:10.1016/j.cam.2013.12.030.

[118] A.R. Hoskinson, Measurements and Simulations of Surface Dielectric Barrier Discharges Used as Plasma Actuators, 2012.

[119] S.T. Surzhikov, J.S. Shang, Two-Component plasma Model for two-dimensional glow discharge in magnetic field, J. Comp. Phys. 199(2004)437-467. (n.d.).

[120] X. Che, T. Shao, W. Nie, P. Yan, Numerical simulation on a nanosecond-pulse surface dielectric barrier discharge actuator in near space, J. Phys. D. Appl. Phys. 45 (2012) 145201. doi:10.1088/0022-3727/45/14/145201.

[121] D. Breden, L.L. Raja, Modeling of an Atmospheric Pressure Plasma Jet with Flow effects, in: AIAA 2013-0920, 2013.

[122] I. Adamovich, S.O. Macheret, J.W. Rich, C.E. Treanor, Vibrational Relaxation and Dissociation behind shock Waves Part2: Master Equation Modeling, AIAA. 33 (1995) 1070–1075.

[123] S.P. AFlitti, Gas heating in fast pulsed discharges in N2O2 mixtures, Eur. Phys. J. Appl. Phys. 45 (2009) 21001.

[124] L.. Pichford, G.J.M. Hagelaar, Solving the Boltzman equation to obtain electron transport coefficients and rate coefficients for fluid models, Plasma Sources Sci. Technol. 14 (2005) 722.

[125] D. V. Gaitonde, Analysis of plasma-based flow control mechanisms through large-eddy simulations, Comput. Fluids. 85 (2013) 19–26. doi:10.1016/j.compfluid.2012.09.004.

[126] S.B. Leonov, D.A. Yarantsev, V.G. Gromov, A.P. Kuriachy, Mechanisms of Flow Control by Near-Surface Electrical Discharge Generation, in: AIAA 2005-780, 2005: pp. 1–10.

[127] D.D. Knight, Survey of Aerodynamic Drag Reduction at High Speed by Energy Deposition, J. Propuls. Power. 24 (2008) 1153–1167. doi:10.2514/1.24595.

[128] M.H.M. D.V. Gaitonde, A Semi-Emprical Model of a Nanosecond Pulsed Plasma Actuator For Flow Control Simulations with LES, AIAA Pap. (2012)-0184. (n.d.).

[129] M.J.K. P.L.G.Ventzek, , R.J. Hoekstra, Two-dimensional modelling of high plasma density inductively coupled sources for materials processing, J. Vac. Sci. Technol. B 12(1994)461-77. (n.d.).

[130] J. Poggie, N.J. Bisek, Numerical Simulation of Nanosecond-Pulse Electrical Discharges, in: AIAA 2012-1025, 2012.

[131] P.L. Roe., Approximate Riemann solvers, Parameter Vectors, and Difference Schemes, J. Comput. Phys. 43 (1981) 357–372.

[132] B.K. F. Menter, J. Carregal Ferreira, T. ESCH, The SST Turbulance Model with improved wall treatment for heat transfer predictions in Gas Turbines., in: Proc. Int. Gas Turbine Congr. Tokyo, Nov. 2-7. IGTC2003-TS-059., n.d.

[133] J. Boeuf, L.C. Pitchford, Electrohydrodynamic force and aerodynamic flow acceleration in surface dielectric barrier discharge, J. Appl. Phys. 97 (2005) 103307. doi:doi:10.1063/1.1901841.

[134] P. Peschke, Interaction Between Nanosecond Pulse DBD Actuators and Transonic Flow, in: AIAA 2011-3734, 2011: pp. 1–11.

[135] S.M. Aulchenko, V.P. Zamuraev, I. a. Znamenskaya, a. P. Kalinina, D.M. Orlov, N.N. Sysoev, On the possibility of controlling transonic profile flow with energy deposition by means of a plasma-sheet nanosecond discharge, Tech. Phys. 54 (2009) 343–353. doi:10.1134/S1063784209030049.

[136] D. V Roupassov, A.A. Nikipelov, M.M. Nudnova, A.Y. Starikovskii, Flow Separation Control by Plasma Actuator with Nanosecond Pulsed-Periodic Discharge, 47 (2009). doi:10.2514/1.38113.

[137] W. Liu, L. Jia, W. Yan, F. Kong, Y. Hao, Study on the glow discharge in the atmospheric pressure, Curr. Appl. Phys. 11 (2011) S117–S120. doi:10.1016/j.cap.2011.05.002.

[138] T. Matsunuma, T. Segawa, Effects of Input Voltage on Flow Separation Control for Low-Pressure Turbine at Low Reynolds Number by Plasma Actuators, Int. J. Rotating Mach. 2012 (2012) 1–10. doi:10.1155/2012/902548.

[139] M.M. Hollick, M. Arjomandi, B.S. Cazzolato, An investigation into the sensory application of DBD plasma actuators for pressure measurement, Sensors Actuators A Phys. 171 (2011) 102–108. doi:10.1016/j.sna.2011.07.011.

[140] T. Shao, H. Jiang, C. Zhang, P. Yan, M.I. Lomaev, V.F. Tarasenko, Time behaviour of discharge current in case of nanosecond-pulse surface dielectric barrier discharge, EPL (Europhysics Lett. 101 (2013) 45002. doi:10.1209/0295-5075/101/45002.

[141] J.A. Valerioti, T.C. Corke, Pressure Dependence of Dielectric Barrier Discharge Plasma Flow Actuators, AIAA J. 50 (2012) 1490–1502. doi:10.2514/1.J051194.

[142] M.J. Pinheiro, A.A. Martins, Electrical and kinetic model of an atmospheric rf device for plasma aerodynamics applications, J. Appl. Phys. 108 (2010) 033301. doi:10.1063/1.3383056.

[143] J. Bai, J. Sun, Q. Zhang, D. Wang, PIC simulation of RF hydrogen discharges in a transverse magnetic field, Curr. Appl. Phys. 11 (2011) S140–S144. doi:10.1016/j.cap.2011.04.023.

[144] T. Unfer, J.-P. Boeuf, F. Rogier, F. Thivet, Multi-scale gas discharge simulations using asynchronous adaptive mesh refinement, Comput. Phys. Commun. 181 (2010) 247–258. doi:10.1016/j.cpc.2009.09.017.

[145] M.M. Bermudez, R. Sosa, D. Grondona, a Márquez, H. Kelly, G. Artana, Study of a pseudo-empirical model approach to characterize plasma actuators, J. Phys. Conf. Ser. 296 (2011) 012023. doi:10.1088/1742-6596/296/1/012023.

[146] J.-S. Yoon, J.-H. Han, Semi-Empirical Thrust Model of Dielectric Barrier Plasma Actuator for Flow Control, J. Aerosp. Eng. (2013) 1934–5525. doi:10.1061/(ASCE)AS.1943-5525.0000353.

[147] A. Abdoli, I. Mirzaee, A. Anvari, N. Purmahmod, Simulation of body force field effects on airfoil separation control and optimization of plasma actuator, J. Phys. D. Appl. Phys. 41 (2008) 175204. doi:10.1088/0022-3727/41/17/175204.

[148] D.M. Orlov, T.C. Corke, Numerical Simulation of Aerodynamic Plasma Actuator Effects, in: 43rd AIAA Aerosp. Sci. Meet. Exhib. 10, AIAA 2005-1083, 2005: pp. 1–12.

[149] D. V Gaitonde, M.R. Visbal, S. Roy, Control of Flow Past a Wing Section with Plasma-based Body Forces, in: 36th AIAA Plasmadynamics Lasers Conf., AIAA 2005-5302, 2005: pp. 1–14.

[150] D.M. Orlov, T.C. Corke, Electric Circuit Model for Aerodynamic Plasma Actuator, in: 44th AIAA Aerosp. Sci. Meet. Exhib. 9 12 January 2006 Reno Nevada, 2006: pp. 9–12.

[151] V.R. Soloviev, Analytical estimation of the thrust generated by a surface dielectric barrier discharge, J. Phys. D. Appl. Phys. 45 (2012) 025205. doi:10.1088/0022-3727/45/2/025205.

[152] I. Maden, R. Maduta, J. Kriegseis, S. Jakirlić, C. Schwarz, S. Grundmann, et al., Experimental and computational study of the flow induced by a plasma actuator, Int. J. Heat Fluid Flow. 41 (2013) 80–89. doi:10.1016/j.ijheatfluidflow.2013.02.013.

[153] I. Maden, J. Kriegseis, R. Maduta, S. Jakirli, C. Schwarz, S. Grundmann, et al., Derivation of a Plasma-Actuator Model Utilizing Quiescent-Air PIV Data, in: Proceeding 20th Annu. Conf. CFD Soc. Canada, Alberta, Canada, 2012.

[154] J. Kriegseis, C. Schwarz, C. Tropea, S. Grundmann, Velocity-information-based force-term estimation of dielectric-barrier discharge plasma actuators, J. Phys. D. Appl. Phys. 46 (2013) 055202. doi:10.1088/0022-3727/46/5/055202.

[155] N. Benard, A. Debien, E. Moreau, Time-dependent volume force produced by a non-thermal plasma actuator from experimental velocity field, J. Phys. D. Appl. Phys. 46 (2013) 245201. doi:10.1088/0022-3727/46/24/245201.

[156] S. Lemire, H.D. Vo, M.W. Benner, Performance Improvement of Axial Compressors and Fans with Plasma Actuation, Int. J. Rotating Mach. 2009 (2009) 1–13. doi:10.1155/2009/247613.

[157] D. Palmeiro, Modeling of Dielectric Barrier Discharge Plasma Actuators for Flow Control Simulations, MSc Thesis , University of Toronto, 2011.

[158] A. Bouchmal, Modeling of Dielectric-Barrier Discharge Actuator, MSc Thesis, Delft University of Technology, 2011.

[159] F.O. Thomas, T.C. Corke, M. Iqbal, A. Kozlov, D. Schatzman, Optimization of Dielectric Barrier Discharge Plasma Actuators for Active Aerodynamic Flow Control, AIAA J. 47 (2009) 2169–2178. doi:10.2514/1.41588.

[160] V.R. Soloviev, V.M. Krivtsov, Phenomenological Model of the Body Force Induced by Surface Dielectric Barrier Discharge, in: 49th AIAA Aerosp. Sci. Meet. Incl. New Horizons Forum Aerosp. Expo., Orlando, Florida, 2011: pp. 1–14.

[161] R. Durscher, S. Roy, Evaluation of thrust measurement techniques for dielectric barrier discharge actuators, Exp. Fluids. 53 (2012) 1165–1176. doi:10.1007/s00348-012-1349-6.

[162] I.H. Ibrahim, M. Skote, Simulations of the linear plasma synthetic jet actuator utilizing a modified Suzen-Huang model, Phys. Fluids. 24 (2012) 113602. doi:10.1063/1.4767724.

[163] R. Anderson, S. Roy, Actuators using Dry and Humid Air, in: 44th AIAA Aerospace Sciences Meeting and Exhibit, AIAA Anderson, R., & Roy, S. (2006). Actuators using Dry and Humid Air (pp. 1–9). 44th AIAA Aerospace Sciences Meeting and Exhibit, AIAA 2006-0369, 2006: pp. 1–9.

[164] Y. Wu, Y. Li, M. Jia, H. Song, Z. Guo, X. Zhu, et al., Influence of operating pressure on surface dielectric barrier discharge plasma aerodynamic actuation characteristics, Appl. Phys. Lett. 93 (2008) 031503. doi:10.1063/1.2964193.

[165] V.M. Litvinov, V. V. Skvortsov, A.A. Uspenskii, Role of the static pressure in experiments on flow control by means of surface capacitor discharges, Fluid Dyn. 41 (2006) 286–291. doi:10.1007/s10697-006-0042-y.

[166] N. Benard, N. Balcon, E. Moreau, Electric wind produced by a surface dielectric barrier discharge operating in air at different pressures: aeronautical control insights, J. Phys. D. Appl. Phys. 41 (2008) 042002. doi:10.1088/0022-3727/41/4/042002.

[167] J.W. Gregory, C.L. Enloe, G.I. Font, T.E. Mclaughlin, S. Member, Force Production Mechanisms of a Dielectric-Barrier Discharge Plasma Actuator, in: 45th AIAA Aerospace Sciences Meeting and Exhibi, AIAA 2007-185, 2007: pp. 1–13.

[168] T. Abe, Y. Takizawa, S. Sato, A Parametric Experimental Study for Momentum Transfer by Plasma Actuator, in: 45th AIAA Aerosp. Sci. Meet. Exhib., AIAA 2007-187, 2007: pp. 1–11.

[169] N. Benard, A. Debien, E. Moreau, Time-dependent volume force produced by a non-thermal plasma actuator from experimental velocity field, J. Phys. D. Appl. Phys. 46 (2013) 245201. doi:10.1088/0022-3727/46/24/245201.

[170] P. Versailles, V. Gingras-Gosselin, H.D. Vo, Impact of Pressure and Temperature on the Performance of Plasma Actuators, AIAA J. 48 (2010) 859–863. doi:10.2514/1.43852.

[171] G. Ilieva, J. Páscoa, A. Dumas, M. Trancossi, MAAT – Promising innovative design and green propulsive concept for future airship's transport, Aerosp. Sci. Technol. 35 (2014) 1–14. doi:10.1016/j.ast.2014.01.014.

[172] C. Montijn, W. Hundsdorfer, U. Ebert, An adaptive grid refinement strategy for the simulation of negative streamers, J. Comput. Phys. 219 (2006) 801–835. doi:10.1016/j.jcp.2006.04.017.

[173] Y.-C. Cho, W. Shyy, Adaptive flow control of low-Reynolds number aerodynamics using dielectric barrier discharge actuator, Prog. Aerosp. Sci. 47 (2011) 495–521. doi:10.1016/j.paerosci.2011.06.005.

[174] C.L. Kelley, Airfoil Leading and Trailing Edge Sepration Control Using sDBD Plasma Actuators, University of Notre Dame, 2013.

[175] M. Kotsonis, S. Ghaemi, Experimental and numerical characterization of a plasma actuator in continuous and pulsed actuation, Sensors Actuators A Phys. 187 (2012) 84–94. doi:10.1016/j.sna.2012.08.002.

[176] M.L. Post, T.C. Corke, Separation control on high angle of attack airfoil Using plasma actuators, AIAA J. 42 (2004) 2177–2184. doi:10.2514/1.2929.

[177] D. Tsubakino, Y. Tanaka, Effective Layout of Plasma Actuators for a Flow Separation Control on a Wing, AIAA. (2007) 474.

[178] N. Balcon, N. Benard, Y. Lagmich, J.-P. Boeuf, G. Touchard, E. Moreau, Positive and negative sawtooth signals applied to a DBD plasma actuator – influence on the electric wind, J. Electrostat. 67 (2009) 140–145. doi:10.1016/j.elstat.2009.01.019.

[179] M. Kotsonis, S. Ghaemi, Performance improvement of plasma actuators using asymmetric high voltage waveforms, J. Phys. D. Appl. Phys. 45 (2012) 045204. doi:10.1088/0022-3727/45/4/045204.

[180] T. Kimura, K. Udagawa Takashima, H. Yamasaki, Experimental Study of DBD Plasma Actuator with Combination of AC and Nanosecond Pulse Voltage, Electr. Eng. Japan. 185 (2013) 21–29. doi:10.1002/eej.22292.

[181] B. Goeksel, D. Greenblatt, I. Rechenberg, Y. Kastantin, C.N. Nayeri, C.O. Paschereit, Pulsed plasma actuators for active flow control at MAV Reynolds numbers, in: Act. Flow Control. Notes Numer. Fluid Mech. Multidiscip. Des., Springer, 2007: pp. 42–55.

[182] K. Asada, Y. Ninomiya, A. Oyama, K. Fujii, Airfoil Flow Experiment on the Duty Cycle of DBD Plasma Actuator, in: AIAA 2009-531, 2009: pp. 1–14.

[183] P. Audier, D. Hong, A. Leroy, Unsteady Forcing of a Post-stall Flow Over a NACA0012 Airfoil by a Surface DBD actuator, in: AIAA 2012-3052, 2012: pp. 1–9.

[184] M.P. Patel, T.T. Ng, S. Vasudevan, T.C. Corke, M. Post, T.E. McLaughlin, et al., Scaling Effects of an Aerodynamic Plasma Actuator, J. Aircr. 45 (2008) 223–236. doi:10.2514/1.31830.

[185] A.A. Sidorenko, B. V Postnikov, A.D. Budovsky, D. V Roupassov, I.N. Zavialov, N.D. Malmuth, et al., Pulsed Discharge Actuators for Rectangular Wing Separation Control, AIAA. (2007) 941.

[186] K. Mitsuo, S. Watanabe, T. Atobe, H. Kato, U. Tatsuro, M. Tanaka, et al., Lift Enhancement of a Pitching Airfoil in Dynamic Stall by, AIAA. (2013) 1119.

[187] N. Benard, J. Jolibois, E. Moreau, Lift and drag performances of an axisymmetric airfoil controlled by plasma actuator, J. Electrostat. 67 (2009) 133–139. doi:10.1016/j.elstat.2009.01.008.

[188] N. Benard, E. Moreau, Capabilities of the dielectric barrier discharge plasma actuator for multi-frequency excitations, J. Phys. D. Appl. Phys. 43 (2010) 145201. doi:10.1088/0022-3727/43/14/145201.

[189] Y.E. Akansu, F. Karakaya, a. Şanlısoy, Active Control of Flow around NACA 0015 Airfoil by Using DBD Plasma Actuator, EPJ Web Conf. 45 (2013) 01008. doi:10.1051/epjconf/20134501008.

[190] A.J. Lombardi, P.O. Bowles, T.C. Corke, Closed-Loop Dynamic Stall Control Using a Plasma Actuator, AIAA J. 51 (2013) 1130–1141. doi:10.2514/1.J051988.

[191] M. Abdollahzadeh, J.C. Pascoa, P.J. Oliveira, Modified Split-Potential Model for Modeling the Effect of DBD Plasma Actuators in High Altitude Flow Control, Curr. Appl. Phys. 14 (2014) 1160–1170. doi:http://dx.doi.org/10.1016/j.cap.2014.05.016.

[192] K. Asada, K. Fujii, Computational Analysis of Unsteady Flow-field Induced by Plasma Actuator in Burst Mode, AIAA. 5090 (2010) 1–12.

[193] E. Garnier, P.Y. Pamart, J. Dandois, P. Sagaut, Evaluation of the unsteady RANS capabilities for separated flows control, Comput. Fluids. 61 (2012) 39–45. doi:10.1016/j.compfluid.2011.08.016.

[194] F. Menter, T. Esch, Elements of industrial heat transfer prediction, in: Proc. 16th Brazilian Congr. Mech. Eng., 2001: pp. 117–127.

[195] W. Haase, M. Braza, A. Revell, DESider- A European Effort on Hybrid RANS-LES Modeling, in: Notes Numer. Fluid Mech. Multidisiplinary Des. Vol 103, Springer, 2009.

[196] C.L. Ladson, Effects of Independent Variation of Mach and Reynolds Numbers on the Low-Speed Aerodynamic Characteristics of the NACA 0012 Airfoil Section, n.d.

[197] C. He, T.C. Corke, N. Dame, Numerical and Experimental Analysis of Plasma Flow Control Over a Hump Model Electrode AC Voltage Source, in: AIAA, 2007: pp. 1–16.

[198] Y.-C. Cho, W. Shyy, Adaptive control of low-Reynolds number aerodynamics in uncertain environments: Part 1. Disturbance regimes and flow characteristics, Comput. Fluids. 86 (2013) 582–596. doi:10.1016/j.compfluid.2013.04.013.

[199] B. Göksel, D. Greenblatt, I. Rechenberg, Y. Singh, C.N. Nayeri, C.O. Paschereit, Pulsed Plasma Actuators for Separation Flow Control, (2006) 1–4.

[200] A. Asghar, Eric J. Jumper, Thomas C. Corke, on the Use of Reynolds Number as the Scaling Parameter for the Performance of a Plasma Actuator in a Weakly Compressible Flow, in: AIAA, 2006: pp. 2006–21.

[201] T. Sulaiman, H. Aono, E. Agency, S. Sekimoto, M. Anyoji, T. Nonomura, et al., Effect of Burst Frequency and Reynolds Number on Flow Control Authority of DBD Plasma Actuator on NACA0012 Airfoil, in: AIAA 52nd Aerosp. Sci. Meet., 2014: pp. 1–21.

[202] ACHEON Project, (n.d.). acheon.eu/.

[203] M. Trancossi, A. Dumas, S. S. Das, J. C. Páscoa, Design Methods of Coanda nozzle with two streams, INCAS Bull. 6 (2014) 83–95.

[204] J. Shin, S. Mahadevan, Forcing mechanisms in supersonic flow actuation achieved by direct-current surface glow discharge plasma, Aerosp. Sci. Technol. 15 (2011) 18–24. doi:10.1016/j.ast.2010.05.007.

[205] J. Little, M. Nishihara, I. Adamovich, M. Samimy, High-lift airfoil trailing edge separation control using a single dielectric barrier discharge plasma actuator, Exp. Fluids. 48 (2009) 521–537. doi:10.1007/s00348-009-0755-x.

[206] A.Y. Starikovskii, D. V Roupassov, A.A. Nikipelov, M.M. Nudnova, Acoustic Noise and Flow Separation Control by Plasma Actuator, AIAA 2009-695. (2009) 1–28.

[207] Y. Li, Y. Wu, M. Zhou, C. Su, X. Zhang, J. Zhu, Control of the corner separation in a compressor cascade by steady and unsteady plasma aerodynamic actuation, Exp. Fluids. 48 (2009) 1015–1023. doi:10.1007/s00348-009-0787-2.

[208] D. Greenblatt, M. Schulman, A. Ben-Harav, Vertical axis wind turbine performance enhancement using plasma actuators, Renew. Energy. 37 (2012) 345–354. doi:10.1016/j.renene.2011.06.040.

[209] H. Do, W. Kim, M.G. Mungal, M.A. Cappelli, Bluff Body Flow Separation Control using Surface Dielectric Barrier Discharges, AIAA 2007-939. (2007) 1–9.

[210] K.B. Ginn, S.. Jenkins, D.M. Wells, N.M. Brent, Nozzele Plasma Flow Control Utilizing Dielectric Barrier Discharge Plasma Actuators, US 2011/0048025 A1, 2011.

[211] N. Benard, J. Jolibois, M. Fort, G. Touchard, E. Moreau, Control of an axisymmetric subsonic air jet by plasma actuator, Exps. in Fluids. 43 (2007) 603–616.

[212] N. Benard, N. Balcon, E. Moreau, Jet Flow Control by Dielectric Barrier Discharge – Excitation by Axisymmetric and Flapping Modes, in: 47th AIAA Aerosp. Sci. Meet., AIAA 2009-776, 2009: pp. 1–17.

[213] N. Benard, P. Braud, J. Pons, G. Touchard, E. Moreau, Quasi-steady and unsteady actuation by surface non-thermal plasma discharge for control of a turbulent round air jet, J. Turbul. 8 (2007) N49. doi:10.1080/14685240701656139.

[214] I.B. V. Kopiev, N. Ostrikov, M. Zaitsev, Vl. Kopiev, S.G. V. Bityurin, A. Klimov, I. Moralev, Jet Noise Control by Nozzle Surface HF DBD Actuators, in: AIAA 2011-911, 2011: pp. 1–16.

[215] J. Kim, M. Nishihara, I. V Adamovich, M. Samimy, Development of Localized Arc Filament RF Plasma Actuators for High-Speed and High Reynolds Number Flow Control Development of Localized Arc Filament RF Plasma Actuators for High-Speed and High Reynolds Number Flow Control, 2010.

[216] M. Samimy, M. Kearney-Fisher, J.-H. Kim, A. Sinha, High Speed and High Reynolds Number Jet Control Using Arc Filament Plasma Actuators for Noise Mitigation and for Flow and Noise Diagnostics, in: AIAA 2011-22, 2011: pp. 1–19.

[217] R.R. Kleinman, D.J. Bodony, J.B. Freund, Shear-flow excitation mechanisms of recessed localized arc-filament plasma actuators, Phys. Fluids. 22 (2010) 116103. doi:10.1063/1.3507317.

[218] M.T. Shyam S. Das, M. Abdollahzadeh, Jose .C. Pascoa,A. Dumas, Numerical modeling of Coanda effect in a Novel Propulsive System, Int. J. Multiphys. 8 (2014) 181–201.

[219] http://clusterdem.ubi.pt/, (n.d.).

[220] T.M. Rodrigues F., Páscoa J.C., Dumas A., Preliminary design, set-up and testing of a plasma DBD actuator for boundary layer control, in: Int. Conf. Eng., 2013: pp. 27–29 November, Covilhã, University of Beira Inter.

[221] C.M. Xisto, J.C. Pascoa, M. Abdollahzadeh, J.A. Leger, P. Masarati, L. Gagnon, et al., PECyt-Plasma Enhanced Cyclodial Thruster, in: AIAA, 2014: pp. 1–13.

[222] A. Santhanakrishnan, D. a. Reasor, R.P. LeBeau, Characterization of linear plasma synthetic jet actuators in an initially quiescent medium, Phys. Fluids. 21 (2009) 043602. doi:10.1063/1.3097004.

[223] A. Santhanakrishnan, J.D. Jacob, Flow control with plasma synthetic jet actuators, J. Phys. D. Appl. Phys. 40 (2007) 637–651. doi:10.1088/0022-3727/40/3/S02.

Publications

Peer-reviewed Journals

- M. Abdollahzadeh, J.C. Páscoa, P.J. Oliveira (2014), Modified Split-Potential Model for Modeling the Effect of DBD Plasma Actuators in High Altitude Flow Control, Current Applied Physics, Volume 14:8, Pages 1160-1170, ISSN 1567-1739, doi:0.1016/j.cap.2014.05.016.
- M. Abdollahzadeh, J.C. Páscoa, P.J. Oliveira (2014), Two-dimensional numerical modeling of interaction of micro-shock wave generated by nanosecond plasma actuators and transonic flow, Journal of Computational and Applied Mathematics, Volume 270, pages 401-416, ISSN 0377-0427, doi:10.1016/j.cam.2013.12.030.
- M. Abdollahzadeh, F. Rodrigues, J.C. Páscoa, P.J. Oliveira (2015), Numerical Design and Analysis of a Multi-DBD Actuator Configuration for the Experimental Testing of ACHEON Nozzle Model, Aerospace Science and Technology, Volume 41, Pages 259–273.
- M. Abdollahzadeh, J.C. Páscoa, P.J. Oliveira (2014), Comparison of DBD Plasma Actuators Flow Control Authority of the in Different Modes of Actuation, Journal of Applied Physics: D, (Submitted).
- M. Abdollahzadeh, J.C. Páscoa, P.J. Oliveira (2014), Implementation of the Classical Plasma-Fluid Model for Simulation of the Dielectric Barrier Discharge Actuators in OpenFoam, Journal of Computational Physics, (Submitted).

Proceedings of International Conferences with Referee

- Abdollahzadeh M., Páscoa J.C., Oliveira P.J. (2013), "Two dimensional numerical Modeling of nanosecond plasma Actuators, a preliminary study of application in propulsion systems", in Proc. EUCASS 2013 5th European Conference for Aeronautics and Space Sciences Munich, Germany, 1-5 July 2013.
- Abdollahzadeh, M., J. Páscoa, P.J. Oliveira, 2013. "Two Dimensional Numerical Modelling of Micro-Shock Wave Creation in Nanosecond Plasma Actuators", In: FEMTEC 4th International Congress on Computational Engineering and Sciences, May 19-24, Las Vegas, USA.
- Abdollahzadeh M., Páscoa J. C. , Oliveira P.J. (2012), "Numerical investigation on efficiency increase in high altitude propulsion systems using plasma actuators", in Proc. European Congress on Computational Methods in Applied Sciences and Engineering, ECCOMAS 2012.

Proceedings of National Conferences with Referee

- Abdollahzadeh M., Páscoa J.C., Oliveira P.J. (2012), “Numerical Modeling of Boundary Layer Control Using Dielectric Barrier Discharge”, in Proc. Conferência Nacional em Mecânica dos Fluidos, Termodinâmica e Energia MEFTE 2012, Paper No 61, pp. 110.